OPTIMAL URBAN DESIGN FOR OUTDOOR THERMAL COMFORT AND AIR QUALITY

LI ZHENGTONG

PhD

The Hong Kong Polytechnic University

2021

The Hong Kong Polytechnic University

Department of Mechanical Engineering

Optimal Urban Design for Outdoor Thermal Comfort and Air Quality

Li Zhengtong

A thesis submitted in partial fulfillment of the requirements

for the degree of

Doctor of Philosophy

June 2021

CERTIFICATE OF ORIGINALITY

I hereby declare that this thesis is my own work and that, to the best of my knowledge and belief, it reproduces no material previously published or written, nor material that has been accepted for the award of any other degree or diploma, except where due acknowledgment has been made in the text.

_____________(Signed)

LI Zhengtong (Name)

ABSTRACT

Air pollution and urban heat island become worldwide growing concerns, which can directly affect public health. Optimal urban design is a promising method to create a more thermally comfortable and cleaner (less air pollution) outdoor urban environment. However, most of the previous papers focused on either thermal comfort or air quality only; only very limited studies addressed them simultaneously. Under certain cases, the impacts of some urban designs on thermal comfort and air quality present opposite trends. This thesis therefore performs a systematic investigation of optimal urban design on thermal comfort and air quality under the same framework to identify critical design parameters. To achieve the research objective, two sub-works are carried out: 1) exploring the influence of urban morphology, including the frontal area density of urban arrays and height-asymmetric street canyon configurations, 2) investigating the effects of local mitigation strategies, including the building setbacks and tree plantings.

First, the investigation on frontal area density λ_F suggests that with an increase in λ_F, the physiologically equivalent temperature (PET) decreases above most of the sidewalks during the daytime, while only a steady reduction of air quality is observed above the west and east sidewalks of spanwise streets. According to the multivariable regression analysis for Hong Kong, the building density should have a λ_F value between 0.82 and 0.84 to realize PET <38 °C and CO concentration < 30000 μg/m^3 at the same time in the daytime in June.

Second, the investigation on height-asymmetric street canyon configurations indicates that for the step-up canyon (the upwind building is lower than downwind building), a higher upwind building is found to produce a hotter air temperature only at a low wind speed and pollute more severely at both high and low wind speeds, compared with its lower upwind building counterpart. In contrast, for the step-down canyon (the upwind building is higher than downwind building), a higher downwind building is found to produce cooler air temperatures at both high and low wind speeds

and accumulate more pollutants only at a low wind speed, compared with its lower downwind building counterpart. On the other hand, at the high wind speed, both air quality and thermal environment are better in the step-up canyon than in the step-down canyon. However, at the low wind speed, the air quality is higher in the step-down canyon than the step-up canyon, while the step-up canyon still provides a better thermal environment than the step-down canyon.

Third, several design parameters of building setbacks are considered, i.e., the dimensionless height (H_{HS}/W) and dimensionless width (D_{HS}/W) for the horizontal setbacks (HS), as well as the dimensionless length (L_{VS}/L) and dimensionless width (D_{VS}/W) for the vertical setbacks (VS), where W and L are the street width and length. The research on the building setback demonstrates that the horizontal building setbacks are advocated within the low-rise street canyon, which simultaneously improves the thermal comfort and air quality. By manipulating its dimensionless vertical cross-section area S_{HS} (increasing $S_{HS} = H_{HS}/W \times D_{HS}/W$) and its dimensionless aspect ratio H_{HS}/D_{HS} (lowering H_{HS}/D_{HS}), the average PET can decline by up to 2.1 °C and the average pollutant concentration can reduce by up to 66% at the two-side pedestrian level. The vertical building setbacks are more suitable for creating a better outdoor environment for the high-rise street canyon. The dimensionless horizontal cross-section area S_{VS} (= $L_{VS}/L \times D_{VS}/W$) should be as large as possible so that the average PET can decrease by up to 0.7 °C and the average pollutant concentration can reduce by up to 35% at the two-side pedestrian level.

Fourth, the investigations on the tree plantings suggest that increasing LAD (from 0.5 to 2) results in a significant reduction of air temperature (up to 1.5 °C), while it increases gaseous concentrations by up to 370%. The trees with LAD $\leq$ 0.5 are advocated since they hardly worsen the air quality but still induce a 0.5–1 °C reduction in air temperature. Increased H_{trunk}/H causes a lower concentration but a weaker cooling effect. Once $H_{trunk}/H > 0.375$, trees hardly increase concentrations compared to tree-free cases. The trees with $H_{trunk}/H \geq 0.375$ are suggested which still declines air temperature by up to 1.5°C. Increasing $W_{spacing}/W_{canopy}$ causes less pollutant accumulation but a poorer cooling effect. When $W_{spacing}/W_{canopy} \geq 2$, trees almost do not worsen the air quality. The trees with $W_{spacing}/W_{canopy} \geq 2$ are recommended which still causes a 1℃ decrease in air temperature.

Besides, the influence of lateral entrainment is investigated. The results of this analysis demonstrate that lateral entrainment could conditionally reduce the pollutant concentration of low-rise canyons. This reduction, which is affected by lateral entrainment, is confined in a range of approximately 2.5 times the street width from the street ends. In contrast, the lateral entrainment causes a more pronounced reduction in the pollutant concentrations of the high-rise canyons. Besides, all three strategies can considerably facilitate the lateral entrainment, leading to a significant reduction in the cross-section pollutant concentrations (by up to 76%) and therefore a significant reduction in the personal intake fraction *P_IF* of the residents (by up to 81%).

PUBLICATIONS ARISING FROM THIS THESIS

Journal publications

[1] **Li, Z.**, Zhang, H., Wen, C. Y., Yang, A. S., & Juan, Y. H. Effects of frontal area density on outdoor thermal comfort and air quality. ***Building and Environment*** 180 (2020): 107028

[2] **Li, Z.**, Zhang, H., Wen, C. Y., Yang, A. S., & Juan, Y. H. Effects of height-asymmetric street canyon configurations on outdoor air temperature and air quality. ***Building and Environment*** 183 (2020): 107195.

[3] **Li, Z.**, Ming, T., Liu, S., Peng, C., de Richter, R., Li, W., ... & Wen, C. Y. Review on pollutant dispersion in urban areas-part A: Effects of mechanical factors and urban morphology. ***Building and Environment*** (2020): 107534.

[4] **Li, Z.**, Zhang, H., Wen, C. Y., Yang, A. S., & Juan, Y. H. The effects of lateral entrainment on pollutant dispersion inside a street canyon and the corresponding optimal urban design strategies. ***Building and Environment*** (2021): 107740.

[5] **Li, Z.**, Ming, T., Shi, T., Zhang, H., Wen, C. Y., Lu, X., ... & Peng, C. Review on the dispersion of traffic-related air pollutants in urban areas-part B: Local mitigation strategies, optimization framework, and evaluation theory. ***Building and Environment*** (2021), 107890.

[6] **Li, Z.**, Zhang, H., Wen, C. Y., Yang, A. S., & Juan, Y. H. Effects of building setback on the outdoor thermal comfort and air quality in street canyons (Submitted to ***Building and Environment***).

[7] **Li, Z.**, Zhang, H., Wen, C. Y., Yang, A. S., & Juan, Y. H. Effects of tree planting on the outdoor thermal comfort and air quality in street canyons (Submitted to ***Science of the total environment***).

ACKNOWLEDGEMENTS

I must show my gratitude to my dear wife Libei Huang, the joy of my life, without whom this Ph.D. thesis cannot be finished within three years. It's my great fortune to grow together with her in both research and life.

The deepest thanks go to my dear supervisor Prof. Chih-Yung Wen. He is the most influential person in my personal and academic life. His illuminating suggestion always makes me feel sorry for my negligence. Meanwhile, his warm encouragement always points to where my path is. His forbearing character and the relaxed research atmosphere let me enjoy studying and working here every day. I feel deeply that research is a happy thing instead of pain and stress. Besides, I would like to express my appreciation to Prof. An-Shik Yang for his help and suggestion as well as Prof. Tingzhen Ming for his valuable guidance and enlightenment.

My sincere appreciation is also given to Dr. Hao Zhang, for patiently reading my draft, kindly giving me her feedback for revisions as well as plentiful care in daily life. The experience of studying with her is valuable to me, which trains me to be an independent researcher. I thank all my colleagues and friends in our research group at PolyU.

I am greatly indebted to my dear friends as well, especially Yingying Zhou, Jiyu Li, Man Wang, Yun Liu, Zijing Zhang, Andy Chen, and Jeremy Chang. Without their friendship and kindness, life in Hong Kong would not have been so warm and sweet.

Finally, I want to thank my dear parents for their love and care. They have been doing their utmost to support my every decision, including this time, in pursuit of a Ph.D. degree. I can concentrate on research without any pressure from life.

Although this thesis is the end of my third-years Ph.D. journey, my happy life is going on. Thank everyone for your generous help!

TABLE OF CONTENTS

ABSTRACT ii

PUBLICATIONS ARISING FROM THIS THESIS v

ACKNOWLEDGEMENTS vi

TABLE OF CONTENTS vii

LIST OF FIGURES xi

LIST OF TABLES xxi

NOMENCLATURE xxii

Chapter 1 Introduction 1

1.1 Background and motivation 1

1.2 Literature review 3

1.2.1 Effects of urban morphology 3

1.2.2 Effects of local mitigation strategies 5

1.3 Research gap and objective 8

1.4 Thesis outline 9

Chapter 2 Effects of frontal area density on outdoor thermal comfort and air quality 11

2.1 Introduction 11

2.2 Description of CFD simulations 11

2.2.1 Description of case studies, computational geometry, and grid 11

2.2.2 Governing equation and turbulence model 13

2.2.3 Boundary conditions 15

2.2.4 Solver settings 17

2.2.5 Grid sensitivity analysis 17

2.3 Description of thermal comfort simulation 19

2.3.1 Rayman model 19

2.3.2 Thermal comfort indices 20

2.4 Validation study 20

2.4.1 Validation study of thermal effect 21
2.4.2 Validation study of pollutant dispersion 22
2.5 Results and discussion 23
2.5.1 Wind velocity and flow structure 23
2.5.2 Thermal comfort 26
2.5.3 Air quality 30
2.6 Summary 34
Chapter 3 Effects of height-asymmetric street canyon configurations on outdoor air temperature and air quality 36
3.1 Introduction 36
3.2 Description of CFD simulations 36
3.2.1 Description of case studies, computational geometry, and grid 36
3.2.2 Numerical models 38
3.2.3 Boundary conditions 39
3.2.4 Grid sensitivity analysis 39
3.3 Validation 40
3.4 Richardson number in the asymmetric street canyons 42
3.5 Results and discussion 43
3.5.1 Effect of asymmetric configurations without solar radiation 43
3.5.2 Effect of asymmetric configurations with solar radiation 44
3.6 Summary 56
Chapter 4 Effects of building setback on the outdoor thermal comfort and air quality in street canyons 57
4.1 Introduction 57
4.2 Description of CFD simulations 58
4.2.1 Description of case studies, computational geometry, and grid 58
4.2.2 Numerical models 60
4.2.3 Boundary conditions 60
4.2.4 Grid sensitivity analysis 61

4.3 Results and discussion 62

4.3.1 Low-rise street canyon (*H*/*W* = 1)... 62

4.3.2 High-rise street canyon (*H/W* = 3)... 72

4.4 Summary 81

Chapter 5 Effects of tree planting on the outdoor thermal comfort and air quality in street canyons.. 84

5.1 Introduction 84

5.2 Description of CFD simulations.. 84

5.2.1 Description of case studies, computational geometry, and grid 84

5.2.2 Boundary conditions 87

5.2.3 Numerical models 88

5.2.4 Description of tree model in CFD simulation 90

5.2.5 Grid sensitivity analysis 94

5.3 Validation... 95

5.3.1 Validation of the aerodynamic effect of trees and pollutant dispersion 95

5.3.2 Validation of the cooling effect of trees.. 96

5.4 Results.. 97

5.4.1 Influence of aerodynamic effect and cooling effect 97

5.4.2 Effects of the leaf area density 101

5.4.3 Effects of the trunk height..106

5.4.4 Effects of the tree spacing 110

5.5 Summary 116

Chapter 6 Effects of lateral entrainment on pollutant dispersion inside a street canyon and the corresponding optimal urban design strategies 120

6.1 Introduction..120

6.2 Description of wind tunnel experiments..121

6.3 Description of CFD simulations...123

6.3.1 Description of case studies, computational geometry, and grid 123

6.3.2 Governing equation and turbulence model 125

6.3.3 Boundary conditions 126

6.3.4 Solver settings..128

6.3.5 Grid sensitivity analysis 128

6.4 Validation study 132

6.5 Results and discussion 133

6.5.1 Effects of the lateral entrainment..133

6.5.2 Optimal urban design strategies for lateral entrainment 145

6.6 Summary..155

Chapter 7 Conclusions and recommendations for future work 158

7.1 Summary of main contributions..158

7.2 Suggestions for future work..160

REFERENCES 163

Appendices..175

LIST OF FIGURES

Figure 2.1 (a) Geometric model, boundary conditions, sun positions (0800, 1200, and 1600 LST), and schematic diagrams showing the pedestrian level and spanwise (Sp-canyon, red) and streamwise (St-canyon, blue) street canyons. (b) Schematic diagrams showing the urban-like geometries investigated with increasing λ_F. (c) Schematic diagrams showing the monitoring points for thermal comfort and air quality. (d) Schematic diagrams showing the volumetric pollutant sources. 13

Figure 2.2 Grid-independent validation. 18

Figure 2.3 Fish-eye images in the middle of the north sidewalk, obtained from SkyHelios. 19

Figure 2.4 Comparison of the simulated data with the wind tunnel data by Uehara et al. [46]. (a) normalized streamwise u/U_{2H} and (b) normalized temperature $(T\text{-}T_g)/(T_{in}\text{-}T_g)$. SKE, RNG, and RKE denote the standard, RNG, and realized k-ε models, respectively; WT denotes the wind tunnel data. 22

Figure 2.5 Comparison of the simulated data with the wind tunnel data by Meroney et al. [112]. SKE, RNG, and RKE denote the standard, RNG, and realized k-ε models, respectively, WT denotes the wind tunnel data, LS represents the data on the leeward side and WS represents the data on the windward side. 23

Figure 2.6 Predicted wall temperature and 3D streamlines in the Sp-canyon at various solar times for $\lambda_F = 0.25$. 25

Figure 2.7 Predicted wall temperature contours and 3D streamlines in the Sp-canyon for different frontal area densities at 1200 LST and 1600 LST. 26

Figure 2.8 Predicted air temperature contours at the pedestrian level at various solar times when $\lambda_F = 0.125$ (the black-dashed frames indicate the regions shaded by the surrounding buildings). 27

Figure 2.9 Predicted air temperature contours at the pedestrian level for various λ_F settings at 1200 LST and 1600 LST (the black-dashed frames indicate the regions shaded by the surrounding buildings). 28

Figure 2.10 Predicted average air temperatures at the pedestrian level above the sidewalks in the (a) Sp-canyon and (b) St-canyon for different λ_F values at 0800 LST, 1200 LST and 1600 LST. 29
Figure 2.11 Predicted PET profiles at the pedestrian level above sidewalks in the (a) Sp-canyon and (b) St-canyon for different λ_F values at 0800 LST, 1200 LST and 1600 LST. 30
Figure 2.12 Predicted CO concentration contours at the pedestrian level for various λ_F settings at 1200 LST and 1600 LST. 31
Figure 2.13 Predicted average CO concentration profiles at the pedestrian level above the sidewalks: (a) Sp-canyon and (b) St-canyon for different λ_F values at 0800 LST, 1200 LST and 1600 LST. 32
Figure 3.1 (a) The geometric model and boundary condition and (b) various asymmetric street canyon configurations 38
Figure 3.2 Field measurements by Idczak et al. [117]: (a) An overview, (b) the instrumentation in the investigated street and (c) CFD model for the validation of wall temperature 42
Figure 3.3 Predicted wind velocity at the pedestrian level and 3D streamlines for various asymmetric street canyon configurations under a high wind speed without solar radiation: the wind velocity at the pedestrian level for (a) H_1/ H_2= 1/3, (b) H_1/ H_2= 2/3, (e) H_1/ H_2= 3/1, and (f) H_1/ H_2= 3/2; and 3D streamlines for (c) H_1/ H_2= 1/3, (d) H_1/ H_2= 2/3 (g) H_1/ H_2= 3/1, and (h) H_1/ H_2= 3/2. (The blue arrow denotes the flow direction within the street canyon.)... 44
Figure 3.4 Predicted wind velocity at the pedestrian level and 3D streamlines for various step-up street canyon configuration at LSTs of 0800 and 1600 under the high wind speed of 3 m/s: the wind velocity at the pedestrian level for (a) H_1/ H_2= 1/3 at 0800 LST, (b) H_1/ H_2= 2/3 at 0800 LST, (e) H_1/ H_2= 1/3 at 1600 LST, and (f) H_1/ H_2= 2/3 at 1600 LST; and 3D streamlines for (c) H_1/ H_2= 1/3 at 0800 LST, (d) H_1/ H_2= 2/3 at 0800 LST, (g) H_1/ H_2= 1/3 at 1600 LST, and (h) H_1/ H_2= 2/3 at 0800 LST. (The blue arrow denotes the flow direction within the street canyon.)..................................... 46

Figure 3.5 Predicted wind velocity at the pedestrian level and 3D streamlines for various step-down street canyon configurations at LSTs of 0800 and 1600 under the high wind speed of 3 m/s: the wind velocity at the pedestrian level for (a) H_1/ H_2= 3/1 at 0800 LST, (b) H_1/ H_2= 3/2 at 0800 LST, (e) H_1/ H_2= 3/1 at 1600 LST, and (f) H_1/ H_2= 3/2 at 1600 LST; and 3D streamlines for (c) H_1/ H_2= 3/1 at 0800 LST, (d) H_1/ H_2= 3/2 at 0800 LST, (g) H_1/ H_2= 3/1 at 1600 LST, and (h) H_1/ H_2= 3/2 at 0800 LST. (The blue arrow denotes the flow direction within the street canyon.) 47

Figure 3.6 Predicted CO concentrations at the pedestrian level for various asymmetric street canyon configurations at LSTs of 0800 and 1600 under the high wind speed of 3 m/s: the step-up canyon with (a) H_1/ H_2= 1/3 at 0800 LST, (b) H_1/ H_2= 2/3 at 0800 LST, (c) H_1/ H_2= 1/3 at 1600 LST, and (d) H_1/ H_2= 2/3 at 1600 LST; and the step-down canyon with (e) H_1/ H_2= 3/1 at 0800 LST, (f) H_1/ H_2= 3/2 at 0800 LST, (g) H_1/ H_2= 3/1 at 1600 LST, and (h) H_1/ H_2= 3/2 at 1600 LST. 48

Figure 3.7 Predicted air temperatures at the pedestrian level for various asymmetric street canyon configurations at LSTs of 0800 and 1600 under the high wind speed of 3 m/s: the step-up canyon with (a) H_1/ H_2= 1/3 at 0800 LST, (b) H_1/ H_2= 2/3 at 0800 LST, (c) H_1/ H_2= 1/3 at 1600 LST, and (d) H_1/ H_2= 2/3 at 1600 LST; and the step-down canyon with (e) H_1/ H_2= 3/1 at 0800 LST, (f) H_1/ H_2= 3/2 at 0800 LST, (g) H_1/ H_2= 3/1 at 1600 LST, and (h) H_1/ H_2= 3/2 at 1600 LST. 49

Figure 3.8 Predicted average values at the pedestrian level for step-up and step-down cases: (a) the wind velocities, (b) CO concentration, and (c) Air temperature under the high wind speed of 3 m/s at LSTs of 0800 and 1600. The *y*-axis of Fig. 12 (c) starts from the reference air temperature (27.3 °C) at 0800 LST, and the grey line denotes the reference air temperature (29.1°C) at 1600 LST.. 50

Figure 3.9 Predicted wind velocity at the pedestrian level and 3D streamlines for various step-up street canyon configurations at LSTs of 0800 and 1600 under the low wind speed of 0.5 m/s: the wind velocity at the pedestrian level for (a) H_1/ H_2= 1/3 at 0800 LST, (b) H_1/ H_2= 2/3 at 0800 LST, (e) H_1/ H_2= 1/3 at 1600 LST, and (f) H_1/ H_2= 2/3 at 1600 LST; and 3D streamlines for (c) H_1/ H_2= 1/3 at 0800 LST, (d) H_1/ H_2= 2/3 at 0800 LST, (g) H_1/ H_2= 1/3 at 1600 LST, and (h) H_1/ H_2= 2/3 at 0800 LST. (The blue arrow denotes the flow direction within the street canyon.)..................................... 51

Figure 3.10 Predicted wind velocity at the pedestrian level and 3D streamlines for various step-down street canyon configurations at LSTs of 0800 and 1600 under the low wind speed of 0.5 m/s: the wind velocity at the pedestrian level for (a) H_1/ H_2= 3/1 at 0800 LST, (b) H_1/ H_2= 3/2 at 0800 LST, (e) H_1/ H_2= 3/1 at 1600 LST, and (f) H_1/ H_2= 3/2 at 1600 LST; and 3D streamlines for (c) H_1/ H_2= 3/1 at 0800 LST, (d) H_1/ H_2= 3/2 at 0800 LST, (g) H_1/ H_2= 3/1 at 1600 LST, and (h) H_1/ H_2= 3/2 at 0800 LST. (The blue arrow denotes the flow direction within street canyon.)................................... 52

Figure 3.11 Predicted CO concentrations at the pedestrian level for various asymmetric street canyon configurations at LSTs of 0800 and 1600 under low wind speed: the step-up canyon with (a) H_1/ H_2= 1/3 at 0800 LST, (b) H_1/ H_2= 2/3 at 0800 LST, (c) H_1/ H_2= 1/3 at 1600 LST, and (d) H_1/ H_2= 2/3 at 1600 LST; and the step-down canyon with (e) H_1/ H_2= 3/1 at 0800 LST, (f) H_1/ H_2= 3/2 at 0800 LST, (g) H_1/ H_2= 3/1 at 1600 LST, and (h) H_1/ H_2= 3/2 at 1600 LST. 53

Figure 3.12 Predicted air temperature at the pedestrian level for various asymmetric street canyon configurations at LSTs of 0800 and 1600 under low wind speed: the step-up canyon with (a) H_1/ H_2= 1/3 at 0800 LST, (b) H_1/ H_2= 2/3 at 0800 LST, (c) H_1/ H_2= 1/3 at 1600 LST, and (d) H_1/ H_2= 2/3 at 1600 LST; and the step-down canyon with (e) H_1/ H_2= 3/1 at 0800 LST, (f) H_1/ H_2= 3/2 at 0800 LST, (g) H_1/ H_2= 3/1 at 1600 LST, and (h) H_1/ H_2= 3/2 at 1600 LST. 54

Figure 3.13 Predicted average values at the pedestrian level: (a) the wind velocity, (b) the CO concentration and (c) the air temperature under low wind speed of 0.5 m/s at LSTs of 0800 and 1600. The *y*-axis starts from the reference air temperature (27.3 °C) at 0800 LST, and the grey line denotes the reference air temperature (29.1°C) at 1600 LST.. 55

Figure 4.1 Computational geometry and boundary conditions................................. 60

Figure 4.2 Comparison of (a) U/U_{ref}, (b) T, and (c) K along a center vertical line inside the target street canyon in the vertical center plane in coarse, basic, and fine grids... 62

Figure 4.3 Predicted contours of wind velocity for a different horizontal setback with the low-rise street canyon: leeward heating scenario for (a)–(d) and windward heating scenario for (e)–(h).. 64
Figure 4.4 Predicted contours of air temperature for a different horizontal setback with the low-rise street canyon: leeward heating scenario for (a)–(d) and windward heating scenario for (e)–(h).. 66
Figure 4.5 Predicted contours of dimensionless pollutant concentration for a different horizontal setback with the low-rise street canyon: leeward heating scenario for (a)–(d) and windward heating scenario for (e)–(h)... 67
Figure 4.6 Average values of (a) Wind velocity, (b) Air temperature, (c) PET, and (d) Pollutant concentration under different horizontal setback in the low-rise street canyon at the leeward and windward pedestrian level under leeward heating (LH) and windward heating (WH) scenarios... 67
Figure 4.7 Predicted contours of wind velocity for different vertical setbacks with the low-rise street canyon: leeward heating scenario for (a)–(d) and windward heating scenario for (e)–(h)... 69
Figure 4.8 Predicted contours of air temperature for different vertical setbacks with the low-rise street canyon: leeward heating scenario for (a)–(d) and windward heating scenario for (e)–(h)... 70
Figure 4.9 Predicted contours of pollutant concentration for different vertical setbacks with the low-rise street canyon: leeward heating scenario for (a)–(d) and windward heating scenario for (e)–(h)... 71
Figure 4.10 Average values of (a) Wind velocity, (b) Air temperature, (c) PET, and (d) Pollutant concentration under different vertical setback in the low-rise street canyon at the pedestrian level of leeward and windward side under leeward heating (LH) and windward heating (WH) scenarios... 71
Figure 4.11 Predicted contours of wind velocity for different horizontal setbacks with the high-rise street canyon: leeward heating scenario for (a)–(d) and windward heating scenario for (e)–(h)... 73

Figure 4.12 Predicted contours of air temperature for different horizontal setbacks within the high-rise street canyon: leeward heating scenario for (a)–(d) and windward heating scenario for (e)–(h).. 74
Figure 4.13 Predicted contours of pollutant concentration for different horizontal setbacks within the high-rise street canyon: leeward heating scenario for (a)–(d) and windward heating scenario for (e)–(h). 75
Figure 4.14 Average values of (a) Wind velocity, (b) Air temperature, (c) PET, and (d) Pollutant concentration under different horizontal setback in the high-rise street canyon at the pedestrian level of the leeward and windward side under leeward heating (LH) and windward heating (WH) scenarios 76
Figure 4.15 Predicted contours of wind velocity for different vertical setbacks within the high-rise street canyon: leeward heating scenario for (a)–(d) and windward heating scenario for (e)–(h)... 77
Figure 4.16 Predicted contours of air temperature for different vertical setbacks within the high-rise street canyon: leeward heating scenario for (a)–(d) and windward heating scenario for (e)–(h)... 79
Figure 4.17 Predicted contours of pollutant concentration for different vertical setbacks with the high-rise street canyon: leeward heating scenario for (a)–(d) and windward heating scenario for (e)–(h).. 80
Figure 4.18 Average values of (a) Wind velocity, (b) Air temperature, (c) PET, and (d) Pollutant concentration under different vertical setback in the high-rise street canyon at the pedestrian level of the leeward and windward side under leeward heating (LH) and windward heating (WH) scenarios.. 80
Figure 5.1 Computational geometry and boundary conditions................................. 86
Figure 5.2 Grid distributions of the geometric model for the case of H_{trunk}/H = 0.25 and $W_{spacing}/W_{crown}$ = 0 with the basic grid 87
Figure 5.3 Comparison of (a) U/U_{ref}, (b) T, and (c) K along a center vertical line inside the street canyon in the vertical center plane in coarse, basic, and fine grids. 94
Figure 5.4 Comparison results of dimensionless pollutant concentration at the (a) leeward surface and (b) windward surface of the street canyon. 96

Figure 5.5 (a) Measured short- and long-wavelength solar radiation, (b) Measured relative humidity, (c) Measured inlet air and ground temperature, and (d) Comparison of the measured and simulated air temperature in the middle position of the canopy. 97
Figure 5.6 Predicted contours for different effects of trees with the street canyon: ..101
Figure 5.7 Average values of (a) Wind velocity, (b) Air temperature, and (c) Pollutant concentration under different effects of trees at pedestrian level 101
Figure 5.8 Predicted contours for various leaf area density with the street canyon: .104
Figure 5.9 Vertical profiles of air temperature (AT) and pollutant concentration (PC) close to both leeward surface and windward surface for various LAD under (a) LH scenario and (b) WH scenario. These two profiles were drawn from the average AT and PC at each floor (3 m per level). 105
Figure 5.10 Profiles of average air temperature (AT) of (a) pedestrian level, (b) leeward side, and (c) windward side, and average pollutant concentration (PC) of (d) pedestrian level, (e) leeward side, and (f) windward side with various LAD (LAD from 0.5 to 2). 105
Figure 5.11 Predicted contours for various trunk height with the street canyon: (a) Wind velocity, (b) Air temperature, and (c) Pollutant concentration 109
Figure 5.12 Vertical profiles of air temperature (AT) and pollutant concentration (PC) close to both leeward surface and windward surface for various H_{trunk} under (a) Leeward heating scenario (0900) and (b) Windward heating scenario (1500)........................109
Figure 5.13 Profiles of average air temperature (AT) of (a) pedestrian level, (b) leeward side, and (c) windward side, and average pollutant concentration (PC) of (d) pedestrian level, (e) leeward side, and (f) windward side with various H_{trunk} (H_{trunk}/H from 1/8 to 3/4) 110
Figure 5.14 Predicted contours for various tree spacing with the street canyon: (a) Wind velocity, (b) Air temperature, and (c) Pollutant concentration 113
Figure 5.15 Vertical profiles of air temperature (AT) and pollutant concentration (PC) close to both leeward surface and windward surface for various $W_{spacing}$ under (a) Leeward heating scenario (0900) and (b) Windward heating scenario (1500)..........113

Figure 5.16 Profiles of average air temperature (AT) of (a) pedestrian level, (b) leeward side, and (c) windward side, and average pollutant concentration (PC) of (d) pedestrian level, (e) leeward side, and (f) windward side with various $W_{spacing}$ ($W_{spacing}$ /W from 0 to 4)..114

Figure 6.1 Schematic illustration of the canyon vortex caused by the top entrainment and corner vortex caused by the lateral entrainment within a 3-D regular street canyon (H/W = 1) and subjected to perpendicular approaching wind. 121

Figure 6.2 Schematics of (a) test section of the wind tunnel, and (b) wind tunnel model of the urban street canyon (scale 1:150) [165,166]..123

Figure 6.3 (a) Computational geometry and boundary conditions; (b) 3D street canyon configuration with for high-rise and low-rise street canyons 125

Figure 6.4 (a-c) Comparison of dimensionless streamwise mean velocity (u/U_{ref}) along three vertical lines inside the street canyon in the vertical center plane in coarse, basic, and fine grids; (d-f) grid-convergence index (GCI) along the same three vertical lines. 129

Figure 6.5 (a-c) Comparison of dimensionless pollutant concentration K along three vertical lines inside the street canyon in the vertical center plane in coarse, basic, and fine grids; (d-f) grid-convergence index (GCI) along the same three vertical lines. .130

Figure 6.6 Comparison results of (a) dimensionless vertical velocity at y/L = 0, and (b) dimensionless pollutant concentration at the walls of the street canyon..................133

Figure 6.7 Predicted pedestrian level pollutant concentration contours, and pedestrian level wind velocity contours for the low-rise street canyons (H/W= 1) with various street lengths: (a) L/W= ∞, infinite-long street canyon, (b) L/W= 1, short street canyon, (c) L/W= 5, medium street canyon, and (d) L/W= 10, long street canyon......................137

Figure 6.8 Predicted 3D streamlines, x-z cross-section pollutant concentration and wind velocity contours for the low-rise street canyons (H/W= 1) with various street lengths: (a) L/W= ∞, infinite-long street canyon, (b) L/W= 1, short street canyon, (c) L/W= 5, medium street canyon, and (d) L/W= 10, long street canyon. 138

Figure 6.9 Average pollutant concentration along half of the street length for the low-rise street canyon (*H/W*= 1) with various street lengths: (a) average pedestrian level pollutant concentration, and (b) average cross-section pollutant concentration........139
Figure 6.10 Predicted 3D streamlines, pedestrian level pollutant concentration contours, and pedestrian level wind velocity contours for the high-rise street canyons (*H/W*= 3) with various street lengths: (a) *L/W*= ∞, infinite-long street canyon, (b) *L/W*= 1, short street canyon, (c) *L/W*= 5, medium street canyon, and (d) *L/W*= 10, long street canyon. 143
Figure 6.11 Predicted pollutant concentration and wind velocity contours at different *x-z* cross-sections for the high-rise street canyons (*H/W*= 3) with various street lengths: (a) *L/W*= ∞, infinite-long street canyon, (b) *L/W*= 1, short street canyon, (c) *L/W*= 5, medium street canyon, and (d) *L/W*= 10, long street canyon. 145
Figure 6.12 Average pollutant concentration along half of the street length for the high-rise street canyon (*H/W*= 3) with various street lengths: (a) average pedestrian level pollutant concentration and (b) average cross-section pollutant concentration.........145
Figure 6.13 Cross-comparison of the pollutant concentration at the pedestrian level between the base case and the corner-cut design case: (a) low-rise street canyon and (b) high-rise street canyon..149
Figure 6.14 Cross-comparison of the pollutant concentration and personal intake fraction *P_IF* along the street length between the base case and corner-trim design case: (a) Average cross-section pollutant concentration along the street length, (b) *P_IF*, low-rise street canyon, and (c) *P_IF*, high-rise street canyon 149
Figure 6.15 Cross-comparison of the pollutant concentration at the pedestrian level between the base case and design II case: (a) low-rise street canyon and (b) high-rise street canyon 152
Figure 6.16 Cross-comparison of the pollutant concentration and personal intake fraction *P_IF* along the street length between the base case and design II case: (a) Average cross-section pollutant concentration along the street length, (b) *P_IF*, low-rise street canyon, and (c) *P_IF*, high-rise street canyon. 152

Figure 6.17 Cross-comparison of the pollutant concentration at the pedestrian level between the base case and design III case: (a) low-rise street canyon and (b) high-rise street canyon 155
Figure 6.18 Cross-comparison of the pollutant concentration and personal intake fraction *P_IF* along the street length between the base case and design III case: (a) Average cross-section pollutant concentration along the street length, (b) *P_IF*, low-rise street canyon, and (c) *P_IF*, high-rise street canyon 155

LIST OF TABLES

Table 1.1 Overview of studies on urban microclimate problems in the built environment 3

Table 3.1 Mesh independence study (0800 LST, U_{ref}= 3 m/s and T_{in}= 27.3 °C)........ 40

Table 3.2 Comparison of the predicted non-uniform wall temperature with the field measurement data.. 42

Table 3.3 Bulk Richardson numbers in the asymmetric street canyons under high wind speed.. 47

Table 3.4 Bulk Richardson numbers in the asymmetric street canyons under low wind speed.. 52

NOMENCLATURE

Abbreviations

ACH	Air change rate per hour
AE	Aerodynamic effect
ABL	Atmospheric boundary layer
BCR	Building coverage ratio
CE	Cooling effect
CFD	Computational fluid dynamics
DO	Discrete ordinates model
ESP	Electrostatic precipitator
FAD	Frontal area density
GCI	Grid convergence Index
LH	Leeward heating
LST	Local solar time
PLW	Pedestrian-level wind
PM	Particulate matter
PPL	Pedestrian pathway layer
Sp-canyon	Spanwise street canyon
St-canyon	Streamwise street canyon
SVF	Sky view factor
UDS	User Defined Scalar
UHI	Urban heat island
WH	Windward heating

Symbols

g_i	Gravity acceleration
h_c	Heat transfer coefficients [W/(m^{2}K)]
k_s	Sand grain roughness height

r_a	aerodynamic resistance to transpiration for trees [s/m]
r_s	stomatal resistance to vapor diffusion for trees (= 200– 400) [s/m]
u_i	Velocity component in the i axis
u , v , w	Velocity components in the X, Y, Z directions
z_0	Roughness length, [m]
z_{ref}	Reference building height [m]
C	Pollutant concentration [mg/m^3]
C^*, C^+	Normalized pollutant concentration
D	Molecular diffusion coefficients
D_l	characteristic diameter of leaf [m]
D_t	(= ν_t/S_{ct}) turbulent diffusion coefficients
D_{HS}	Width of horizontal building setback [m]
D_{VS}	Width of vertical building setback [m]
H_{trunk}	Trunk height of tree [m]
H_{HS}	Height of horizontal building setback [m]
H/W	Aspect ratio of street canyon
H_1/H_2	(= upstream (H_1)/ downstream building height (H_2)) Asymmetric aspect ratios of street canyon
I_{in}	Inlet turbulent intensity
K	(= $CU_{ref}HL/S_PV_P$) Dimensionless pollutant concentration
L	Street length [m]
LAD	Leaf area density [m^2/m^3]
LAI	Cumulative leaf area index [m^2/m^2]
L_{canopy}	Canopy length of trees [m]
L_v	Latent heat of vaporization (= 2.5×10^6) [J/kg]
L_P	Length of pollutant source [m]
L_{VS}	Length of vertical building setback [m]
P_IF	Personal intake fraction
PET	Physiologically equivalent temperature [°C]

Q/l	Tracer gas source strength per unit length [g/m/s]
$Q^*(z)$	Attenuation of radiation through the tree canopy [W/m^2]
Q_a^*	Incident net solar radiation from above [W/m^2]
Q_l^*	Net radiative fluxes at the leaf surface [W/m^2]
Q_{El}	Latent heat fluxes at the leaf surface [W/m^2]
Q_{Hl}	Sensible heat fluxes at the leaf surface [W/m^2]
Re	Reynolds number
Ri	Bulk Richardson number
S_{ct}	Turbulent Schmidt number
S_{ui}	Sink term of momentum due to trees [Pa/m]
S_k	Source term of turbulent kinetic energy due to trees [kg/m/s^3]
S_ε	Sink term of turbulent dissipation rate due to trees [kg/m/s^4]
S_p	Pollutant source term [kg/(m^3·s)]
S_T	Source term of energy due to trees [W/m^3]
T_g	Ground temperature [°C]
T_{in}	Inlet air temperature [°C]
T_l	Leaf surface temperature [°C]
T_{lee}	Average leeward air temperature [°C]
T_{ref}	Reference temperature [°C]
T_{win}	Average windward air temperature [°C]
U_{ref}	Reference wind speed [m/s]
U_{ABL}	Neutral ABL velocity [m/s]
V_P	Volume of pollutant source [m^3]
W	Street width [m]
W_b	Building width [m]
W_{crown}	Crown width of trees [m]
$W_{spacing}$	Tree spacing [m]
W_P	Width of pollutant source [m]
Y	Mass fraction of the pollutant distribution

Greeks

α	Power-law exponent for power-law velocity inlet profile
α_T	Thermal diffusivity
β	Thermal expansion coefficient
β_s	Extinction coefficient of solar radiation (=0.78)
γ	Psychometric constant [Pa/°C]
ε_{vl}	Vapor pressure at the leaf surface [Pa]
ε_v	Vapor pressure of the ambient air [Pa]
λ	Pressure loss coefficient for trees [m^{-1}]
λ_F	(= A_F (frontal area [m^2]) / A_T (total surface area [m^2])) Frontal area density
ρ_{ref}	Reference density [kg/m^3]
u^*_{ABL}	ABL friction velocity [m/s]
μ	Dynamic viscosity
μ_t	Turbulent viscosity
κ	von Karman's constant (= 0.42)

Chapter 1 Introduction

1.1 Background and motivation

The recent decades have been characterized by ongoing global urbanization, which accompanies intensive global warming and renders the urban area susceptible to elevated temperature (i.e., the urban heat island (UHI)). It is predicted that the global average surface and air temperature in urban areas, will increase by 2.6– 4.8°C and 2–4°C at the end of this century, respectively [1]. As a result, this more irresistible extreme temperature and associated higher intensity of urban heat stress undoubtedly have negative effects on life's quality of urban dwellers, especially during summer seasons [2,3]. In effect, this global warming phenomenon and UHI is rarely a stand-alone issue during intense and rapid urbanization, which is closely associated with other urban challenges such as urban air pollution. Air pollution also has become one of the worldwide growing concerns, especially in metropolises, which can directly affect public health (e.g., respiratory and lung diseases) [4]. Under this circumstance, there is a more imminent need to solve these two problems, which calls for the creation and maintenance of a more thermally comfortable and cleaner (less air pollution) outdoor urban environment.

In conjunction with full-scale field measurements and wind tunnel experiments, the application of computational fluid dynamics (CFD) simulation to the urban environment has been endorsed as a powerful tool to cover a range of topics involving thermal comfort and air quality [5–10]. Urban wind flow affected by thermal effect could be investigated via two groups of methods. One is full-scale measurements and reduced-scale wind-tunnel experiments, and the other group is a numerical simulation with Computational Fluid Dynamic (CFD). These approaches have their advantages and disadvantages. For full-scale measurement, it could obtain the real-life data under real atmospheric boundary layer conditions [11], but it is relatively difficult to derive the pattern of urban wind flow without the impact of inherently uncontrollable and unsteady meteorological [12]. And the tremendous expense of this method goes into offering a whole image of the flow field because it should be performed in considerable discrete positions equip many samplers and receptors [13]. For the wind-tunnel experiments, it provides more controllable initial and boundary conditions, but it also has the technical difficulties in setting realistic uneven surface temperature under the impact of solar position and shading effect. Thus, the wind tunnel experiment could be a powerful reference experiment to validate the CFD simulation [14], but it is fairly difficult to investigate the urban wind flow affected by realistic thermal effects. To overcome these limitations, CFD simulation is also a useful tool to fully control the initial and boundary conditions considering realistic thermal effects. Meanwhile, it is a cost-effective way to predict reasonably the whole image of the urban wind field. Thus, the CFD method was adopted to investigate the thermal comfort and air quality problem mentioned above. Table 1.1 provides an overview (23 papers) of the studies on thermal comfort and air quality by using the CFD technique, listed in chronological order. Even if not all the related studies are included in this table, it tries to summarize the main measures to improve thermal comfort and air quality.

As summarized in Table 1.1, three main measures for improving the thermal comfort and air quality have been studied in the literature: a) changing the surrounding environment parameters, consisting of ambient wind parameters (wind velocity [15,18,22,23] and direction [19,20]), and the distribution and strength of surface thermal fluxes (e.g. thermal stratifications [18,21,22] and thermal position (or solar position) [17,20,23,24]); b) altering urban morphologies (urban density (e.g. aspect ratio of street canyon [13,16,18,21,25,26], frontal area density [27], and planar area density [13,28],) and urban heterogeneity (e.g. deviation of building height [27] and urban skyline configuration [29]); c) implementing local mitigation strategies (optimizing local features of buildings (e.g. lift-up design [30] and building setback design [31]), adding extra devices/facilities (tree planting [26,32,33], artificial pollutant source [34], and shade facilities [35]), and changing thermal properties of building materials [36,37]). All three measures are directly related to thermal comfort and air quality. From an urban planner standpoint, the latter two measures tend to be a more controllable factor in the pursuit of a better outdoor environment. Consequently, this thesis attempts to investigate the optimal urban morphologies and local mitigation strategies. The outcomes will facilitate our understanding of the enhancement of pollutant and heat dispersion and enable us to create a better outdoor thermal environment and air quality at the same time.

Table 1.1 Overview of studies on urban microclimate problems in the built environment

Study	Ref.	Focus	Sensitivity analysis
Xie et al. (2007)	[25]	Air quality	b (Aspect ratio of street canyon)
Xie et al. (2006)	[15]	Air quality	a (Thermal stratifications & wind velocity)
Buccolieri et al. (2010)	[28]	Air quality	a (wind velocity) & b (Planar area density)
Memon et al. (2010)	[16]	Thermal comfort	a (Aspect ratio of street canyon) & b (Thermal stratifications)
Zhang et al. (2011)	[19]	Air quality & Thermal comfort	b (Frontal area density)
Hwang et al. (2011)	[35]	Thermal comfort	c (Shade devices)
Hang et al. (2012)	[27]	Air quality	b (Deviation of building height)
Qu et al. (2012)	[36]	Air quality	a (Thermal stratifications) & c (Building material)
Vos et al. (2013)	[32]	Air quality	c (Tree filtering capacity)
Santiago et al. (2014)	[23]	Thermal comfort	a (Thermal stratifications & thermal position)
Ramponi et al. (2015)	[13]	Air quality	a (Planar area density)
Tan et al. (2015)	[17]	Air quality	c (Thermal stratifications, thermal position & wind velocity)
Nazarian and Kleissl (2016)	[24]	Air quality	a (Thermal position)
Liu et al. (2016)	[30]	Thermal comfort	c (Lift-up design)
Mei et al. (2016)	[21]	Air quality	b (Aspect ratio of street canyon) & a (Wind velocity & Thermal stratifications)
Lin et al. (2016)	[18]	Air quality	b (Aspect ratio of street canyon) & a (Thermal stratifications)
Nazarian et al. (2017)	[20]	Thermal comfort	a (Thermal position & wind direction) & b (Frontal area density)
Yang et al. (2017)	[38]	Thermal comfort	a (Wind velocity)
Juan et al. (2017)	[31]	Air quality	c (Building setback design)
Sun et al. (2017)	[26]	Thermal comfort	c (Tree coverage ratio)
Wang and Ng (2018)	[22]	Air quality	a (Thermal stratifications)
Taleghani et al. (2018)	[37]	Thermal comfort	c (Building material)
Dash and Elsinga (2018)	[34]	Air quality	c (Artificial pollutant source)
Mei et al. (2019)	[29]	Air quality	b (Urban skyline configuration)
Wang et al. (2020)	[33]	Air quality	c (Tree coverage ratio)

The entry "Sensitivity analysis" refers to different aspects that have been investigated in each study: (a) surrounding environment parameters (ambient wind velocity and direction, thermal stratifications and thermal position), (b) urban morphologies (urban density, e.g., frontal area density and planar area density and urban heterogeneity, e.g., deviation of building height), and (c) local mitigation strategies (optimizing local features of buildings, creating a pollutant sink and a cooling source, adding shade facilities, and changing thermal properties of building materials)

1.2 Literature review

1.2.1 Effects of urban morphology

1.2.1.1 Effects of urban density

Urban density is more than just a ratio that affects the resource efficiency or livability of cities. It also considerably impacts the pollutant distribution and thermal environment in the urban context. This section reviews the effects of urban density (frontal and planar area density) on air quality, as well as thermal comfort.

Typically, planar urban density is described by the building coverage ratio (BCR), which is the ratio of the buildings' footprint area to the total area under consideration

[39]. Kubota et al. [40] found a negative linear correlation between BCR (%) and the average wind velocity at the pedestrian level. This result may be attributable to a reduction in the pressure difference between buildings, which limits the ventilation potential in areas of high urban density [28,41,42]. Therefore, it follows that there is a negative relationship between air quality and BCR [42].

Srebric et al. [43] pointed out that it is more practical to classify urban using frontal area density (FAD) for the most densely populated cities, e.g., Singapore and Hong Kong. The reason is that the FAD reflects the height blockage in dense areas. Yang et al. [41] reported that the wind velocity increased with an increase in the FAD in the main street canyons (streamwise canyons) due to a strong “Venturi effect”, but it decreased gradually in the secondary street canyons (spanwise canyons). Thus, the average wind speed ratio at the entire pedestrian level decreased with an increase in the FAD, causing the accumulation of pollutants [44]. Shi et al. [45] found that an increase in the FAD resulted in the reduction of the horizontal permeability of urban ventilation, further impeding the dispersion of airborne pollution. However, Nazarian et al. [20] found the thermal comfort did not change monotonically with FAD. With increasing FAD, direct exposure to solar radiation (mean radiant temperature) decreased significantly, while wind sheltering increased. Thus, the influence of the increasing shading effect on thermal comfort level could be set off by the reduced wind velocity.

1.2.1.2 Effects of urban heterogeneity

In urban arrays, the building height and the layout of buildings are rarely uniforms [157]. The irregular building geometry and non-uniform building spacing, height, and layout cause complex flow characteristics, which affect the dilution of pollutants. Therefore, it is crucial to obtain an in-depth understanding of the influence of urban heterogeneity (planar and frontal heterogeneity) and even utilize the heterogeneity to improve pollutant dispersion and thermal environment.

The staggered layout of buildings is a typical non-uniform urban configuration, resulting in planar heterogeneity [46]. Bady et al. [47] observed that the flow structures of aligned and staggered layouts were fundamentally different. Under perpendicular wind, the staggered arrays diverted airflow to downstream obstacles, whereas the aligned arrays caused a channeling flow. Accordingly, higher passive gaseous pollutant concentration was found in the staggered arrays due to their poorer ability to remove pollutants under this wind direction. However, for an oblique wind (θ =45°), the staggered array yielded better ventilation potential because the aligned blocks produced more circular vortices in this wind direction. Differently, Lin et al. [48] stated that the staggered arrays always yielded a lower ventilation efficiency than the aligned arrays under any wind direction (45° < θ < 90°). The possible explanation might be the different distances between two rows of building arrays (different planar building densities). Similarly, Jiang et al. [49] indicated that only by properly staggering the buildings, the staggered urban pattern could have a more superior thermal environment than the uniform urban pattern.

Vertical urban heterogeneity is the result of differences in building heights. Cheng and Castro [50] demonstrated that the non-uniformity of the building height notably enhanced the vertical momentum transport compared with the uniform height model. Similarly, Hang and Li [51] pointed out that the ventilation of secondary streets benefited from a variation in the building height due to the stronger vertical mean flow at the rooftop. Accordingly, Hang et al. [52] concluded that suitable building height configurations improved the breathability level in high-rise urban areas. However, Lin et al. [48] observed that building height differentials weakened horizontal flows along the street, although the vertical air exchange was improved. Therefore, it is difficult to conclude the effectiveness of a non-uniform building height on urban ventilation. In addition, the effects of the building height are strongly spatially dependent [53].

1.2.2 Effects of local mitigation strategies

1.2.2.1 Optimizing local features of buildings

In this section, two approaches to optimizing local features of buildings are reviewed, i.e., the lift-up design and building setback. Because both approaches are believed to play positive roles in improving ventilation, thereby decreasing the accumulation of pollutants and heat in urban areas.

The lift-up design of buildings is frequently used to enhance shading [54]. It creates a semi-open space underneath high-rise residential buildings as a public space for social activities [55,56]. The space created by the lift-up design can act as a wind corridor to increase urban wind circulation and mitigate negative health impacts [57,58]. Therefore, the wind speed nearby elevated buildings (removing low-floor building layers) is enhanced [59,60]. The benefits of integrating the lift-up design into existing buildings for improving ventilation conditions have been demonstrated. The wind tunnel experiments conducted by Xia et al. [61] indicated that the pedestrian-level wind (PLW) ventilation was better for a row of lift-up buildings and the PLW speed was almost 11% higher than that of the non-lift-up buildings. Therefore, it is reported that the lift-up design can result in a 34–50% reduction in the daily pollutant exposure [62]. Meanwhile, Du et al. [63] reported that the thermal comfort can be effectively improved by the lift-up design, especially in summer.

Two kinds of building setbacks have been assessed by different studies, in terms of removing air pollutants or reducing the UHI effect, i.e., the horizontal building setback and vertical building setback. The horizontal building setbacks, also known as the arcade design, are a unique architectural form, and popular in regions with hot and humid climates including China, Japan, and Malaysia. This design is primarily implemented as a half-open space by creating an outside corridor on the side of the main building [64]. The arcade can effectively provide a comfortable passage space for pedestrians, as well as improved ventilation [65]. Wen et al. [66] found that incorporating an arcade design into the ideal street canyon arrangements resulted in a 60% increase in the air change rate per hour (ACH) in the pedestrian pathway layer (PPL) for perpendicular wind since the arcade design increases the total volumetric airflow rate into the PPL through the windward and arcade openings. Accordingly, Huang et al. [67] reported that the presence of the arcade contributed to a lower pedestrian-level pollutant concentration when compared with the reference case without an arcade. Besides the enhancement of ventilation, a field measurement indicated that the air temperature within the arcade space was 3.9 °C lower than the outside sidewalk, thereby generating more pedestrian thermal comfort in summer [68]. This is because the arcade design is capable of offering this cooler space by sheltering from direct solar radiation (short-wave radiation) [35,69,70]. In addition to the typical horizontal building setback, Ng and Chau [71] reported that the vertical setback also improved the in-canyon air quality by enhancing the vertical dispersion of pollutants in the vertical setback area under a perpendicular wind. Moreover, the vertical setback could significantly reduce sunshine hours in the east-west street to create a cool resting space in summer [70]. Therefore, it can be concluded that both vertical and horizontal building setbacks undoubtedly have positive implications on air quality and thermal comfort. In practice, there is probably some opposite influences on the thermal comfort and air quality, when changing the geometry of the building setbacks. Huang et al. [72] found that increasing the height of the arcade was capable of improving ventilation at the measurement points. However, Yin et al. [73] suggested that the height of the arcade should be as low as possible; otherwise, the pedestrians started losing the protection from the thermal stress of solar radiation.

1.2.2.2 Adding extra devices/facilities

Besides improving ventilation to reduce pollutant concentrations or UHI intensity, mitigation of pollutants and heat can be achieved by adding extra devices/facilities.

Powered by electricity, an electrostatic precipitator (ESP) improves the local air quality as an artificial pollutant sink. The potential of ESPs for air pollution exposure reduction has been demonstrated. ESPs were installed to ensure clean air in critical urban areas (such as hospitals or schools) to benefit particularly vulnerable people (such as patients or students) [74]. The ESPs were also installed near sources of high pollutant emissions, such as the major arterial roads or parking garages [75]. Boppana et al. [76] investigated the influence of an ESP installed in a typical street canyon in Singapore. A group of ESPs resulted in a 7.6% reduction in the average particulate matter (PM) levels. Similarly, Lauriks et al. [77] analyzed the pollutant removal by an ESP in an urban street canyon in Antwerp, Belgium. In locations with poor ventilation, the ESP units significantly reduced the concentration level (up to 40%). Nonetheless, the ESP only can solely improve the air quality but does not contribute to better thermal comfort [78].

Differently, tree planting has the potential to achieve better air quality and thermal environment at the same time. It is conventionally deemed that there is a positive relationship between the increased tree coverage ratio and lowered air pollution at the city scale [79–82]. This is based on an underlying argument that trees have the capacity of filtering the air pollution to clean the air flowing through them, i.e. the deposition effect (the deposition of gaseous pollutants and PMs onto leaf surfaces) [32,83]. Therefore, tree planting is generally regarded as a natural pollutant sink to reduce pollutant concentrations in urban areas [84,85]. In effect, trees probably bring some unintended consequences and even potentially “pollute” the urban environment [32]. The deterioration of air quality is attributed to the aerodynamic effect of trees, which greatly obstructs the airflow and decreases air ventilation [86]. Under certain scenarios, the aerodynamic effects might set off the positive impact of trees on pollutant concentration as a natural pollutant sink.

Trees also can directly lead to a reduction in air temperature using evapotranspiration as a cooling source. By releasing water vapor to the surrounding air from the leaf stomata during photosynthesis, the evapotranspiration effect will mediate the latent heat loss [87]. As a result of the conversion of liquid water to vapor, the leaf and the surrounding environment are cooled with the dissipation of the energy load on the leaf [88]. In addition to direct cooling by the evapotranspiration effect, trees can offer the shading effect. Most short-wave radiation by reflection and transmission through their leaves can be effectively removed, which leads to solar attenuation [89,90]. Therefore, it is reported that the presence of trees causes a reduction in air temperature between 0.6 and 2.5°C under the tree crown coverage in summer [91].

1.3 Research gap and objective

Although previous studies have provided many findings regarding the design of urban morphology or local mitigation strategies for the realization of higher air quality or a better thermal environment, they are still not sufficient for the formulation of guidelines for practical urban planning to reduce thermal stress and improve air quality simultaneously. First, the effect of solar radiation was neglected by most previous studies on these urban designs. In practice, the thermally induced flow is typically combined with the mechanically induced flow, which significantly affects the flow field and dispersion of pollutants and heat [24,92–94]. The conclusion obtained from the neutral condition may not be suitable when solar radiation is considered. Second, most of the papers focused on either thermal comfort or air quality only when solar radiation was considered; only very limited studies addressed the increasingly severe issues of air temperature and air quality simultaneously. Under certain cases, the impacts of some urban designs on thermal comfort and air quality are opposite in trend based on the results mentioned above. For instance, lower urban densities enhance the removal of pollutants [27,28], but a better thermal comfort state occurs at higher urban densities [20]. Hence, it is worth investigating the joint effects of these optimal urban design measures on air quality and thermal comfort.

Based on this background, the objectives of this thesis are to 1) study emissions from vehicle exhausts and the thermal environment considering the effects of solar radiation and thereby to evaluate the influence of optimal urban design on the pollutant concentration and thermal comfort level under the same framework; 2) identify critical design parameters for urban morphologies and local mitigation strategies that would enhance pollutant dispersion and improve the thermal environment for some tropical or subtropical cities suffering strong urban heat island effects and poor air quality (e.g. Hong Kong, Singapore, and Kuala Lumpur) [95].

1.4 Thesis outline

Chapter 1 presents a brief description of the background and motivation, the literature review, the research gap, and the objective. The literature review mainly focuses on two aspects, namely, effects of urban morphology and local mitigation strategies,

Chapter 2 presents the effects of frontal area density on outdoor thermal comfort and air quality.

Chapter 3 presents the effects of height-asymmetric street canyon configurations on outdoor air temperature and air quality.

Chapter 4 presents the effects of building setback on the outdoor thermal comfort and air quality in street canyons.

Chapter 5 presents the effects of tree planting on outdoor thermal comfort and air quality in street canyons.

Chapter 6 presents the effects of lateral entrainment on pollutant dispersion inside a street canyon and the corresponding optimal urban design strategies.

Chapter 7 concludes this thesis and provides recommendations for future studies.

Chapter 2 Effects of frontal area density on outdoor thermal comfort and air quality

2.1 Introduction

As discussed above, the urban density can be classified by its frontal area density, λ_F (defined as the ratio of the frontal area, A_F, to the total surface area, A_T; see Figure 2.1(b)), or plan area density, λ_P (defined as the ratio of the plan area, A_P, to the total surface area, A_T). However, utilization of the frontal area density to represent the building arrays in the most densely populated cities is more practical, as numerous high-rise buildings that cause height blockages can be found in urban areas such as Hong Kong, Singapore, and New York [43]. Based on previous literature, the typical frontal area density of Hong Kong ranges from 0.4 to 1.07 [51,52,57,96].

Accordingly, the frontal density area will be chosen to study its influence on pollutant concentration and thermal comfort in the first place. In this chapter, the objective is to find out the critical frontal area density for the improvement of the outdoor thermal environment with reduced outdoor air pollution at the same time.

2.2 Description of CFD simulations

2.2.1 Description of case studies, computational geometry, and grid

The urban geometry under consideration is a 6×6 matrix of buildings with various frontal area densities λ_F (= 0.0825, 0.125, 0.25, 0.75 and 1.25), as shown in Figure 2.1 (a) and (b). As mentioned earlier, λ_F is the ratio of the frontal area (A_F) to the total surface area (A_T). For various H (building height) at a fixed W (street width) of 20 [m], the corresponding aspect ratios, H/W, for the above λ_F are 0.33, 0.5, 1, 3, and 5, respectively. Apart from the effect of various λ_F, the calculations are conducted under steady-state weather conditions at a Local Solar Time (LST) between 7 and 17 on a clear summer day (June 15) in Hong Kong.

The size and discretization of the computational domain are referred from the practice guidelines by Tominaga et al. [97]. Thus, the dimensions of the computational domain are based on the parameter H as follows: the axial distance between the velocity inlet and windward faces of the first row of buildings is $5H$, the spanwise ranges between the sidewalls of buildings and symmetric boundaries on both sides are all $5H$, and the outlet boundary is $15H$ away from the leeward faces of the last row of buildings, as displayed in Figure 2.1(a).

Besides, as depicted in Figure 2.1(a) and (c), the space among building arrays is separated into two kinds of street canyons, namely, the streamwise street canyon (St-canyon) and the spanwise street canyon (Sp-canyon) [98]. In addition, this chapter adopts the space amid the central four buildings to replicate the scenario of any single building surrounded by many other buildings in Hong Kong. Since the distributions of the air temperature and wind velocity can vary significantly on different sidewalks due to the shadow effect, ten monitoring points on each sidewalk are chosen to examine the associated thermal comfort and air quality at the pedestrian level, as shown in Figure 2.1(c). These points are arranged 1 m away from the building's surface and 1.5 m above ground (the pedestrian height).

ANSYS/ICEM® is employed as a preprocessor to construct computational grids for our numerical models. Herein, this chapter implements fully structured hexahedral (HEX) cells to ensure the high quality of the computational mesh system. With consideration of the relatively large temperature and pollutant concentration gradients near the ground and building surfaces, the finest grids are arranged around these two kinds of walls. To conduct the mesh-independent study, the case of $\lambda_F = 0.25$ is referred to as the base model, with three different grid densities. For coarse/medium/fine meshes (with cell numbers of 3,569,046, 6,625,578, and 9,778,068, respectively), the finest grid sizes of 1/0.5/0.25 m are set directly above the ground and building surfaces. Then, the results of grid-sensitivity analysis discussed later indicate that the medium grid provides nearly grid-independent results, which can be further used for the remainder of this chapter.

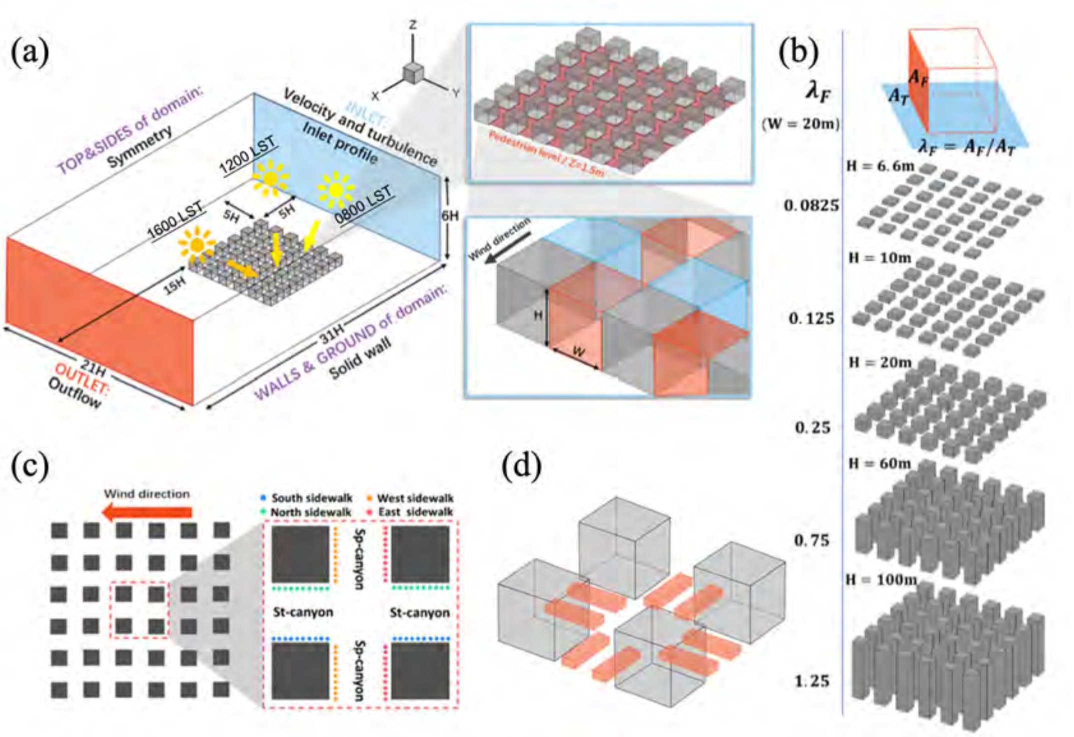

Figure 2.1 (a) Geometric model, boundary conditions, sun positions (0800, 1200, and 1600 LST), and schematic diagrams showing the pedestrian level and spanwise (Sp-canyon, red) and streamwise (St-canyon, blue) street canyons. (b) Schematic diagrams showing the urban-like geometries investigated with increasing λ_F. (c) Schematic diagrams showing the monitoring points for thermal comfort and air quality. (d) Schematic diagrams showing the volumetric pollutant sources.

2.2.2 Governing equation and turbulence model

The numerical analysis is based on the steady-state three-dimensional (3D) Reynolds-averaged Navier–Stokes (RANS) conservation equations of mass, momentum, and energy for the incompressible turbulent flow. The governing equations are given below:

Continuity equation:

$$\frac{\partial u_i}{\partial x_i} = 0 \tag{2.1}$$

Momentum equation:

$$\frac{\partial \rho u_i u_j}{\partial x_j} = -\frac{\partial p}{\partial x_i} + \frac{\partial}{\partial x_j}\left[(\mu + \mu_t)\left(\frac{\partial u_i}{\partial x_j} + \frac{\partial u_j}{\partial x_i}\right)\right] + \rho_{ref}\, g_i \beta\left(T - T_{ref}\right) \tag{2.2}$$

Energy equation:

$$\frac{\partial u_i T}{\partial x_i} + \frac{\partial}{\partial x_i}(\alpha_T \frac{\partial T}{\partial x_i}) = 0 \tag{2.3}$$

where u_i denotes the air velocity component along the *i* axis; p, ρ, T, μ, μ_t, g_i, and α_T represent the pressure, density, temperature, dynamic viscosity, turbulent viscosity, gravity acceleration, and thermal diffusivity, respectively. To model the buoyancy-driven flow, the Boussinesq approximation is adopted in the numerical model, $\rho = \rho_{ref}$ $\beta(T\text{-}T_{ref})$ in Eq. (2.2), where β, T_{ref}, and ρ_{ref} are the thermal expansion coefficient, reference temperature, and reference density, respectively. In this chapter, the air density is treated as a constant value in all equations, except for the buoyancy term in the momentum equation.

In addition, the species transport equation is solved to probe the pollutant dispersion in an urban environment as follows:

$$\frac{\partial u_i Y}{\partial x_i} - \frac{\partial}{\partial x_i}\left[\left(D + D_t\right)\frac{\partial Y}{\partial x_i}\right] = S_P \tag{2.4}$$

where D and D_t (= v_t/S_{ct}) denote the molecular and turbulent diffusion coefficients of pollutants. Here, v_t is the turbulent viscosity, and S_{ct} is the turbulent Schmidt number, which is set as 0.4 to account for the underestimation of the turbulent mass diffusion from the RANS models [99]. Y is the mass fraction of the pollutant distribution. Herein, we selected CO as a tracer gas, and S_P is the source term for CO. The constant emission rate per hour and unit street length (36.1 [g/h/m], i.e., total mass release rate of $L_p \times 1.0 \times 10^{-5}$ [kg/s]) is adopted for each CO source with reference to Ng and Chau [71]. Considering the type and number of vehicles passing by a realistic street per hour in Mongkok, Hong Kong, Ng and Chau [71] calculated the pollutant release rate above.

The simulation sensitivity checked by different turbulence models (standard, RNG, and realizable k-ε model) is performed against the wind tunnel experimental data. According to the validation study in Section 2.4, the RNG k-ε model is most suitable in this chapter to provide reliable predictions of the mean flows with the thermal effect and pollutant dispersion. The RNG k-ε model, developed by Yakhot and Orszag [100], can simulate a wide range of turbulent flow phenomena to effectively characterize the airflow and pollutant transport in street canyons under the thermal buoyancy force effects [15,25]. The conservation equations of the RNG k-ε turbulence model for the turbulence kinetic energy (k) and dissipation rate (ε) are as follows:

$$\frac{\partial \rho k u_i}{\partial x_i} = \frac{\partial}{\partial x_i}\left[(\mu + \frac{\mu_t}{\sigma_k})\frac{\partial k}{\partial x_i} \right] + P_k + G_b - \varepsilon \tag{2.5}$$

$$\frac{\partial \rho \varepsilon u_i}{\partial x_i} = \frac{\partial}{\partial x_i}\left[(\mu + \frac{\mu_t}{\sigma_\varepsilon})\frac{\partial k}{\partial x_i} \right] + C_{\varepsilon 1}\frac{\varepsilon}{k}(P_k + C_{\varepsilon 3}G_b) - C_{\varepsilon 2}\frac{\varepsilon^2}{k} \tag{2.6}$$

where the production terms of the turbulent kinetic energy due to buoyancy (G_b) and shear (P_k) can be expressed as follows:

$$G_b = \beta \frac{\mu_t}{\Pr_t}\frac{\partial T}{\partial x_i} g_i \tag{2.7}$$

$$P_k = \nu_t (\frac{\partial u_i}{\partial x_j} + \frac{\partial u_j}{\partial x_i})\frac{\partial u_i}{\partial x_j} \tag{2.8}$$

Here, $\mu_t = C_\mu \rho k^2/\varepsilon$. The constants C_μ, σ_k, σ_ε, $C_{\varepsilon 1}$, and $C_{\varepsilon 2}$ are 0.0845, 0.7194, 0.7194, 1.42 and 1.68, respectively. The factor $C_{\varepsilon 3} = \tanh\left|\frac{v}{u}\right|$, where v and u are the velocity components of the flow parallel and perpendicular to the gravitational vector, respectively.

2.2.3 Boundary conditions

The flow of ambient wind over ideal urban street canyons is simulated under the effect of realistic solar heating. According to the observation data from the Hong Kong Observatory Weather Station (longitude: 22°18'07" N, latitude: 114°10'27" E and elevation of the ground above mean sea level: 32 m) [101], the hourly means of meteorological data in June in Hong Kong (for 20 years) are obtained for the inlet boundary condition. The wind speed occurs most frequently at 3 m/s from the east (90°) at a height of 32 m above sea level. The mean hourly air temperature is summarized in

Table A1.1, which is used for the setting of constant air temperature at the inlet of the domain. The profiles of the neutral Atmospheric Boundary Layer (ABL) velocity (U_{ABL}), turbulent kinetic energy (k), and turbulence dissipation rate (ε) are resolved as the incoming airflow conditions at the velocity inlet.

$$U_{ABL} = \frac{u^*_{ABL}}{K} \ln\left(\frac{z+z_0}{z_0}\right) \tag{2.9}$$

$$k = \frac{(u^*_{ABL})^2}{\sqrt{C_\mu}} \tag{2.10}$$

$$\varepsilon = \frac{(u^*_{ABL})^3}{K(z+z_0)} \tag{2.11}$$

where u^*_{ABL} is the ABL friction velocity for the calculation of inlet U_{ABL}, k, and ε, which can be computed from the reference wind velocity U_{ref} = 3 m/s at a reference height z_{ref} (32 m) as follows:

$$u^*_{ABL} = \frac{KU_{ref}}{\ln\left(\frac{z_{ref}+z_0}{z_0}\right)} \tag{2.12}$$

where K and z_0 are the von Karman's constant (≈ 0.4) and the aerodynamic roughness, respectively.

To accurately resolve the surface temperatures of buildings, the radiative heat fluxes resulting from the significant solar radiation effect need to be computed. With the input of the specific time data and the global location, the accurate position of the sun can be calculated by the Solar Calculator dialog box of ANSYS/Fluent®, and its Ray-Tracing model can provide the incident radiation on those exposed surfaces. Thus, direct solar radiation is added to the energy equation as a source term. In other words, the thermal load resulted from the solar radiation will be applied as a boundary condition. Moreover, this chapter applies the discrete ordinates (DO) radiation model to evaluate the radiant heat fluxes between the surfaces since it is appropriate to account for the optical problems in a complex-geometry system with a high degree of accuracy [36]. As reported by Dugaria et al. [102], the DO model could yield a close coupling between wall temperature and radiative energy, in which the same mesh is adopted to effectively cope with radiative transfer, energy, mass, and momentum conservation problems. The spectral optical and thermophysical properties of the involved materials are summarized in Table A1.2. In addition, the heat transfer coefficients (h_c) of the building faces and ground are calculated by the following empirical correlation [38].

$$h_c = 5.7 + 3.8V_{air} \tag{2.13}$$

where V_{air} is the airflow velocity.

To calculate the pollutant concentration, eight uniform volume sources (width W_p = 2 m and length L_p = 20 m) are specified near the ground between z = 0 m and 0.5 m to represent traffic lanes in opposite directions on two sides of the street canyon, as shown in Figure 2.1(d).

2.2.4 Solver settings

The aforementioned governing equations are discretized by the finite volume scheme in ANSYS/Fluent®. This chapter utilizes the pressure-linked equations-consistent (SIMPLEC) numerical method for the pressure-velocity coupling. The second-order upwind scheme [103] is used to discretize both the convective terms and the diffusion terms. A double-precision solver is also selected for the CFD calculations. The convergence of the normalized residual errors of the energy equation is set to 10^{-9}, whereas the convergence criterion of the remaining equations is set to 10^{-6}.

2.2.5 Grid sensitivity analysis

Figure 2.2 compares the predicted wind velocity and air temperature of the three calculation cases on the west (Sp-canyon) and north (St-canyon) sidewalks (average value of 10 monitoring points at each sidewalk) in Figure 2.1(c). The differences in the computed wind velocity on the north and west sidewalks are 8.3% and 9.5% between the coarse grids and medium grids, respectively. Alternatively, the corresponding discrepancies of the predictions on the north and west sidewalks are reduced to 1.5% and 2.3%, respectively, between the medium grids and fine grids. Although only 3.2% and 1.7% deviations in the air temperature on the north and west sidewalks occurred between the coarse grids and medium grids, respectively, the differences in the computed air temperature are further reduced to 0.7% and 0.8% between the medium grids and fine grids, respectively. Due to intricate physical problems involved (short-wave solar irradiation, long-wave radiation amongst building surfaces, and pollutant dispersion), almost 61 hours of central processing unit (CPU) time is required to reach a converged steady-state solution on an Intel Core® X900-3.47 GHz (128 GB RAM) high-performance workstation. Notably, the average *y*+ of the building surfaces and grounds are 1038.6 for the medium mesh, which is slightly higher than the upper bound of *y*+ (500) for the standard wall function recommended by An et al. [104]. Here, *y*+ is a dimensionless wall distance to judge the applicability of wall functions [105], $y+ = u_T y / \nu$, where u_T is the friction velocity, *y* is the absolute distance from the wall, and ν is the kinematic viscosity. Although *y*+ of the fine mesh (519.3) could basically reach the requirement of *y*+, nearly 12 hours extra processing time is need for the convergence. As reported by An et al. [104], a suitable relaxation of the restriction in *y*+ value should be allowed, with a compromise made among the prediction accuracy, the numerical stability, and the computational time. Consequently, the medium grid (with a total cell number of 6,625,578), is considered reliable and adopted to perform the numerical analysis. Notably, the grid independence tests of other cases with various urban geometries are also conducted in the same manner before performing the numerical analysis.

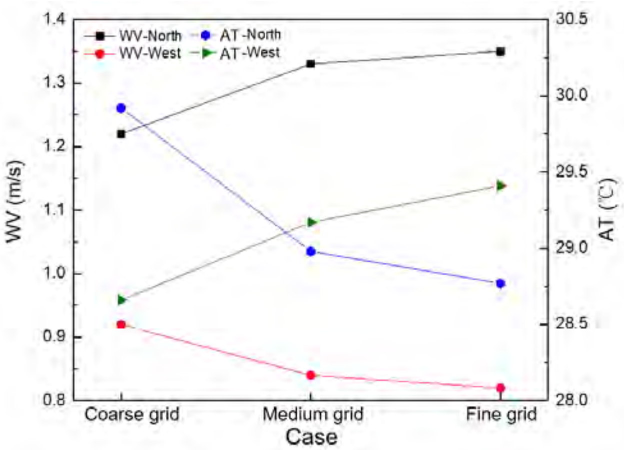

Figure 2.2 Grid-independent validation.

2.3 Description of thermal comfort simulation

2.3.1 Rayman model

The Rayman model (version 1.2) [106] is a recently developed radiation and thermal comfort model [107]. This model has been widely adopted and extensively evaluated for outdoor thermal comfort in urban areas [108,109] with good validation [110,111]. The final output of the Rayman model is the assessment of the thermal comfort with the use of indices, such as the PET.

To calculate these thermal comfort indices, this model needs air temperature, wind velocity, time of day, global location at the point of interest, and sky view factor (SVF) as the input. The air temperature and wind velocity can be obtained from CFD calculations. With the time of day, global, and SVF as input, the Rayman model allows for the estimation of mean radiant temperature (MRT) via the calculations of the short-wave and long-wave radiation fluxes. The MRT is most important parameter for human thermal comfort assessment [112]. The SkyHelios model [113] is used to generate virtual fish-eye images for the calculation of the SVF. Because ten observation points are used to characterize one sidewalk (see Figure 2.1(c)), 80 virtual fish-eye images in total are needed for the simulation case. Figure 2.3 shows some representative fish-eye images in the middle of the north sidewalk for different urban arrays. Finally, the thermal indices can be obtained at the pedestrian level after inputting personal data, as listed in Table A1.3.

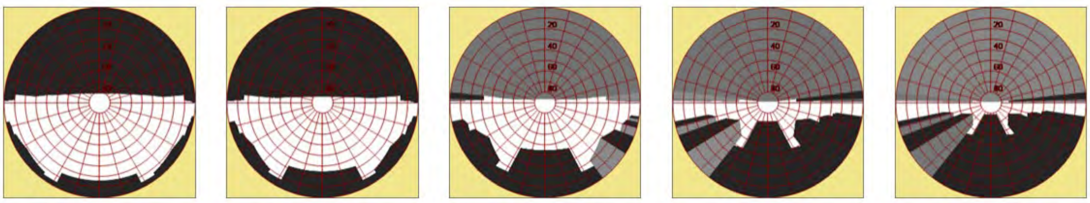

λ_F = 0.0825 λ_F = 0.125 λ_F = 0.25 λ_F = 0.75 λ_F = 1.25

Figure 2.3 Fish-eye images in the middle of the north sidewalk, obtained from SkyHelios.

2.3.2 Thermal comfort indices

To facilitate a deeper understanding of the influences of urban geometry and realistic solar radiation on the thermal sensation, the PET is a suitable evaluation index. The PET has been used regularly for the assessment of outdoor thermal comfort [114], considering the impacts of shortwave and longwave radiation fluxes in an outdoor environment on the energy budget of the human body [115]. One of its advantages is that it is a real climatic index describing the thermal environment in a thermal physiologically weighted manner [116]. Second, there is a good agreement with the thermal comfort perception of the interviewers in Hong Kong [117]. Third, the PET has a commonly known unit (℃) to measure the thermal stress on outdoor human pedestrians, which could easily be accepted by the public, who are generally not familiar with modern human-bio meteorological terms [118]. The thermal sensation of the PET can be summarized into different "thermal comfort ranges" based on the subjective thermal perception of local people [119,120]. For instance, Lin and Matzarakis [120] conducted a series of studies to define PET ranges in the hot and humid subtropical context of Taiwan. Due to similar behavioral adjustments of the residents and climatic conditions between Taiwan and Hong Kong, this chapter introduced the thermal sensation classification in Taiwan (see Table A1.4) as a criterion to evaluate the thermal environment above sidewalks.

2.4 Validation study

To the best of our knowledge, wind tunnel experiments considering both the pollutant dispersion and thermal effect simultaneously are not available. Accordingly, the thermal measurement data (wind velocity and air temperature) from the wind tunnel experiment by Uehara et al. [121] and the pollutant measurement data (pollutant concentration) from that by Meroney et al. [122] are employed separately to validate the present computational model in CFD simulations.

2.4.1 Validation study of thermal effect

To validate the thermal effect of the current numerical model, this chapter refers to the wind tunnel experiment performed by Uehara et al. [121]. The reason to choose this wind tunnel experiment is that there is a similar order of magnitude for Richardson number (R_i, defined as $gH(T_{in}\text{-}T_g/\{(273.15+T_{in})(U_{ref})^2\})$ between this wind tunnel experiment (-0.21) and the following study case (around -1). T_g and T_{in} are the ground temperature and ambient temperature. Also, the Reynolds number is almost 6500 for the wind tunnel experiment. It is over the critical Reynolds number (=4000) to ensure the Reynolds number independence [123]. This wind tunnel experiment has 14 rows of simply shaped blocks with a characteristic height = width = length = 0.1 m for an aspect ratio of 1. The floor panel in the urban areas is heated to a constant T_g. In this validation, the settings of the CFD simulation are consistent with those of the wind tunnel experiment (e.g., the boundary condition and building geometry). Herein, we compare different turbulence models to find out which one is more suitable to predict the distribution of wind velocity and air temperature inside the street canyon with considering the thermal effect. The measured data in terms of the streamwise wind velocity and air temperature are obtained at the vertical section (z/H= 0–2) in the center of the street canyon between the fifth and sixth rows of the building arrays.

Figure 2.4 illustrates a comparison of the simulated vertical profiles of the (a) normalized streamwise velocity u/U_{2H} and (b) temperature $(T\text{-}T_g)/(T_{in}\text{-}T_g)$ (by the standard, realizable, and RNG k-ε models) with the experimental results from the wind tunnel tests. u and U_{2H} are the streamwise velocity and mean wind speed at a height of $2H$, respectively. Clearly, all three turbulence models reasonably predict the streamwise flow velocities in the vortex recirculation region, with some discrepancies occurring at z/H = 1.25. Nevertheless, the normalized temperature simulated with the RNG model is in better agreement with that of the wind tunnel experiment than those of the standard and realizable k-ε models. The temperature profile predicted by the RNG model near the ground is very close to the wind tunnel data, suggesting good agreement of the sharp near-ground temperature gradient computed using the RNG model. Overall, the RNG

k-ε turbulence model demonstrates the best prediction capability for the study of thermal effects.

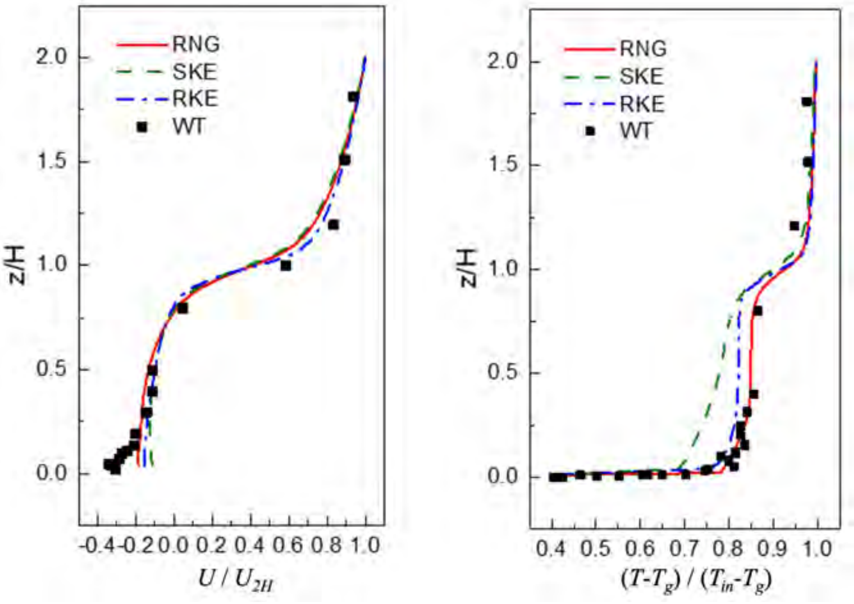

(a) (b)

Figure 2.4 Comparison of the simulated data with the wind tunnel data by Uehara et al. [46]. (a) normalized streamwise u/U_{2H} and (b) normalized temperature $(T\text{-}T_g)/(T_{in}\text{-}T_g)$. SKE, RNG, and RKE denote the standard, RNG, and realized k-ε models, respectively; WT denotes the wind tunnel data.

2.4.2 Validation study of pollutant dispersion

The current computational model for pollutant dispersion simulations is validated against the wind tunnel measurements conducted by Meroney et al. [122], who explored the street geometry effect on the dispersion of traffic pollutants within a two-dimensional (2D) street canyon. Two wooden bars with height = width = 0.06 m were mounted across the whole wind tunnel, with the approaching wind direction perpendicular to the canyon axis. A ground-level pollutant line source (ethane, C_2H_6) parallel to the canyon axis was laid in the center of the canyon to represent traffic exhaust. Moreover, the pollutant was continually released at a steady rate of Q_e. The reference wind speed, U_{ref}, was recorded at a reference height of 0.65 m above the floor. To validate the predicted pollutant concentration, the settings of the CFD simulation are consistent with those of the wind tunnel experiment. The predictions of the normalized ethane concentration $C^* = CU_{ref}HL/Q_e$ are compared with the wind tunnel experiment data measured along the leeward and windward walls in the center vertical section of the canyon. Here, C is the volume fraction of ethane, and H and L are the height and the length of the buildings, respectively.

As demonstrated in Figure 2.5, on the windward side, the standard *k-ε* turbulence model provides the best-simulated results, whereas the RNG and realizable *k-ε* turbulence models slightly overestimate the pollutant concentration. On the leeward side, the RNG *k-ε* turbulence model provides the best-simulated results, although it slightly underpredicts the pollutant concentration in the lower part of the street canyon. Generally, the RNG *k-ε* turbulence model is the most suitable for predicting the pollutant dispersion and thermal effects with reasonable accuracy simultaneously.

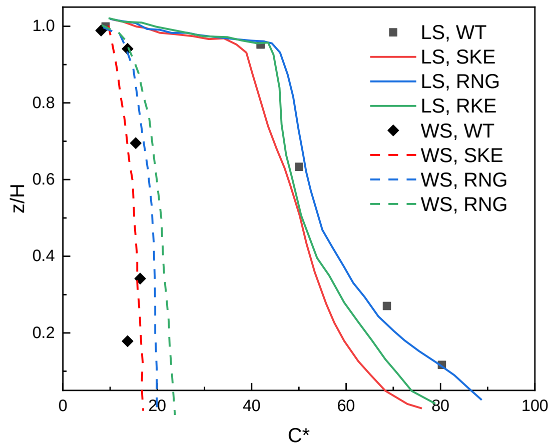

Figure 2.5 Comparison of the simulated data with the wind tunnel data by Meroney et al. [122]. SKE, RNG, and RKE denote the standard, RNG, and realized k-ε models, respectively, WT denotes the wind tunnel data, LS represents the data on the leeward side and WS represents the data on the windward side.

2.5 Results and discussion

2.5.1 Wind velocity and flow structure

First, the flow structures at various solar times (0800, 1200, and 1600 LST) are tested under λ_F= 0.25. The surfaces along the St-canyon are almost parallel to the solar irradiation (see Figure 2.1(a)), causing a relatively minor change in the wall temperature and consequential flow structure. During the daytime, there are at most 0.4 ℃ and 1.7 ℃ changes in the mean surface temperature of south and north walls, respectively. Additionally, the channel flow almost dominates the St-canyon. In contrast, in the Sp-canyon, the related change is more significant. An approximate 20 ℃ variation on the surfaces along the Sp-canyon is observed in Figure 2.6 and Figure 2.7. Accordingly, we will probe the distribution of the wall temperature and flow structure in the Sp-canyon in the following discussion.

Figure 2.6 illustrates the predicted wall temperature and 3D streamlines in the Sp-canyon. The location of these analyses is shown in the inset at the upper right corner. Distinct 3D-flow patterns are observed for these three solar times, attributable to the respective buoyancy-driven mechanisms resulting from the discrete wall temperature distributions. At 1200 LST, the solar radiation directly heats the ground, and the wall temperatures of leeward and windward surfaces are both symmetric in effect, leading to a lasting symmetric structure of the double-elevated eddies. In contrast, asymmetric wall temperatures are observed on either the leeward or windward surfaces at 0800 and 1600 LST. Thus, similar asymmetric flow structures appear at 0800 and 1600 LST; the northern and southern parts of the Sp-canyon are occupied by the primary circulation and elevated eddies, respectively. This observation is supported by Nazarian and Kleissl [24]. They also revealed that a similar flow structure of a short Sp-canyon could be both found at 0800 and 1600 LST due to the strong influence from the St-canyon, under realistic non-uniform thermal forcing. Notably, this phenomenon can differ from that in some infinite street canyon cases based on the uniform wall heating assumption. Hence, the influences of λ_F on the flow structures are analyzed considering the symmetric (1200 LST) and asymmetric (0800 or 1600 LST) wall temperatures.

Figure 2.7 shows the predicted wall temperature contours and 3D streamlines in the Sp-canyon (the orange area at the upper right corner of Figure 2.6) for various λ_F values at 1200 LST and 1600 LST. Under the symmetric wall temperature (1200 LST), the flow structure remains symmetric elevated eddies as λ_F increased. Under the asymmetric wall temperature (1600 LST), the flow structure first becomes asymmetric and then become symmetric again as λ_F increased. When λ_F increases to 0.25, the shading effect on the west surface becomes significant, along with the increasing wall temperature on the north part of the east facade. This strong buoyancy force causes a primary vortex in the northern part of the street canyon. Thus, the airflow structure becomes asymmetric. When λ_F increases to 1.25, symmetric elevated eddies results, since most of the east surface is also subject to the shading effect, and the buoyancy force resulting from the high temperature on the north part of the east surface is not strong enough to generate another primary vortex.

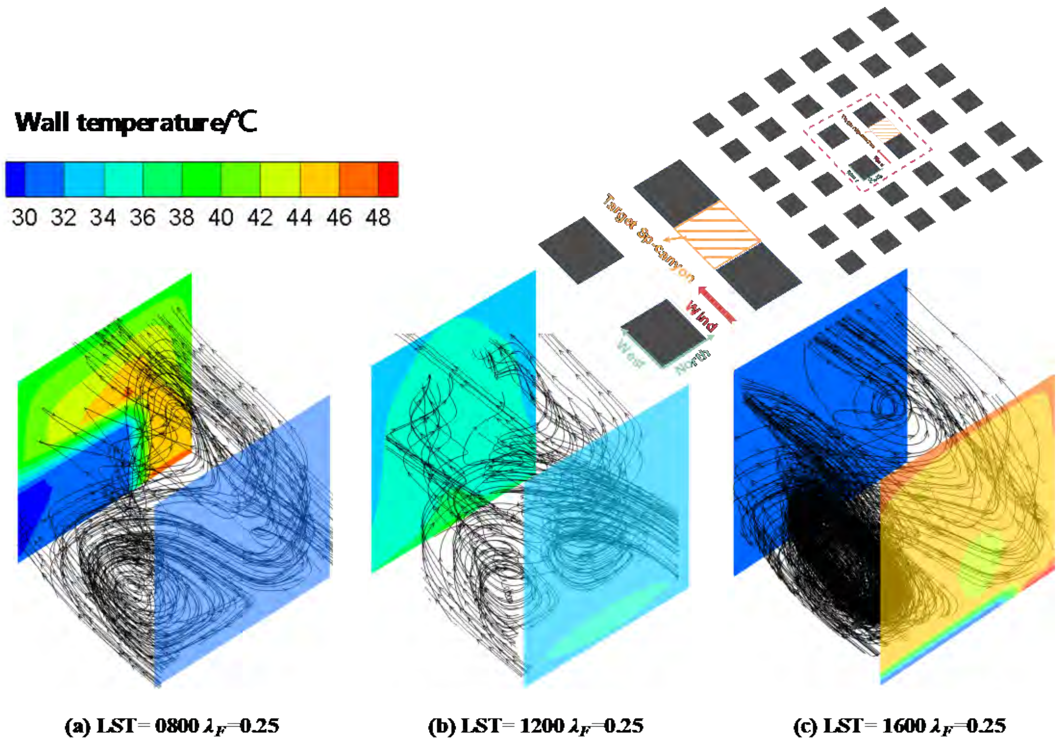

Figure 2.6 Predicted wall temperature and 3D streamlines in the Sp-canyon at various solar times for λ_F = 0.25.

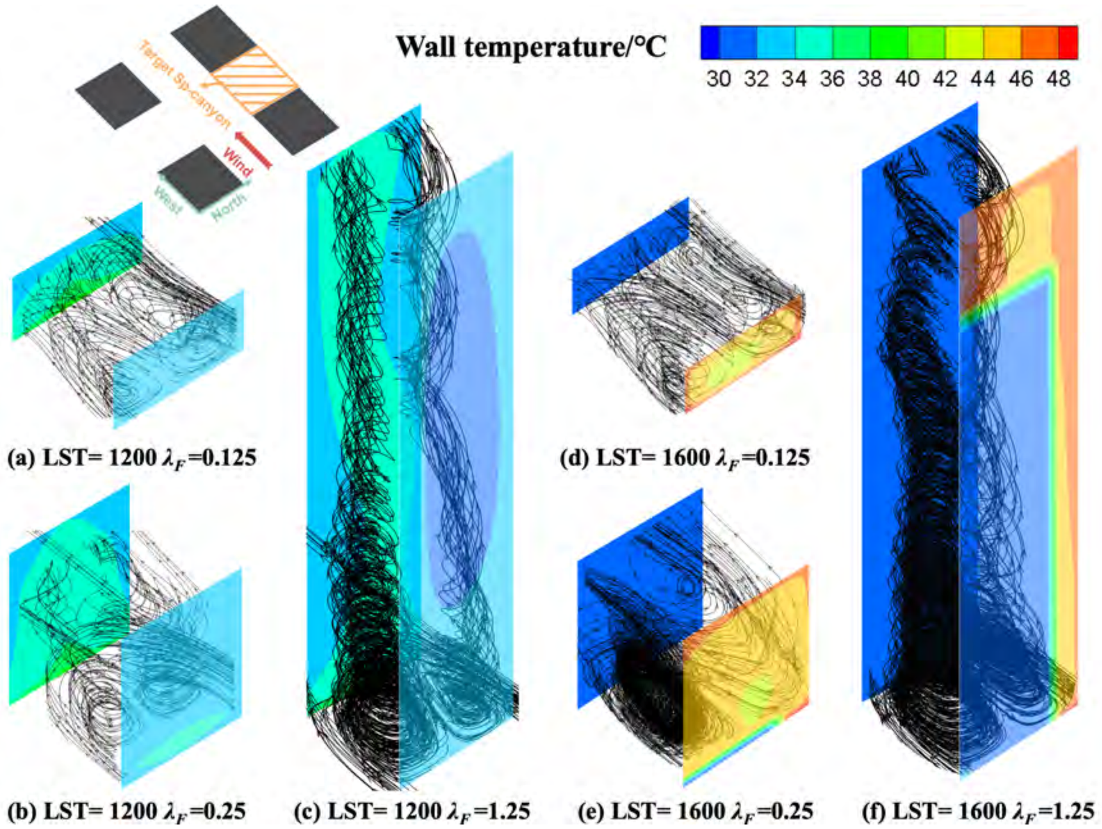

Figure 2.7 Predicted wall temperature contours and 3D streamlines in the Sp-canyon for different frontal area densities at 1200 LST and 1600 LST.

2.5.2 Thermal comfort

2.5.2.1 Air temperature

First, the air temperature at the pedestrian level at various solar times (0800 LST, 1200 LST, and 1600 LST) is tested under $\lambda_F = 0.125$. To elucidate the shading effect attributable to different solar positions, the black-dashed frames in Figure 2.8 indicate the regions shaded by surrounding buildings at different LSTs. Obviously, the shading effect is the most critical factor in the distribution of the air temperature. Thus, the air temperature at 1200 LST is significantly higher than that at 0800 LST and 1600 LST (2–4 °C higher in the Sp-canyon and 1–3 °C higher in the St-canyon). Meanwhile, the air temperature in the areas exposed to solar radiation (the west side at 0800 LST and the east side at 1600 LST) is 2–3 °C higher than in other regions. Therefore, the influences of λ_F on air temperature are analyzed considering the weak (1200 LST) and strong (1600 LST) shading effects in the following.

Figure 2.9 illustrates the predicted air temperature at the pedestrian level for various λ_F values at 1200 LST and 1600 LST. At 1200 LST, the air temperature on the east and the west sidewalks first increases with λ_F because of the increasingly strong elevated eddies, which are adverse to the dispersion of heat, and then decrease due to the enhancement of ventilation and shading. The air temperature on the south sidewalk changes slightly with λ_F because this sidewalk is always exposed to solar radiation. The air temperature on the north sidewalk changes insignificantly with λ_F at first and then decreases by approximately 1 °C due to the increase in shading area. At 1600 LST, the air temperature on the north and west sidewalks remains nearly constant and then decreases by approximately 1–2 °C with increasing λ_F. The possible explanation is that these two sidewalks are always shaded at 1600 LST, and the reduction in air temperature is related to the increase in wind velocity for $\lambda_F = 1.25$. The air temperature on the south sidewalk first increases with λ_F and then decreases as a result of the wind shadow area. The air temperature on the east sidewalk reduces significantly by approximately 3 °C when λ_F increases to 0.25 since the east sidewalk begins to be completely shaded (the black-dashed frames started to cover the east sidewalk); then, it decreases slightly for $\lambda_F = 1.25$.

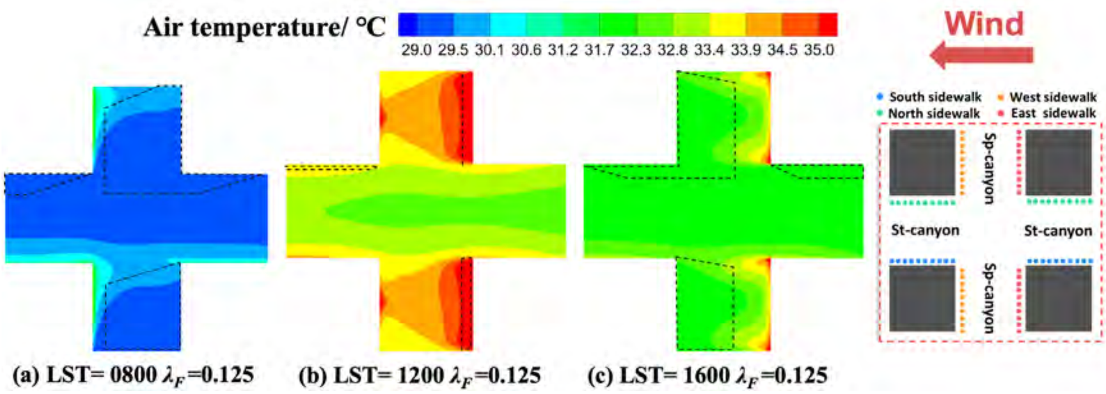

Figure 2.8 Predicted air temperature contours at the pedestrian level at various solar times when λ_F = 0.125 (the black-dashed frames indicate the regions shaded by the surrounding buildings).

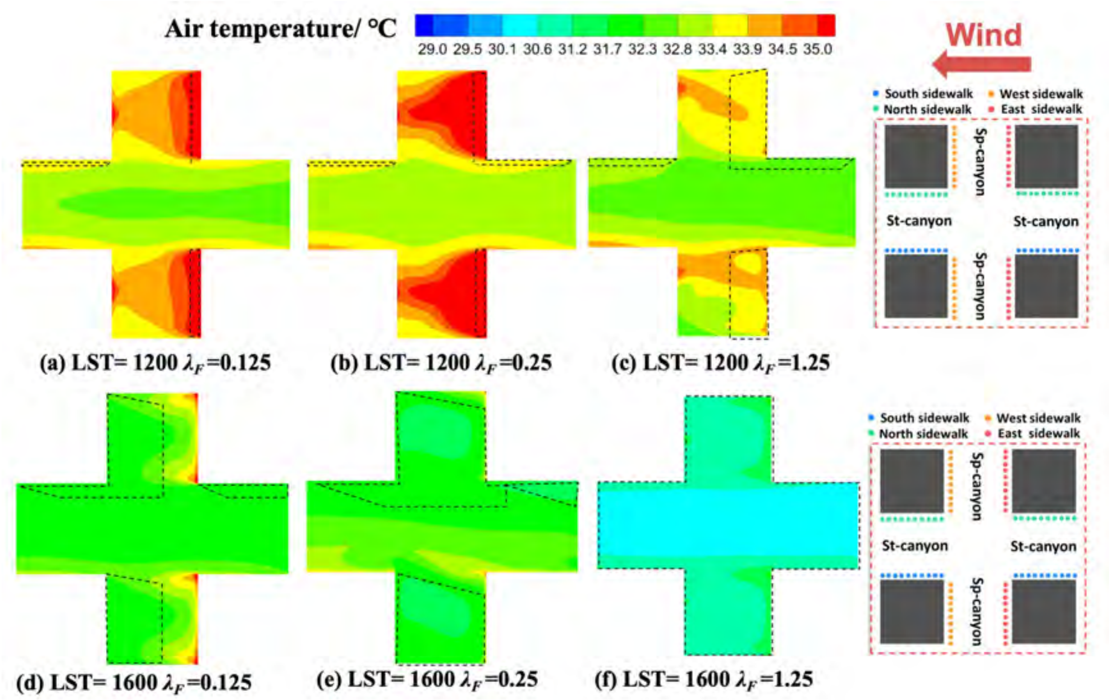

Figure 2.9 Predicted air temperature contours at the pedestrian level for various λ_F settings at 1200 LST and 1600 LST (the black-dashed frames indicate the regions shaded by the surrounding buildings).

Figure 2.10 summarizes the predicted average air temperature (over the 10 monitoring points at the pedestrian level) for different λ_F values at 0800 LST, 1200 LST, and 1600 LST. Generally, the trends at 0800 LST and 1600 LST are again similar and very different from the pattern at 1200 LST. At 1200 LST, the air temperature on the four sidewalks first increases to $\lambda_F = 0.25$ and then decreases or changes only slightly. At 0800 LST or 1600 LST, the air temperature on the west or the east sidewalk decreases gradually with λ_F, especially when λ_F increases to 0.25. The air temperature on the south sidewalk first increases with λ_F and then decreases, but it gradually reduces with λ_F on the north sidewalk.

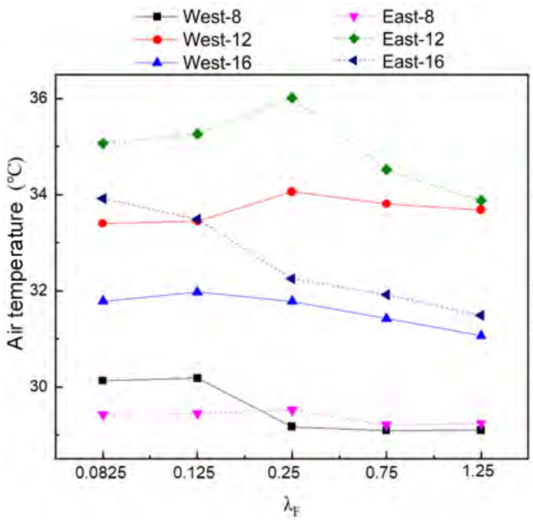

(a) Sp-canyon

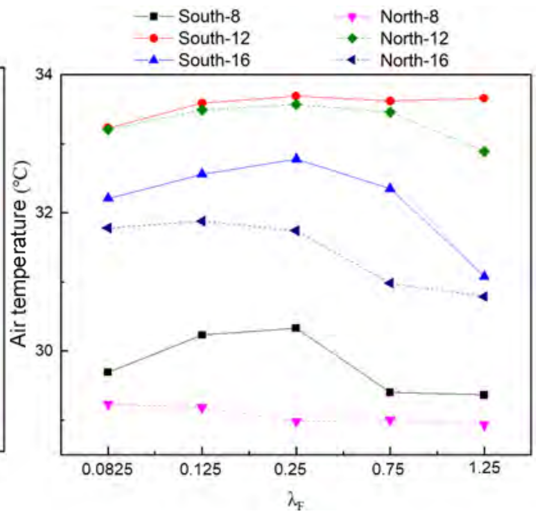

(b) St-canyon

Figure 2.10 Predicted average air temperatures at the pedestrian level above the sidewalks in the (a) Sp-canyon and (b) St-canyon for different λ_F values at 0800 LST, 1200 LST, and 1600 LST.

2.5.2.2 PET profiles

As shown in Figure 2.11, the mean PET development with λ_F at the pedestrian level on the four sidewalks (from 10 monitoring points on each sidewalk, as shown in Figure 2.1(c)) shows the same tendencies as those of the wind velocity and air temperature. The PET at 0800 LST and 1600 LST still shows similar trends, with both being different from that at 1200 LST. For 1200 LST, the PET on the four sidewalks changes slightly with λ_F, and a sharp decrease (up to 5 ℃) occurs in the PET from $\lambda_F = 0.25$ to 0.75, as an apparent increase in the wind velocity lowers the PET, although the air temperature does not decline progressively. Nevertheless, the minimum PET is larger than 40 ℃ (hot level). For 0800 LST or 1600 LST, the PETs on the east, the west, and the north sidewalks tend to decrease with λ_F, and an evident decrease in the PET from $\lambda_F = 0.125$ to 0.25 occurs for the west sidewalk at 0800 LST and the east sidewalk at 1600, possibly because the increase in λ_F strengthens the wind velocity and the shading effect and thereby causes the decrease in the PET. In addition, the apparent reduction in air temperature leads to a significant decrease in the PET (up to 6 ℃) when λ_F increases to 0.25 on these three sidewalks. The PET on the south sidewalk escalates at an early stage

($\lambda_F \leq 0.25$) and then obviously declines (up to 7 ℃) because of the wind shadow area. In general, the warm level or the slightly warm level could be achieved when λ_F exceeded 0.75 at 0800 LST and 1600 LST.

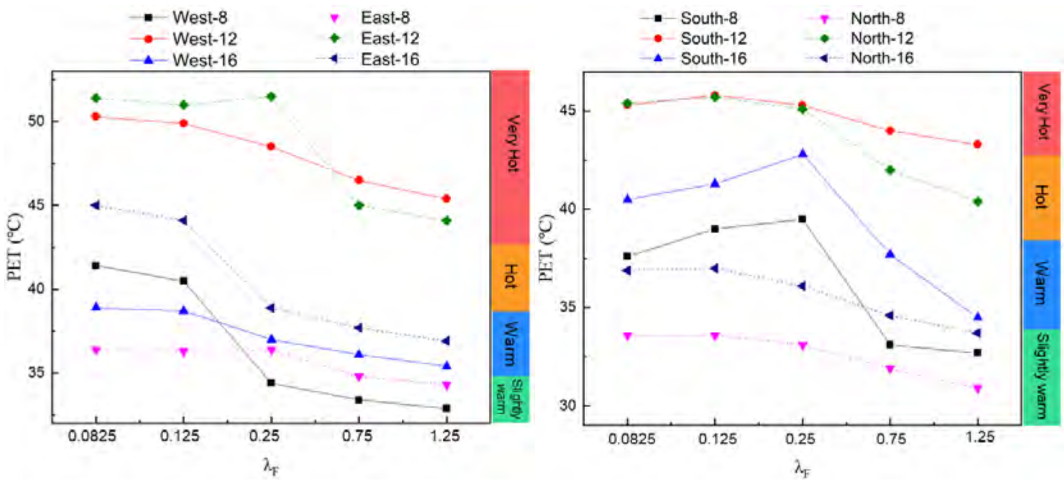

(a) Sp-canyon (b) St-canyon

Figure 2.11 Predicted PET profiles at the pedestrian level above sidewalks in the (a) Sp-canyon and (b) St-canyon for different λ_F values at 0800 LST, 1200 LST, and 1600 LST.

2.5.3 Air quality

Since the distribution of the CO concentration is directly related to the flow structure and wind velocity, the impact of λ_F on the CO concentration is also analyzed considering the symmetric (1200 LST) and asymmetric (0800 or 1600 LST) wall temperature cases. Figure 2.12 presents the predicted CO concentration contours at the pedestrian level for various λ_F settings at 1200 LST and 1600 LST. At 1200 LST, the CO concentrations on the north and south sidewalks decrease slightly with λ_F and then decrease dramatically due to the noticeable increase in wind velocity at large λ_F. The concentrations on the east sidewalk increase gradually with λ_F due to an increase in upward flow resistance and a decrease in buoyancy force. In contrast, the concentrations on the west sidewalk change slightly since the pollutants tend to accumulate on the east side (leeward side). At 1600 LST, the concentrations on the east and west sidewalks increase gradually due to the increase in upward flow resistance caused by the elevated eddies, especially on the east sidewalk. The concentrations on the south sidewalk first increase and then decrease due to the wind shadow area. The concentrations on the north sidewalk decrease slightly with the increase in λ_F.

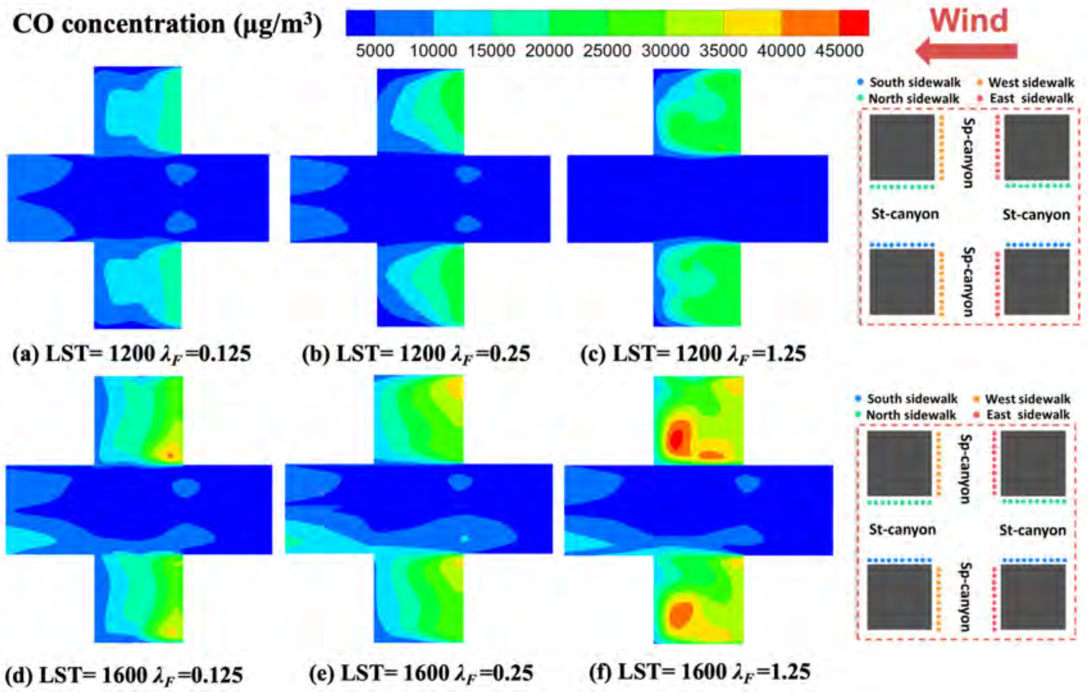

Figure 2.12 Predicted CO concentration contours at the pedestrian level for various λ_F settings at 1200 LST and 1600 LST.

Figure 2.13 summarizes the predicted average CO concentration (over the 10 monitoring points at the pedestrian level above the four sidewalks) for different λ_F values at 0800 LST, 1200 LST, and 1600 LST. Similar trends of the pollutant concentration to those of the λ_F appear at 0800 LST and 1600 LST for each sidewalk. At 1200 LST, the CO concentrations on the north or south sidewalks only slightly decrease and then significantly decrease from 4100 μg/m^3 at λ_F = 0.25 to approximately 3000 μg/m^3 at λ_F = 0.75. The CO concentrations on the west sidewalk are nearly unchanged. The CO concentrations on the east sidewalk increase notably when λ_F increase from 0.125 to 0.25 (from 18000 μg/m^3 at λ_F = 0.125 to 24000 μg/m^3 at λ_F = 0.25). For 0800 LST or 1600 LST, the concentrations on the east or west sidewalks increase significantly; the concentrations on the south sidewalk first increase until λ_F = 0.25 and then decrease; and a slight reduction in the concentration occurs on the north sidewalk.

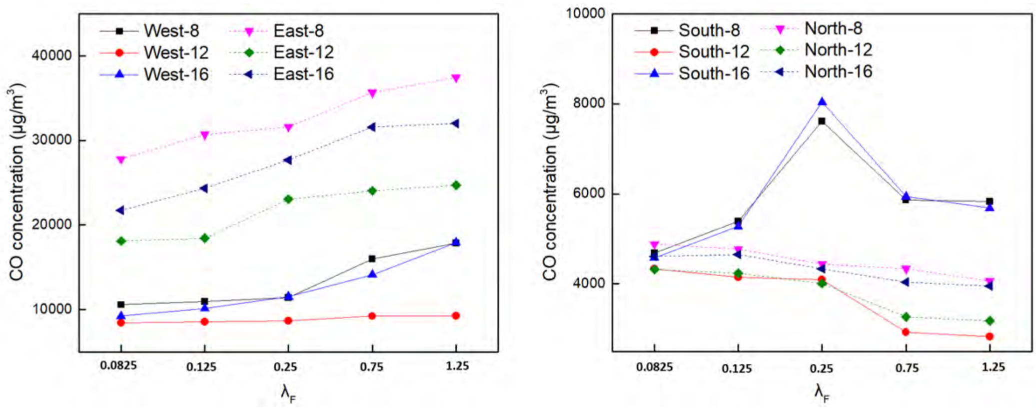

(a) Sp-canyon (b) St-canyon

Figure 2.13 Predicted average CO concentration profiles at the pedestrian level above the sidewalks: (a) Sp-canyon and (b) St-canyon for different λ_F values at 0800 LST, 1200 LST, and 1600 LST.

2.5.4 Multivariable regression analyses on thermal comfort and air quality

To achieve better air quality and thermal comfort, the values of both the CO concentration and PET should be small. However, the trends of the average CO concentration at various LSTs on different sidewalks (Figure 2.13) are basically opposite that of the average PET (Figure 2.11). For example, for the south and north sidewalks, at 1200 LST, the average CO concentrations are lower than those at 0800 LST and 1600 LST, whereas the average PET at 1200 LST is higher than those at 0800 LST and 1600 LST. Therefore, the multivariable regression analyses become meaningful because we can evaluate the local thermal comfort and air quality simultaneously based on the regression outcomes.

To generalize and sum up the correlation of the evaluation parameters of interest – normalized CO concentration and PET – with λ_F (from 0.0825 to 1.25) and the LST (0700 to 1700), 8 multivariable regression analyses for the four sidewalks are conducted among a group of dimensionless parameters based on all 50 cases simulated, as shown in Table 2.1. Herein, the CO concentration (C^*) is normalized by the ambient wind velocity (U_{ref}), reference height (H), and traffic emission rate (Q_c), and the PET is likewise normalized by the ambient air temperature (T_{ref}).

According to these 8 correlations, the local PET and CO concentrations for various LSTs and λ_F values could be obtained after inputting the ambient air temperature, ambient wind velocity, reference height, and traffic emission rate. Taking Hong Kong as an example, PET < 38 °C (warm level) and CO concentration < 30000 μg/m^3 (1-hour threshold value of CO set by the Hong Kong Air Quality Objectives) for 70% of the daytime (0700 LST to 1700 LST) on all four sidewalks are introduced as criteria of the frontal area density. For PET < 38 °C in 70% of the daytime, λ_F should be higher than 0.82, 0.52, 0.72, and 0.81 for the north, south, west, and east sidewalks, respectively. For CO concentrations < 30000 μg/m^3 in 70% of the daytime, λ_F should be lower than 1.25, 1.25, 1.25, and 0.84 for the north, south, west, and east sidewalks, respectively. Therefore, the building arrays should have λ_F values less than 0.84 but greater than 0.82 to realize a CO concentration < 30000 μg/m^3 and PET < 38 °C for 70% of the daytime.

Principally, the correlations obtained with multiple dimensionless parameters can provide a meaningful reference for decision-makers and urban planners in formulating appropriate building density design policies to improve the outdoor thermal comfort and air quality at the pedestrian level.

Table 2.1 Multivariable regression analysis for PET and CO concentration

Index	Sidewalk	Correlation	R^2
PET	East	$\left.\frac{PET}{T_{ref}}\right\|_E = -1.3 + 0.05\lambda_F + 0.47LST + 0.12\lambda_F{}^2 - 0.018LST^2 - 0.033LST\lambda_F$	0.89
	West	$\left.\frac{PET}{T_{ref}}\right\|_W = -0.33 - 0.899\lambda_F + 0.37LST + 0.22\lambda_F{}^2 - 0.017LST^2 - 0.03LST\lambda_F$	0.92
	South	$\left.\frac{PET}{T_{ref}}\right\|_S = -0.34 + 0.05\lambda_F + 0.31LST - 0.04\lambda_F{}^2 - 0.01LST^2 - 0.005LST\lambda_F$	0.89
	North	$\left.\frac{PET}{T_{ref}}\right\|_N = -1.02 - 0.23\lambda_F + 0.43LST + 0.04\lambda_F{}^2 - 0.017LST^2 - 0.001LST\lambda_F$	0.87
CO concentration	East	$\left.\frac{C*U_{ref}*H^2}{Q_C}\right\|_E = 1639.08 + 230.07\lambda_F\text{-}289.82LST + 1485.65\lambda_F{}^2 + 12.23LST^2 - \text{-}25.91LST\lambda_F$	0.98
	West	$\left.\frac{C*U_{ref}*H^2}{Q_C}\right\|_W = 1394.52 - 144.52\lambda_F - 240.68LST + 777.76\lambda_F{}^2 + 10.03LST^2 - 4.1LST\lambda_F$	0.97
	South	$\left.\frac{C*U_{ref}*H^2}{Q_C}\right\|_S = 181.83 + 11.14\lambda_F\text{-}31.57LST + 138.43\lambda_F{}^2 + 1.31LST^2 - 0.8LST\lambda_F$	0.99
	North	$\left.\frac{C*U_{ref}*H^2}{Q_C}\right\|_N = 154.2 + 24.86\lambda_F - 27.24LST + 155.71\lambda_F{}^2 + 1.14LST^2 - 0.65LST\lambda_F$	0.99

2.6 Summary

This chapter investigates the influence of the frontal area density (λ_F ranges from 0.0825 to 1.25) of 3D building arrays on the thermal comfort and air quality at the pedestrian level above four sidewalks (north, south, east, and west) considering realistic solar irradiation. With the coupling of the ANSYS/Fluent® software and the Rayman model, we then obtained the outdoor parameters of the thermal comfort (PET) and air quality (CO concentration). The major results are as follows.

(1) With the increase in λ_F, similar trends of the wind velocity, air temperature, PET, and CO concentration are observed at 0800 LST and 1600 LST, all of which differed from those at 1200 LST.

(2) With the increase in λ_F, the PET on the four sidewalks decreases gradually, but the values are still higher than the warm level at 1200 LST. A steady reduction in the PET occurs on the east, west, and north sidewalks, but the PET on the south sidewalk increases until $\lambda_F = 0.25$ and then decreases. The PET could achieve a warm level when λ_F exceeds 0.75 at 0800 LST or 1600 LST.

(3) With the increase in λ_F, a decrease in the CO concentration occurs on the south and north sidewalks, but the CO concentrations on the east and west sidewalks increase significantly and change slightly, respectively, at 1200 LST; the maximum concentration is lower than 30000 μg/m^3 at 1200 LST. At 0800 LST or 1600 LST, the concentration first increases and then decreases on the south sidewalk; the maximum concentration is approximately 8000 μg/m^3. The concentration on the east or the west sidewalk increases gradually and can exceed 30000 μg/m^3 when $\lambda_F > 0.25$.

(4) The elevated eddy is adverse to the updating of air, in contrast to the primary circulation. The elevated eddy in-between the buildings should, therefore, be minimized to improve the AQ.

(5) Two multivariable regression analyses for all of the simulated cases are conducted. Two dimensionless parameters of the CO concentration and PET were correlated with the LST and λ_F separately. These correlations provide a reference for the design of urban density, which will improve the thermal comfort and air quality

simultaneously. In Hong Kong, the building arrays should have λ_F values less than 0.84 but greater than 0.82 to realize a CO concentration < 30000 μg/m^3 and PET < 38 ℃ for 70% of the daytime in June.

Chapter 3 Effects of height-asymmetric street canyon configurations on outdoor air temperature and air quality

3.1 Introduction

During the urban renewal process, there are always variations in terms of building height; thus, urban structures often present irregular building patterns in urban canyons [124]. However, the effect of the uneven building layout is often neglected. According to Gu et al. [125], studies that are based on uniform street canyon models cannot identify the flow structure in non-uniform street canyons. Consequently, investigation of the effects of asymmetric urban arrangement will facilitate our understanding of pollutant and heat dispersion in actual urban areas and enable us to create better outdoor environments at the phase of urban renewal.

Based on this background, the objectives of this chapter are 1) to simulate emissions from vehicle exhausts and the thermal environment under the effects of solar radiation; 2) to evaluate the effects of realistic solar radiation and the corresponding shading effects for various configurations (the step-up and step-down street canyons) under two different incoming wind conditions; and 3) to identify critical building configurations that will enhance ventilation and improve the thermal environment for some tropical or subtropical cities suffering strong urban heat island effects and poor air quality.

3.2 Description of CFD simulations

3.2.1 Description of case studies, computational geometry, and grid

Two urban renewal processes that are associated with asymmetric street canyons are investigated in this chapter: 1) The high building that is present, the low building that will be rebuilt, and the height to which this low building should be rebuilt to realize our objectives will be explored. 2) One of the buildings of the asymmetric street canyon will be replaced by a higher building, and the side of the street on which it should be rebuilt will be investigated.

A step-up (or step-down) street canyon, as illustrated in Figure 3.1(a), is defined as a street canyon in which the upstream building height (H_1) is smaller (or larger) than the downstream building height (H_2) with a fixed street width of W = 20 m, a building width of W_b = 20 m, and a building length of L = 100 m. As illustrated in Figure 3.1 (b), four configurations with various asymmetric aspect ratios, which are defined as H_1/ H_2, were considered for these two urban renewal processes. In June, the wind speed of Hong Kong occurs most frequently at 3 m/s from the east (measured at the height of 32 m above sea level) [101]. Considering the perpendicular wind generally yields a worse air quality within the street canyon [126]. The street orientation is set as a North-South direction (Figure 3.1(a)), accordingly.

According to the practice guidelines by Tominaga et al.[97], the dimensions of the computational domain are based on the parameter H_{max} (= max(H_1, H_2)= 60 m) as follows: the axial distance between the velocity inlet and the windward face of the upstream building is 5 H_{max}, the transverse distances between the sidewalls of the buildings and the symmetric boundaries on both ends are all 5 H_{max}, and the outlet boundary is 15 H_{max} from the leeward faces of the downstream buildings, as specified in Figure 3.1(a).

To ensure the high quality of the computational mesh system, the computational domain is constructed using structured hexahedral cells. A grid expansion ratio of 1.05 in conjunction with the bi-geometric mesh law is set in both the vertical and horizontal directions in street canyons. Considering the relatively large gradients of the velocity and temperature near the ground and building surfaces, the finest grids around these two types of walls are deployed. Because the evaluation height should be located at the third or higher grid from the ground [46]. To conduct the mesh-independent study, the canyon (H_1= H_2= 20 m) is referred to as the base model, with three different grid densities. The minimum sizes for the coarse grid, the medium grid, and the fine grid are set to be 0.5m, 0.4m, and 0.3m, respectively. In this way, all these three grids have an adequate resolution (at least three cells from the ground) for resolving the airflow and the distributions of temperature and pollutants at the pedestrian level, which is 1.5m above the ground. The total cell numbers for the coarse grid, the medium grid, and the fine grid are 0.5 million, 3.5 million, and 12.3 million, respectively. Therefore, the ratio of two consecutive cell numbers for grid refinement in the mesh independent study can be at least 3.4 [97].

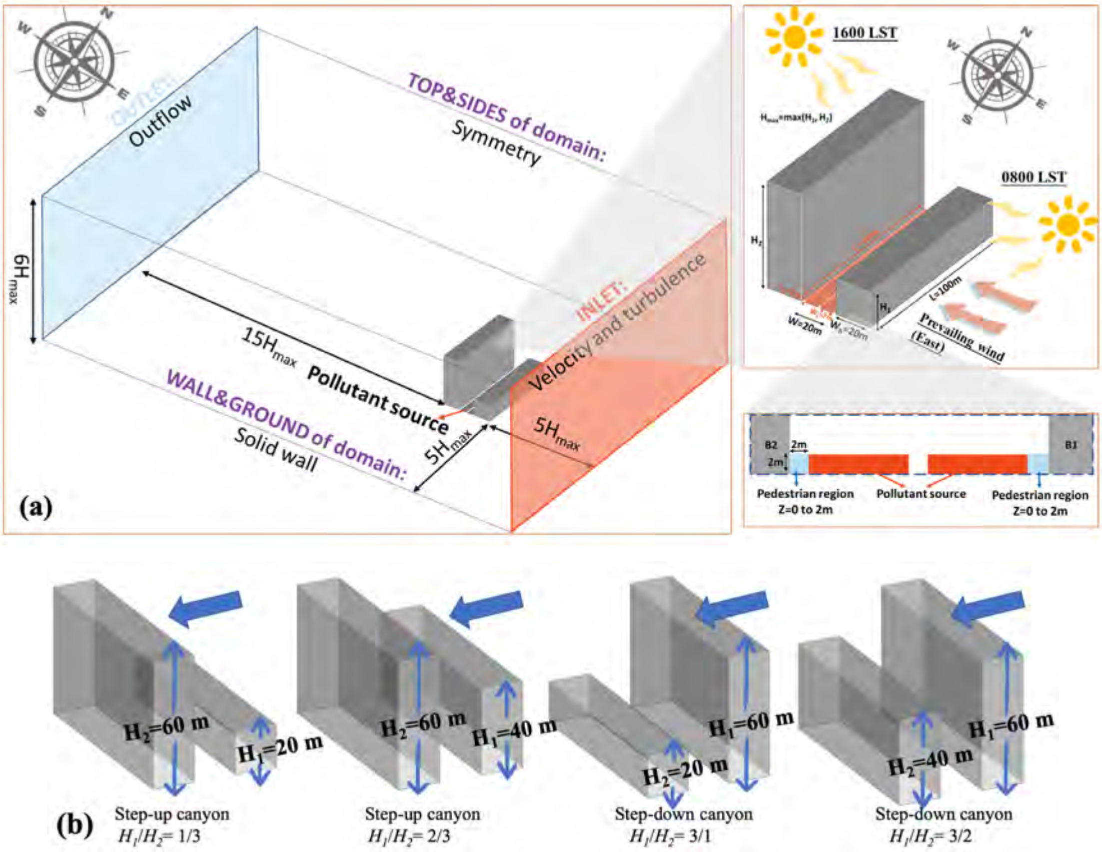

Figure 3.1 (a) The geometric model and boundary condition and (b) various asymmetric street canyon configurations

3.2.2 Numerical models

The commercial software ANSYS/Fluent® CFD software (Release 15.0) [127] is used to simulate the airflow of ambient wind over this isolated street canyon. The numerical analysis is based on the steady-state 3D RANS conservation equations of mass, momentum, and energy for the incompressible turbulent flow. RNG k-ε model is chosen in this chapter to provide reliable predictions of the mean flows with the thermal effect and pollutant dispersion. Besides, this chapter utilizes SIMPLEC numerical method for the pressure-velocity coupling. The second-order upwind scheme [103] is used to discretize both the convective terms and the diffusion terms. A double-precision solver is also selected for the CFD calculations. The convergence of the normalized residual errors of the energy equation is set to 10^{-9}, whereas the convergence criterion of the remaining equations is set to 10^{-6}.

3.2.3 Boundary conditions

Simulations are conducted for steady-state weather conditions at LSTs (local solar times) of 8 am (0800 LST) and 16 pm (1600 LST) on a clear summer day in Hong Kong with two different inlet temperatures (27.3 ℃ for 8 am and 29.1 ℃ for 16 pm). As shown in Figure 3.1(a), the sun rises in the east in the morning (8 am) and sets in the west in the afternoon (16 pm). Additionally, two different incoming airflow conditions (0.5 m/s for low wind speed (supplement) and 3 m/s high wind speed (main consideration)) are considered for various Richardson numbers. The velocity inlet and the calculation of solar radiation are the same as the settings in Chapter 2.

3.2.4 Grid sensitivity analysis

Further, three types of meshes are tested under the same environmental conditions (0800 LST, U_{ref}= 3 m/s, and T_{in} = 27.3 ℃). According to Table 3.1, the comparisons of average wind speed, air temperature, and pollutant concentration at the pedestrian level show that the corresponding mean deviations between the fine grid and medium grid are less than 4%, indicating that the fine grid and medium grid yield considerably close results. In contrast, the mean deviation between the predictions of average wind speed and pollutant concentration by the medium grid and those by the coarse grid are even more than 34%. Accordingly, the medium grid (with a total cell number of 3.5 million), is considered adequate and adapted to perform further numerical analysis.

Table 3.1 Mesh independence study (0800 LST, U_{ref}= 3 m/s and T_{in}= 27.3 °C).

Cell numbers	First-layer thickness (m)	Maximum element size (m)	Average wind velocity at pedestrian level (m/s)	Average CO concentration at pedestrian level (mg/m^3)	Average air temperature at the pedestrian level (°C)
0.5 million	0.5	5	0.832	3.156	28.197
3.5 million	0.4	4	0.585	4.242	28.612
12.3 million	0.3	3	0.562	4.309	28.731

3.3 Validation

The in-canyon air temperature and wind speed and pollutant dispersion have been validated in Chapter 2. Besides, this chapter attempts to validate the wall temperature to further evaluate the numerical accuracy of solar radiation prediction. The surface temperature data are compared with the field measurements that were obtained by Idczak et al. [128], who explored the thermal conditions inside a street canyon in an industrial area of Guerville, France (48°56' N, 1°44' E) on a sunny day (July 28). In the field experiment (Figure 3.2 (a)), the measurements were conducted in three parallel scaled street canyons that consisted of four empty steel containers covered by cement panels, with a corresponding length of 18.3 m, a height of 5.2 m, and a width of 2.4 m. The width of the street was 2.1 m; therefore, the aspect ratio of the street canyon (defined as the ratio of the height of the building to the width of the street) is approximately 2.48. The street axis was oriented at an angle of 54° to the north. To evaluate the predicted thermal environment at 0800 LST and 1600 LST, the settings of the CFD simulation are consistent with those of the field measurement, including the physical model (Figure 3.2(c)), the inlet air temperature (19.2 °C for 0800 LST and 28.3 °C for 1600 LST), wind speed (1.6 m/s for 0800 LST and 2.1 m/s for 1600 LST), and wind direction (south-west direction for both cases, almost parallel to the street axis). Meanwhile, the CFD validation cases share the same spectral optical and thermos-physical material properties of the container surface, including the specific heat (800 J/kg K), thermal conductivity (0.9 W/m K), and emissivity (0.95). The same coordinate (48°56' N, 1°44' E) and the time (July 28) of field measurements are input into the solar calculator of ANSYS/Fluent® to yield similar short-wave solar radiation for the validation case. Finally, the predictions of the wall temperature are compared with the field measurements in the southern façade of the second container at two levels (the average wall temperature along two sections, z/H = 0.21 and 0.84, as shown in Figure 3.2(b)).

The predicted wall temperature is in satisfactory agreement with the recorded field measurement data (Table 3.2). At 0800 LST, the upper part of the southern façade is directly heated by solar radiation, while its lower part is still shaded by the downwind building. Accordingly, the field measurement data show that there is a 3.5 ℃ higher wall temperature at z/H= 0.84 than that at z/H = 0.21 (Table 3.2). This non-uniform distribution of wall temperature is also well-predicted by the present CFD model (wall temperature at z/H= 0.84 is 4.5 ℃ higher than that at z/H= 0.21). Similarly, at 1600 LST, the northern façade is directly heated by solar radiation while the upwind building shades the whole southern façade. Then, the air in the vicinity of the northern façade becomes hotter, and this hotter air further heats the southern façade along with the in-canyon primary recirculation (from northern façade to southern façade near the ground). Accordingly, the field measurement results show that the wall temperature at z/H= 0.21 is 0.3 ℃ higher than that at z/H= 0.87 (see Table 3.2). The present CFD model well catches this trend again (the wall temperature at z/H= 0.21 is 1.8 ℃ higher than that at z/H= 0.87). Generally, although there are still some differences between the predicted CFD results and field measurement data since the heat storage effects of the building walls are not considered, the prediction of the non-uniform wall temperature within the street canyon due to the realistic solar radiation is acceptable.

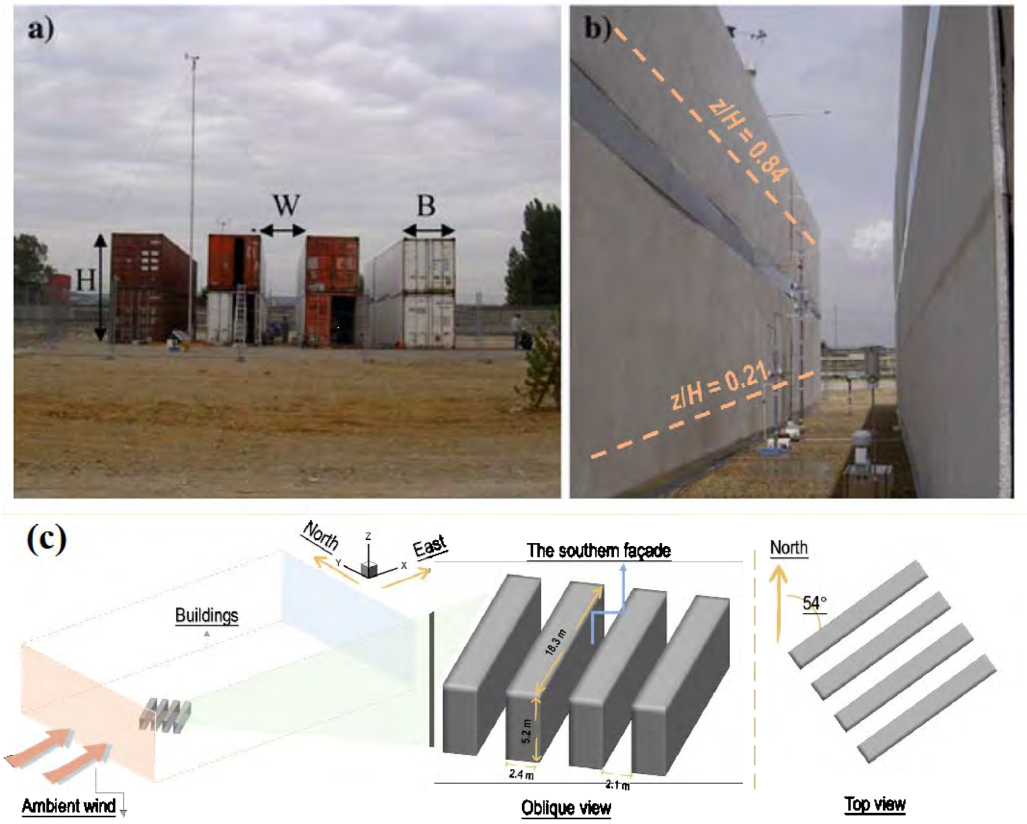

Figure 3.2 Field measurements by Idczak et al. [128]: (a) An overview, (b) the instrumentation in the investigated street, and (c) CFD model for the validation of wall temperature

Table 3.2 Comparison of the predicted non-uniform wall temperature with the field measurement data

Horizontal section	0800 LST (Background air temperature= 19.2 °C)		1600 LST (Background air temperature= 28.3°C)	
	CFD simulation	Field measurement	CFD simulation	Field measurement
z/H = 0.21	19.6 °C	21.4°C	30.1°C	29.2°C
z/H = 0.84	24.1°C	24.9°C	28.3°C	28.9°C

3.4 Richardson number in the asymmetric street canyons

Typically, the bulk Richardson number, *Ri*, is used to represent the atmospheric stability in the vertical direction [8]. *Ri* can be used to determine whether the induced flow field is dominated by the thermal or mechanical effect [129]. Herein, *Ri* of an asymmetric street canyon is defined as the ratio of the characteristic buoyancy force to the inertial force that is experienced by a fluid element, in consideration of the distribution of the wall temperature:

$$Ri = \frac{g\frac{H_1 + H_2}{2}(T_{in} - \frac{T_L + T_W}{2})}{U_{ref}{}^2 T_{in}} \tag{3.1}$$

In Eq. (3.1), T_W and T_L are the averaged surface temperatures on the windward and leeward surfaces, respectively, and U_{ref} is the volume-average wind speed within the asymmetric canyons (blue regions in Figure A3.1). The reference height is $(H_1+H_2)/2$. T_{in} is the inlet air temperature (27.3 °C for 0800 LST and 29.1 °C for 1600 LST). If $|Ri|$ approaches ∞, the airflow within the street canyon that is induced by the mechanical effect can be ignored [129,130].

3.5 Results and discussion

3.5.1 Effect of asymmetric configurations without solar radiation

To investigate the influence of solar radiation, the flow structures of asymmetric configurations are investigated without solar radiation as the baseline. According to Cui et al. [131], the flow structure does not change once the building Reynolds number Re_h (h = H_{max} =60 m) exceeded the critical value ($Re_h = 3.4\times10^4$). In this chapter, the value of Re_h for low-wind-speed conditions is 1.88×10^6, which is far larger than the critical value of Re_h. Thus, the influence of the canyon configuration on the flow structure is similar for low and high wind speeds. Figure 3.3 presents the wind velocity contours and 3D streamlines for the step-up and step-down street canyons, respectively, under a high wind speed. For the step-up street canyon, the flow structure changes only minimally with the increase of H_1, and the lower part of the street canyon is occupied by divergent flows that are caused by the strong downdraft flow (Figure 3.3(c) and (d)). However, the wind velocity decreases slightly since the higher upstream building blocks the incoming flow and, therefore, attenuates the strength of the downdraft flow (Figure 3.3(a) and (b)). For the step-down street canyon with H_1/H_2= 3/1, a large clockwise vortex occurs in the leeward region of the upstream building, resulting in the formation of a downdraft flow and divergent flows in the lower space of the step-down street canyon (Figure 3.3(g)). With the increase of H_2, the flow structure changes substantially. As shown in Figure 3.3(h), the downdraft flow disappears, and the divergent flows are replaced by two elevated eddies. Moreover, the wind velocity changes minimally in the center of the street canyon, but it increases slightly near the lateral exit (Figure 3.3(e) and (f)).

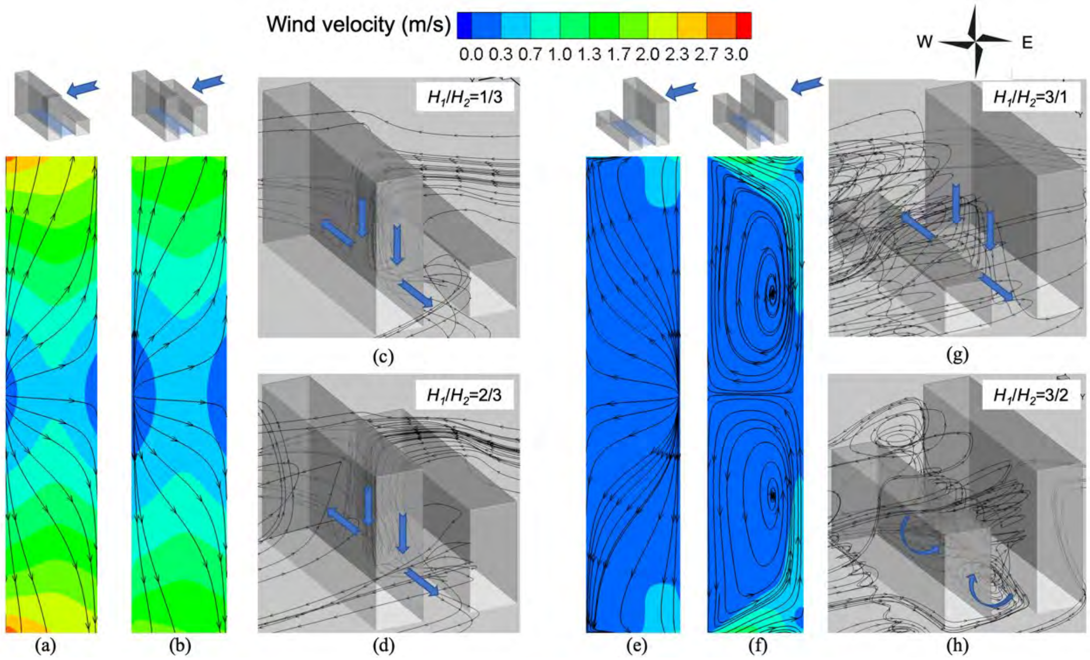

Figure 3.3 Predicted wind velocity at the pedestrian level and 3D streamlines for various asymmetric street canyon configurations under a high wind speed without solar radiation: the wind velocity at the pedestrian level for (a) H_1/H_2= 1/3, (b) H_1/H_2= 2/3, (e) H_1/H_2= 3/1, and (f) H_1/H_2= 3/2; and 3D streamlines for (c) H_1/H_2= 1/3, (d) H_1/H_2= 2/3 (g) H_1/H_2= 3/1, and (h) H_1/H_2= 3/2. (The blue arrow denotes the flow direction within the street canyon.)

3.5.2 Effect of asymmetric configurations with solar radiation

Considering the solar radiation, Memon et al. [16] reported that the flow structure could differ significantly among incoming flow conditions. Thus, for the thermal flow, the influence of asymmetric configurations with solar radiation is analyzed at high wind speed (3 m/s) and low wind speed (0.5 m/s). This thermal flow with solar radiation is dependent on the Reynolds number within our study range.

3.5.2.1 High incoming wind speed

Process I: To what height should the lower building be rebuilt?

Figure 3.4 and Figure 3.5 present the 3D streamlines and wind velocity contours under the high wind speed of 3 m/s for step-up and step-down street canyons, respectively. In the step-up street canyon, the buoyancy effect is relatively weak because the $|Ri|$ is low (1.27 to 4) (Table 3.3). The flow structure is still dominated by forced convection at 0800 LST (Figure 3.4(c) and (d)) and at 1600 LST (Figure 3.4(g) and (h)). The distributions of the 3D streamlines are similar to those in the cases without solar radiation (Figure 3.3(c) and (d)), although the wind velocity decreases with the increase of H_1 (Figure 3.4(a) and (b), and (e) and (f)). The average wind velocity at the pedestrian level decreases by approximately 0.4 m/s at 0800 and 1600 LST (as summarized in Figure 3.8(a)). In the step-down street canyon, the forced convection still dominates the flow structure when $H_1/ H_2= 3/1$ at 0800 LST (Figure 3.5(c) with $|Ri|$ of 15.51) (Table 3.3). However, although the higher upwind building shaded the solar radiation into the street canyon at 0800 LST, the natural convection that is caused by solar radiation played a more critical role in the increase of H_2 ($|Ri|$ increased to 20.33 (Table 3.3)), thereby leading to the formation of an updraft flow (Figure 3.5(d)), in contrast to the 3D streamlines without solar radiation (Figure 3.3(d)). The possible explanation lies in the weak forced convection within this kind of street canyon. Once the airflow heated by the windward surface enters the step-down canyon from the lateral shear layer (Figure 3.5(d)), air flows upwards because the natural convection is stronger than the weak forced convection. Furthermore, the lower part of the street canyon is occupied by convergent flows, and the wind velocity increases rapidly (Figure 3.5(a) and (b)). The average wind velocity at the pedestrian level increases by 0.2 m/s (Figure 3.8(a)). At 1600 LST, the updraft flows are always observed (Figure 3.5(g) and (h)) due to high $|Ri|$ (from 29.73 to 30.89) (Table 3.3)). When H_2 increases, $|Ri|$ decreases (a stronger shading effect on the downstream building leads to weaker natural convection), and, thus, the wind velocity, which is affected by natural convection, decreases slightly (Figure 3.5(e) and (f)).

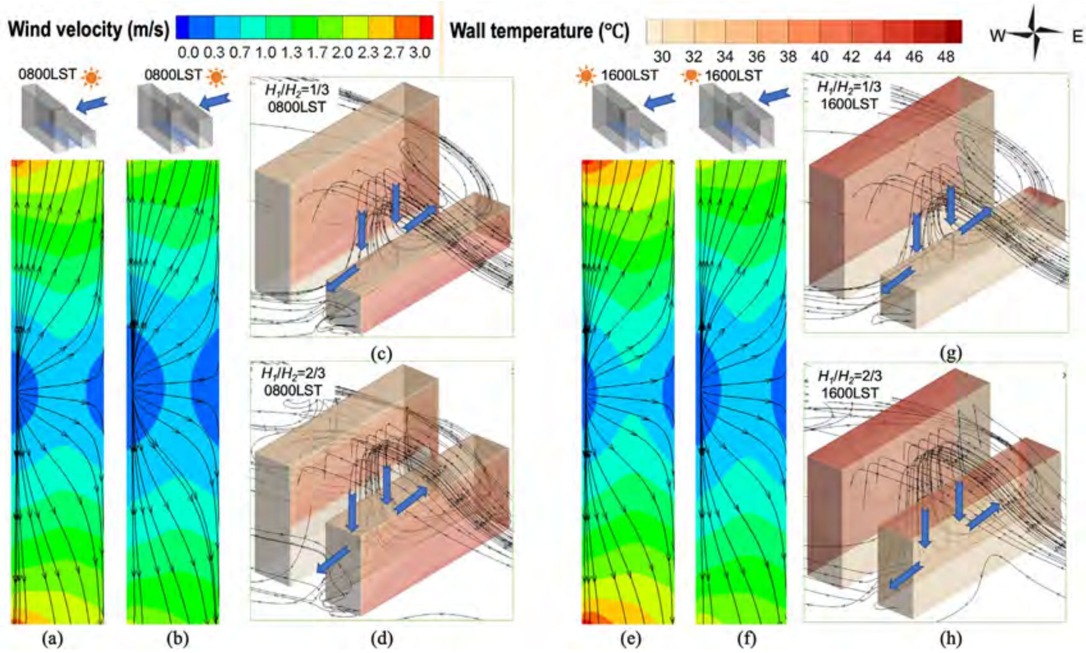

Figure 3.4 Predicted wind velocity at the pedestrian level and 3D streamlines for various step-up street canyon configuration at LSTs of 0800 and 1600 under the high wind speed of 3 m/s: the wind velocity at the pedestrian level for (a) H_1/ H_2= 1/3 at 0800 LST, (b) H_1/ H_2= 2/3 at 0800 LST, (e) H_1/ H_2= 1/3 at 1600 LST, and (f) H_1/ H_2= 2/3 at 1600 LST; and 3D streamlines for (c) H_1/ H_2= 1/3 at 0800 LST, (d) H_1/ H_2= 2/3 at 0800 LST, (g) H_1/ H_2= 1/3 at 1600 LST, and (h) H_1/ H_2= 2/3 at 0800 LST. (The blue arrow denotes the flow direction within the street canyon.)

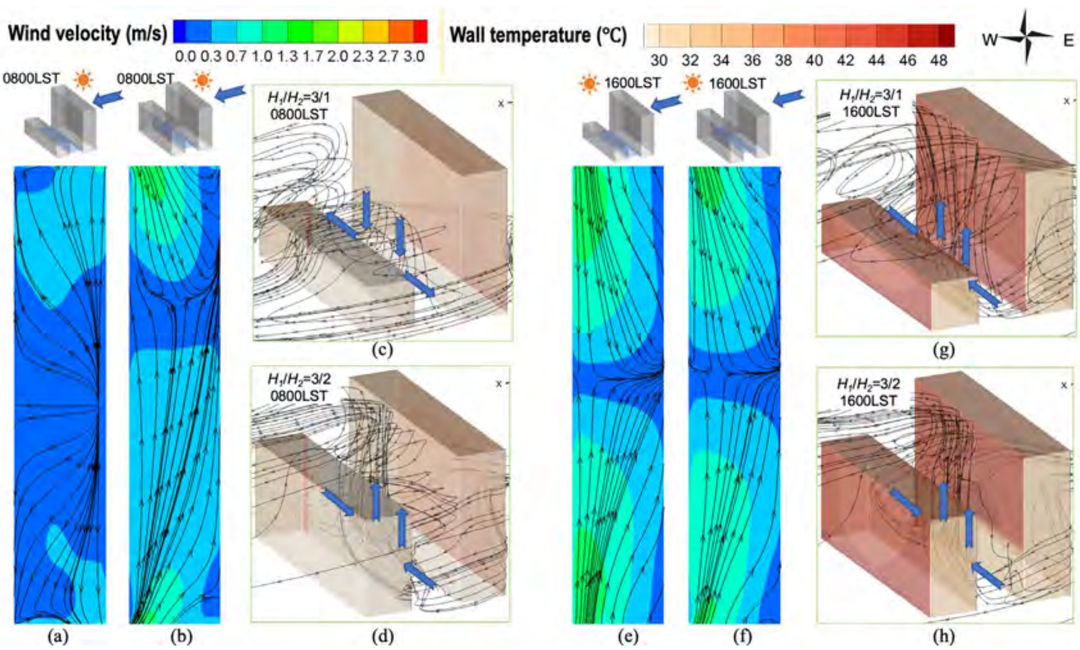

Figure 3.5 Predicted wind velocity at the pedestrian level and 3D streamlines for various step-down street canyon configurations at LSTs of 0800 and 1600 under the high wind speed of 3 m/s: the wind velocity at the pedestrian level for (a) H_1/H_2= 3/1 at 0800 LST, (b) H_1/H_2= 3/2 at 0800 LST, (e) H_1/H_2= 3/1 at 1600 LST, and (f) H_1/H_2= 3/2 at 1600 LST; and 3D streamlines for (c) H_1/H_2= 3/1 at 0800 LST, (d) H_1/H_2= 3/2 at 0800 LST, (g) H_1/H_2= 3/1 at 1600 LST, and (h) H_1/H_2= 3/2 at 0800 LST. (The blue arrow denotes the flow direction within the street canyon.)

Table 3.3 Bulk Richardson numbers in the asymmetric street canyons under high wind speed

Case	Configuration	LST	$\|Ri\|$	Case	Configuration	LST	$\|Ri\|$
1	H_1/H_2= 1/3	0800	4.00	5	H_1/H_2= 3/1	0800	15.51
2		1600	1.27	6		1600	30.89
3	H_1/H_2= 2/3	0800	3.98	7	H_1/H_2= 3/2	0800	20.33
4		1600	2.38	8		1600	29.73

Figure 3.6 presents the distribution of the CO concentration under the high wind speed of 3 m/s. In the step-up street canyon, the concentrations increase with the increase of H_1 due to the reduction of the wind velocity at 0800 (Figure 3.6(a) and (b)) and 1600 LST (Figure 3.6(c) and (d)). The average concentrations increase by 48.8% at 0800 LST and by 39.0% at 1600 LST (see the summary in Figure 3.8(b)). In the step-down street canyon, the divergent flows (Figure 3.5(c)) transform into convergent flows (Figure 3.5(d)) near the ground at 0800 LST when H_2 increases. Therefore, more pollutants accumulate in the center of the street canyon, while the concentration near the lateral exit decreases (Figure 3.6(e) & (f)). At 0800 LST, the average concentration decreases by 8.2% (Figure 3.8(b)). At 1600 LST, the concentrations remain nearly unchanged (1.3%) due to only minor changes in the wind velocity (Figure 3.5(g) and (h)).

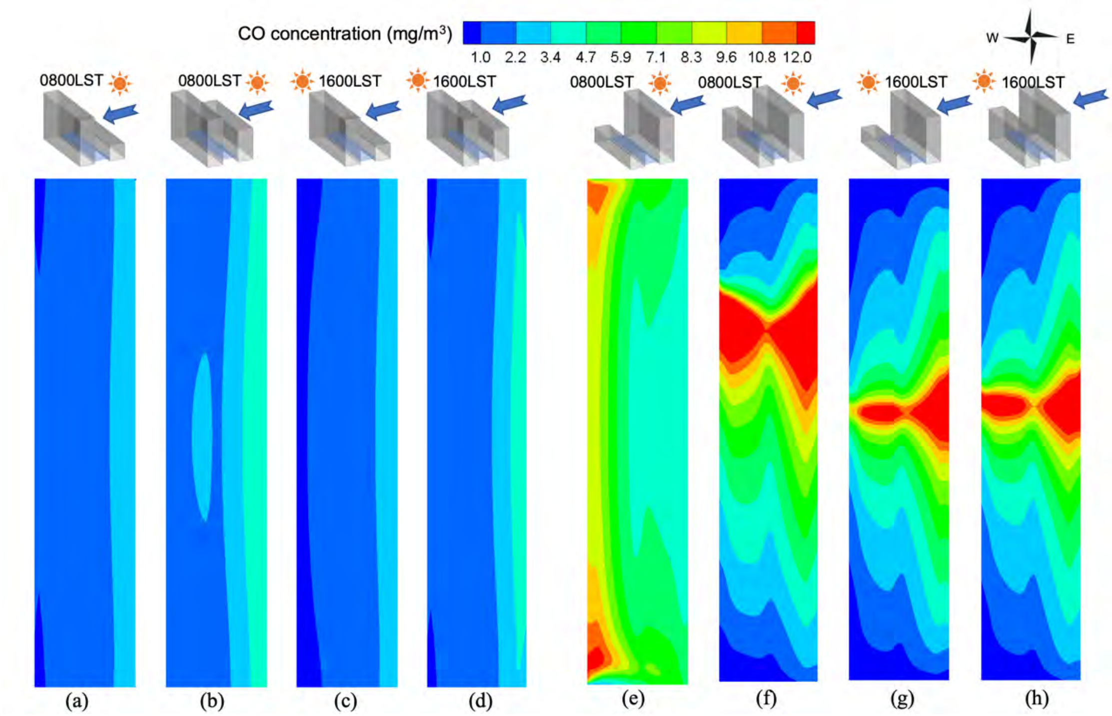

Figure 3.6 Predicted CO concentrations at the pedestrian level for various asymmetric street canyon configurations at LSTs of 0800 and 1600 under the high wind speed of 3 m/s: the step-up canyon with (a) H_1/ H_2= 1/3 at 0800 LST, (b) H_1/ H_2= 2/3 at 0800 LST, (c) H_1/ H_2= 1/3 at 1600 LST, and (d) H_1/ H_2= 2/3 at 1600 LST; and the step-down canyon with (e) H_1/ H_2= 3/1 at 0800 LST, (f) H_1/ H_2= 3/2 at 0800 LST, (g) H_1/ H_2= 3/1 at 1600 LST, and (h) H_1/ H_2= 3/2 at 1600 LST.

Figure 3.7 presents the contours of the air temperature under the high wind speed of 3 m/s. In the step-up street canyon, the air temperature at the pedestrian level is directly related to the temperature of the incoming flow because the relatively high wind velocity (up to 1.4 m/s) at the pedestrian level contributes to the dispersion of heat. Thus, the variation of the air temperature is small with an increase of H_1 (Figure 3.7(a) and (b), (c) and (d)). In the step-down street canyon, the air temperature increases by 0.2- 0.4 °C in the northern part of the street canyon (Figure 3.7(e) and (f)), because the convergent flows have adverse effects on the heat dispersion at 0800 LST. The average air temperature increases slightly by 0.1°C (Figure 3.8(c)). At 1600 LST, the air temperature decreases slightly due to the stronger shading effect provided by the high downstream building (Figure 3.7(g) and (h)). The average air temperature decreases by 0.4°C (Figure 3.8(c)).

In summary, the height increase of the lower building in the step-down canyon leads to higher air quality and lower air temperature under high wind speed. However, the higher upstream building of the step-up canyon results in lower air quality but has only a minor influence on the thermal environment. When $|Ri| < 20$, the flow field is dominated by forced convection. The variation of $|Ri|$ slightly influences air quality and air temperature. When $|Ri| > 20$, the flow field is dominated by natural convection. The increase of $|Ri|$ increases the air temperature and the decrease in the pollutant concentration at the pedestrian level.

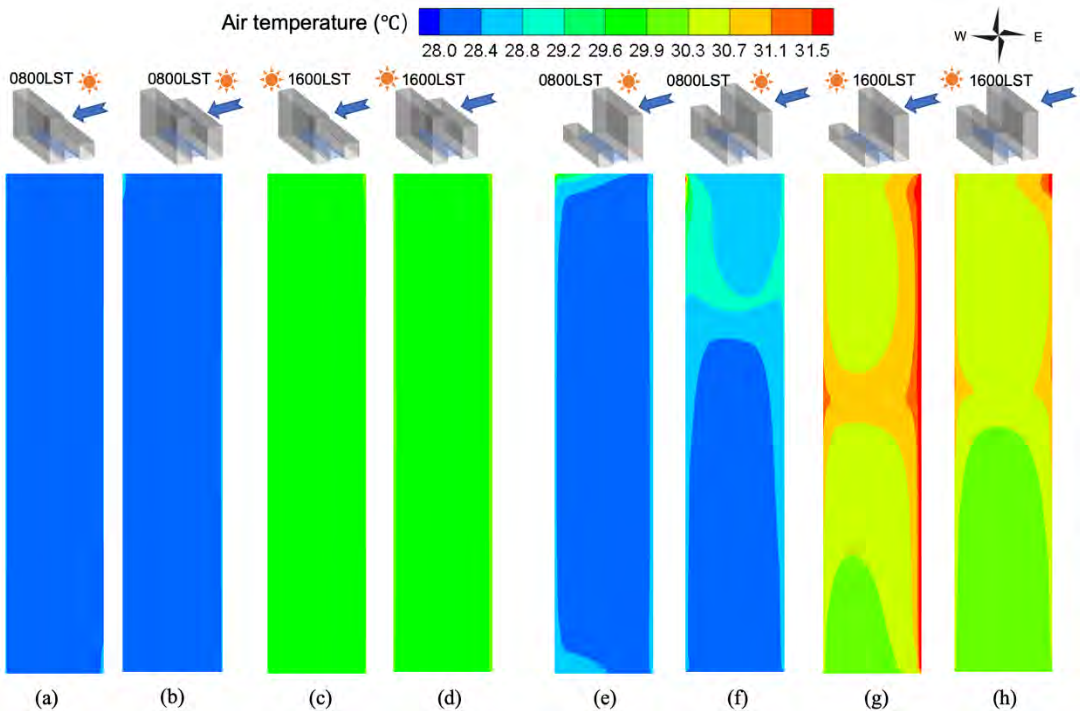

Figure 3.7 Predicted air temperatures at the pedestrian level for various asymmetric street canyon configurations at LSTs of 0800 and 1600 under the high wind speed of 3 m/s: the step-up canyon with (a) H_1/ H_2= 1/3 at 0800 LST, (b) H_1/ H_2= 2/3 at 0800 LST, (c) H_1/ H_2= 1/3 at 1600 LST, and (d) H_1/ H_2= 2/3 at 1600 LST; and the step-down canyon with (e) H_1/ H_2= 3/1 at 0800 LST, (f) H_1/ H_2= 3/2 at 0800 LST, (g) H_1/ H_2= 3/1 at 1600 LST, and (h) H_1/ H_2= 3/2 at 1600 LST.

Process II: Which side of the street should be rebuilt?

To evaluate rebuilding process II, the average CO concentration and air temperature at the pedestrian level are compared between the step-up and the step-down street canyons in Figure 3.8. For the step-up canyon with H_1/ H_2= 1/3 and the step-down canyon with H_1/ H_2= 3/1, the average CO concentration of the step-down canyon is 261.4% higher than that of the step-up canyon at 0800 LST (Figure 3.8(b)), and the average air temperature of the step-down canyon is up to 1.1℃ (3.7%) higher than that of the step-up canyon at 1600 LST (Figure 3.8(c)). For the step-up canyon with H_1/ H_2= 2/3 and the step-down canyon with H_1/ H_2= 3/2, lower air quality and higher air temperature are observed in the step-down canyon again. The average CO concentration of the step-down canyon (H_1/ H_2= 3/2) is 123.1% higher than that of the step-up canyon (H_1/ H_2= 2/3) at 0800 LST (Figure 3.8(b)), and the average air temperature of the step-down canyon is up to 0.6℃ (2.0%) higher than that of the step-up canyon at 1600 LST (Figure 3.8(c)). In summary, the step-down street canyon is outperformed by the step-up street canyon in both scenarios.

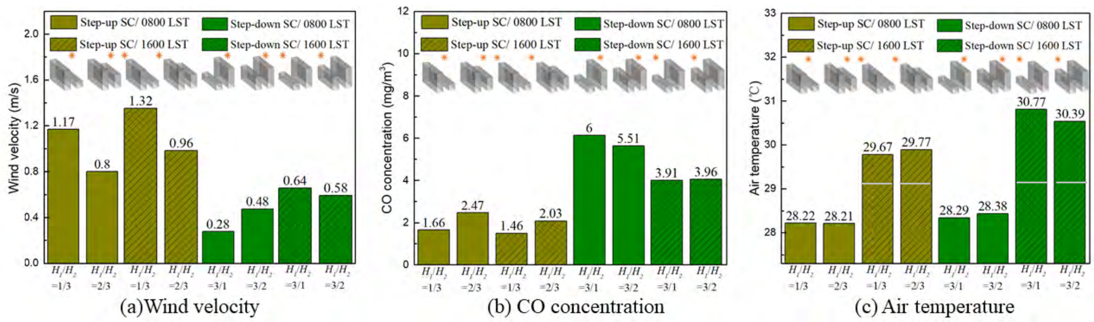

Figure 3.8 Predicted average values at the pedestrian level for step-up and step-down cases: (a) the wind velocities, (b) CO concentration, and (c) Air temperature under the high wind speed of 3 m/s at LSTs of 0800 and 1600. The *y*-axis of Fig. 12 (c) starts from the reference air temperature (27.3 ℃) at 0800 LST, and the grey line denotes the reference air temperature (29.1 ℃) at 1600 LST.

3.5.2.2 Low incoming wind speed

Process I: To what height should the lower building be rebuilt?

Figure 3.9 and Figure 3.10 present the 3D streamlines and wind velocity contours under the low wind speed of 0.5 m/s. Natural convection has a significant influence on the flow structure. In the step-up street canyon, at 0800 LST, an updraft flow that is caused by the heated windward surface occurs in the street canyon with H_1/ H_2= 1/3 (Figure 3.9(c)), in contrary to the high-wind case (Figure 3.4(c)). The lower part is still occupied by divergent flows. With the increase of H_1, the natural convection strengthens ($|Ri|$ increased) (Table 3.4) and leads to the formation of convergent flows (Figure 3.9(d)). Thus, the average wind velocity at the pedestrian level increases by 0.3 m/s due to the convergent flows (see the summary in Figure 3.13 (a)). At 1600 LST, a downdraft flow is also observed in the street canyon with H_1/H_2= 1/3 (Figure 3.9(g)) since the forced convection dominates the flow structure ($|Ri|$ = 7.50). With the increase of H_1, the downdraft flow still dominates within the canyon, but the natural convection strengthens ($|Ri|$ increased to 16.18). Thus, the average wind velocity at the pedestrian level decreases by 0.3 m/s (Figure 3.13(a)) due to the reduction of the forced convection and the stronger natural convection. In the step-down street canyon, the flow structure is affected mainly by the stronger natural convection (higher $|Ri|$); therefore, updraft flows are observed (Figure 3.10). At 0800 LST, the natural convection weakens (with relatively small $|Ri|$) due to lower wall temperature with the increase of H_2. Thus, the average wind velocity at the pedestrian level decreases slightly. Similarly, the average wind velocity decreases by 0.2 m/s at 1600 LST (Figure 3.13(a)).

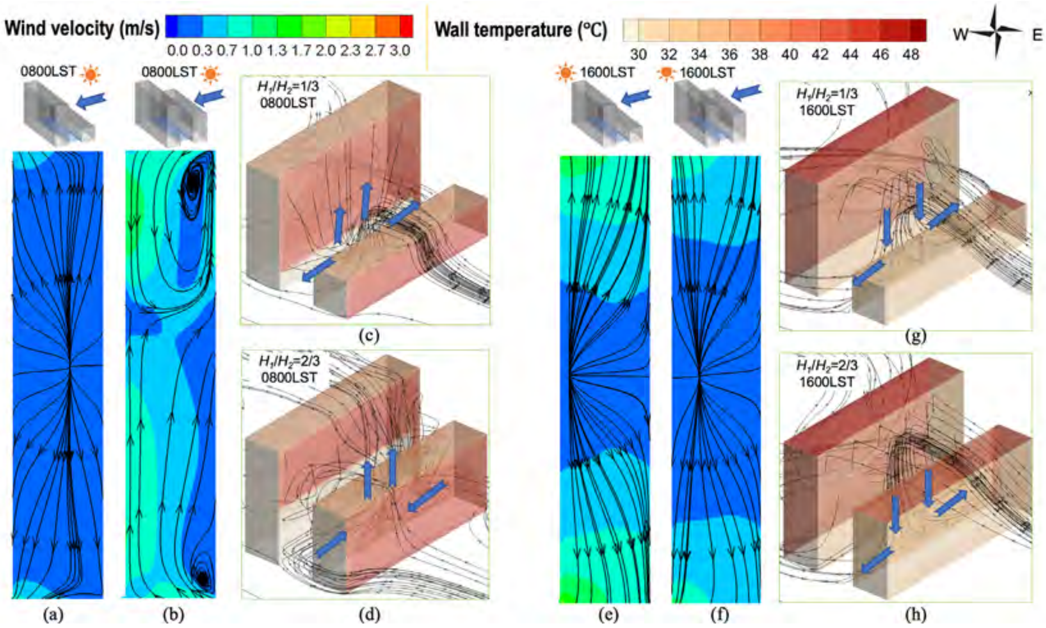

Figure 3.9 Predicted wind velocity at the pedestrian level and 3D streamlines for various step-up street canyon configurations at LSTs of 0800 and 1600 under the low wind speed of 0.5 m/s: the wind velocity at the pedestrian level for (a) H_1/H_2= 1/3 at 0800 LST, (b) H_1/H_2= 2/3 at 0800 LST, (e) H_1/H_2= 1/3 at 1600 LST, and (f) H_1/H_2= 2/3 at 1600 LST; and 3D streamlines for (c) H_1/H_2= 1/3 at 0800 LST, (d) H_1/H_2= 2/3

at 0800 LST, (g) H_1/ H_2= 1/3 at 1600 LST, and (h) H_1/ H_2= 2/3 at 0800 LST. (The blue arrow denotes the flow direction within the street canyon.)

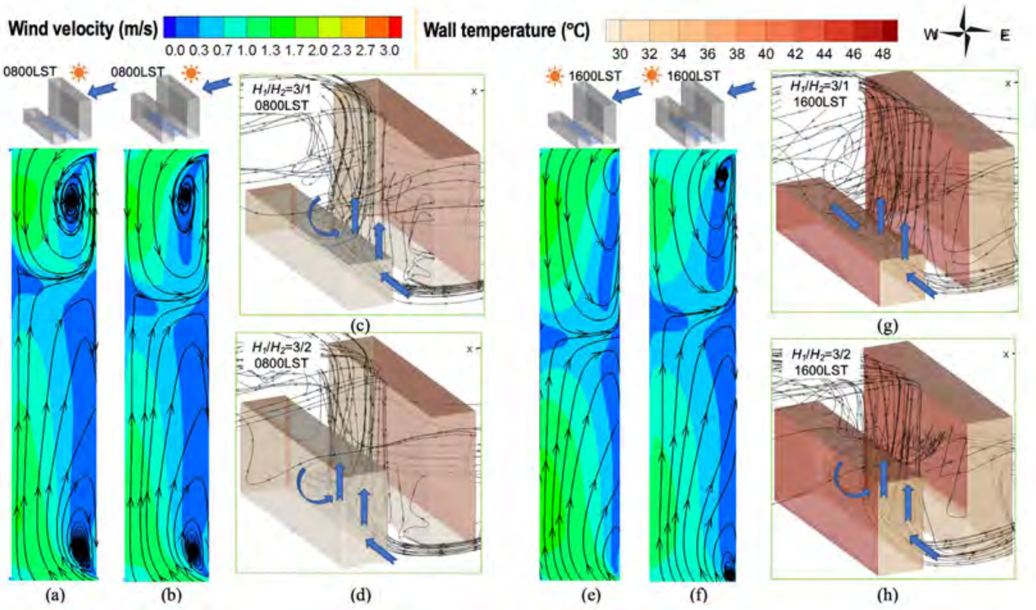

Figure 3.10 Predicted wind velocity at the pedestrian level and 3D streamlines for various step-down street canyon configurations at LSTs of 0800 and 1600 under the low wind speed of 0.5 m/s: the wind velocity at the pedestrian level for (a) H_1/ H_2= 3/1 at 0800 LST, (b) H_1/ H_2= 3/2 at 0800 LST, (e) H_1/ H_2= 3/1 at 1600 LST, and (f) H_1/ H_2= 3/2 at 1600 LST; and 3D streamlines for (c) H_1/ H_2= 3/1 at 0800 LST, (d) H_1/ H_2= 3/2 at 0800 LST, (g) H_1/ H_2= 3/1 at 1600 LST, and (h) H_1/ H_2= 3/2 at 0800 LST. (The blue arrow denotes the flow direction within street canyon.)

Table 3.4 Bulk Richardson numbers in the asymmetric street canyons under low wind speed

Case	Configuration	LST	$\lvert Ri \rvert$	Case	Configuration	LST	$\lvert Ri \rvert$
1	H_1/ H_2= 1/3	0800	25.16	5	H_1/ H_2= 3/1	0800	26.73
2		1600	7.50	6		1600	29.13
3	H_1/ H_2= 2/3	0800	26.01	7	H_1/ H_2= 3/2	0800	26.13
4		1600	15.67	8		1600	28.42

Figure 3.11 presents the CO concentration contours under low wind speed. With the increase of H_1 at 0800 LST in the step-up street canyon, pollutants gather in the northern part of the street canyon, but the concentrations in other areas decrease (Figure 3.11(a) and (b)) due to the variation of the flow structure. Thus, the average concentrations decrease by 24.4% (Figure 3.13(b)). At 1600 LST, the average

concentrations increase by 77.1% due to a decrease in the wind velocity with the increase of H_1 (Figure 3.13(b)). In the step-down street canyon, there is a minor increase of the concentration (3.4%), which is due to the similar wind velocity and flow structure at 0800 LST (Figure 3.10(e) and (f)), while it increases by 46.9% due to the decrease of the wind velocity at 1600 LST (Figure 3.13(b)).

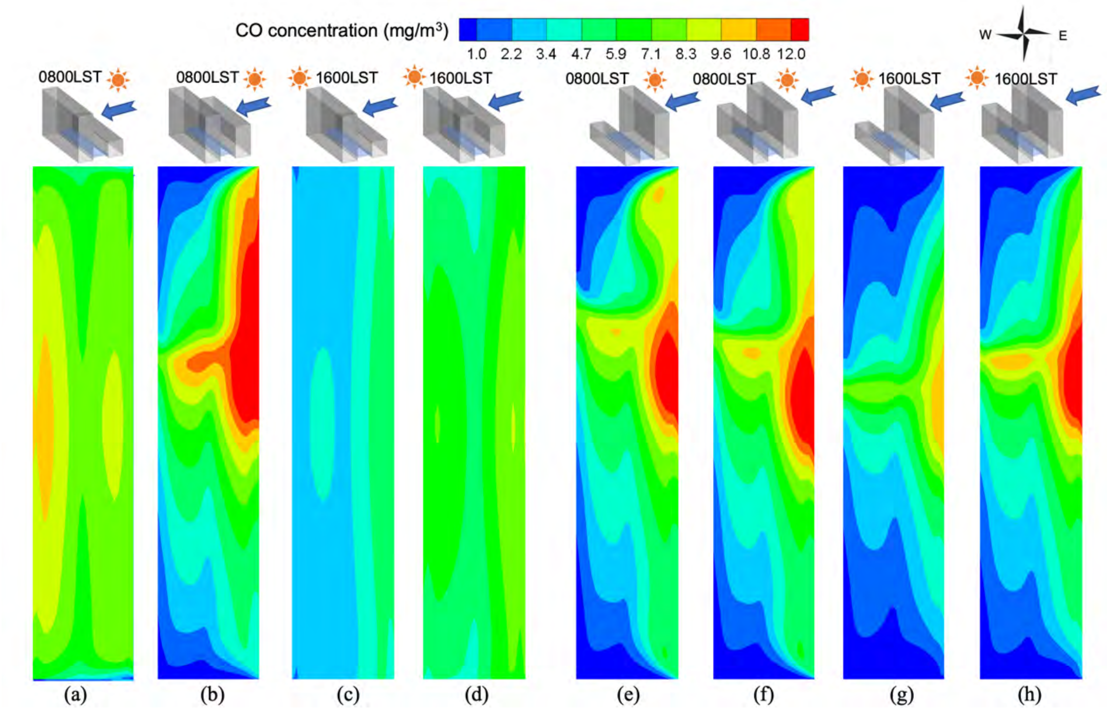

Figure 3.11 Predicted CO concentrations at the pedestrian level for various asymmetric street canyon configurations at LSTs of 0800 and 1600 under low wind speed: the step-up canyon with (a) $H_1/H_2= 1/3$ at 0800 LST, (b) $H_1/H_2= 2/3$ at 0800 LST, (c) $H_1/H_2= 1/3$ at 1600 LST, and (d) $H_1/H_2= 2/3$ at 1600 LST; and the step-down canyon with (e) $H_1/H_2= 3/1$ at 0800 LST, (f) $H_1/H_2= 3/2$ at 0800 LST, (g) $H_1/H_2= 3/1$ at 1600 LST, and (h) $H_1/H_2= 3/2$ at 1600 LST.

Figure 3.12 presents the air temperature contours under low wind speed. In the step-up street canyon, the air temperature increases in the north but decreases in the south due to the convergent flow at 0800 LST (Figure 3.12(a) and (b)). The average temperature changes slightly. At 1600 LST, the average temperature increases slightly, namely, by 0.3°C (Figure 3.13(c)), due to the reduction of the wind velocity. In the step-down street canyon, the average air temperature changes slightly at 0800 LST (Figure 3.12(e) and (f)). This is because the higher upstream building almost blocks the solar radiation and the wind velocity also changes slightly. However, it decreases by 0.2℃ at 1600 LST due to the increase of the shading effect of the downstream building (Figure 3.13(c)).

In summary, the height increase of the lower building results in the higher air quality at 0800 LST and lower air quality at 1600 LST in the step-up canyon under low wind speed; it results in lower air quality in the step-down canyon for all the scenarios. The higher upstream building of the step-up canyon leads to higher air temperature, while the higher downstream building of the step-down canyon results in lower air temperature. Similarly, the flow structure is dominated by forced convection when $|Ri| < 20$, and the variation of $|Ri|$ is not directly related to air quality or air temperature. In contrast, when $|Ri| > 20$, the flow field is dominated by natural convection, and the increase of $|Ri|$ also leads to an increase in the air temperature and a decrease in the pollutant concentration at the pedestrian level.

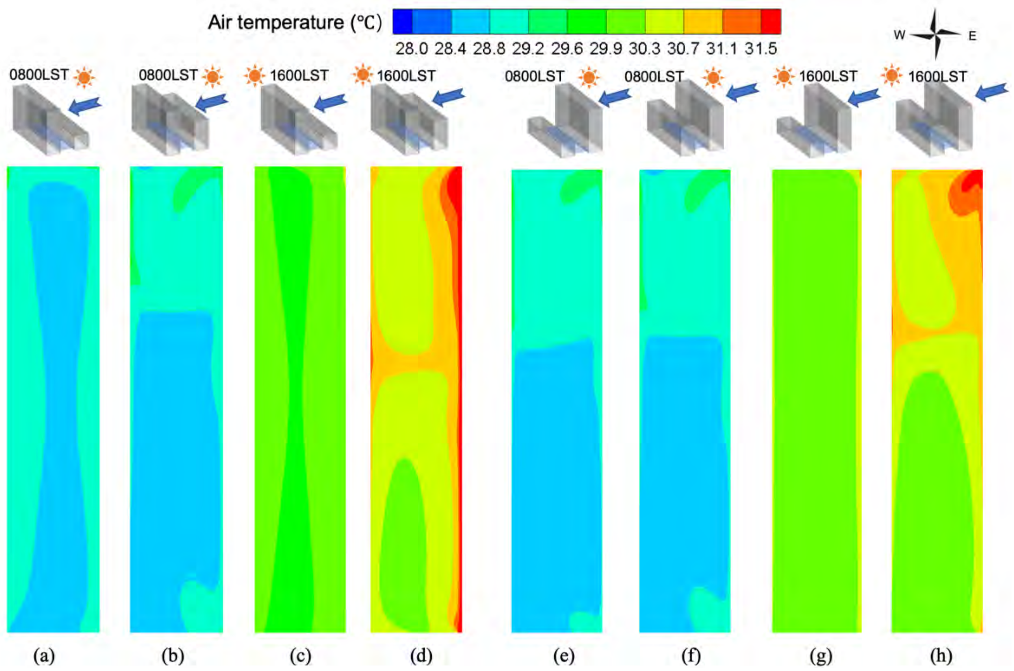

Figure 3.12 Predicted air temperature at the pedestrian level for various asymmetric street canyon configurations at LSTs of 0800 and 1600 under low wind speed: the step-up canyon with (a) $H_1/ H_2= 1/3$ at 0800 LST, (b) $H_1/ H_2= 2/3$ at 0800 LST, (c) $H_1/ H_2= 1/3$ at 1600 LST, and (d) $H_1/ H_2= 2/3$ at 1600 LST; and the step-down canyon with

(e) H_1/ H_2= 3/1 at 0800 LST, (f) H_1/ H_2= 3/2 at 0800 LST, (g) H_1/ H_2= 3/1 at 1600 LST, and (h) H_1/ H_2= 3/2 at 1600 LST.

Process II: On which side of the street should rebuilding be conducted?

The CO concentration and air temperature are further compared between the step-up and step-down street canyons in Figure 3.13. For the step-up canyon (H_1/ H_2= 1/3) and the step-down canyon (H_1/ H_2= 3/1), divergent flows and convergent flows, respectively, occur. Thus, higher CO concentrations occur in the center of the step-down canyon, but the concentrations are substantially lower in other areas. The average concentrations of the step-up canyon are 55.5% higher than that of the step-down canyon (Figure 3.13(b)) at 0800 LST. However, the average temperature of the step-down canyon is 0.6℃ higher than that of the step-up canyon at 1600 LST (Figure 3.13(c)), due to a weak shading effect. For the step-up canyon (H_1/ H_2= 2/3) and the step-down canyon (H_1/ H_2= 3/2), the flow structures are similar, but the wind velocity of the step-up canyon is lower (Figure 3.13(a)). Thus, the average concentration of the step-up canyon is 38.1% higher than that of the step-down canyon at 1600 LST (Figure 3.13(b)). The average air temperature of the step-down canyon is 0.3℃ higher than that of the step-up canyon (Figure 3.13(c)) at 1600 LST.

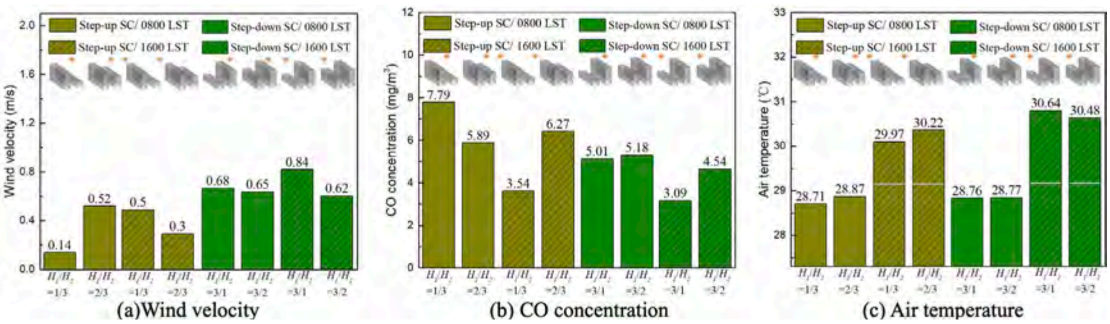

Figure 3.13 Predicted average values at the pedestrian level: (a) the wind velocity, (b) the CO concentration, and (c) the air temperature under low wind speed of 0.5 m/s at LSTs of 0800 and 1600. The *y*-axis starts from the reference air temperature (27.3 ℃) at 0800 LST, and the grey line denotes the reference air temperature (29.1℃) at 1600 LST.

3.6 Summary

This chapter investigated the influence of the asymmetric street canyon configuration on air temperature and air quality at the pedestrian level by considering realistic estimates of solar irradiation. Based on CFD calculations that were conducted using the ANSYS/Fluent® software, we obtained two outdoor parameters: the air temperature and the CO concentration. The major results are summarized as follows:

(1) Without solar radiation, the variation of the height of the lower building leads to a minor change in the flow structure in the step-up canyon but a significant change in the step-down canyon.

(2) With solar radiation, the increase of the height of the lower building of the step-up canyon leads to an increase in the average CO concentration by 39% – 49% under high wind speed, and a decrease by 24% for 0800 LST and an increase by 77% for 1600 LST under low wind speed. In addition, the average air temperature increases by 0.2℃ – 0.3℃ under low wind speed, while it is virtually unchanged under high wind speed. In contrast, when the height of the lower building of the step-down canyon increases, the average CO concentrations increase by 47% for 1600 LST under low wind speed, while it is almost unchanged in the other three cases (<8%). In the meanwhile, the average air temperature reduces by nearly 0.2℃ – 0.3 ℃ for 1600 LST under both high and low wind speeds, while it essentially does not change for the two 0800 LST cases.

(3) When $|Ri| < 20$, the flow field is dominated by forced convection, and the variation of Ri had an insignificant influence on air quality and air temperature. In contrast, when $|Ri| > 20$, the flow field is dominated by natural convection, and the increase of $|Ri|$ increases the air temperature and a decrease in the pollutant concentration.

(4) Under high wind speed, the thermal environment or air quality of the step-up canyon is always better than that of the step-down canyon; under low wind speed, the air quality is higher in the step-down canyon than in the step-up canyon, although the step-up canyon is still found to be cooler than the step-down canyon.

Chapter 4 Effects of building setback on the outdoor thermal comfort and air quality in street canyons

4.1 Introduction

Among many local mitigation strategies to design UHI and air pollution mitigation strategies effectively, the building setbacks attract less attention [78]. As discussed in Section 1.2, both horizontal (arcade design) and vertical building setback can help to improve pollutant dispersion by enhancing ventilation. Nonetheless, they are still not sufficient for practical urban planning to reduce thermal stress and improve air quality simultaneously. First, most previous studies neglected the solar radiation when the influence of building setback on airflow structure was considered. In effect, the thermally induced flow is typically combined with the mechanically induced flow, which significantly affects the flow field and corresponding dispersion of pollutants and heat. Only considering the isothermal condition cannot totally reflect the realistic effectiveness of building setback. Second, most previous papers focused on either thermal comfort or air quality; scarcely, studies address the increasingly severe issues of air temperature and air quality simultaneously. In effect, there is probably some opposite influence on the thermal comfort and air quality, when changing the geometry of the building setbacks. Huang et al. [72] found that increasing the height of the arcade was capable of improving ventilation at the measurement points. However, Yin et al. [73] suggested that the height of the arcade should be as low as possible; otherwise, the pedestrians started losing the protection from shading strategy to thermal stress. Therefore, more effort should be devoted to simultaneously considering the influence of building setbacks on thermal comfort and air quality under the same framework.

Based on this background, the objectives of this chapter are to 1) explore the effectiveness of horizontal and vertical setbacks on the improvement of the total environmental quality in a street canyon, involving both thermal comfort and air quality at the same time, 2) conduct a sensitivity analysis to investigate the influence of different design parameters (the height and width of the horizontal setback or the length and width of the vertical setback) on the effectiveness of building setbacks to the local air quality and thermal comfort by considering different street canyons under different heating scenarios, 3) provide some suggestions to enhance the building setback's benefits and to avoid some unfavorable or unintended consequences by testing various parameters related to the design of the building setback.

4.2 Description of CFD simulations

4.2.1 Description of case studies, computational geometry, and grid

As seen in Figure 4.1, this chapter employs full-scale 3D street canyon models consisting of five uniform buildings and four street canyons (street width W = 20 m, building height H = 20 m and 40 m for low-rise and high-rise street canyon, respectively, street length L = 160 m, and building width W_b = 20 m). The target street canyon locates between the 3rd and 4th building, while the other upstream and downstream identical street canyons are used to represent the influence of roughness elements [18,25,132–134].

Within the target canyon, we separately investigate the influence of horizontal and vertical building setbacks. For horizontal setback configurations, the lower part of the buildings is recessed by D_{HS} from the street, with a height of H_{HS}. Three horizontal setbacks cases are studied: (i) H_{HS}/W= 0.4 and D_{HS}/W= 0.2, (ii) H_{HS}/W= 0.2 and D_{HS}/W= 0.2, (iii) H_{HS}/W= 0.2 and D_{HS}/W= 0.1. Case (i) and (ii) are used to study the influence of the height parameters, while (ii) and (iii) are for the width parameters. A vertical setback differs from a horizontal setback by having part of the long building wall recessed D_{VS} from the street, with a length of L_{VS}. Similarly, three vertical setback cases are investigated, (iv) L_{VS}/L= 0.125 and D_{HS}/W= 0.45, (v) L_{VS}/L= 0.25 and D_{HS}/W= 0.45, (vi) L_{VS}/L= 0.25 and D_{HS}/W= 0.225. Case (iv) and (v) are used to compare the different length parameters, while (v) and (vi) are for different width parameters. Besides, the cases without building setbacks are regarded as the baselines.

Considering the symmetry of flow structure within street canyons, only half of the street canyon is chosen to reduce the computational time (Figure 4.1). The wind is assumed to go from the west, considering a worse air quality within the street canyon generally yielded by the perpendicular wind. Accordingly, the street orientation is set as a North-South direction. To represent the leeward heating (LH) scenario and windward heating (WH) scenario, the simulation is conducted for steady-state weather conditions at LSTs (local solar times) of 10 a.m. (1000 LST) and 2 p.m. (1400 LST) on a clear summer day in Hong Kong, respectively (Figure 4.1).

The size and discretization of the computational domain refer to the practice guidelines by Tominaga et al. [97]. Thus, as shown in Figure 4.1, the distances between the building and the inlet boundary, lateral boundaries, top boundary, and outflow boundary are 5 H, 5 H, 5 H, and 15 H, respectively.

The computational domain is discretized into almost three million hexahedral cells. Considering the relatively large gradients of the velocity near the ground and building surfaces, the finest grids are deployed around these two types of walls. In this chapter, a grid-sensitivity analysis is performed based on two additional grids: a coarser grid and a finer grid for the low-rise street canyon with horizontal setback (H_{HS}/W= 0.2 and D_{HS}/W= 0.2). For the coarse, basic, and fine grids, the minimum sizes are set to be 0.4 m, 0.1 m, and 0.05 m, respectively. The total cell numbers for the coarse, basic, and fine grids are 0.92 million, 3.15 million, and 10.95 million, respectively. Therefore, the ratios of the two consecutive cell numbers for the grid refinement meet the criterion of 3.4 in the mesh-independent study [97]. The results of the grid-sensitivity analysis in Section 4.2.4 indicate that the basic grid provides nearly grid-independent results, which can be used for the remainder of this chapter.

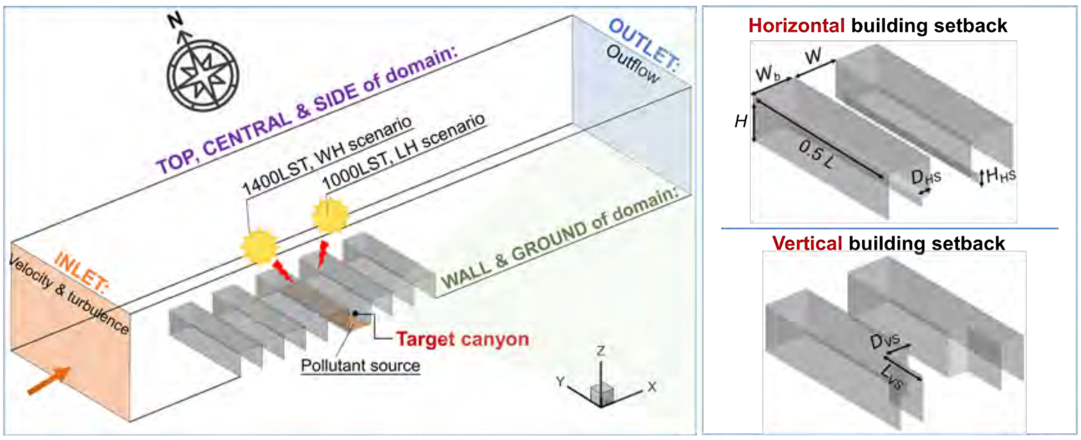

Figure 4.1 Computational geometry and boundary conditions

4.2.2 Numerical models

The commercial software ANSYS/Fluent® CFD software (Release 15.0) [127] is used to simulate the airflow of ambient wind over this isolated street canyon. The numerical analysis is based on the steady-state 3D RANS conservation equations of mass, momentum, and energy for the incompressible turbulent flow. RNG k-ε model is chosen in this chapter to provide reliable predictions of the mean flows with the thermal effect and pollutant dispersion. Besides, this chapter utilizes the pressure-linked equations-consistent (SIMPLEC) numerical method for the pressure-velocity coupling. The second-order upwind scheme [103] is used to discretize both the convective terms and the diffusion terms. A double-precision solver is also selected for the CFD calculations. The convergence of the normalized residual errors of the energy equation is set to 10^{-9}, whereas the convergence criterion of the remaining equations is set to 10^{-6}. Besides, it should be mentioned that the setting of the current CFD model is similar to the studies in Chapters 2 and 3, which have well-validated the predicted wall temperature, thermal airflow, and pollutant dispersion with the previous wind tunnel experiments and field measurement. For simplicity, the validation of this study can refer to Section 2.4 and 3.3.

4.2.3 Boundary conditions

At the domain inlet, a power-law velocity profile is applied as follows,

$$U(z) = U_{ref}\left(\frac{z}{z_{ref}}\right)^{\alpha} \tag{4.1}$$

$$k(z) = \left(U(z)\times I_{in}\right)^2 \tag{4.2}$$

$$\varepsilon(z) = \frac{C_\mu^{3/4} k(z)^{3/2}}{\kappa z} \tag{4.3}$$

where z_{ref} is the reference height (= 20 [m]), α is the power-law exponent (= 0.22, stands for the underlying surface roughness above medium-dense urban area), I_{in} is the turbulent intensity (= 0.1, refers to [132]), κ is the von Karman's constant (= 0.42), and C_μ is the model constant (= 0.085). Moreover, U_{ref} is the reference wind speed (= 3 [m/s]), the reference Reynolds number ($\mathrm{Re} = U_{ref} H / \nu$) is about 4.1 × 10^6, which is far larger than 11,000 to satisfy the requirement of Reynolds number independence [135].

As seen in Figure 4.1, the top and lateral boundaries of the domain are set as symmetry boundaries, namely setting normal velocity and normal gradients of all variables to zero. On the outlet of the domain, a zero diffusive flux is imposed for all flow variables in the direction normal to the outflow plane since the domain downstream is long enough to ensure a fully developed outlet flow. For near-wall treatment, no-slip wall boundary conditions with standard wall function are applied.

CO is used as the pollutant representative. As shown in Figure 4.1, a uniform volume source (width W_p = 2/3 W and length L_p = street length L) of CO is specified near the ground with a depth of 1/20 H to represent the traffic lanes. The constant emission rate per hour and unit street length (36.1 [g/h/m], i.e., total mass release rate of $L_p \times 1.0 \times 10^{-5}$ [kg/s]) are adopted for each CO source.

4.2.4 Grid sensitivity analysis

Three densities of mesh systems are tested for the low-rise street canyon with horizontal setback (H_{HS}/W= 0.2 and D_{HS}/W= 0.2). Figure 4.2 compares the results of the three grids along the central vertical line at the vertical center plane of the street canyon, including the dimensionless mean velocity (U/U_{ref}), air temperature (T), and dimensionless pollutant concentration (K). Herein, the dimensionless pollutant concentration is defined as $K = CU_{ref} HL / S_p V_p$, where C is the local pollutant concentration [kg/m^3] and V_p is the volume of pollutant source [m^3]. Along this line, the fine and the basic grid provide almost identical results, while some deviations are found between the results of the coarse and the basic grid. Besides, the near-wall area is resolved by the standard wall functions directly on the condition that the $y+$ of the first near-wall mesh for building surfaces and ground is 245.3 on average, which is in the log-law layer 30 < y + < 300 [127,136].

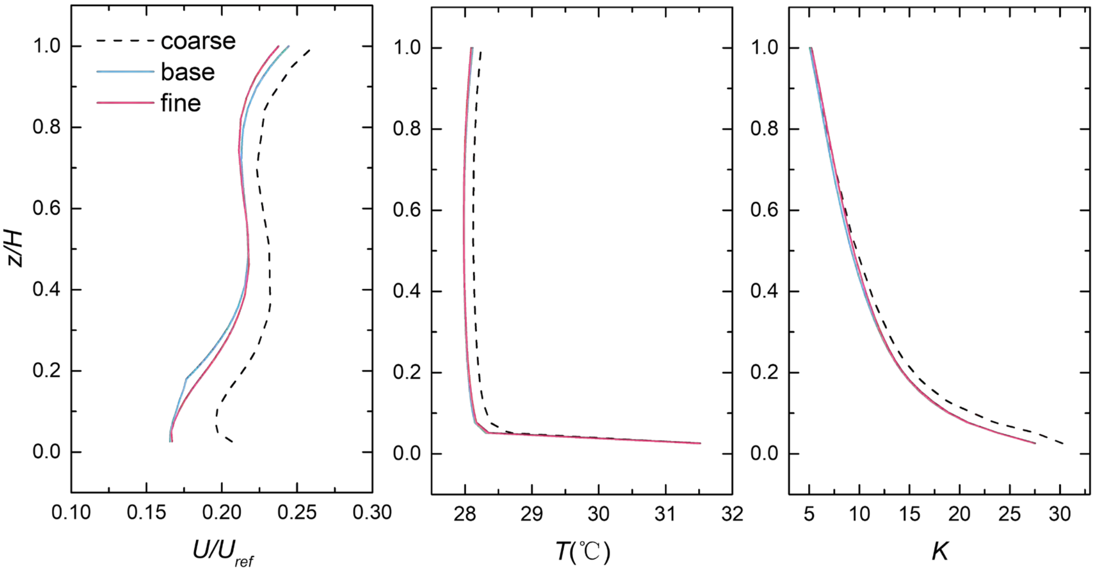

Figure 4.2 Comparison of (a) U/U_{ref}, (b) T, and (c) K along a center vertical line inside the target street canyon in the vertical center plane in coarse, basic, and fine grids.

4.3 Results and discussion

4.3.1 Low-rise street canyon (H/W = 1)

4.3.1.1 Effect of horizontal building setback

The effects of horizontal building setbacks within the low-rise street canyons (H/W = 1) are explored in this section. Figure 4.3, Figure 4.4, and Figure 4.5 show the predicted wind velocity U, air temperature T, and dimensionless pollutant concentration K contours for different horizontal setback configurations (different height and width of setback) at the pedestrian level and three vertical cross-sections, respectively. To quantitatively estimate the effects on thermal comfort and air quality, Figure 4.6 compares the average U, T, PET, and K at the two-side pedestrian level. The width of the leeward/windward pedestrian level is defined as a distance (= 2+D_{HS} [m]) from the leeward/windward surface of the horizontal setback (Figure A4.1(a)).

First, the influence of horizontal setbacks on wind velocity and flow structure is discussed under both LH and WH scenarios. The setting of horizontal setback creates a larger low-layer space and thereby a wider region for pedestrians. Comparing the case of H_{HS}/W= 0.2 and D_{HS}/W= 0.2 with the base case, this expanded low-layer space enhances the windward pedestrian-level wind velocity U_{win}, while reduces the leeward pedestrian-level wind velocity U_{lee} (Figure 4.3 and Figure 4.6). This is because the inclusion of horizontal setback leads to a significant "venturi effect" at the windward side, which improves the inward channeling flow from the lateral entrainment at this side. Hence, most of the lateral entrainment air mainly tends to flow beneath the windward horizontal setback instead of flowing toward the leeward side. As increasing the height of the horizontal setback, the increment of U_{win} reduces while the U_{lee} continues to decrease (Figure 4.3 and Figure 4.6). The possible reason is that a larger space created by a higher horizontal setback causes a relatively weaker "venturi effect". Similarly, an increase in the width of the horizontal setback also reduces the increment of U_{win} and leads to a lower U_{lee} (Figure 4.3 and Figure 4.6). Thus, it can be deduced that the dimensionless area of the cross-section of horizontal setback S_{HS} (= $H_{HS}/W \times D_{HS}/W$) is directly related to two-side pedestrian level wind velocity, i.e., larger S_{HS} causes a lower U_{win} and U_{lee}. Among these three horizontal setbacks, the horizontal setback with H_{HS}/W= 0.2 and D_{HS}/W= 0.1 creates the best wind environment for two-side pedestrians. Compared to the base case, the U_{win} is 0.2–0.3 m/s higher, while U_{lee} still almost 0.1 m/s lower.

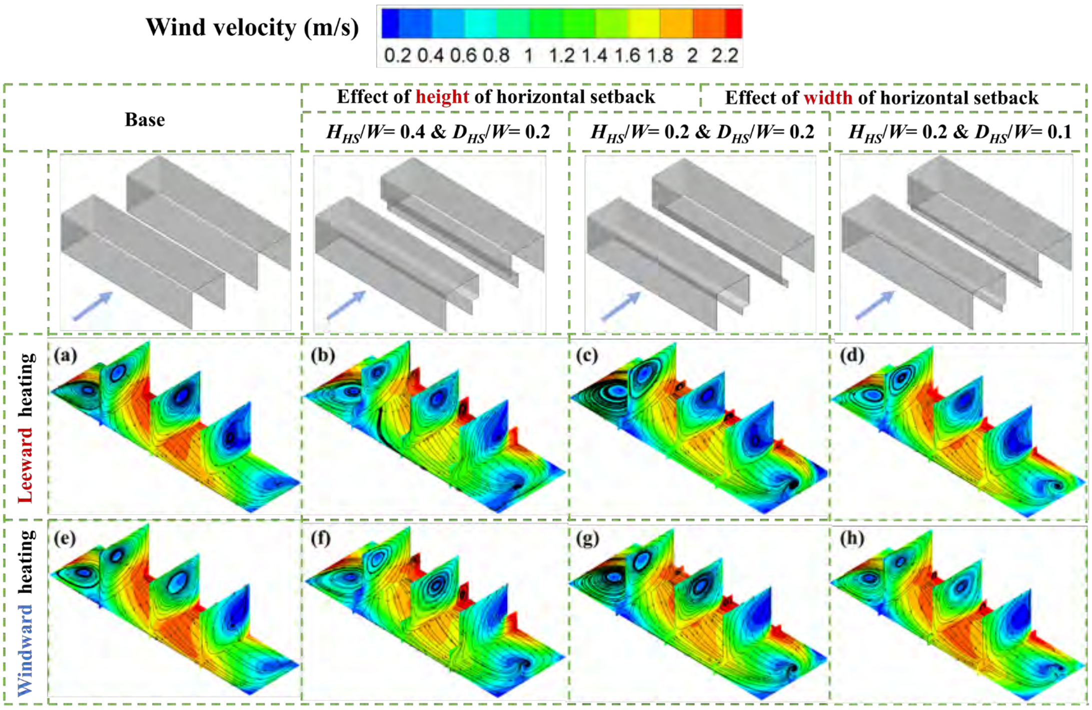

Figure 4.3 Predicted contours of wind velocity for a different horizontal setback with the low-rise street canyon: leeward heating scenario for (a)–(d) and windward heating scenario for (e)–(h)

Second, the influence of horizontal setbacks on air temperature is discussed. Compared with the base case, the horizontal setback of H_{HS}/W= 0.2 and D_{HS}/W= 0.2 results in a lower pedestrian level air temperature, especially at the windward side (Figure 4.4). The possible reason is that the horizontal setback can greatly enhance windward-side flow rate and thereby introduce more air with lower temperature into the pedestrian level across the lateral opening. Moreover, Figure 4.6 (b) indicates that this kind of cooling effect becomes more significant under the WH scenario. Under this certain, more heat is supposed to accumulate at the windward side of the base street canyon due to direct solar radiation; a stronger windward inward channeling flow caused by the horizontal setback greatly reduces the accumulation of heat at this windward side. Thus, the inclusion of horizontal setback declines both T_{win} and T_{lee} under the WH scenario, particularly for the T_{win} (by up to 0.6 °C) (Figure 4.6 (b)). This finding is further confirmed by altering the dimensionless S_{HS} (changing width or height of setback). Under the WH scenario, a larger dimensionless S_{HS} always creates a better thermal environment. However, under the LH scenario, this trend is not more observed by adjusting the dimensionless S_{HS}. No matter increasing H_{HS} or decreasing D_{HS}, a worse thermal environment can be found under this scenario (Figure 4.6 (b)). Hence, another dimensionless parameter is introduced to explain this phenomenon, i.e., H_{HS}/D_{HS}. Either increasing H_{HS} or decreasing D_{HS} causes a smaller H_{HS}/D_{HS}, which results in more exposure to direct solar radiation for the leeward pedestrian level under the LH scenario. Therefore, a smaller H_{HS}/D_{HS} provides a lower air temperature due to less heat accumulation under the LH scenario (Figure 4.6 (b)). The horizontal setback with H_{HS}/W= 0.2 and D_{HS}/W= 0.2 (H_{HS}/D_{HS}= 1) declines both the T_{win} and T_{lee} by almost 0.1 °C compared to the base case. Nonetheless, it should be noted that the T_{win} for all horizontal setbacks is lower than that of the base case under the LH scenario, due to the influence of windward channeling flow. Generally, the air temperature within the street canyon is affected by two dimensionless design parameters of horizontal setback, i.e., S_{HS} and H_{HS}/D_{HS}. Both larger S_{HS} and lower H_{HS}/D_{HS} can help to reduce the pedestrian level air temperature. S_{HS} and H_{HS}/D_{HS} play a more important role on the T_{win} and T_{lee} under WH and LH scenarios, respectively.

Third, the effects of horizontal setbacks on outdoor thermal comfort are discussed. In this chapter, PET is chosen for the evaluation of outdoor thermal comfort. The calculation of PET is conducted by Rayman Pro [137,138]. More details can refer to Section 2.3. It should be noted that higher wind velocity, lower air temperature, and lower mean radiant temperature (more shading effect) can result in a lower PET (better thermal comfort) [138,139]. Therefore, as shown in Figure 4.6 (c), it is found that the horizontal setback always provides better thermal comfort for the windward pedestrians because of better ventilation and a lower air temperature at this side. Moreover, among these three horizontal setbacks, the horizontal setback with H_{HS}/W= 0.2 and D_{HS}/W= 0.2 significantly declines the average value of windward PET (PET_{win}) by up to 2.1 °C, compared to the base case. This can be attributed to less exposure to direct solar radiation caused by this kind of horizontal setback with lower H_{HS}/D_{HS}. In contrast, compared with the base case, the horizontal setback probably leads to a worse thermal sensation at the leeward side due to poorer ventilation at this side, except the setback with lower H_{HS}/D_{HS} under the LH scenario. Therefore, this phenomenon indicates that the ratio of H_{HS}/D_{HS} plays a more important role in the improvement of thermal comfort at the pedestrian level. This ratio should be as small as possible to provide more shading effects for pedestrians, which is in line with the observation of Yin et al. [73]. Moreover, the S_{HS} should be larger for a lower in-canyon air temperature to achieve a better thermal sensation, although it plays a minor role in thermal comfort.

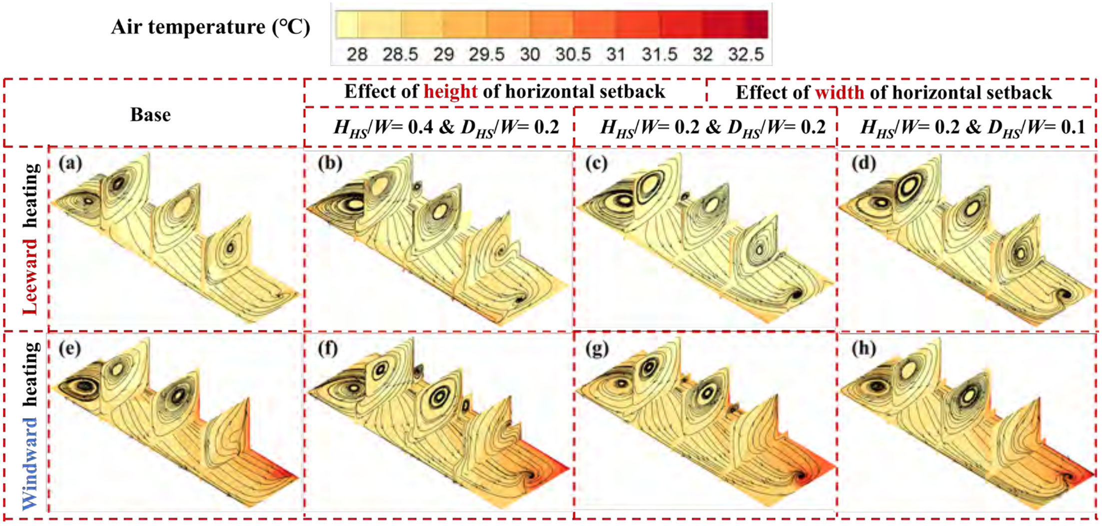

Figure 4.4 Predicted contours of air temperature for a different horizontal setback with the low-rise street canyon: leeward heating scenario for (a)–(d) and windward heating scenario for (e)–(h)

Four, the effects of horizontal setbacks on pollutant concentration are discussed. Comparing the case of H_{HS}/W= 0.2 and D_{HS}/W= 0.2 with the base case, the horizontal setback effectively improves the air quality for both-side pedestrians (Figure 4.5). This is attributed to the “venturi effect” for both side pedestrian levels induced by the horizontal setback. Traffic-related pollutant concentration tends to accumulate in the center of the street instead of the two-side sidewalks in the low-rise street canyon. Moreover, the horizontal setback broadens the lower space of the street canyon, which helps to dilute the pollutant concentration. Accordingly, it is found that both-side pollutant concentration is directly proportional to S_{HS} (Figure 4.6(d)). The horizontal setback with H_{HS}/W= 0.4 and D_{HS}/W= 0.2 creates the best air quality for two-side pedestrians. Its K_{lee} and K_{win} are almost 24–29% and 57–66% lower than the base case, respectively (Figure 4.6(d)).

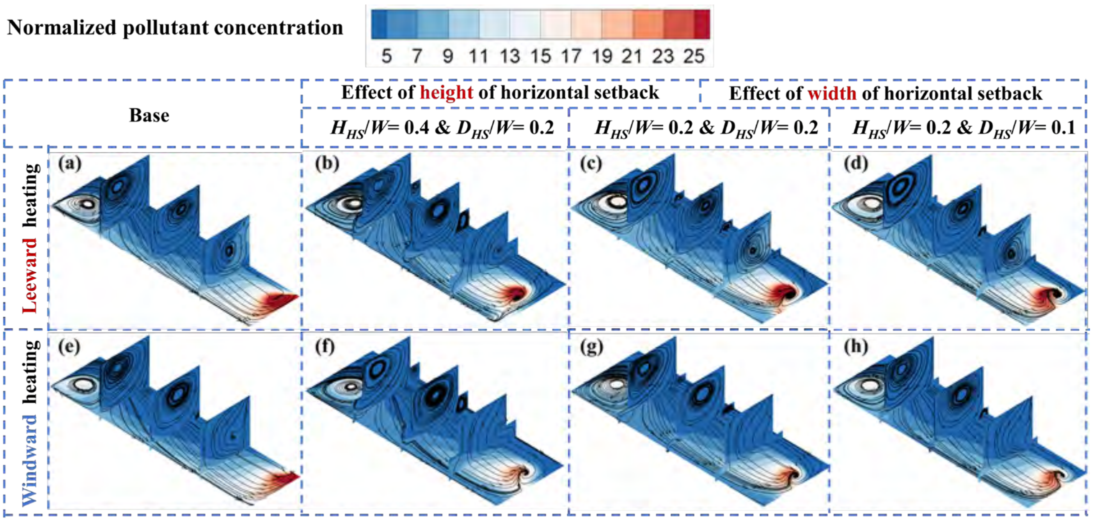

Figure 4.5 Predicted contours of dimensionless pollutant concentration for a different horizontal setback with the low-rise street canyon: leeward heating scenario for (a)–(d) and windward heating scenario for (e)–(h)

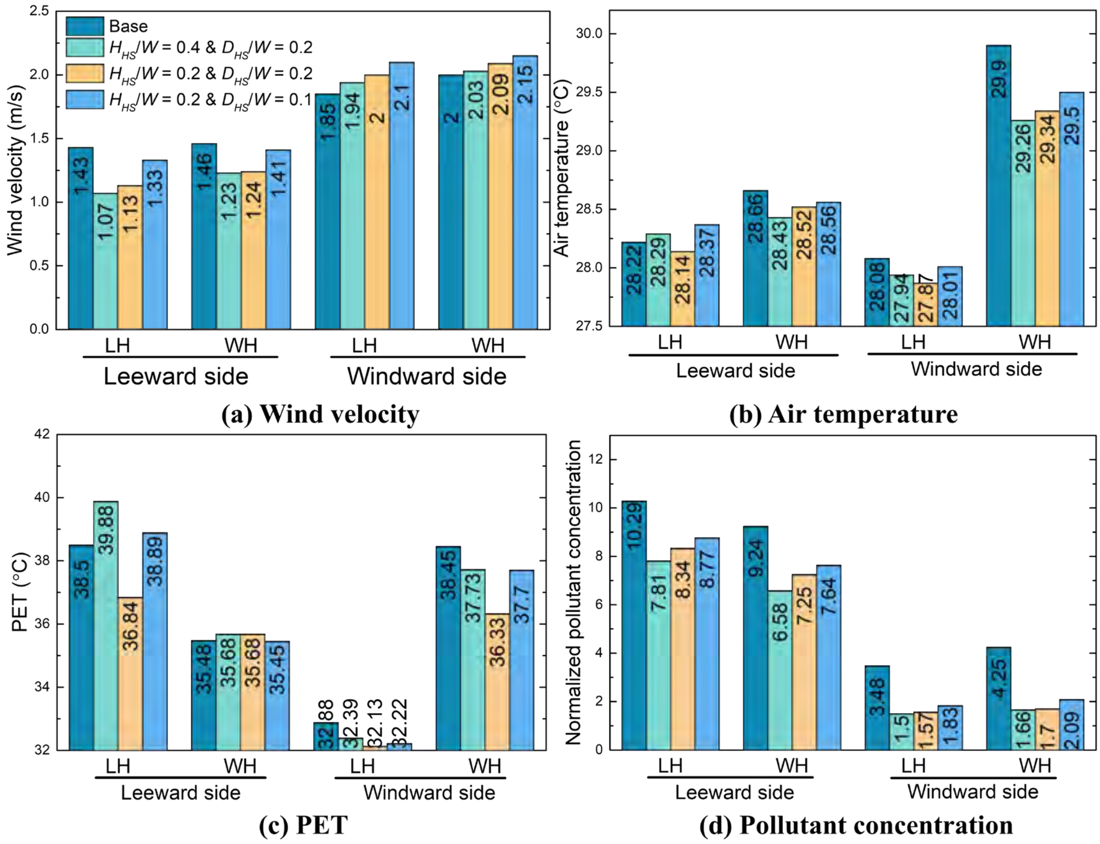

Figure 4.6 Average values of (a) Wind velocity, (b) Air temperature, (c) PET, and (d) Pollutant concentration under different horizontal setback in the low-rise street canyon at the leeward and windward pedestrian level under leeward heating (LH) and windward heating (WH) scenarios

4.3.1.2 Effect of vertical building setback

The effects of vertical building setback within the low-rise street canyons (H/W = 1) are explored in this section. Figure 4.7, Figure 4.8, and Figure 4.9 show the predicted wind velocity, air temperature, and dimensionless pollutant concentration K contours for different vertical setback configurations (various lengths and widths of setbacks) at the pedestrian level and three vertical cross-sections, respectively. To quantitatively estimate the effects on thermal comfort and air quality, Figure 4.10 compares the average U, T, PET, and K at the two-side pedestrian level. The width of the leeward/windward pedestrian level is defined as a distance (= 2 m) from the leeward/windward surface of vertical setback and building (Figure A4.1(b)).

First, the influence of vertical setbacks on wind velocity and flow structure is discussed. Comparing the case of L_{VS}/L= 0.25 and D_{HS}/W= 0.45 and the base case, the inclusion of the vertical setback in the center of the low-rise street canyon significantly enhances the ventilation of the non-setback section, especially at the leeward side (Figure 4.7). However, it also induces a minor vortex with lower wind velocity at the location of vertical setback, particularly at the windward side. Hence, this kind of setback results in a slightly slower U_{win} (the decrement is almost 0.1 m/s) but almost does not affect the U_{lee} (Figure 4.10 (a)). As a decrease in the dimensionless length L_{VS}/L to 0.125, the vertical setback can enhance both U_{lee} and U_{win}. A smaller stagnant flow region at the position of vertical setback leads to the increase in U_{lee} and U_{win} although this kind of setback induces a relatively weaker inward channeling flow at the non-setback section. Moreover, for a smaller D_{VS}/W, lower U_{lee} and U_{win} can be observed (Figure 4.10 (a)). This is because that the enhancement of ventilation at the non-setback section becomes weaker, while the stagnant region of the setback section hardly changes with the D_{HS}/W. Thus, it can be deduced that the vertical setback with a short dimensionless length L_{VS}/L and a large dimensionless width D_{VS}/W indeed improves both-side wind velocity.

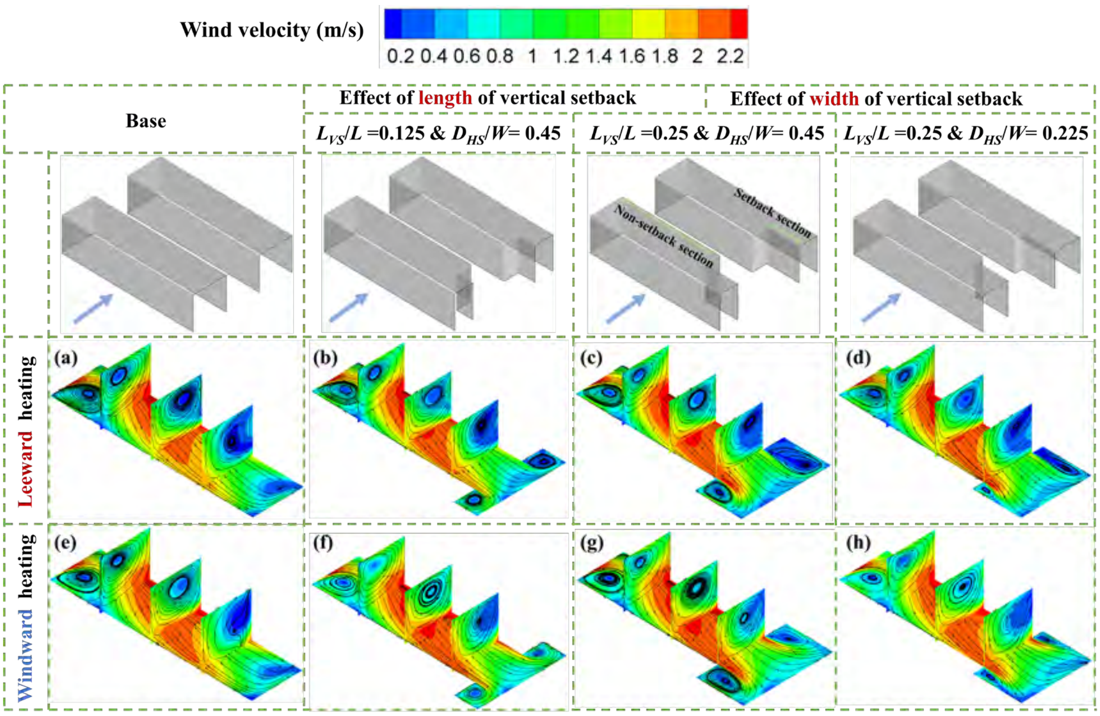

Figure 4.7 Predicted contours of wind velocity for different vertical setbacks with the low-rise street canyon: leeward heating scenario for (a)–(d) and windward heating scenario for (e)–(h).

Second, the effects of vertical setbacks on the air temperature are investigated in the low-rise street canyon. Compared with the base case and case of L_{VS}/L= 0.25 and D_{VS}/W= 0.45, the air temperature of the non-setback section only slightly decreases although there is better ventilation in this region. However, it is quite easy to accumulate warmer air at the setback section, especially at the directly heated side (Figure 4.8). The air temperature at the leeward/windward setback section is significantly higher under the LH/WH scenario. Accordingly, this kind of vertical setback always causes a higher T_{lee} and T_{win} compared with the base case (Figure 4.10 (b)). On this account, a decrease in either L_{VS}/L or D_{VS}/W results in a lower air temperature. In other words, a lower area of dimensionless horizontal section S_{VS} ($=L_{VS}/L \times D_{VS}/W$) has a lower pedestrian level air temperature. Nonetheless, it should be noted that their T_{lee} and T_{win} are still higher than that of the base case; the vertical setback can not effectively reduce both-side average air temperature.

Third, the influence of vertical setbacks on outdoor thermal comfort is explored. Unlike the horizontal setback, the vertical setback cannot provide an extra shading effect for pedestrians. Hence, compared with the base case, only the vertical setback with L_{VS}/L= 0.125 and D_{VS}/W= 0.45 results in better thermal comfort because of its better ventilation (Figure 4.10 (c)). Meanwhile, it should be noted that the improvement of thermal comfort is minor within the low-rise street canyon. The maximum reduction of PET is less than 0.5 °C, which is far less than the horizontal setback.

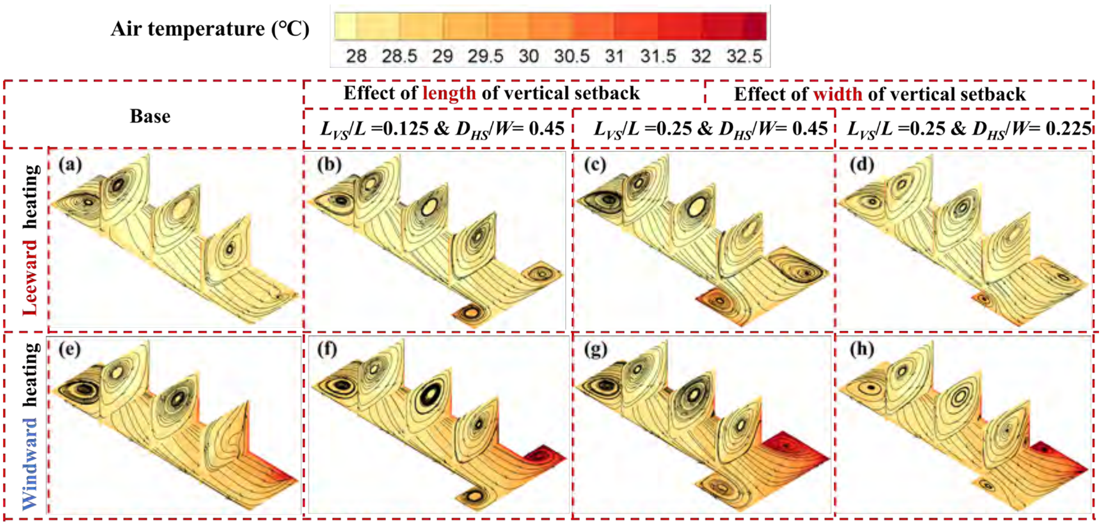

Figure 4.8 Predicted contours of air temperature for different vertical setbacks with the low-rise street canyon: leeward heating scenario for (a)–(d) and windward heating scenario for (e)–(h).

Four, the impacts of vertical setbacks on pollutant concentration are studied. Compared to the base case, all the vertical setbacks only slightly improve both-side air quality. Among them, the vertical setback with the largest S_{VS} has the best air quality since this kind of setback creates a larger space to dilute the pollutant concentration (Figure 4.10 (a)). Nonetheless, it only reduces the K_{lee} by almost 7% compared to the base case. Meanwhile, it even increases the K_{win} by approximately 19% under the LH scenario. Generally, when compared with the horizontal setback, the vertical setback cannot effectively dilute the pollutants in the low-rise street canyon.

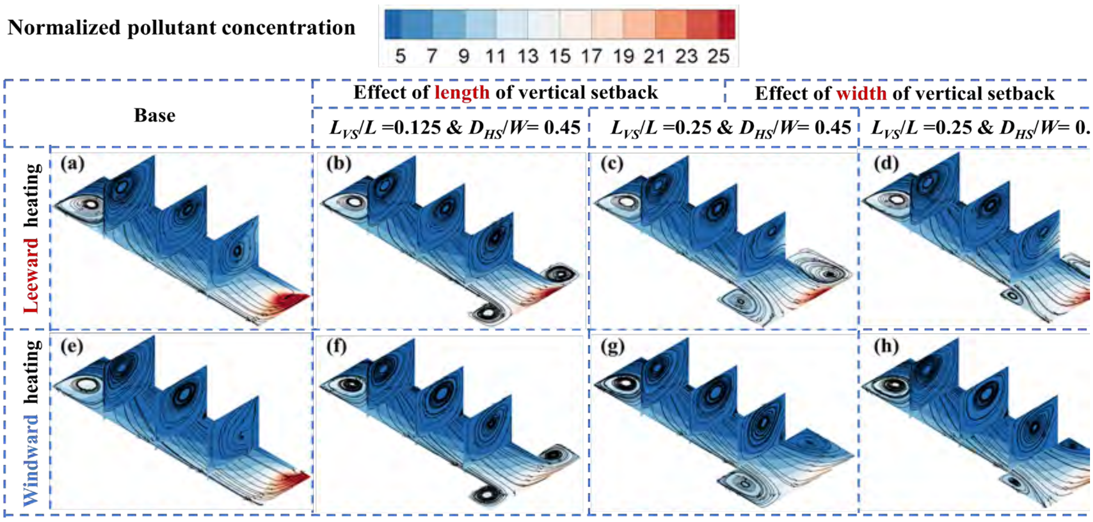

Figure 4.9 Predicted contours of pollutant concentration for different vertical setbacks with the low-rise street canyon: leeward heating scenario for (a)–(d) and windward heating scenario for (e)–(h).

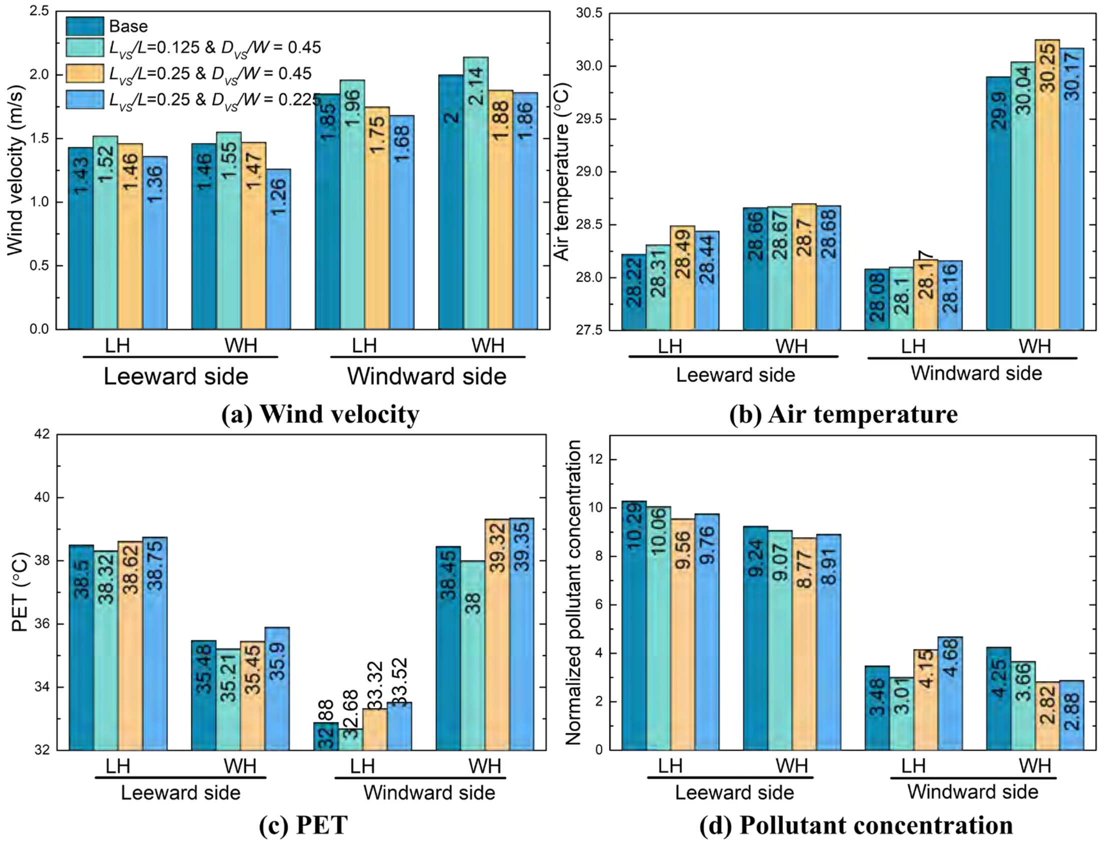

Figure 4.10 Average values of (a) Wind velocity, (b) Air temperature, (c) PET, and (d) Pollutant concentration under different vertical setback in the low-rise street canyon at the pedestrian level of leeward and windward side under leeward heating (LH) and windward heating (WH) scenarios

4.3.2 High-rise street canyon (*H/W* = 2)

4.3.2.1 Effect of horizontal building setback

The effects of horizontal building setbacks within the high-rise street canyons (H/W = 2) are explored in this section. Figure 4.11, Figure 4.12, and Figure 4.13 show the predicted wind velocity, air temperature, and dimensionless pollutant concentration K contours for different horizontal building setback configurations (different height and width of setback) at the pedestrian level and three vertical cross-sections, respectively. To quantitatively estimate the effects on thermal comfort and air quality, Figure 4.14 compares the average U, T, PET, and K at the two-side pedestrian level.

First, the influence of horizontal setbacks on wind velocity and flow structure is discussed within the high-rise street canyon. Similar to the low-rise street canyon, the horizontal setback also introduces more lateral entrainment airflow through the windward side, compared with the base case. Likewise, U_{win} is also directly related to the dimensionless area of the cross-section of this horizontal setback S_{HS}; a higher S_{HS} also has a lower U_{win} (Figure 4.11 and Figure 4.14). The horizontal setback of H_{HS}/W= 0.2 and D_{HS}/W= 0.1 has the highest U_{win}, which is only 0.1 m/s higher than that of the base case. Unlike the low-rise street canyon, the U_{lee} is affected by the flow volume of the windward side in the high-rise street canyon. Greater windward flow volume due to larger S_{HS} results in higher wind velocity at the leeward side. Therefore, the case of H_{HS}/W= 0.4 and D_{HS}/W= 0.2 has the highest U_{lee}, which is 0.2 m/s higher than that of the base case. Also, it should be noted that the horizontal setback leads to two minor vortices with a relatively stagnant flow close to the leeward surface, although there is a higher average wind velocity at this side.

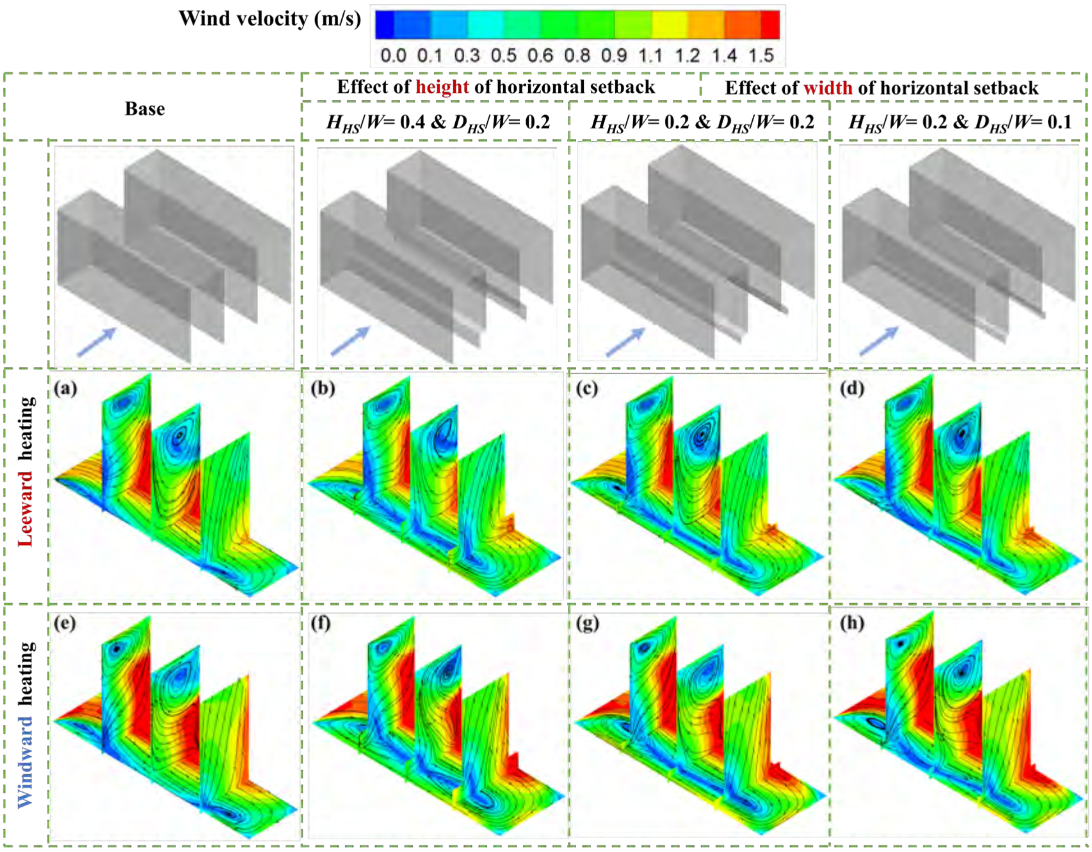

Figure 4.11 Predicted contours of wind velocity for different horizontal setbacks with the high-rise street canyon: leeward heating scenario for (a)–(d) and windward heating scenario for (e)–(h).

Second, the effects of horizontal setbacks on the air temperature are discussed. Interestingly, except in the case of H_{HS}/W= 0.4 and D_{HS}/W= 0.2, the horizontal setback rather leads to a higher air temperature than the setback-free counterpart (Figure 4.12 and Figure 4.14 (b)). The pedestrian-level air temperature is affected by two aspects within the high-rise street canyon. One is that leeward stagnant region leads to the accumulation of heat, which probably causes a higher air temperature; another is that horizontal setback induces more lateral entrainment air with lower temperature, which can reduce in-canyon air temperature. For the case of H_{HS}/W= 0.4 and D_{HS}/W= 0.2, its stronger windward ventilation caused by a higher S_{HS} results in a lower air temperature for the whole high-rise canyon. In contrast, for the other two cases, the cooling performance caused by the windward fresh air can not set off the accumulation of heat at the leeward side. Thus, the horizontal setbacks for the other two cases have a higher in-canyon air temperature. Generally, the both-side air temperature is inversely proportional to the S_{HS} within the high-rise street canyon; only the horizontal setback with higher S_{HS} has a lower air temperature than that of the base case.

Third, the effects of horizontal setbacks on thermal comfort are discussed. It should be noted that the high-rise street canyon has provided enough shading effect on the ground level. Thus, the shading effect caused by the horizontal setback in the high-rise street canyon is not more important than that in the low-rise street canyon. In contrast, wind velocity plays a more crucial role in affecting the thermal sensation of two-side pedestrians. At the leeward side, a larger S_{HS} causes a better thermal comfort due to better ventilation at the side; at the windward side, a larger S_{HS} results in a worse thermal sensation because of its worse windward ventilation (Figure 4.14 (c)). Besides, it should be noted that all the horizontal setbacks can improve the both-side thermal comfort in the high-rise street canyon, although its largest decrement of PET is less than that in the low-rise street canyon. For instance, compared with the base case, the PET_{lee} declines by at most 0.8 °C by the horizontal setback with the largest S_{HS} (H_{HS}/W= 0.4 and D_{HS}/W= 0.2).

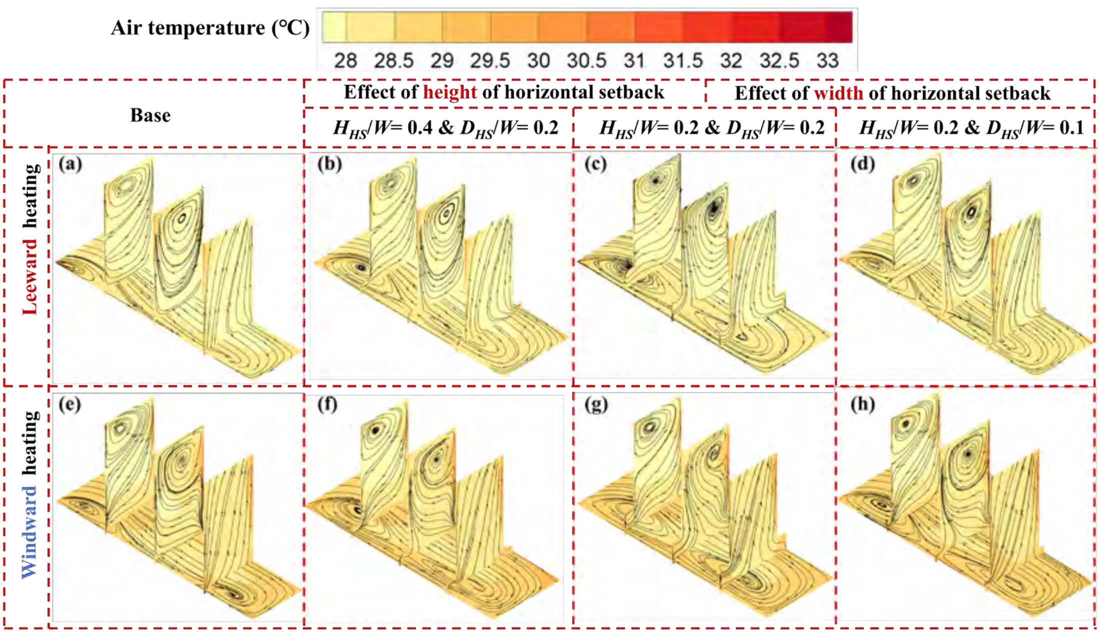

Figure 4.12 Predicted contours of air temperature for different horizontal setbacks within the high-rise street canyon: leeward heating scenario for (a)–(d) and windward heating scenario for (e)–(h).

Four, the influence of horizontal setbacks on the pollutants is studied. Comparing the base case with the case of H_{HS}/W= 0.2 and D_{HS}/W= 0.2, the inclusion of horizontal setback in the high-rise street canyon still helps to disperse the windward pollutants (Figure 4.13). Unfortunately, these pollutants transported towards the leeward side are trapped by the two minor vortices at the leeward side. Hence, the horizontal setback causes a worse leeward air quality. With an increase in H_{HS}/W, a larger space is created for the dilution of leeward pollutants. Nonetheless, its K_{lee} is still 4–9% higher than that of the base case (Figure 4.14 (d)). With a decrease in D_{HS}/W, fewer pollutants are transported towards the leeward side. Similarly, its K_{lee} is also 4–11% higher than that of the base case. Generally, all kinds of horizontal setbacks in the high-rise street canyon are not beneficial for the dilution of in-canyon pollutants.

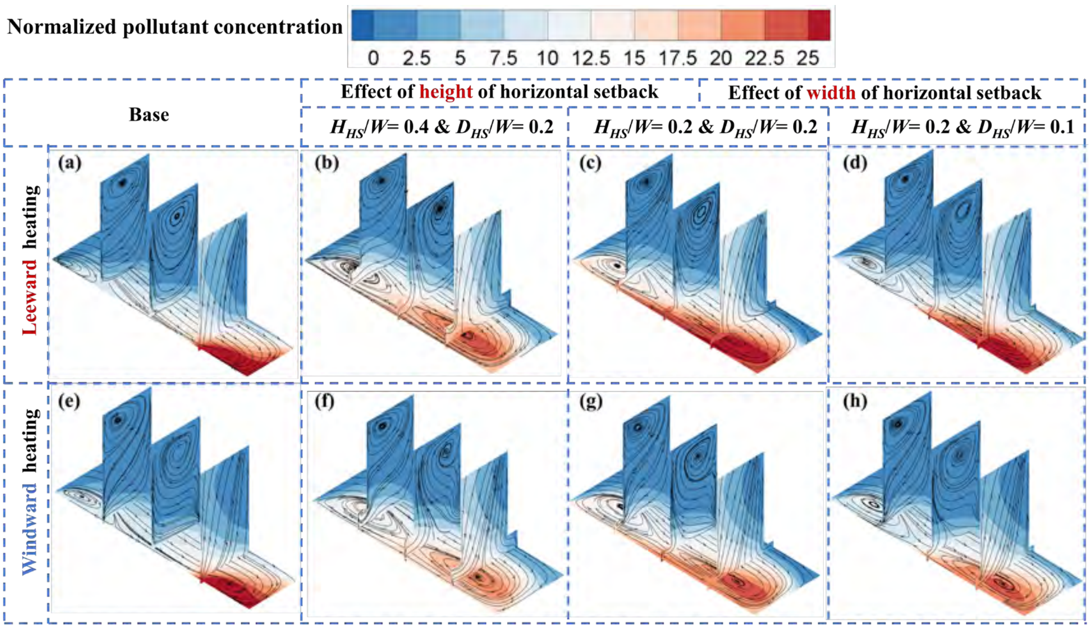

Figure 4.13 Predicted contours of pollutant concentration for different horizontal setbacks within the high-rise street canyon: leeward heating scenario for (a)–(d) and windward heating scenario for (e)–(h).

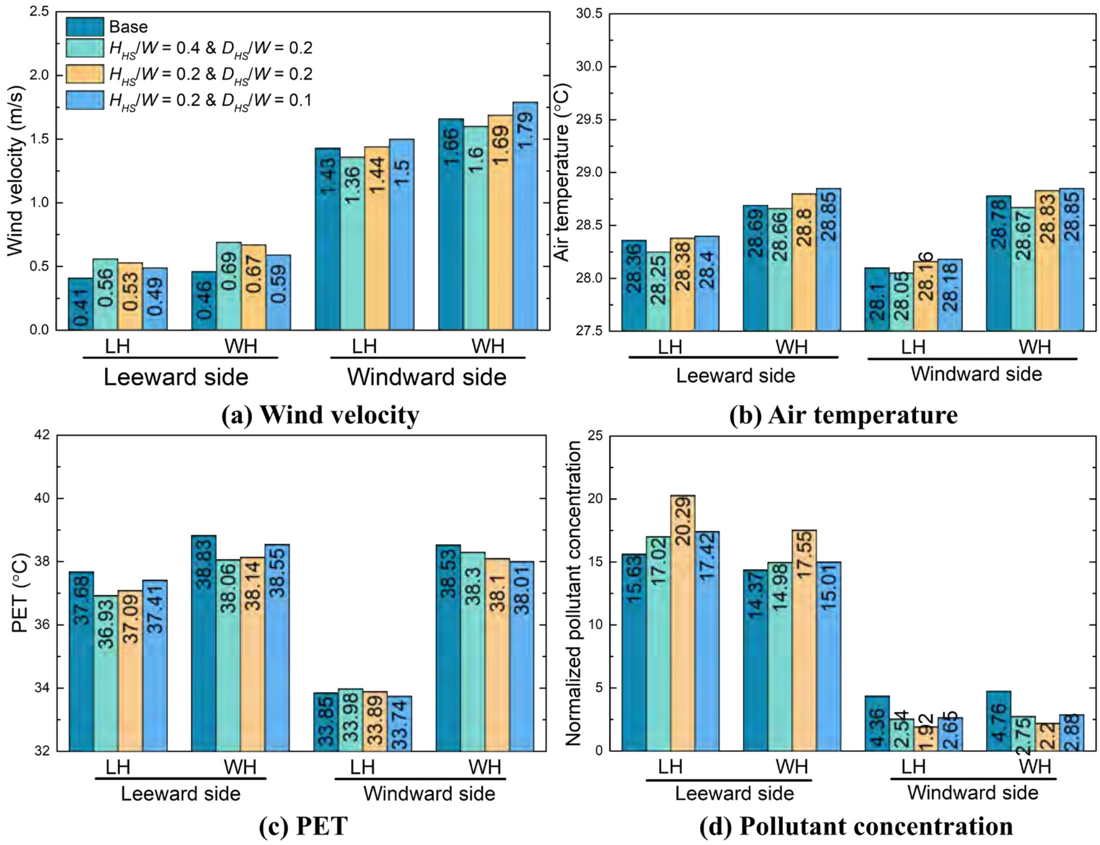

Figure 4.14 Average values of (a) Wind velocity, (b) Air temperature, (c) PET, and (d) Pollutant concentration under different horizontal setback in the high-rise street canyon at the pedestrian level of the leeward and windward side under leeward heating (LH) and windward heating (WH) scenarios

4.3.2.2 Effect of vertical building setback

The effects of vertical building setbacks within the high-rise street canyons (H/W = 2) are explored in this section. Figure 4.15, Figure 4.16, and Figure 4.17 show the predicted wind velocity, air temperature, and dimensionless pollutant concentration K contours for different vertical building setback configurations (various lengths and widths of setback) at the pedestrian level and three vertical cross-sections, respectively. To quantitatively estimate the effects on thermal comfort and air quality, Figure 4.18 compares the average U, T, PET, and K at the two-side pedestrian level.

First, the influence of vertical setbacks on wind velocity and flow structure is discussed within the high-rise street canyon. Comparing the base case with the case of L_{VS}/L= 0.25 and D_{VS}/W= 0.45, the vertical setback also significantly improves the non-setback ventilation, similar to the low-rise street canyon (Figure 4.15). Differently, although there is still a minor vortex at the position of vertical setback, the airflow in that area is not more stagnant, especially for the leeward side. Nonetheless, this kind of vertical setback still causes a slightly higher U_{lee} but lower U_{win} compared to the base case (Figure 4.18 (a)). When decreasing the L_{VS}/L to 0.125, weaker lateral entrainment results in a lower U_{lee}; the U_{win} still becomes higher. When the width of the vertical setback decreases, the non-setback ventilation becomes worse, and the recirculation region at the setback section also becomes more stagnant. Both U_{lee} and U_{win} reduce with a decrease in the width of vertical setback. Accordingly, it could be deduced that a larger dimensionless S_{VS} leads to a higher U_{lee} while a smaller dimensionless L_{VS}/L has a higher U_{win}.

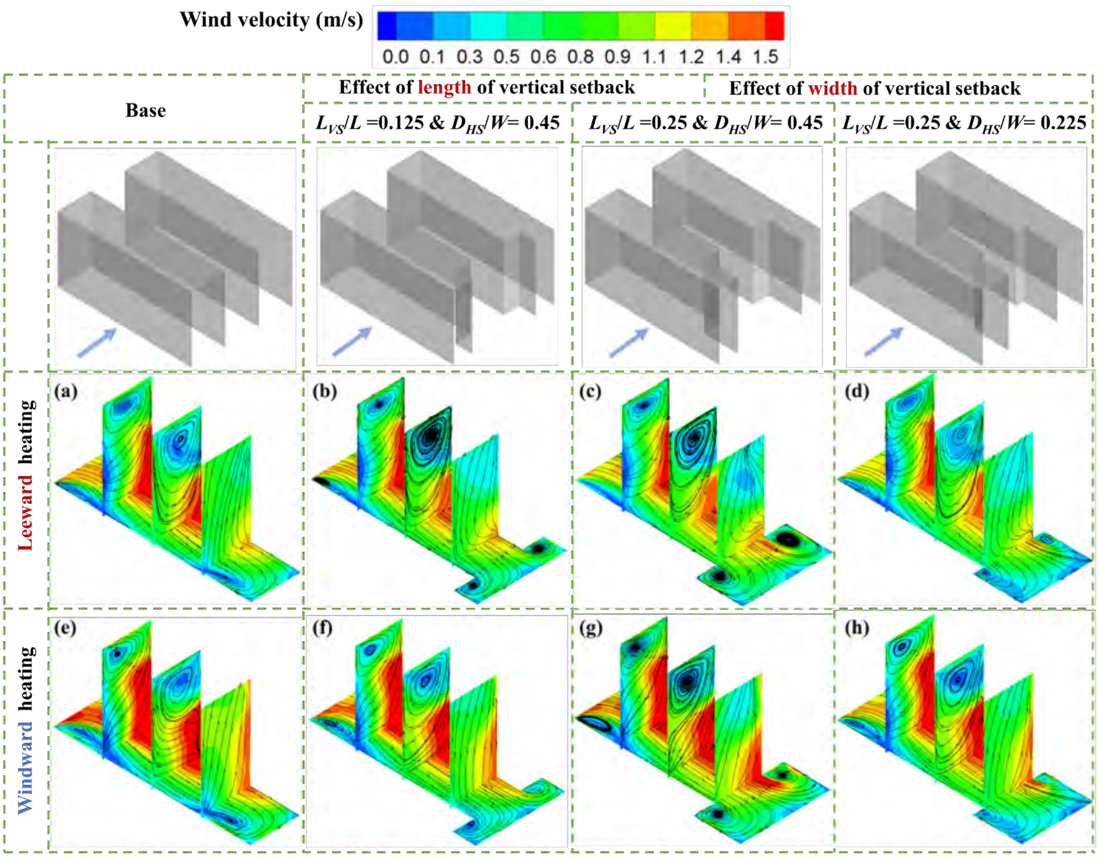

Figure 4.15 Predicted contours of wind velocity for different vertical setbacks within the high-rise street canyon: leeward heating scenario for (a)–(d) and windward heating scenario for (e)–(h).

Second, the influence of vertical setbacks on air temperature is discussed. Comparing the base case with the case of L_{VS}/L= 0.25 and D_{VS}/W= 0.45, the vertical setback effectively reduces the accumulation of heat in the non-setback section due to stronger ventilation in that area (Figure 4.16). The position of vertical setback still has a relatively high air temperature, where is directly heated by solar radiation, especially at the windward side. Hence, this kind of vertical setback reduces T_{lee} but slightly increases T_{win} under the WH scenario (Figure 4.18 (b)). With a decrease in the length and width of vertical setback, the accumulation of heat at the minor vortex becomes less, and both T_{lee} and T_{win} thereby reduce. Generally, compared to the base case, all three vertical setbacks provide a lower air temperature for two-side pedestrians in most cases, especially for the vertical setbacks with lower S_{VS}.

Third, the influence of vertical setbacks on thermal comfort is explored. As discussed in Section 4.3.2.1, the enhancement of wind velocity plays a more important role in the improvement of thermal comfort in the high-rise street canyon with building setbacks. Comparing the base case with the case of L_{VS}/L= 0.25 and D_{VS}/W= 0.45, the PET_{lee} largely decreases by 0.7–1°C due to a higher U_{lee} while the PET_{win} slightly increases (less than 0.1°C) (Figure 4.18 (c)). A decrease in L_{VS}/L leads to a slight increase in PET_{lee}. Nonetheless, the PET_{lee} for larger L_{VS}/L is still 0.3–0.4°C lower than that of the base case. Meanwhile, its PET_{win} is 0.1–0.3°C lower than that of the base case. However, when decreasing D_{VS}/W, both PET_{lee} and PET_{win} increase, especially at the windward side. Hence, to achieve a better thermal comfort for the entire high-rise street canyon, the dimensionless length L_{VS}/L should be smaller while the dimensionless area S_{VS} should be larger.

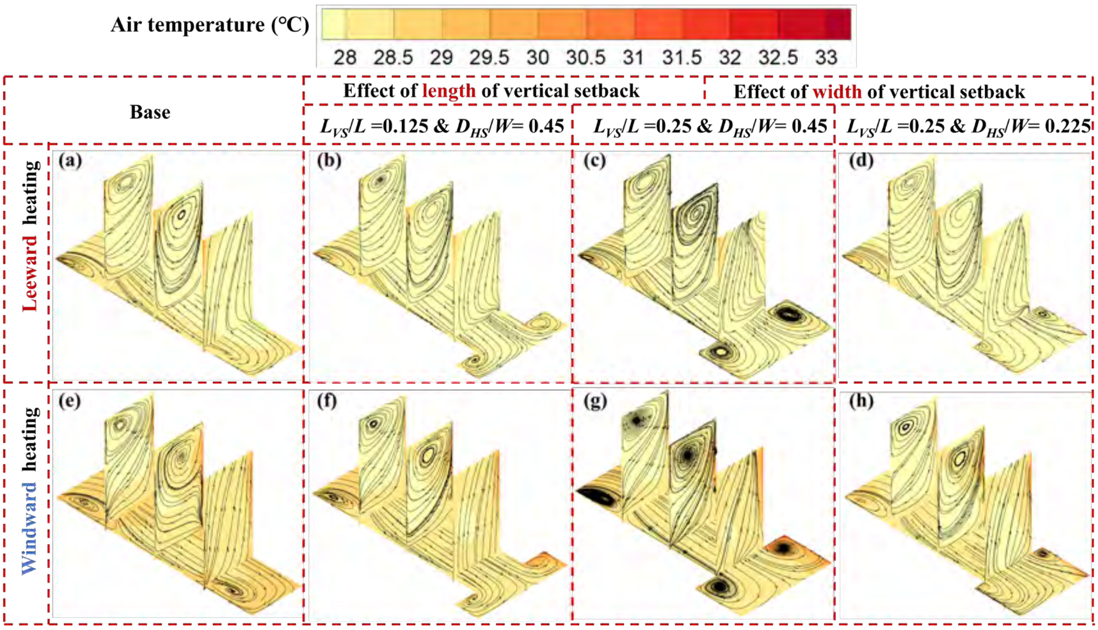

Figure 4.16 Predicted contours of air temperature for different vertical setbacks within the high-rise street canyon: leeward heating scenario for (a)–(d) and windward heating scenario for (e)–(h).

Four, the effects of vertical setbacks on the pollutant concentration are discussed. Comparing the base case with the case of L_{VS}/L= 0.25 and D_{VS}/W= 0.45, the vertical setback greatly reduces the K_{lee} by up to 35%, while only slightly increase the K_{lee} by less than 6% (Figure 4.17 and Figure 4.18(d)). Besides, as decreasing either L_{VS}/L or D_{VS}/W, the vertical setbacks has relatively higher leeward concentrations, while hardly change the windward concentrations. It also should be noted that their K_{lee} is far lower than that of the base case. Hence, it can be deduced that all three vertical setbacks effectively improve the air quality for pedestrians. Meanwhile, the dimensionless area S_{VS} of vertical setback should be as large as possible.

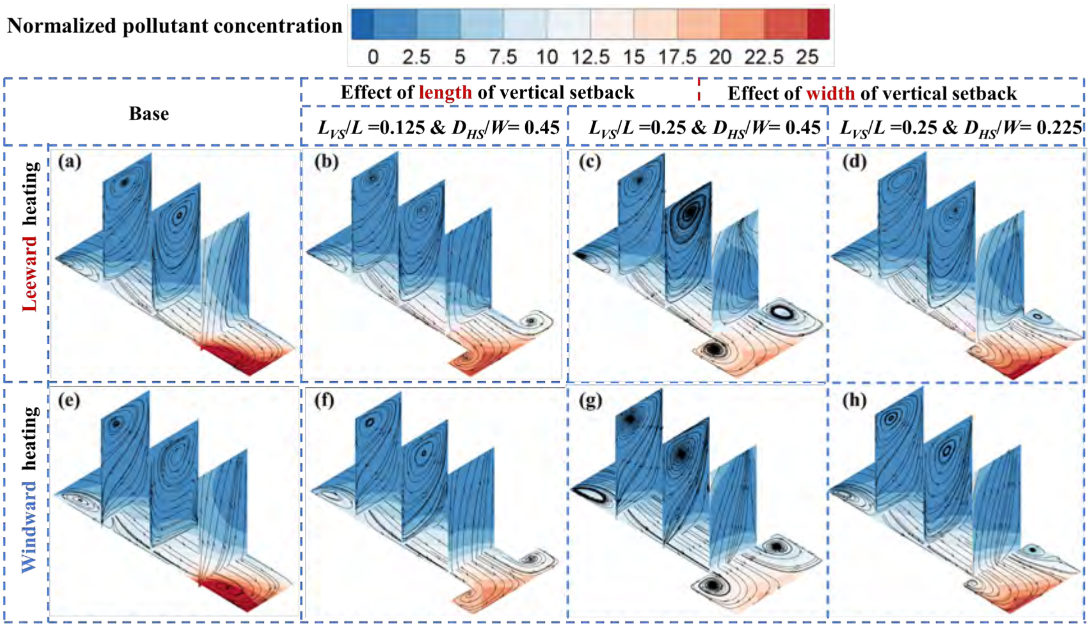

Figure 4.17 Predicted contours of pollutant concentration for different vertical setbacks with the high-rise street canyon: leeward heating scenario for (a)–(d) and windward heating scenario for (e)–(h).

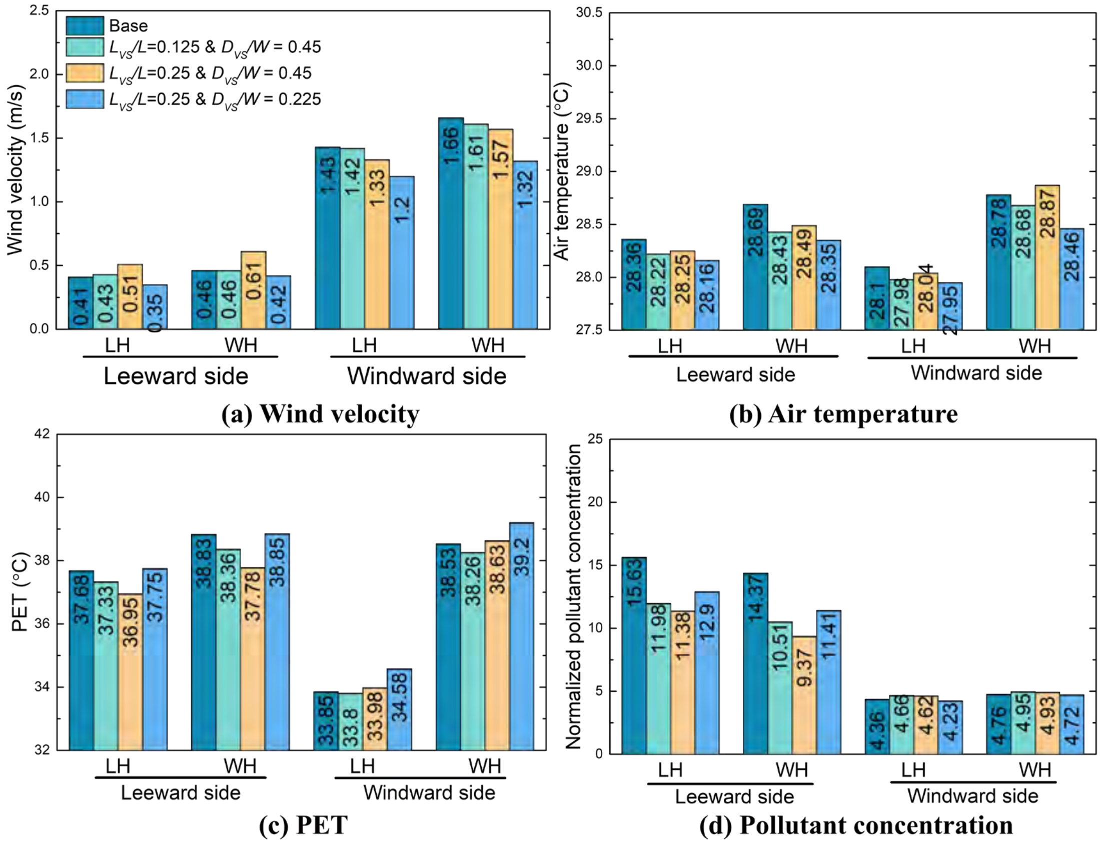

Figure 4.18 Average values of (a) Wind velocity, (b) Air temperature, (c) PET, and (d) Pollutant concentration under different vertical setback in the high-rise street canyon at

the pedestrian level of the leeward and windward side under leeward heating (LH) and windward heating (WH) scenarios

4.4 Summary

This chapter has presented the numerical simulations to simultaneously investigate the impact of horizontal and vertical building setbacks on the outdoor thermal environment jointly with outdoor air quality in the low-rise (H/W= 1) and high-rise (H/W= 2) street canyon under the perpendicular wind on a clear summer day. Hereafter, these two aspects can be evaluated under the same framework, hopefully, to provide some clues to find out whether these two building setbacks can potentially contribute to the urban environment. Besides, several parameters directly associated with the influence of building setbacks are taken into account to propose some general guidelines for the design of building setbacks, including the dimensionless height (H_{HS}/W) and dimensionless width (D_{HS}/W) for horizontal setbacks and the dimensionless length (L_{VS}/L) and dimensionless width (D_{HS}/W) for the vertical setbacks. Besides, all the simulations are conducted under both leeward heating (LH) and windward heating (WH) scenarios. Moreover, the simulations are based on grid-sensitivity analysis and validation of the CFD results from the literature. The major results are summarized as follows:

(1) In the low-rise street canyon, the horizontal setback improves the average wind velocity at the leeward pedestrian level (U_{win}), while reduces it at the windward side (U_{lee}). The change of wind velocity is directly related to the dimensionless area of the vertical cross-section of horizontal setback S_{HS} (= H_{HS}/W×D_{HS}/W), i.e., larger S_{HS} causes lower U_{win} and U_{lee}. The horizontal setback can reduce the average air temperature at both leeward (T_{win}) and windward (T_{win}) pedestrian levels. The reduction of air temperature is affected by two dimensionless design parameters of horizontal setback, i.e., S_{HS} and H_{HS}/D_{HS}. Both larger S_{HS} (better ventilation) and lower H_{HS}/D_{HS} (more shading effect) can help to reduce the pedestrian level air temperature. The horizontal setback reduces the average PET at the windward side (PET_{win}). However, it probably increases the PET_{lee}, except for the setback with lower H_{HS}/D_{HS}. The horizontal setback

with H_{HS}/D_{HS} =1 reduces both PET_{win} and PET_{lee} by up to 2.1 °C. The horizontal setback effectively reduces the average two-side pollutant concentrations (K_{win} and K_{lee}), especially for the setback with larger S_{HS}. The setback with a larger S_{HS} declines K_{win} and K_{lee} by almost 24–29% and 57–66%, respectively.

(2) In the low-rise street canyon, only the vertical setbacks with a short dimensionless length L_{VS}/L and a large dimensionless width D_{HS}/W improve both U_{win} and U_{lee}. The vertical setback cannot effectively reduce both T_{win} and T_{lee} compared with the base, although the dimensionless area of horizontal dimensionless horizontal section S_{VS} (=$L_{VS}/L \times D_{HS}/W$) is proportional to air temperature. Thus, only the vertical setbacks with a short dimensionless length L_{VS}/L and a large S_{VS} can reduce both PET_{win} and PET_{lee}. However, its maximum reduction of PET is less than 0.5 °C, which is far lower than that of the horizontal setback. The vertical setbacks only slightly improve both-side air quality. The vertical setback with the largest S_{VS} has the best air quality, but it only reduces the K_{lee} by almost 7%.

(3) In the high-rise street canyon, except for the horizontal setback with higher S_{HS}, most horizontal setbacks have a higher U_{win} and U_{lee} than that of the base. An increase in S_{HS} of horizontal setback decreases U_{win} but increases U_{lee}. However, except for the horizontal setback with larger S_{HS}, most horizontal setbacks cause a higher air temperature than the setback-free counterpart. The shading effect of horizontal setback becomes minor due to a higher building height. All the horizontal setbacks can improve the both-side thermal comfort in the high-rise street canyon, but its largest decrement of PET (only up to 0.8 °C) is less than that in the low-rise street canyon. A larger S_{HS} causes a better leeward thermal comfort but a worse windward thermal comfort. Besides, all kinds of horizontal setbacks in the high-rise street canyon result in higher K_{lee} compared to the base case.

(4) In the high-rise street canyon, a larger dimensionless S_{VS} of vertical setback leads to a higher U_{win}, but their U_{win} is less than that of the base case. Except for the case with smaller S_{VS}, the vertical setbacks can significantly improve the U_{lee}. Besides, compared to the base case, all three vertical setbacks provide a lower air temperature for two-side pedestrians in most cases. Although the vertical setbacks with smaller S_{VS}

have a higher air temperature, a larger S_{VS} can achieve better thermal comfort for two-side pedestrians. The vertical setback with the largest S_{VS} can reduce PET_{lee} by up to 0.7 °C. Moreover, the vertical setbacks effectively improve the air quality for pedestrians. Meanwhile, the dimensionless area S_{VS} of vertical setback should be as large as possible. The vertical setback with the largest S_{VS} can decrease K_{lee} by up to 35%.

Chapter 5 Effects of tree planting on the outdoor thermal comfort and air quality in street canyons

5.1 Introduction

As discussed in Section 1.2.2, the combined solar attenuation and evaporative cooling capacity of trees can effectively tackle the intense UHI effect [140,141]. However, tree planting has a negative influence on ventilation, resulting in an accumulation of pollutants below the tree canopy, in terms of airborne pollutants [142]. Besides, an altering of trees parameters, including the tree canopy density (e.g., leaf area density (LAD) [132,143,144]), the tree coverage density (e.g., tree spacing [145,146]), the tree geometry (e.g., trunk height [147–149]) have been demonstrated to significantly affect both thermal environment and pollutant dispersion.

Based on this background, the objectives of this chapter are to 1) investigate the influence of tree planting on the distribution of air temperature and pollutants with consideration of cooling effect and aerodynamic effect at the same time, 2) to find out the critical parameters of tree planting (LAD, tree spacing, and trunk height) for a good enough thermal comfort but not bad air quality.

5.2 Description of CFD simulations

5.2.1 Description of case studies, computational geometry, and grid

This chapter employs full-scale 3D street canyon models consisting of five uniform buildings (building height H = 24 m and building width W_b = 24 m) and four street canyons (street width W = 24 m and, street length L = 240 m,), as seen in Figure 5.1. The target street canyon locates between the 3rd and 4th building, while the other upstream and downstream identical street canyons are used to reproduce the influence of roughness elements [18,25,132–134]. Considering the symmetry of flow structure within street canyons, only half of the model is chosen to reduce the computational power (Figure 5.1). The street orientation is set as a North-South direction. Considering a worse air quality within the street canyon generally yielded by the perpendicular wind, the wind is assumed to go from the west. To represent the leeward heating (LH) scenario and windward heating (WH) scenario, the simulation is conducted for steady-state weather conditions at LSTs (local solar times) of 9 a.m. (0900 LST) and 3 p.m. (1500 LST) on a clear summer day in Hong Kong, respectively (Figure 5.1).

The tree canopy model is employed in this research. This simplification model is one of the most commonly used models to evaluate the impact of trees on urban outdoor microclimate, in which the tree trunk for supporting the tree crown is neglected [150,151]. This tree canopy model consists of a cluster of tree crowns, as shown in Figure 5.1. The whole tree canopy can be considered as a porous medium [132]. Eventually, the tree-air interactions are resolved through a set of volumetric sources and sink terms [43,74,75], including the calculation of momentum source (S_{ui}), turbulence source (S_k), turbulence dissipation sink (S_ε), and energy source (S_T). By using this approach, the aerodynamic effect (AE) and cooling effect (CE) of trees, as well as their combined effects, will be represented and parameterized via the LAD.

The LAD, the trunk height (H_{trunk}), and tree spacing (W_{spacing}) are key influencing factors, which are chosen to investigate the in-canyon distribution of pollutant dispersion and air temperature. For all the cases, the length (L_{crown} = 6 m), width (W_{canopy} = 4 m), and height (H_{crown} = 6 m) of the tree crown are fixed. For the effects of LAD, the LAD varies from 0.5 to 2 with 0.5 intervals, which represent sparse to lush foliage. The other dependent parameters (i.e., the trunk height (H_{trunk}/H = 0.25) and tree spacing ($W_{spacing}/W_{crown}$ = 0)) are kept constant. For the influences of trunk height, the ratio of H_{trunk} and H (H_{trunk}/H) increases from 0.125 to 0.75 with an interval of 0.125, and all other parameters (i.e., the LAD (= 1) and tree spacing ($W_{spacing}/W_{crown}$ = 0) are kept constant, denoting the crown being “close to” to “far away from” the pedestrian level. Figure A6.1 (a) shows the set-up of the target street canyon for the case of H_{trunk}/H = 0.125 and 0.25. As for the impact of tree spacing, different tree spacing is studied (the ratio of $W_{spacing}/W_{crown}$ ranges from 0 to 4), with a constant LAD (= 1) and trunk height (H_{trunk}/H = 0.25). Herein, the case of $W_{spacing}/W_{crown}$ = 0 represents a continuous tree canopy. With this regard, the tree canopy 100% occupies the street canyon in the spanwise direction. Figure A6.1(b) presents the set-up of the target street canyon for the case of $W_{spacing}/W_{crown}$ = 1 and 4. Besides, the tree-free case does not involve the tree canopy, which is treated as the base case.

The size and discretization of the computational domain are referred from the practice guidelines by Tominaga et al. [97]. Thus, as shown in Figure 5.1, the distances between the building and the inlet boundary, lateral boundaries, top boundary, and outflow boundary are 5 H, 5 H, 5 H, and 15 H, respectively.

As shown in Figure 5.2, the computational domain is discretized into approximately four million hexahedral cells. Considering the relatively large gradients of the velocity near the ground and building surfaces, the finest grids are deployed around these two types of walls. In this chapter, a grid-sensitivity analysis is performed based on two additional grids: a coarser grid and a finer grid for the street canyon with trees of H_{trunk}/H = 0.25 and $W_{spacing}/W_{crown}$ = 0. For the coarse, basic, and fine grids, the minimum sizes are set to be 0.4 m, 0.1 m, and 0.05 m, respectively. The total cell numbers for the coarse, basic, and fine grids are 1.07 million, 3.83 million, and 13.22 million, respectively. Therefore, the ratios of the two consecutive cell numbers for the grid refinement meet the criterion of 3.4 in the mesh-independent study [97]. The results of the grid-sensitivity analysis in Section 5.2.5 indicate that the basic grid provides nearly grid-independent results, which can be further used for the remainder of this study.

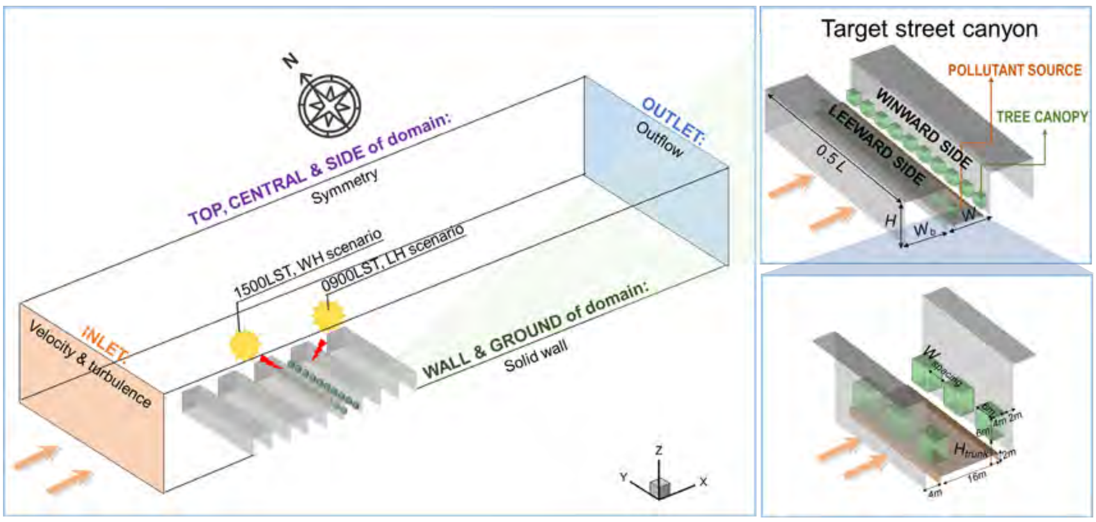

Figure 5.1 Computational geometry and boundary conditions

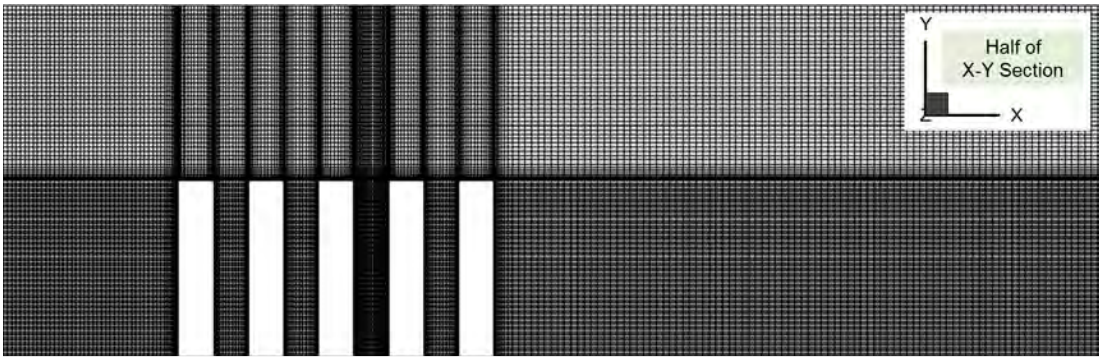

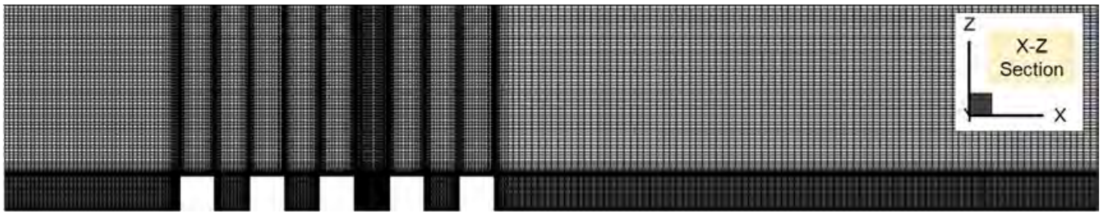

Figure 5.2 Grid distributions of the geometric model for the case of H_{trunk}/H = 0.25 and $W_{spacing}/W_{crown}$ = 0 with the basic grid

5.2.2 Boundary conditions

At the domain inlet, a power-law velocity profile is applied as follows,

$$U(z) = U_{ref}\left(\frac{z}{z_{ref}}\right)^{\alpha} \tag{5.1}$$

$$k(z) = \left(U(z)\times I_{in}\right)^2 \tag{5.2}$$

$$\varepsilon(z) = \frac{C_\mu^{3/4} k(z)^{3/2}}{\kappa z} \tag{5.3}$$

where z_{ref} is the reference height (= 24 [m]), α is the power-law exponent (= 0.22, stands for the underlying surface roughness above medium-dense urban area), I_{in} is the turbulent intensity (= 0.1, refers to [132]), κ is the von Karman's constant (= 0.42), and C_μ is the model constant (= 0.085). Moreover, U_{ref} is the reference wind speed (= 3 [m/s]), the reference Reynolds number ($\mathrm{Re} = U_{ref} H / \nu$) is about 4.9 × 10^6, which is far larger than 11,000 to satisfy the requirement of Reynolds number independence [135].

Besides, as seen in Figure 5.1, the top and lateral boundaries of the domain are set as symmetry boundaries, namely setting normal velocity and normal gradients of all variables to zero. On the outlet of the domain, a zero diffusive flux is imposed for all flow variables in the direction normal to the outflow plane since the domain downstream is long enough to ensure a fully developed outlet flow. For near-wall treatment, no-slip wall boundary conditions with standard wall function are applied.

Moreover, CO is used as the pollutant representative. As shown in Figure 5.1, a uniform volume source (width W_p = 2/3 W and length L_p = street length L) of CO is specified near the ground with a depth of 1/12 H to represent the traffic lanes. The constant emission rate per hour per unit street length (36.1 g/h/m, i.e., total mass release rate of $L_p \times 1.0 \times 10^{-5}$ [kg/s]) is adopted for each CO source.

5.2.3 Numerical models

The commercial software ANSYS/Fluent® CFD software (Release 15.0) [127] is used to simulate the airflow of ambient wind over this isolated street canyon. The numerical analysis is based on the steady-state 3D RANS conservation equations of mass, momentum, and energy for the incompressible turbulent flow. RNG k-ε model is chosen in this chapter to provide reliable predictions of the mean flows with the thermal effect and pollutant dispersion. The governing equations are as follows:

Continuity equation:

$$\frac{\partial(\rho u_i)}{\partial x_i} = 0 \tag{5.4}$$

Momentum equation:

$$\frac{\partial(\rho u_i u_j)}{\partial x_j} = -\frac{\partial p}{\partial x_i} + \frac{\partial \tau_{ij}}{\partial x_j} + \rho g_i + S_{u_i} \tag{5.5}$$

Energy equation:

$$\frac{\partial u_i T}{\partial x_i} + \frac{\partial}{\partial x_i}(\alpha_T \frac{\partial T}{\partial x_i}) = S_T \tag{5.6}$$

where the stress tensor τ_{ij} is defined as:

$$\tau_{ij} = \rho\left[\nu_t\left(\frac{\partial u_i}{\partial x_j}+\frac{\partial u_j}{\partial x_i}\right)\right]-\frac{2}{3}\rho k\delta_{ij} \tag{5.7}$$

where the term u_i denotes the i-axis component of the air velocity; p and ρ represent the pressure and density; ν_t is the turbulent kinematic viscosity; δ_{ij} is the Kronecker delta; k is the turbulence kinetic energy; S_{ui} is the sink of momentum term due to the aerodynamic effects of trees; T, α_T, and S_T represent the air temperature, thermal diffusivity, and energy source due to the cooling effect of trees, respectively. The Boussinesq approximation is applied to calculate the buoyancy force, i.e., $\rho=\rho_{ref}-\beta\rho_{ref}(T-T_{ref})$. Here, β, T_{ref}, and ρ_{ref} are the thermal expansion coefficient, reference temperature, and reference air density, respectively. Therefore, air density is treated as a constant value in all solved equations, except for the buoyancy term in the momentum equations.

The species transport equation is solved to probe the pollutant dispersion in an urban environment, as follows:

$$\frac{\partial u_i Y}{\partial x_i}-\frac{\partial}{\partial x_i}\left[\left(D+D_t\right)\frac{\partial Y}{\partial x_i}\right]=S_p \tag{5.8}$$

where S_p is the pollutant source term [kg/(m^3·s)]; D and D_t (= ν_t/Sc_t) denote the molecular and turbulent diffusion coefficients of the pollutant, respectively. Sc_t is the turbulent Schmidt number, which is set to 0.4 to account for the underestimation of the turbulent mass diffusion from the RANS models [99,152]. Y is the mass fraction of the pollutants. This dispersion of pollutants is simulated with the User Defined Scalar (UDS) option in ANSYS/Fluent®.

This chapter utilizes the pressure-linked equations-consistent (SIMPLEC) numerical method for the pressure-velocity coupling. The second-order upwind scheme [103] is used to discretize both the convective terms and the diffusion terms. A double-precision solver is also selected for the CFD calculations. The convergence of the normalized residual errors of the energy equation is set to 10^{-9}, whereas the convergence criterion of the remaining equations is set to 10^{-6}.

5.2.4 Description of tree model in CFD simulation

5.2.4.1 Parameterization of aerodynamic effect of trees

As one of the aerodynamic effects of trees, the drag force of trees induces a reduction in ventilation around the crown [153]. In most CFD studies on the influence of trees, the sink of momentum term S_{ui} has been established [154], which well-captures both the viscous and inertial losses due to the presence of trees. It is defined as a function of air density (ρ_{air}) [kg/m^3], LAD, drag coefficient (C_d = 0.2) [155], absolute wind speed $|u|$ [m/s], and wind velocity component (u_i) [m/s] in Eq. (5.9) [153,156], as follow,

$$S_{ui} = -\rho_{air} LADC_d |u| u_i \tag{5.9}$$

Moreover, the drag force modifies the mean flow motion into wake turbulence, which leads to the production of turbulent kinetic energy as a result. However, the length scale of wake turbulence induced by trees is larger than that of the shear turbulence, hence causing a fast dissipation. Similar to the drag force, the turbulent kinetic energy (k) and turbulent dissipation rate (ε) are also parametrized as the source and sink terms in Eqs. (5.10)–(5.11), respectively [144,157–159].

$$S_k = \rho_{air} LADC_d (\beta_p |u|^3 - \beta_d |u| k) \tag{5.10}$$

$$S_\varepsilon = \rho_{air} LADC_d (C_{\varepsilon 4} \beta_p \frac{\varepsilon}{k} |u|^3 - C_{\varepsilon 5} \beta_d |u| \varepsilon) \tag{5.11}$$

where β_p is the fraction of mean kinetic energy converted into turbulent kinetic energy by means of drag (= 1) [155,157]; β_d is the dimensionless coefficient for the short-circuiting of the turbulence cascade (= 4) [155,157]; $C_{\varepsilon 4}$ (= 1.5) and $C_{\varepsilon 5}$ (= 1.5) are model constants [157,159].

5.2.4.2 Parameterization of cooling effects of trees

The parameterization of the cooling effects is based on the tree-canopy cooling model established by Grylls and van Reeuwijk [160], with consideration of the effects of trees on transpiration and shading of solar radiation at the same time. Besides, this model does not need to resolve the leaf temperature via a derivation of the Penman-

Monteith equation. The implement of tree-canopy cooling effects is based on the energy balance model on the leaf surface in Eq. (5.12), which can effectively capture the cooling effects of trees.

$$\Delta Q_{sl} = Q_l^* - Q_{Hl} - Q_{El} \tag{5.12}$$

where ΔQ_{sl} [W/m^2] is the heat storage term, encompassing both the change in internal energy of the leaf and the photosynthetic heat component on the leaf; Q_l^*, Q_{Hl} and Q_{El} are the net radiative fluxes [W/m^2], sensible heat fluxes [W/m^2], and latent heat fluxes [W/m^2] on the leaf; The subscript, *l*, denotes the values at the leaf surface. It is noteworthy that the heat storage term is negligible by many studies [161,162]. Therefore, Eq. (5.12) can be rewritten as follow,

$$Q_l^* = Q_{Hl} + Q_{El} \tag{5.13}$$

For the terms on the left-hand side of Eq. (5.13), the calculation of Q_l^* should consider the absorption, reflection, transmission, and emission of both short- and long-wave radiation within the tree crown. Since 3D radiative model for Q_l^* is computationally intensive and requires several additional free parameters [72], a common simplification method is introduced to the current model. By assuming relative horizontal homogeneity within the canopy [163], the net radiative flux of a tree canopy is reduced to a one-dimensional problem, which is dominated by the incident net solar radiation from above, Q_a^* [W/m^2]. The attenuation of radiation through the tree canopy $Q^*(z)$ [W/m^2] can be estimated by the Beer-Lambert law [164],

$$Q^*(z) = Q_a^* \exp(-\beta_s LAI(z)) \tag{5.14}$$

where β_s is the extinction coefficient of solar radiation (= 0.78) [161]; *LAI(z)* is the cumulative leaf area index [m^2/m^2], which can be calculated as follow,

$$LAI(z) = \int_z^{Z_{ct}} LAD(z')dz' \tag{5.15}$$

where Z_{ct} is the absolute height of the tree-crown top.

Therefore, the net radiation at the leaf Q_l^* can be obtained from the net radiation $Q^*(z)$ within the tree canopy is given by,

$$Q_l^*(z) = \frac{1}{LAD}\frac{dQ^*}{dz} \tag{5.16}$$

For the terms on the right-hand side of Eq. (5.12), sensible heat flux Q_{Hl} and latent heat flux Q_{El} at the leaf can be calculated by Eqs. (5.17) and (5.18) [165,166],

$$Q_{Hl} = \frac{2}{r_a}\rho_{air}C_{p,air}(T_l - T) \tag{5.17}$$

$$Q_{El} = \frac{2}{r_a + r_s}\frac{\rho_{air}R_a L_v}{p_0 R_v}(\varepsilon_{vl} - \varepsilon_v) \tag{5.18}$$

where T_l and T are the leaf surface and ambient air temperature [°C]; ε_{vl} and ε_v are the vapor pressure at the leaf surface and the vapor pressure of the ambient air [Pa], respectively; ρ_{air} is the density of air [kg/m^3]; $C_{p,\,air}$ is the specific heat of air [J/kg·°C]; R_a and R_v are the gas constants of dry air (= 287.042 [J/(kg·K)]) and water vapor (= 461.524 [J/(kg·K)]), respectively; L_v is the latent heat of vaporization (2.5 × 10^6 [J/kg]); P_0 is atmospheric pressure [Pa]; r_s is the stomatal resistance to vapor diffusion (= 200–400 [s/m] for trees and shrubs [167]); r_a is the aerodynamic resistance to transpiration [s/m], which can be calculated by Eq. (5.19)[168],

$$r_a = A_l\left(\frac{D_l}{|u|}\right)^{0.5} \tag{5.19}$$

where D_l is the characteristic diameter of leaf [m] and A_l is a constant related to tree species (=200 [s$^{0.5}$/m] for deciduous trees) [168].

ε_{vl} in Eq. (5.18) is close to the saturation vapor pressure at the leaf surface temperature since evapotranspiration is assumed to be only induced by the transpiration through the leaf stomata without considering the condensation or rain on the leaf surface [169]. Therefore, the Eq. (5.17) and (5.18) can be solved by calculating the leaf temperature T_l at every iteration step. However, we need to perform an initial estimation of leaf temperature at the beginning, which might affect the convergence of CFD simulation. Therefore, Grylls and van Reeuwijk [160] indicated that there was a way to solve the Eq. (5.13) without the need to model the leaf temperature. This problem can be achieved by following the derivation of the classical Penman-Monteith equation [170]. In effect, the key idea of this method is to replace the leaf temperature T_l with ambient air temperature T.

First, we employ a Taylor series expansion of the saturation pressure around T as follow,

$$\varepsilon_{vl} - \varepsilon_v = \varepsilon_s(T_l) - \varepsilon_v = \left[\varepsilon_s(T) - \varepsilon_v\right] + \left[\varepsilon_s(T_l) - \varepsilon_s(T)\right] = D + s(T_l - T). \quad (5.20)$$

Thus, the pressure difference between the leaf surface and the surrounding air ($\varepsilon_{vl} - \varepsilon_v$) is partitioned into the vapor pressure deficit of the surrounding air D (= $\varepsilon_s(T) - \varepsilon_v$) and a term $s(T_l - T)$ that is proportional to the surface-air temperature difference. $\varepsilon_s(T) = 610\exp\left(17.27T/(T+237.3)\right)$ is the saturation pressure at T. $\varepsilon_v = RH \times \varepsilon_s(T)$ is the vapor pressure of the ambient air, where RH is the relative humidity of the air. $s = 4098\varepsilon_s/(T+237.3)^2$ is the slope of the curve relating saturation vapor pressure to the air temperature T [171].

Second, substituting Eqs. (5.20), (5.13) and (5.17) into Eq. (5.18) gives,

$$Q_{El} = \frac{sQ_l^* + \frac{2}{r_a}\rho_{air}C_{p,air}D}{s + 2\gamma\frac{r_a + r_s}{r_a}}. \quad (5.21)$$

Finally, sensible heat flux Q_{Hl} at the leaf can be obtained by rearranging Eq. (5.13),

$$Q_{Hl} = -\omega_l \frac{2\rho_{air}C_{p,air}D}{sr_a} + (1-\omega_l)Q_l^* \quad (5.22)$$

where $\omega_l = \left(1 + \frac{2\gamma}{s}\frac{r_a + r_s}{r_a}\right)^{-1}$ is a dimensionless decoupling factor; $\gamma = P_0 C_{p,air} R_v / (R_a L_v)$ is the psychometric constant [Pa/°C].

Eventually, we can determine the energy source term S_T [W/m^3] induced by the tree canopy for the energy conservation since the sensible heat flux is the energy supplied to heat or cool the surrounding air as follow,

$$S_T = LADQ_{Hl}. \quad (5.23)$$

5.2.5 Grid sensitivity analysis

Three densities of mesh systems are tested for the case of LAD = 1, $H_{trunk}/H = 0.25$ and $W_{spacing}/\ W_{crown} = 0$ under the same environmental conditions. Figure 5.3 compares the results of the three grids along the central vertical line at the vertical center plane of the street canyon, including the dimensionless mean velocity (U/U_{ref}), air temperature (T), and dimensionless pollutant concentration (K). Herein, the dimensionless pollutant concentration is defined as $K = CU_{ref}HL/S_pV_p$, where C is the local pollutant concentration [kg/m^3] and V_p is the volume of pollutant source [m^3]. Along this line, the fine and the basic grid provide almost identical results, while some deviations are found between the results of the coarse and the basic grid. Besides, the near-wall area is resolved by the standard wall functions directly on the condition that the $y+$ of the first near-wall mesh for building surfaces and ground is 267.7 on average, which is in the log-law layer $30 < y+ < 300$ [127,136].

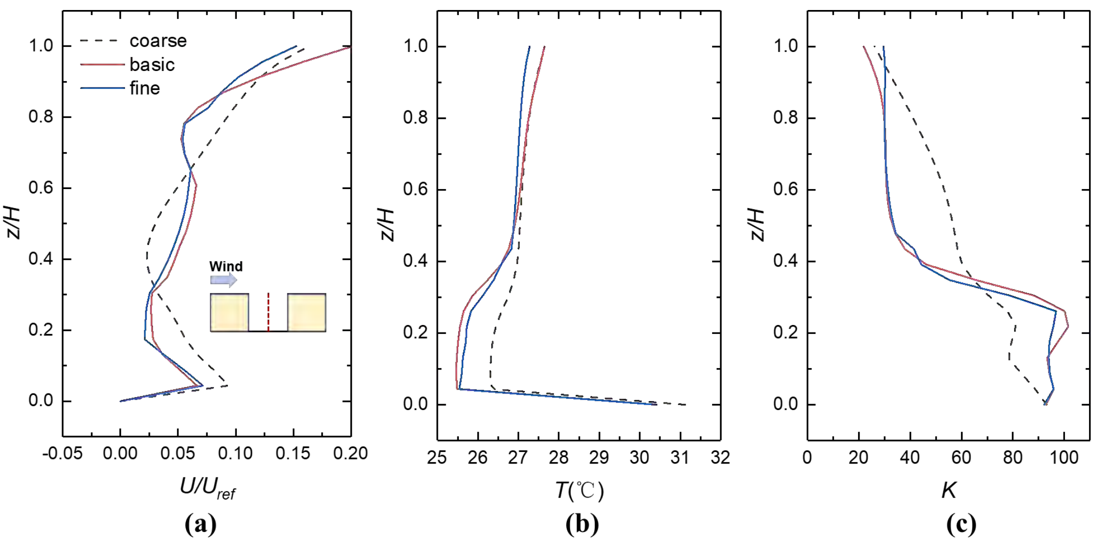

Figure 5.3 Comparison of (a) U/U_{ref}, (b) T, and (c) K along a center vertical line inside the street canyon in the vertical center plane in coarse, basic, and fine grids.

5.3 Validation

5.3.1 Validation of the aerodynamic effect of trees and pollutant dispersion

The current computational model to reproduce concentration fields within street canyons is validated by a wind tunnel experiment conducted earlier at the Laboratory of Building and Environmental Aerodynamics, University of Karlsruhe [172,173]. The wind tunnel had a test section of 2 m long, 2 m wide, and 1 m high (Fig. A5.2(a)), in which a scaled model (1:150) of a three-dimensional isolated street canyon constructed by two parallel model-buildings with the dimension of $H \times W_b \times L$= 0.12 m × 0.12 m × 1.2 m (Fig. A5.2 (c)) was tested. Meanwhile, the street width W was equal to the building width W_b. This isolated street canyon was simulated in a neutral atmospheric boundary layer (ABL) by using vortex generators and a 5 m long fetch covered with roughness elements (Fig. A5.2 (a)). This combination produced a simulated boundary layer with a power-law exponent α of 0.30, reference velocity of the incoming flow of 4.7 m/s at $z = H$, and a friction velocity u^*_{ABL} of 0.52 m/s. Besides, as seen in Fig. A5.2 (b) and (c), a single-row tree canopy model with a pressure loss coefficient λ of 80 m^{-1} (corresponding to a porous volume fraction of 97.5%) was placed in the center of the street canyon along the street axis. Moreover, Sulfur hexafluoride (SF6) was used as a tracer gas for modeling the release of traffic exhaust fumes and was emitted homogenously by four-line sources mounted at the bottom of the model. To account for the traffic exhaust fumes released on the street intersections, each line source exceeds the street canyon by approximately 10% on each side. For more information related to the wind tunnel experiments, the reader is referred to [172,173].

In this validation study, the concentration value is calculated in the non-dimensional form as $C^* = CU_{ref}H/(Q/l)$, where C is the measured concentration [g/m^3], and Q/l is the tracer gas source strength per unit length [g/m/s]. As shown in Figure 5.4, the experimental and numerical distributions of the dimensionless pollutant concentration are consistent. Therefore, this numerical model with the presence of trees is capable of predicting in-canyon pollutant dispersion.

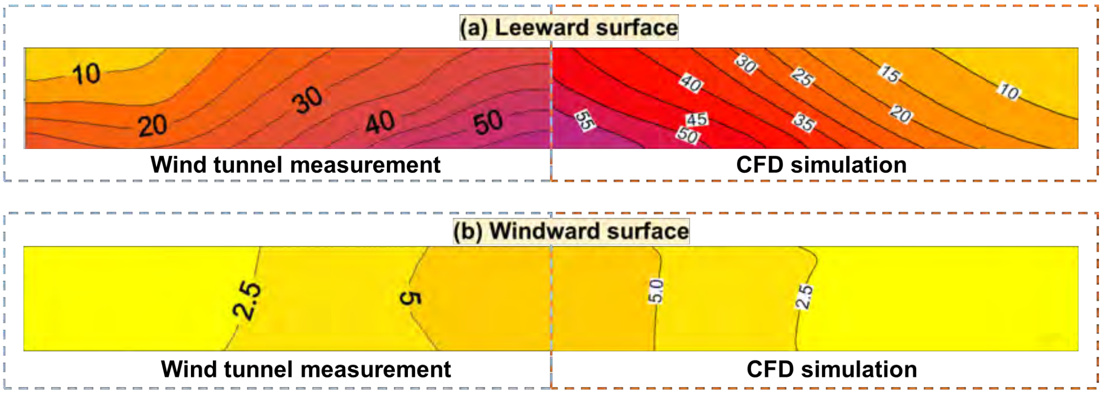

Figure 5.4 Comparison results of dimensionless pollutant concentration at the (a) leeward surface and (b) windward surface of the street canyon.

5.3.2 Validation of the cooling effect of trees

The tree-canopy cooling model is validated against the experimental study of Kichah et al. [162], which was conducted within a glasshouse compartment located in Angers of France (latitude: 47.5°N, longitude: -0.5°W) in July 2009. As seen in Figure A5.3(a), this experiment investigated the airflow through mature impatiens plants grown in pots in a greenhouse and corresponding heat exchanges between vegetation and the air. A comprehensive dataset of environmental conditions was provided by the experiments and further comparisons, including the short- and long-wavelength solar radiation, inlet temperature, relative humidity, and ground temperature (Figure 5.5(a)-(c)), which can be set as the boundary conditions for the CFD simulations. For more information related to this experiment, the reader is referred to [162]. Furthermore, Kichah et al. [162] indicated that their study mainly showed a 2D characteristic due to simple experimental conditions. Therefore, the CFD simulation for validation can be considered as a 2D model, as presented in Figure A5.3(b). To justify the cooling model used in this chapter, the measured and simulated air temperature in the middle position of the canopy are compared in Figure 5.5(d). The comparison indicates that the numerical results are basically in agreement with the experiments from 9 am to 6 pm. The relatively large deviation of air temperature during the afternoon could be attributed to an underestimation of inlet wind velocity induced by a stronger buoyancy force. Generally, the predicted results of air temperature are sufficiently accurate.

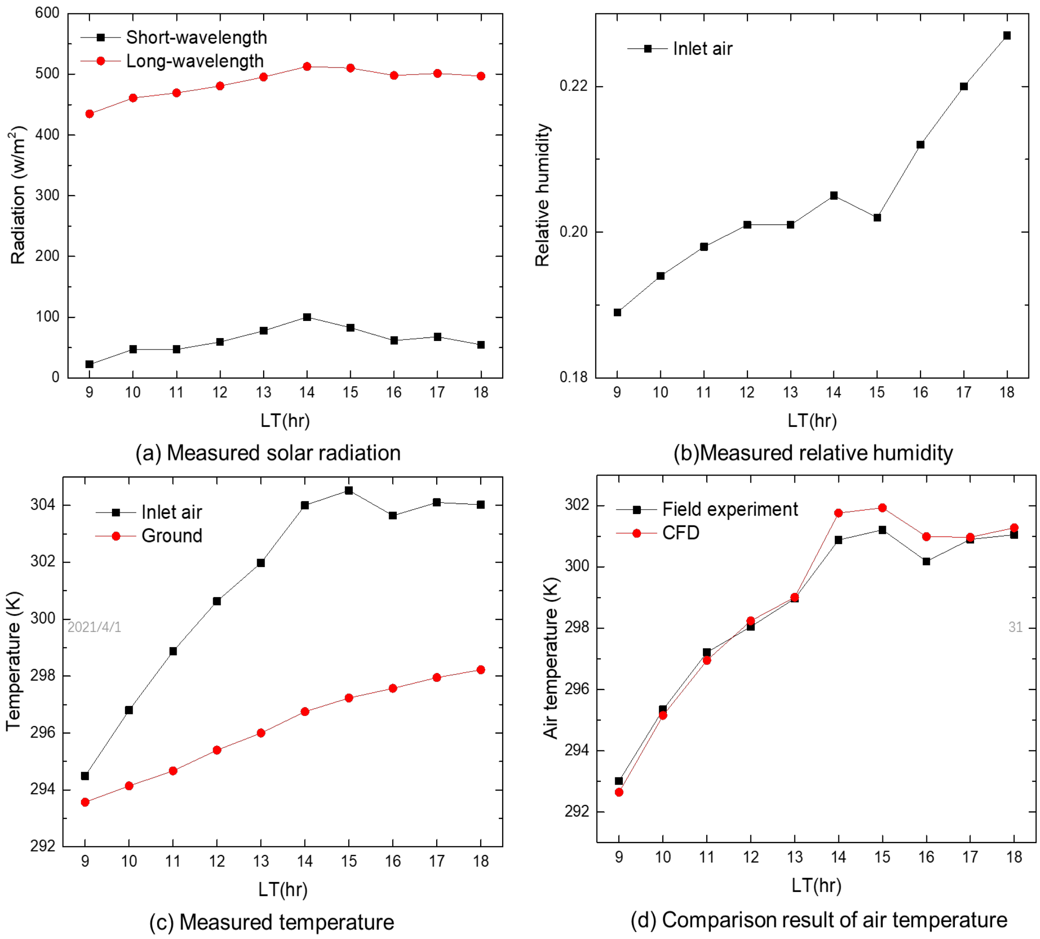

Figure 5.5 (a) Measured short- and long-wavelength solar radiation, (b) Measured relative humidity, (c) Measured inlet air and ground temperature, and (d) Comparison of the measured and simulated air temperature in the middle position of the canopy.

5.4 Results

5.4.1 Influence of aerodynamic effect and cooling effect

In this section, the influence of aerodynamic effect (AE) and cooling effect (CE) of tree canopy on the wind velocity, air temperature, and pollutant concentration will be explored. It should be noted that only the momentum source (S_{ui}) is considered for the case of AE, while only the energy source (S_T) is considered for the case of CE. Besides, for all cases, LAD (= 1), trunk height (H_{trunk}/H = 0.25), and tree spacing ($W_{spacing}/W_{crown}$ = 0) are kept constant to isolate the influence of AE and CE.

First, the change in wind velocity under both LH and WH scenarios is studied. Under the LH scenario, the AE of the tree canopy significantly reduces the pedestrian level wind velocity close to the lateral boundary of the street canyon, comparing with the tree-free case (Figure 5.6 (a)). This is because the AE of the tree canopy greatly weakens the influence of lateral entrainment, which impedes the lateral airflow. Therefore, there is degraded ventilation within the street canyon. As seen in Figure 5.7 (a), the average pedestrian level wind velocity (U_{ped}) declines by 15% compared to the tree-free case. Interestingly, the CE also lowers the in-canyon ventilation since it leads to a stagnant region in the center of the street canyon (Figure 5.6 (a)). When compared with the tree-free case, its U_{ped} reduces by 11% (Figure 5.7 (a)). This might attribute to the inversion layer caused by the CE. The inversion layer induces a negative buoyancy force around the tree canopy, which competes with the buoyancy force caused by solar radiation. As a result, the ventilation of the center of the street canyon is restrained. Furthermore, when considering the AE and CE simultaneously, the combination of AE and CE leads to a more severe stagnant flow in the center of street canyons (Figure 5.6 (a)), which thus results in a nearly 43% reduction in the U_{ped} (Figure 5.7 (a)). Under the WH scenario, the AE of the tree canopy also restrains the lateral airflow, which thus declines the wind velocity in the vicinity of the lateral boundary of the street canyon (Figure 5.6 (a)). The AE causes an 8% reduction in the U_{ped} (Figure 5.7 (a)). However, different from the case under the LH scenario, the CE of the tree canopy cannot create a stagnant flow region in the center of the street canyon (Figure 5.6 (a)). Nonetheless, the inversion layer induced by the CE still reduces the ventilation of the street canyon. Hence, the U_{ped} reduces by 7% (Figure 5.7 (a)). Then, with consideration of AE and CE at the same time, the presence of trees causes a 29% reduction in U_{ped}, which is lower than that under the LH scenario (Figure 5.7 (a)).

Second, the influence of trees on air temperature is discussed. Under both LH and WH scenarios, weaker ventilation somewhat caused by the AE reduces the upward dispersion of heat induced by the solar radiation around the ground level (Figure 5.6 (b)). Hence, the average air temperature at the pedestrian level T_{ped} increases by almost 0.2 ℃ under both LH and WH scenarios (Figure 5.7 (b)). In contrast, the CE of the tree canopy cools down the air flowing through it, particularly under the LH scenario. As seen in Figure 5.7 (b), the CE under the LH scenario results in a larger reduction in T_{ped}

(0.4 °C) than in the WH scenario (0.2 °C). The possible reason should be attributed to the stagnation region caused by the CE, which enhance the cooling performance of tree canopy (Figure 5.6 (a)). Furthermore, the combined influence of AE and CE leads to a more effective cooling performance, especially under the LH scenario. As a result, the T_{ped} significantly decreases by 1.1 °C under the LH scenario and 0.3 °C under the WH scenario, compared to the tree-free case (Figure 5.7 (b)).

Third, pollutant dispersion phenomena within the street canyon caused by the presence of trees are illustrated in Figure 5.6 (c). For the canyons without trees, under both LH and WH scenarios, the stronger lateral entrainment contributes to the transport of pollutants inward into the canyon center region, which causes a significant accumulation of pollutants. Then, these pollutants disperse upwards along the both-side building surface in the canyon center region. When only the AE is involved, there is weaker lateral entrainment, which deters the pollutant from dispersing upwards to the upper layer of the street canyon. Accordingly, the average normalized pollutant concentration at the pedestrian level (K_{ped}) increases by 29–38% (Figure 5.7 (c)). When only considering the CE of trees, the stagnant flow region in the center of street canyons hinders the pollutant dispersion under the LH scenario. Hence, its K_{ped} increases by 54%. In contrast, under the WH scenario, the increase of K_{ped} becomes relatively slight. It could be concluded that both AE and CE lead to the accumulation of pollutants, especially under the LH scenario. Thus, the combined influence of AE and CE results in a more evident increase in pollutant concentrations. As seen in Figure 5.7 (c), K_{ped} increases by 210% under the LH scenario and by 62% under the WH scenario.

In conclusion, the presence of trees within the street canyon largely alters the distribution of air temperature and pollutant concentration; thus, it is essential to shedding new light on the influence of some characteristic parameters of trees in the following section. Secondly, there is some difference in the influence of in-canyon trees under the LH and WH scenarios. The presence of trees induces a more significant change in air temperature and pollutant concentration under the LH scenario. Hence, the influence of trees will be analyzed under both the LH and WH scenarios. Thirdly, the AE and CE of the tree canopy play different roles in determining the flow field, which thus affects the air temperature and pollutant dispersion. Within this regard, the influence of different AE and CE caused by different design parameters of trees will be further studied.

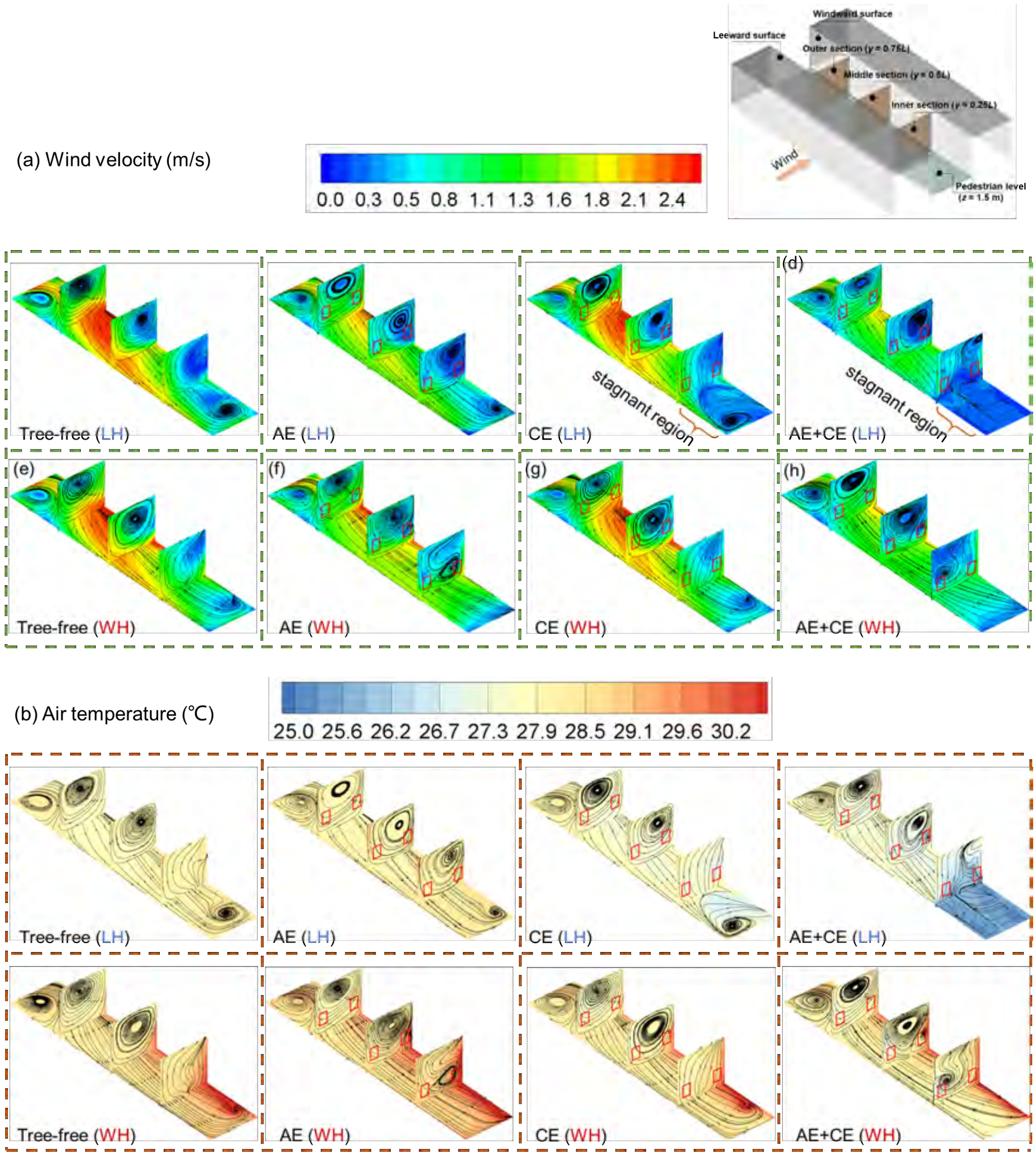

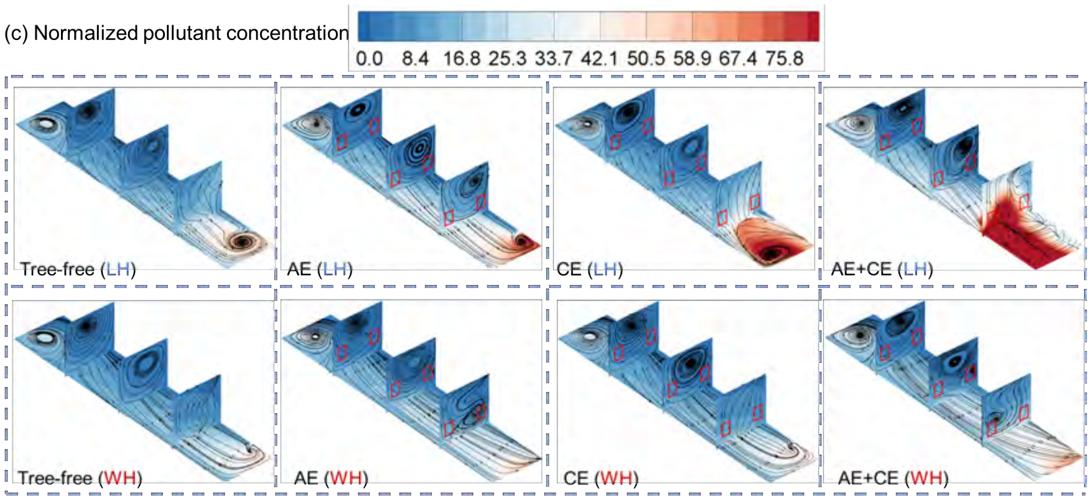

Figure 5.6 Predicted contours for different effects of trees with the street canyon: (a) Wind velocity, (b) Air temperature, and (c) Pollutant concentration. (Red dashed boxes represent the position and boundaries of the trees)

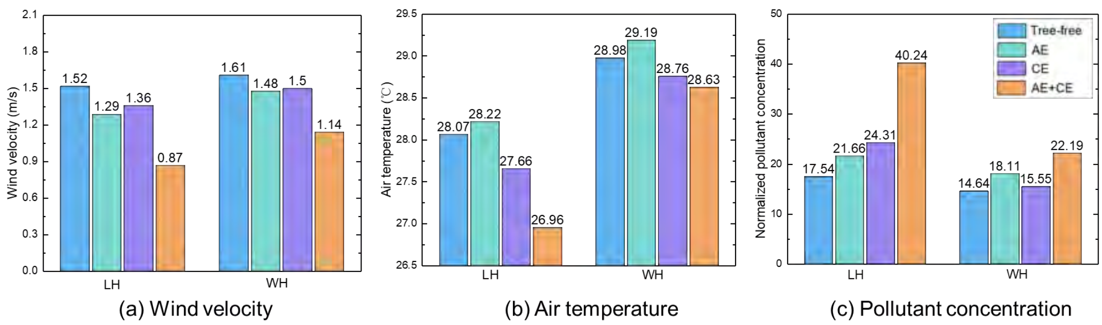

Figure 5.7 Average values of (a) Wind velocity, (b) Air temperature, and (c) Pollutant concentration under different effects of trees at pedestrian level

5.4.2 Effects of the leaf area density

In this section, the influence of LAD of the tree canopy is explored. When varying the LAD (0.5, 1, 1.5, and 2), all other dependent parameters (i.e., the trunk height (H_{trunk}/H = 0.25) and tree spacing ($W_{spacing}/W_{crown}$ = 0)) are kept constant. Besides, as discussed above, there is some difference in the influence of in-canyon trees under the LH and WH scenarios.

First, the influence of LAD is discussed at the pedestrian level. Comparing the tree-free case and case of LAD = 0.5 under both LH and WH scenarios, the presence of the tree with LAD = 0.5 almost does not change the flow structure and corresponding air temperature and pollutant concentrations at the pedestrian level (Figure 5.8). With an increase in LAD (from 0.5 to 1), the stagnant flow region in the center of street canyons enlarges and becomes more stable near ground level, which deters the top entrainment from penetrating down to the ground level (Figure 5.8 (a)). Thus, with the increase in LAD, poorer ventilation within the street canyons can be. This is because that the tree canopy with a higher LAD has a larger flow resistance and a stronger cooling effect according to Eq. (5.9) and (5.23). As a result, the case of LAD = 1 certainly has a lower air temperature (Figure 5.8 (b)) and higher pollutant concentration (Figure 5.8 (c)) than the case of LAD = 0.5 at the pedestrian level, especially under the LH scenario.

Second, the influence of LAD on two-side thermal comfort and air quality is discussed (Figure 5.9). Comparing the tree-free case and case of LAD = 0.5, the tree of LAD = 0.5 results in a significant reduction in air temperature close to both the entire leeward and windward surface (from Level 1 to 8; the calculation of average value at different height is shown in Figure A5.4), particularly for the surface directly heated by solar radiation. For instance, the tree of LAD = 0.5 causes an over 1 ℃ reduction in air temperature close to the leeward surface under the LH scenario. In contrast, the tree of LAD = 0.5 hardly changes the vertical distribution of pollutant concentrations, particularly under the WH scenario. With an increase in LAD (from 0.5 to 1), the cooling effect on the two-side surface is further improved, which causes a more significant reduction of air temperature on the two-side surface, especially for the low-level space (Level 1 to 4). However, the increased LAD can greatly worsen the air quality of the whole leeward surface under the LH scenario due to the stagnant flow region in the center of street canyons. Under the LH scenario, the leeward K_{lee} increased by up to approximately 150% compared to the tree-free counterpart.

Third, a larger variation of LAD (from 0.5 to 2) is investigated. Herein, the surface-average value on the both-side building surface is compared (the calculation of surface average values can refer to Figure A5.5). The aforementioned trends are still found with a larger variation of LAD, as presented in Figure 5.10. The influence of LAD on both air temperature and pollutant concentration is pretty significant. An increase in LAD from 0.5 to 1 has led to an up to almost 1℃ reduction of average air temperature, especially at the pedestrian level. For a large range of LAD (from 0.5 to 2), the air temperature reduction can be up to approximately 4 °C. Similarly, when LAD increases from 0.5 to 1, there has been an obvious increase in K by up to 100%. For a large range of LAD (from 0.5 to 2), K increases by up to almost 370%. Accordingly, it can be deduced that planting higher-LAD trees certainly creates a better thermal comfort environment in the street canyon, but it unavoidably results in a significant accumulation of traffic-related pollutants. Thus, the trees with low LAD (= 0.5) are suggested, since they hardly worsen the air quality but still induce a 0.5–1 °C reduction in air temperature on both-side surfaces.

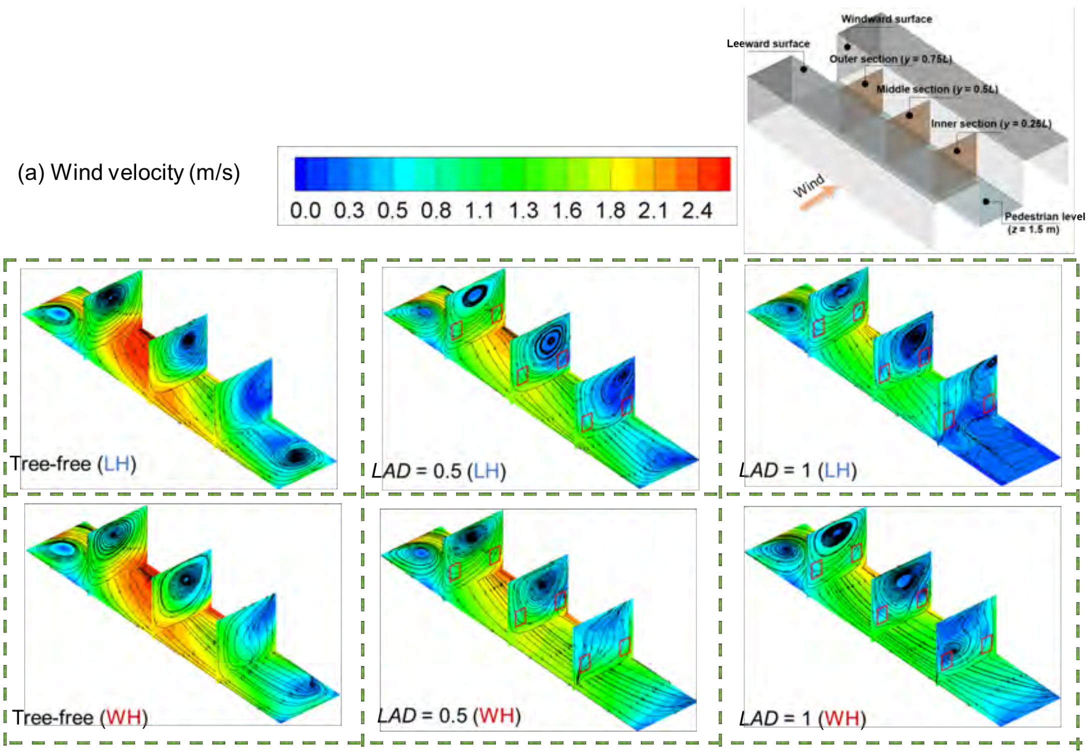

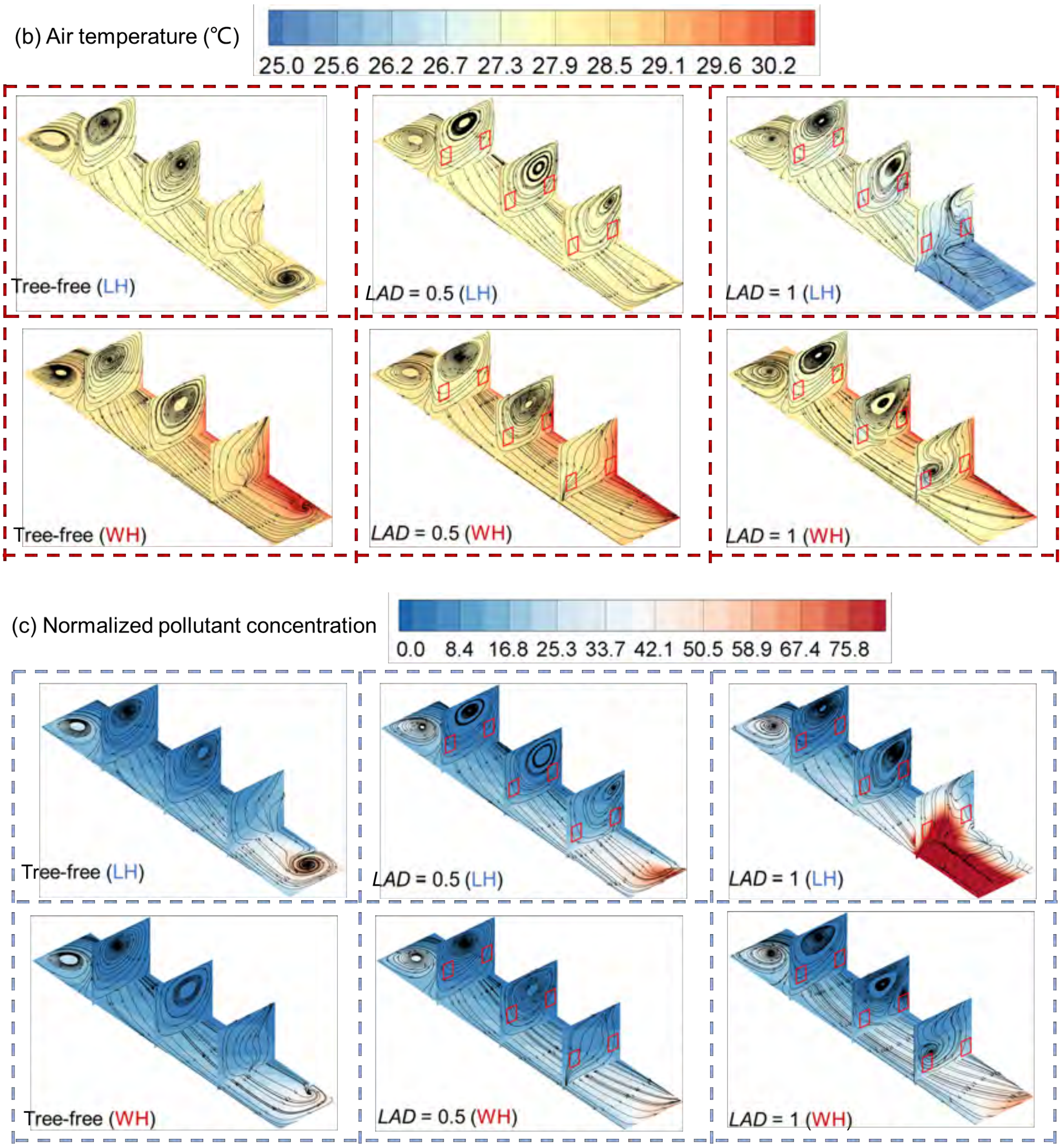

Figure 5.8 Predicted contours for various leaf area density with the street canyon:

(a) Wind velocity, (b) Air temperature, and (c) Pollutant concentration

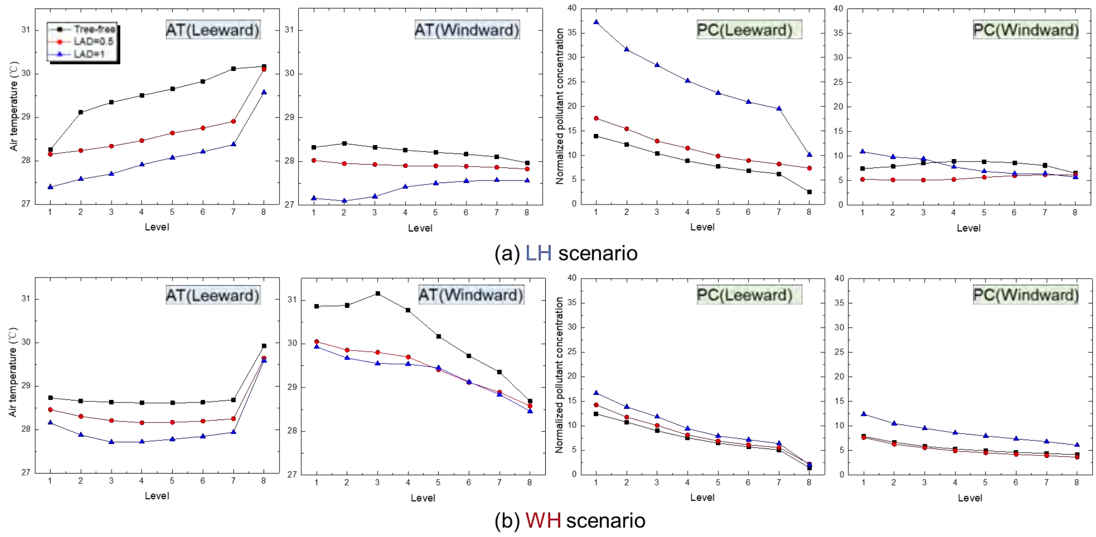

Figure 5.9 Vertical profiles of air temperature (AT) and pollutant concentration (PC) close to both leeward surface and windward surface for various LAD under (a) LH scenario and (b) WH scenario. These two profiles were drawn from the average AT and PC at each floor (3 m per level).

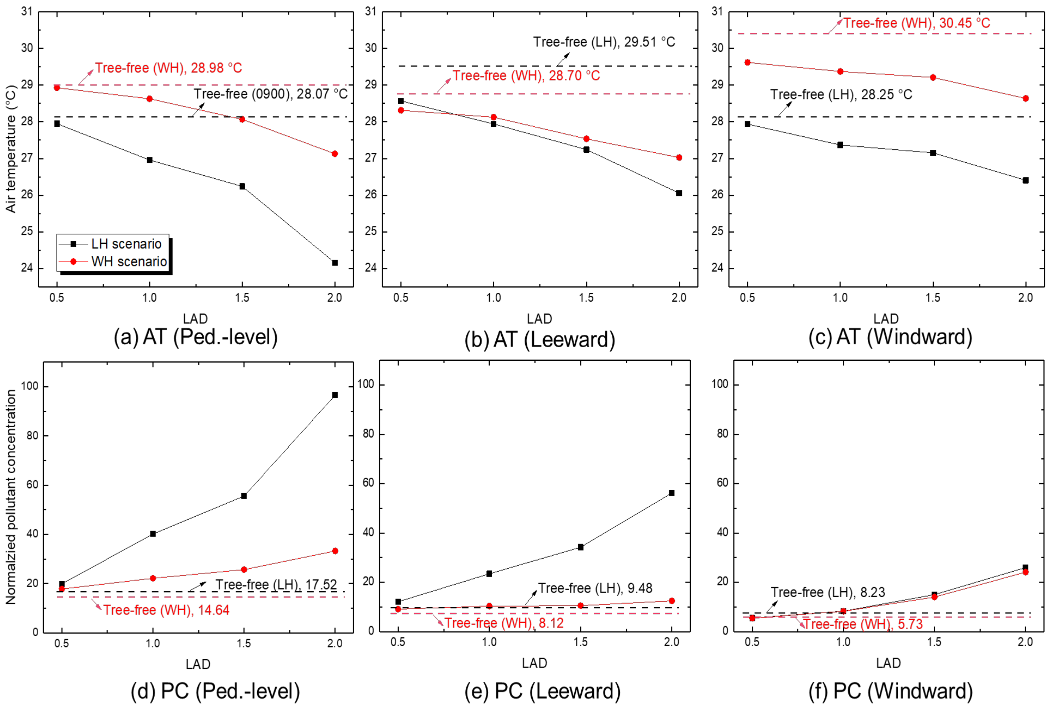

Figure 5.10 Profiles of average air temperature (AT) of (a) pedestrian level, (b) leeward side, and (c) windward side, and average pollutant concentration (PC) of (d) pedestrian level, (e) leeward side, and (f) windward side with various LAD (LAD from 0.5 to 2).

5.4.3 Effects of the trunk height

In this section, the influence of the trunk height of trees is investigated. When varying the ratio of trunk height (H_{trunk}/H from 0.125 to 0.75 with an interval of 0.125), all other dependent parameters (i.e., the LAD (= 1) and tree spacing ($W_{spacing}/W_{crown}$ = 0) are kept constant.

First, the influence of trunk height is explored at the pedestrian level. The comparison of tree-free cases and the case of H_{trunk}/H = 0.25 has been discussed above. With an increase in the trunk height (H_{trunk}/H from 0.25 to 0.5) under both LH and WH scenarios, less flow resistance on the lateral entrainment let more fresh air penetrate more deeply into the center region of the street canyon, leading to the inward contraction of the region with poor ventilation (Figure 5.11 (a)). As a result, there is a relatively larger wind velocity for a higher trunk height. Besides, the lift-up tree canopy leads to a significant change in flow structure under the LH scenario. The stagnant region close to the center plane of the canyon almost disappears. This could be attributed to the lifted-up inversion layer when trunk height increases. Interestingly, the stronger wind velocity due to higher trunk height does not significantly contribute to the enhancement of the thermal environment at the pedestrian level (Figure 5.11 (b)). Instead, the cooling effect of trees on the T_{ped} becomes weaker, particularly under the LH scenario. There are mainly two reasons. One is that the stagnant airflow region near ground level, which can enhance the cooling effect of the tree canopy, disappears with an increase in the trunk height; the other is that when the location of the tree canopy is lifted (higher height of red frame), it is not easy for the cooling airflow through the tree canopy to penetrate the ground level anymore. As for the pollutant concentration in Figure 5.11 (c), the distribution of pollutants is in direct relation to flow structure. Then, the stagnant region is contracted, and the ventilation is improved due to a lifted-up tree canopy, which reduces the accumulation of pollutants near the ground. Accordingly, a substantial reduction of pollutant concentration is observed at the pedestrian level when trunk height increases.

Second, the influence of trunk height is discussed close to the two-side surfaces. As seen in Figure 5.12, the increased trunk height causes a weaker cooling effect of trees on the low-level space. The case of H_{trunk}/H = 0.5 is almost 0.5 ℃ higher than the case of H_{trunk}/H = 0.25 from Level 1 to 3. Nonetheless, its air temperature on both leeward and windward surfaces is still far lower than its tree-free counterpart. The increased trunk height leads to an obvious reduction in pollutant concentrations on both the entire leeward and windward surface. Except for the leeward surface under the LH scenario, the presence of trees almost does not worsen the two-side air quality.

Third, a larger variation of trunk height (H_{trunk}/H ranges from 0.125 to 0.75) is investigated. As seen in Figure 5.13, the trends obtained above can be also observed under a larger variety of trunk height. Generally, an increase in H_{trunk}/H from 0.125 to 0.75 results in a weaker cooling effect and a lower pollutant concentration. Besides, there is a more significant positive correlation between trunk height and air temperature when H_{trunk}/H is less than 0.375, especially for the pedestrian level. Once H_{trunk}/H is over 0.375, the trees hardly improve the thermal comfort at the pedestrian level, when compared with the tree-free case. Interestingly, even the highest tree canopy still results in an improvement of thermal comfort on two-side surfaces, especially for the surface directly heated by solar radiation. For instance, the trees with H_{trunk}/H= 0.75 still have almost 1℃ reduction of air temperature on the windward surface under the WH scenario. Moreover, an increase in trunk height is also in positive relation to the enhancement of air quality. Compared with the tree-free counterpart, the concentration only slightly increases for all positions when the H_{trunk}/H is over 0.375. Therefore, higher trunk height is advocated (H_{trunk}/H > 0.375). Under this certain, the presence of trees still results in a better thermal environment on two-side surfaces. Meanwhile, these kinds of trees hardly worsen the air quality.

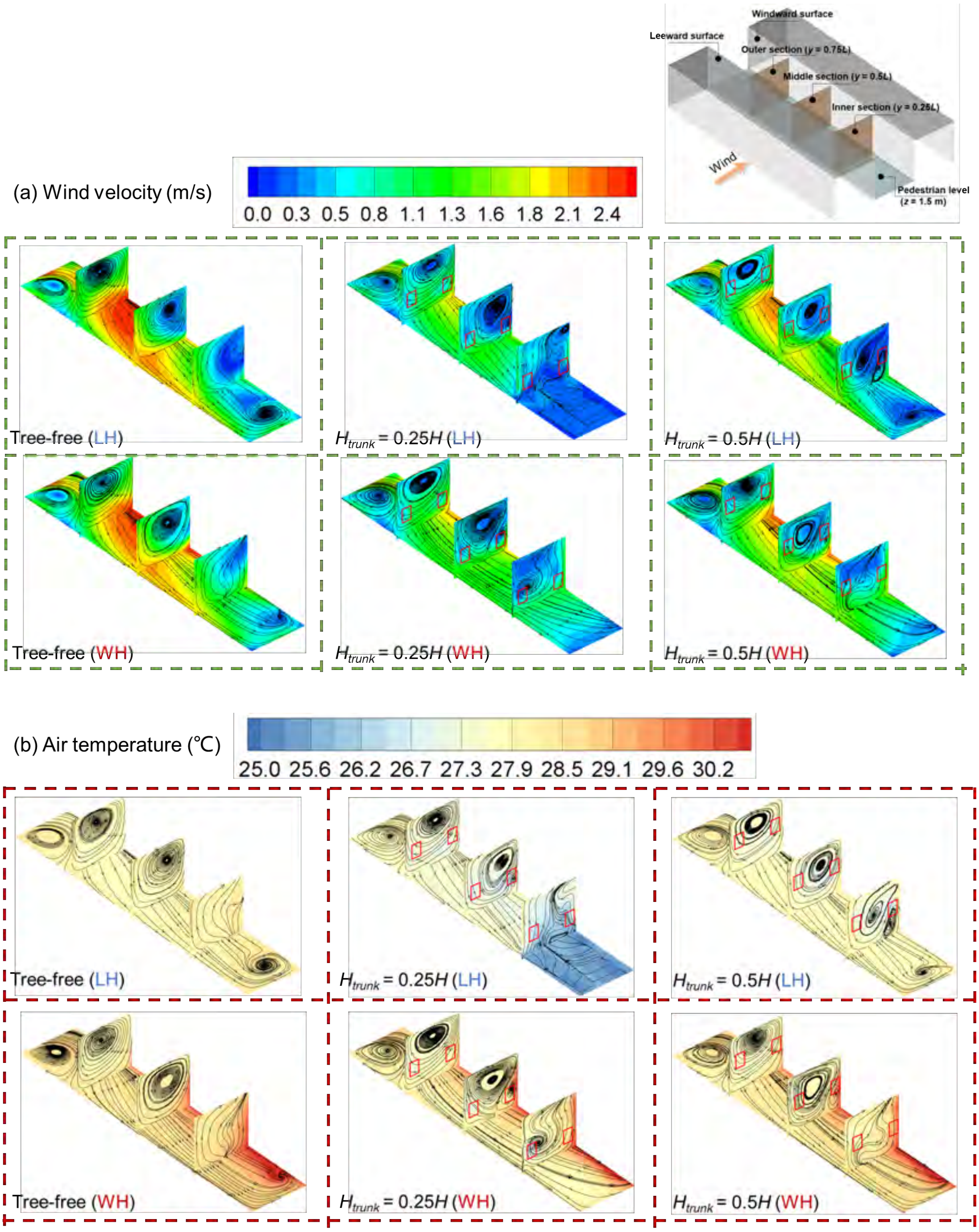
Windward surface
Leeward surface
Outer section (y = 0.75L)
Middle section (y = 0.5L)
Inner section (y = 0.25L)
Wind
Pedestrian level (z = 1.5 m)
(a) Wind velocity (m/s)
0.0 0.3 0.5 0.8 1.1 1.3 1.6 1.8 2.1 2.4
Tree-free (LH)
H_{trunk} = 0.25H (LH)
H_{trunk} = 0.5H (LH)
Tree-free (WH)
H_{trunk} = 0.25H (WH)
H_{trunk} = 0.5H (WH)
(b) Air temperature (℃)
25.0 25.6 26.2 26.7 27.3 27.9 28.5 29.1 29.6 30.2
Tree-free (LH)
H_{trunk} = 0.25H (LH)
H_{trunk} = 0.5H (LH)
Tree-free (WH)
H_{trunk} = 0.25H (WH)
H_{trunk} = 0.5H (WH)

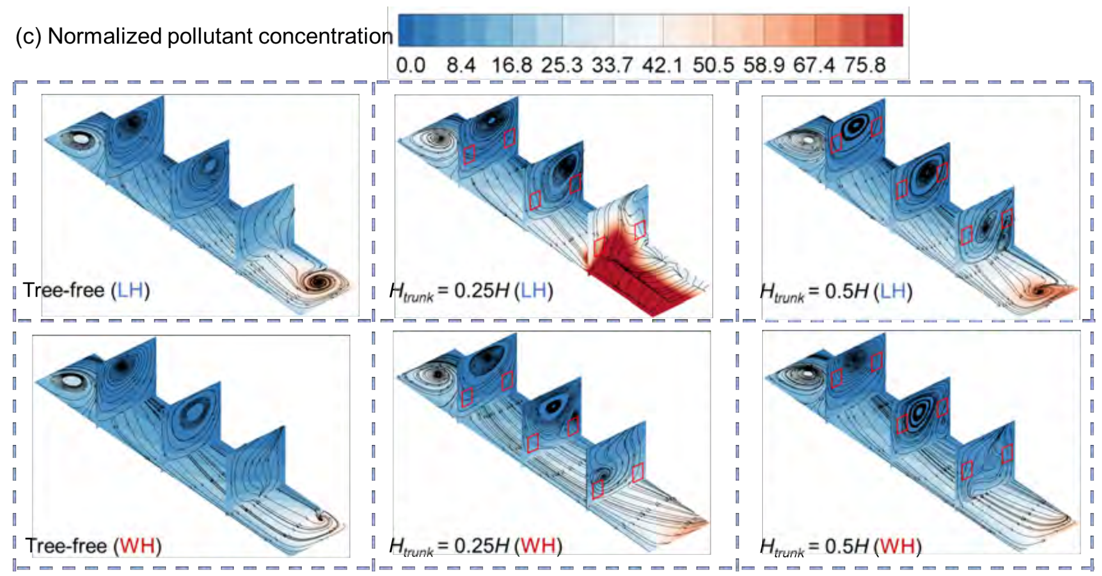

Figure 5.11 Predicted contours for various trunk height with the street canyon: (a) Wind velocity, (b) Air temperature, and (c) Pollutant concentration

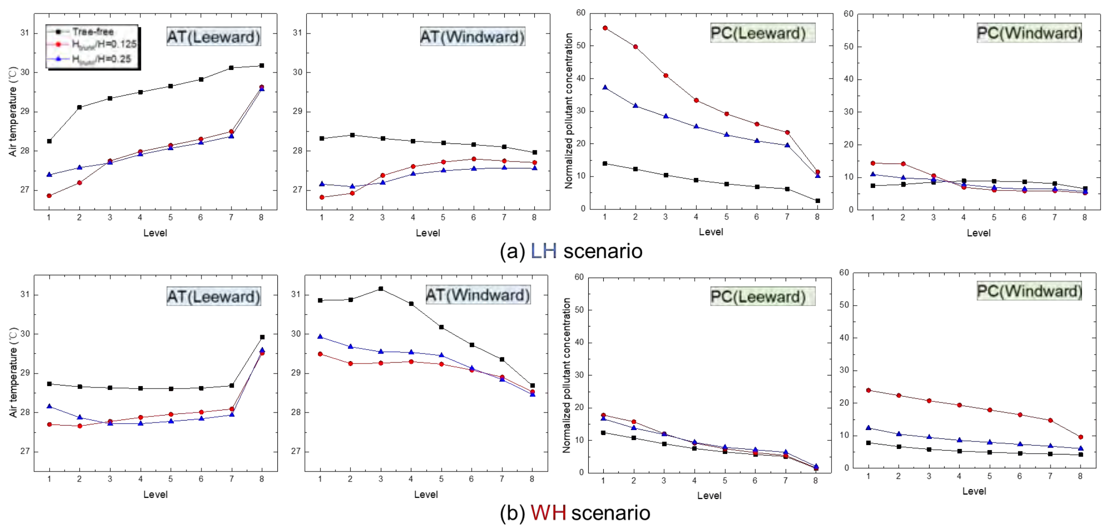

Figure 5.12 Vertical profiles of air temperature (AT) and pollutant concentration (PC) close to both leeward surface and windward surface for various H_{trunk} under (a) Leeward heating scenario (0900) and (b) Windward heating scenario (1500)

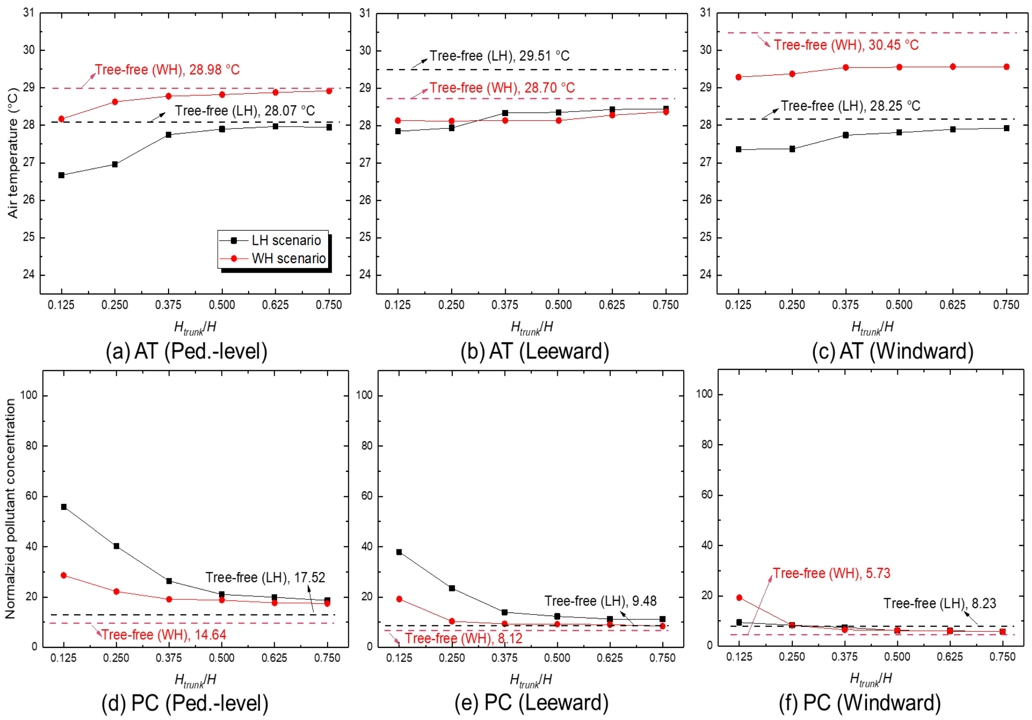

Figure 5.13 Profiles of average air temperature (AT) of (a) pedestrian level, (b) leeward side, and (c) windward side, and average pollutant concentration (PC) of (d) pedestrian level, (e) leeward side, and (f) windward side with various H_{trunk} (H_{trunk}/H from 1/8 to 3/4)

5.4.4 Effects of the tree spacing

In this section, we will study the effects of tree spacing. When varying the tree spacing ($W_{spacing}/W_{crown}$ ranges from 0 to 4), all other dependent parameters (i.e., the LAD (= 1) and trunk height (H_{trunk}/H = 0.25)) are kept constant.

First, the influence of tree spacing is discussed at the pedestrian level. The comparison of tree-free cases and the case of $W_{spacing}/W_{crown}$ = 0 has been discussed above. As seen in Figure 5.14 (a), the increased tree spacing ($W_{spacing}/W_{crown}$ increase from 0 to 1) significantly improves the ventilation, particularly under the LH scenario. Besides, under the LH scenario, the increased tree spacing further makes the stagnant flow region disappear. This is because that the spacing between trees can not hinder the airflow caused by the top entrainment. However, based on a similar reason for trunk height, larger tree spacing results in a relatively weaker cooling effect at the pedestrian level. Moreover, a larger tree spacing promotes pollutant dispersion out of the street canyon. Thus, compared with the tree-free case, the case of $W_{spacing}/W_{crown}$ = 1 almost does not increase the pollutant concentration at the pedestrian level.

Second, the influence of tree spacing is discussed close to the two-side surfaces. As shown in Figure 5.15, the increased tree spacing reduces the cooling effect on the entire vertical distribution of air temperature for both leeward and windward surfaces. Nevertheless, the tree planting with $W_{spacing}/W_{crown}$ = 1 still has a better thermal environment compared to the tree-free case. Moreover, the increased tree spacing largely reduces the accumulation of pollutants on both surfaces. Even for the leeward side under the LH scenario, the presence of trees only causes an approximately 30% increase in K_{lee} compared with the tree-free counterpart.

Third, a larger variation of tree spacing ($W_{spacing}/W_{canopy}$ ranges from 0 to 4) is discussed. Under a larger change in tree spacing, the same trends can be observed in Figure 5.16. Generally, an increase in $W_{spacing}/W_{canopy}$ causes a weaker cooling effect when $W_{spacing}/W_{canopy} \leq 2$. Once $W_{spacing}/W_{canopy}$ is over 2, the cooling effect almost does not change. Nonetheless, even the largest tree spacing ($W_{spacing}/W_{canopy} = 4$) still can effectively decrease the air temperature close to the heated surface by up to 1℃. Similarly, an increase in $W_{spacing}/W_{canopy}$ causes a significant improvement of air quality when $W_{spacing}/W_{canopy} \leq 2$. Once $W_{spacing}/W_{canopy}$ is over 2, the presence of trees does not worsen the air quality compared with the tree-free case. Therefore, larger tree spacing ($W_{spacing}/W_{canopy} > 2$) is advocated to improve the urban environment by tree planting.

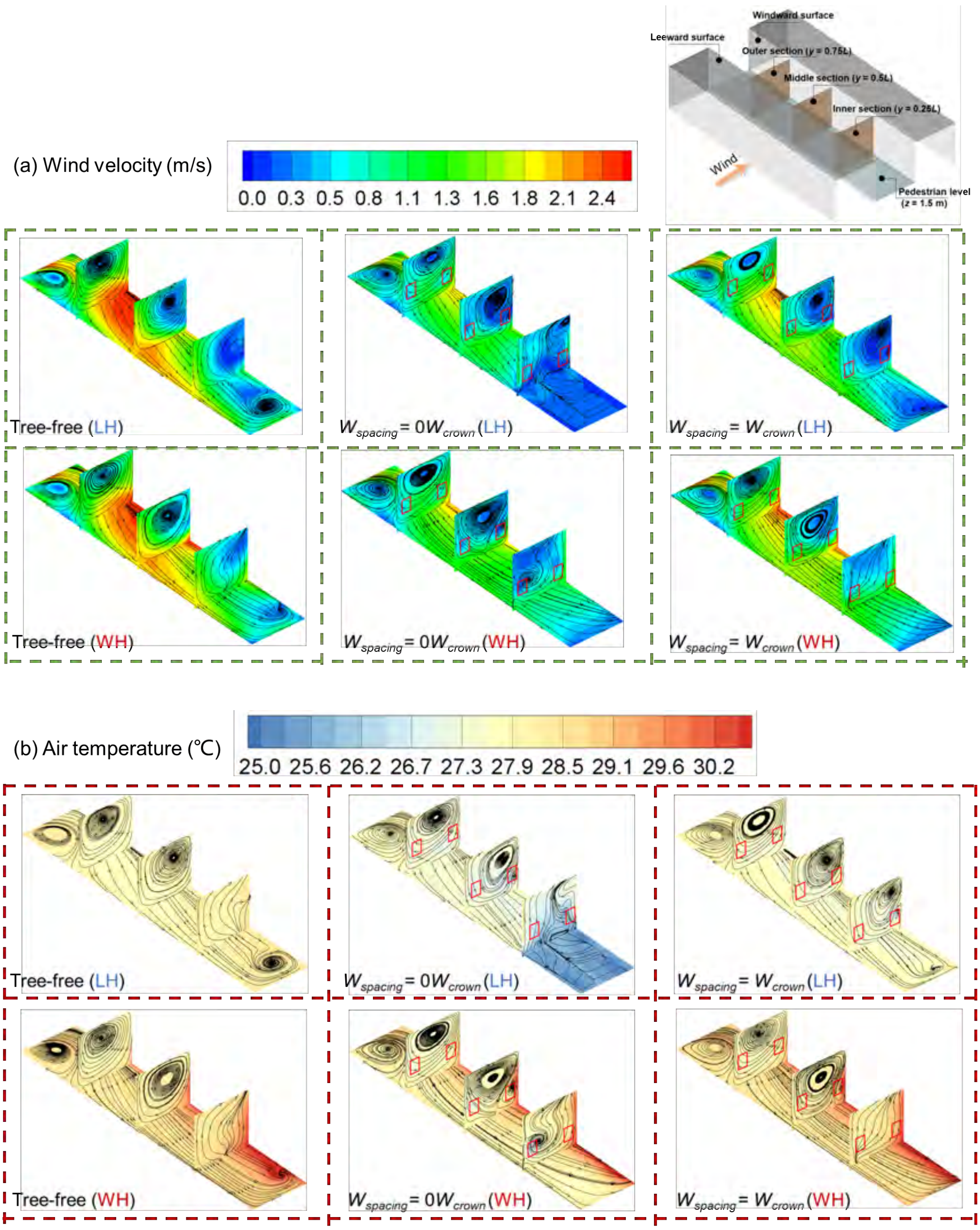
Windward surface
Leeward surface
Outer section (y = 0.75L)
Middle section (y = 0.5L)
Inner section (y = 0.25L)
Pedestrian level (z = 1.5 m)
Wind
(a) Wind velocity (m/s)
0.0 0.3 0.5 0.8 1.1 1.3 1.6 1.8 2.1 2.4
Tree-free (LH)
$W_{spacing}$ = 0W_{crown} (LH)
$W_{spacing}$ = W_{crown} (LH)
Tree-free (WH)
$W_{spacing}$ = 0W_{crown} (WH)
$W_{spacing}$ = W_{crown} (WH)
(b) Air temperature (℃)
25.0 25.6 26.2 26.7 27.3 27.9 28.5 29.1 29.6 30.2
Tree-free (LH)
$W_{spacing}$ = 0W_{crown} (LH)
$W_{spacing}$ = W_{crown} (LH)
Tree-free (WH)
$W_{spacing}$ = 0W_{crown} (WH)
$W_{spacing}$ = W_{crown} (WH)

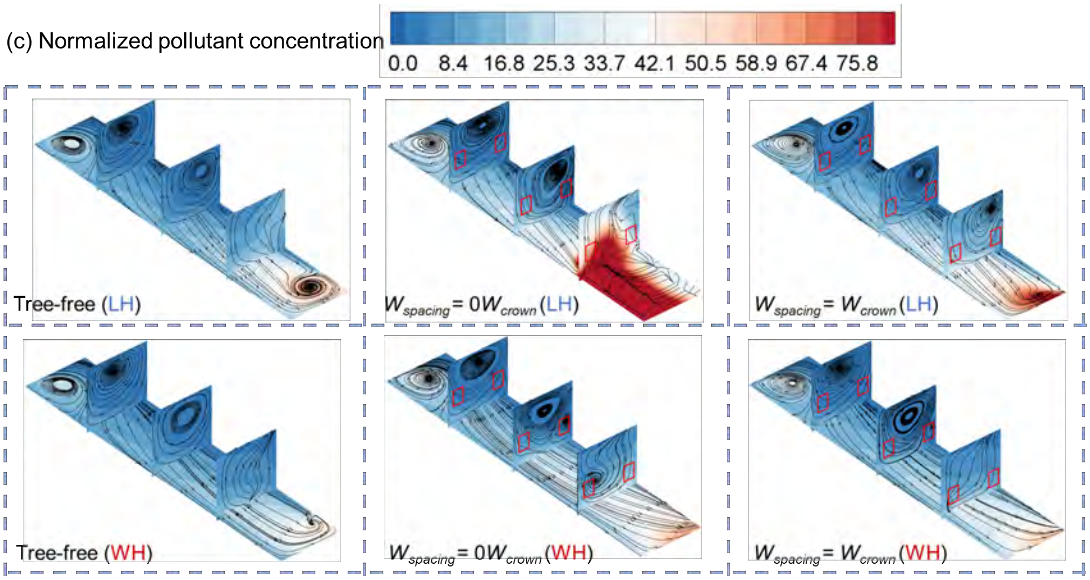

Figure 5.14 Predicted contours for various tree spacing with the street canyon: (a) Wind velocity, (b) Air temperature, and (c) Pollutant concentration

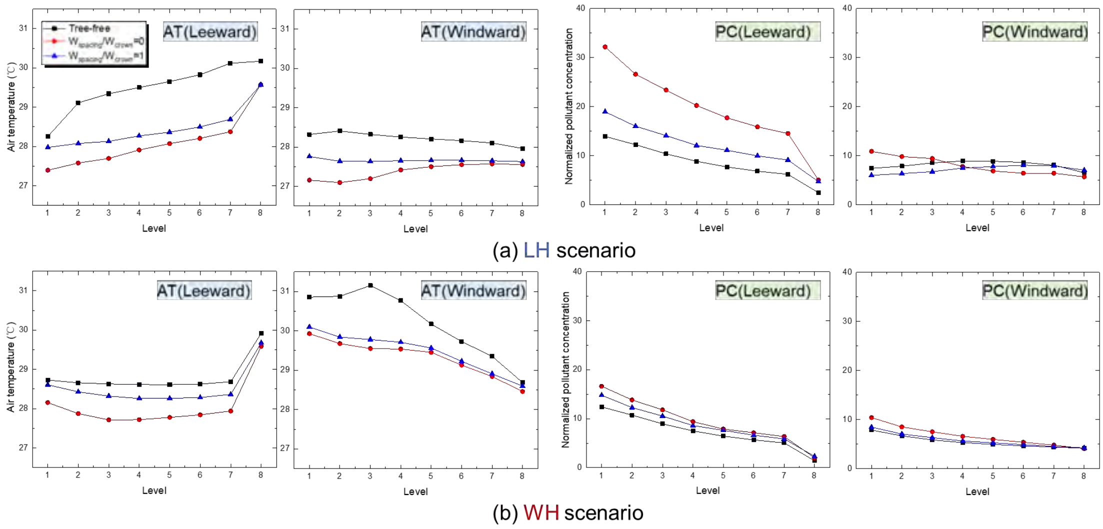

Figure 5.15 Vertical profiles of air temperature (AT) and pollutant concentration (PC) close to both leeward surface and windward surface for various $W_{spacing}$ under (a) Leeward heating scenario (0900) and (b) Windward heating scenario (1500)

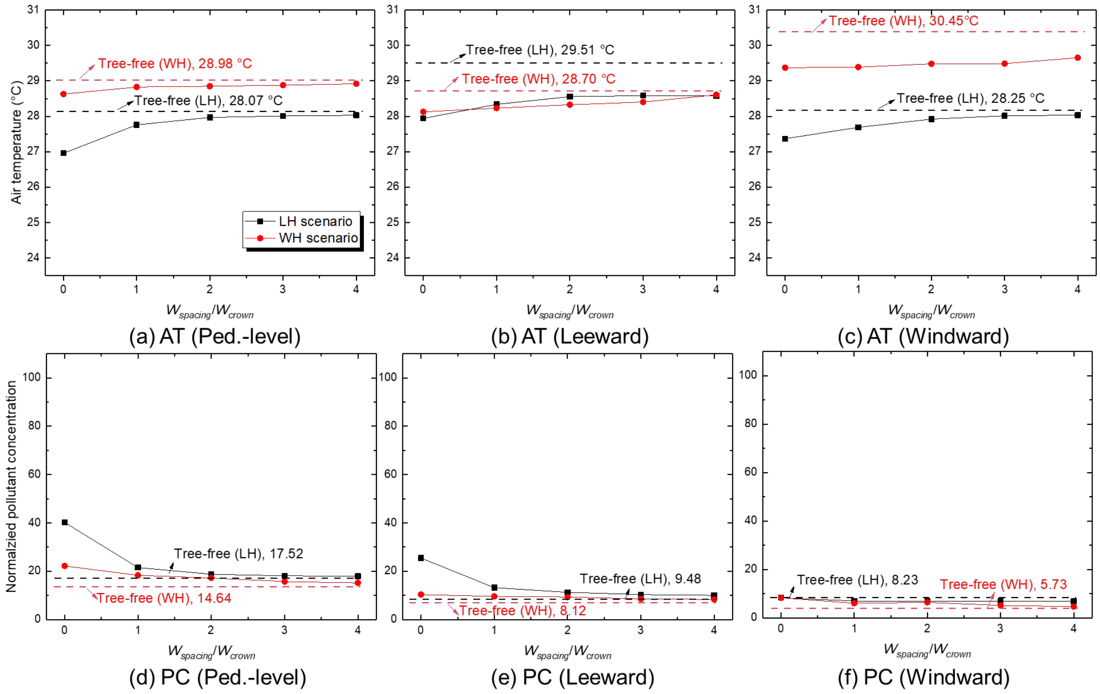

Figure 5.16 Profiles of average air temperature (AT) of (a) pedestrian level, (b) leeward side, and (c) windward side, and average pollutant concentration (PC) of (d) pedestrian level, (e) leeward side, and (f) windward side with various $W_{spacing}$ ($W_{spacing}$ /W from 0 to 4)

5.5 Discussion

5.5.1 Effect of relative humidity

Higher vapor pressure deficit D due to lower RH can result in a stronger cooling effect, which probably affects the distribution of in-canyon pollutant concentration. Thus, this section attempts to investigate the influence of trees under low RH conditions (= 50 %).

First, compared to the high RH, the increasing LAD under the low RH results in a greater reduction of air temperature, particularly at the pedestrian level (over 7 °C), due to a more significant cooling effect (Figure 5.17 (a)). However, this stronger cooling effect certainly causes a more stagnant flow region, which also occupies a larger space near the ground level. Hence, the increasing LAD results in a more significant accumulation of pollutants. Besides, it is noteworthy that the trees with LAD = 1 under low RH have a similar cooling effect for cooling the in-canyon air temperature with that of LAD = 2 under high RH, especially for the two-side building surfaces. However, the trees with LAD = 1 under low RH cause a better in-canyon air quality than that of LAD = 2 under high RH due to lower flow resistance. Hence, under low RH, the trees with a lower LAD are advocated.

Second, when $H_{trunk}/H \geq 0.375$, the change of RH has fewer effects under the WH scenario (Figure 5.17 (b)). Furthermore, when $H_{trunk}/H \geq 0.625$, the variation of RH has a slight influence on the in-canyon pollutant concentration and air temperature under both LH and WH scenarios. Hence, the influence of RH should be taken into consideration for a lower trunk height.

Third, when $W_{spacing}/W_{canopy} \geq 1$, a decrease in RH hardly reduces air temperature or increase pollutant concentration under both LH and WH scenario (Figure 5.17 (c)). In other words, for sparse tree coverage, the influence of RH on the in-canyon pollutant concentration and thermal environment can be ignored.

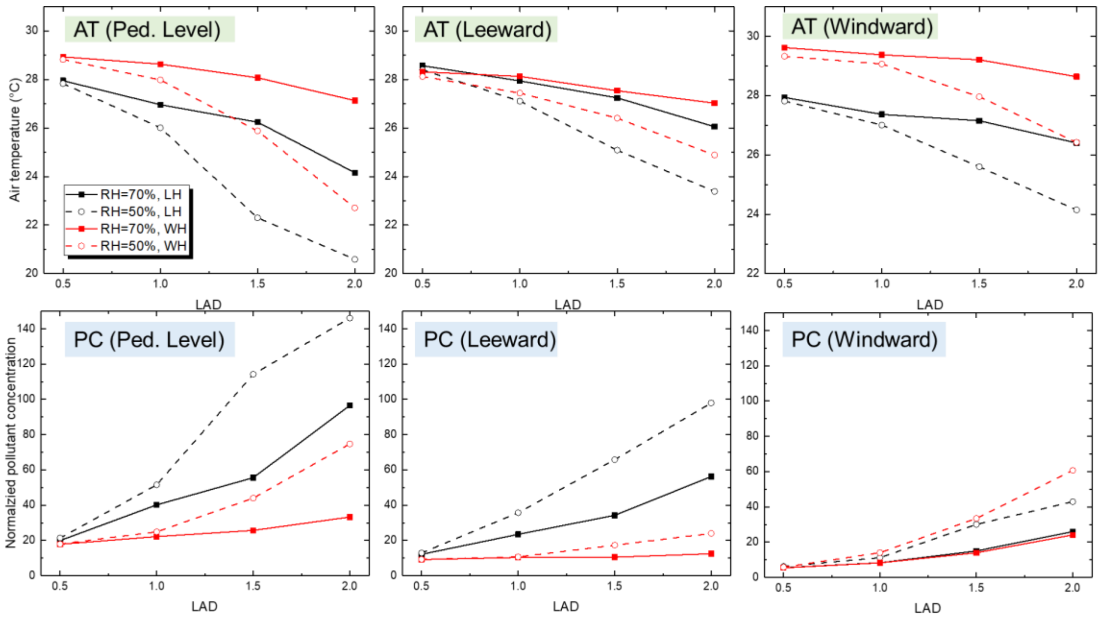

(a) Different LAD

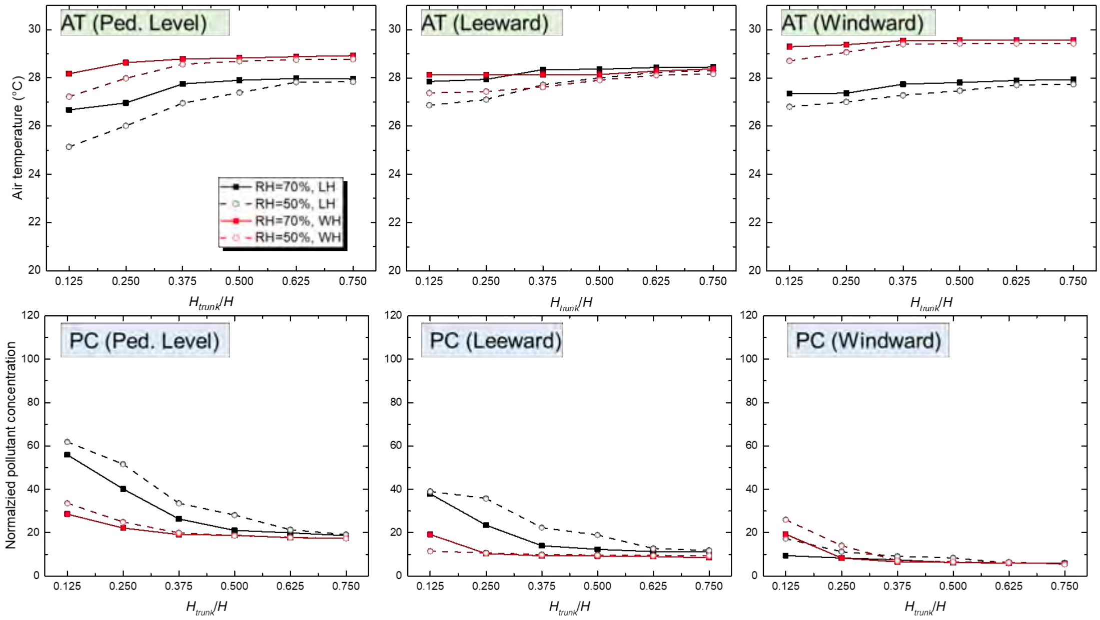

(b) Different H_{trunk}

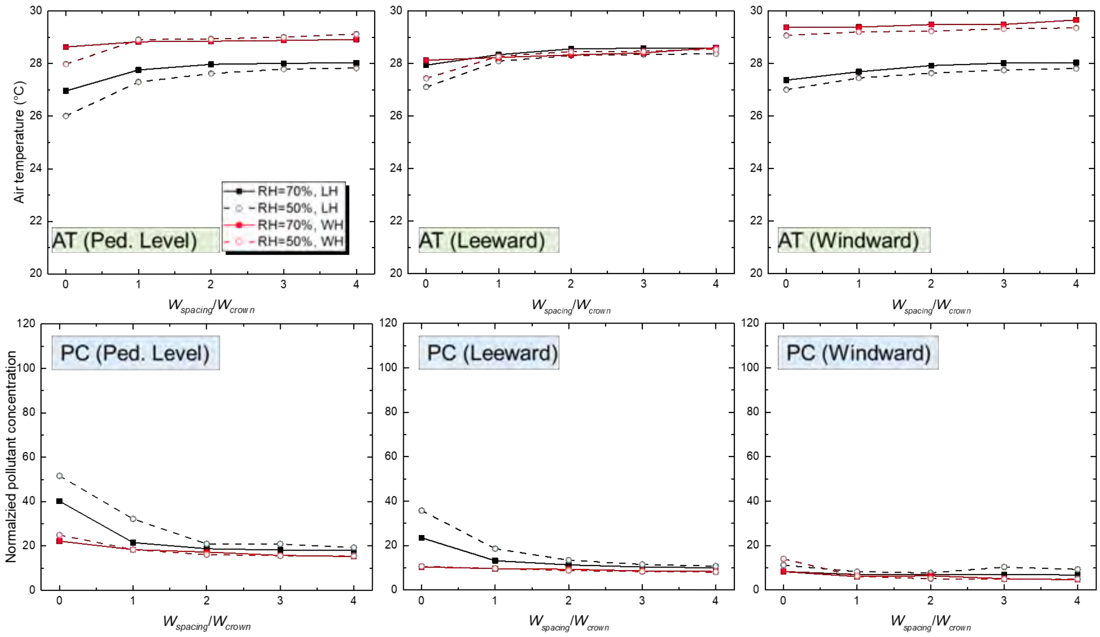

(c) Different $W_{spacing}$

Figure 5.17 Average air temperature (AT) and pollutant concentration (PC) of pedestrian level, leeward side, and windward side under low RH (= 50%) and high RH (= 70%) for various (a) LAD, (b) H_{trunk} and (c) $W_{spacing}$

5.6 Summary

This chapter has presented numerical simulations to simultaneously investigate the impact of trees on the outdoor thermal environment jointly with outdoor air quality within a street canyon under the perpendicular wind on a clear summer day. Hereafter, these two aspects can be evaluated under the same framework, hopefully, to provide some clues to find out whether trees can potentially contribute to the urban environment. Besides, several parameters directly associated with the influence of on-street trees are taken into account to propose some general guidelines for urban tree plantings, including three characteristics of tree canopy (leaf area density (LAD), trunk height (H_{trunk}/H), and tree spacing ($W_{spacing}/W_{crown}$)). Besides, all the simulations are conducted under both leeward heating (LH) and windward heating (WH) scenarios. Moreover, the simulations are based on grid-sensitivity analysis and validation of the CFD results from the literature. The major results are summarized as follows:

(1) Both aerodynamic effect (AE) and cooling effect (CE) of trees largely alter the outdoor thermal environment and air quality, especially for the LH scenario. However, these two effects play different roles in determining in-canyon air temperature and pollutant concentrations. In terms of trees with LAD =1, H_{trunk}/H = 0.25, and $W_{spacing}/W_{crown}$ = 0, the AE of trees can effectively slow the airflow through the tree crown down without changing the flow structure within street canyons, which leads to at most a 0.2 °C increase in T_{ped} and up to a 38% increase in K_{ped} compared with the tree-free counterpart. In contrast, the CE of trees creates an inversion layer around the position of the tree canopy, thus inducing a negative buoyancy force and competing with the buoyancy force due to solar radiation. Therefore, the CE of trees also causes poor ventilation, which results in up to 0.4 °C reductions in T_{ped} and up to 54% increase in K_{ped}. Considering the AE and CE at the same time, the presence of trees causes a more significant reduction of T_{ped} (up to 1.1 °C) and an increase of K_{ped} (up to 210%).

(2) Increasing LAD (from 0.5 to 2) results in a significant reduction of average air temperature by up to 1.5 °C for all positions (two-side surfaces and pedestrian level) under both LH and WH scenarios. This increased LAD unavoidably causes a worse air quality, especially under the LH scenario. This is because a higher LAD has a stronger cooling effect but a larger flow resistance. Therefore, the trees with low LAD (= 0.5) are suggested since they hardly worsen the air quality but still induce a 0.5–1 °C reduction in air temperature.

(3) An increase in H_{trunk}/H from 0.125 to 0.75 causes a weaker cooling effect but a lower pollutant concentration. This is because the lift-up tree canopy makes the lateral entrainment more easily penetrate into the inner of the street canyon, contributing to pollutant dispersion, while the cooling airflow through the tree canopy is not easy to penetrate into the lower space anymore with the lifted location of the canopy. Interestingly, when the H_{trunk}/H is over 0.375, increased trunk height causes a minor change in air temperature and pollutant concentration. However, it should be noted that, compared to the tree-free case, even the highest tree canopy causes up to nearly 1.5 ℃ reductions on two-side surfaces, especially for the surface directly heated by the solar radiation. Hence, higher trunk height ($H_{trunk}/H > 0.375$) is advocated.

(4) Increasing $W_{spacing}/W_{canopy}$ from 0 to 4 causes a higher in-canyon air temperature and a lower pollutant concentration under both LH and WH scenarios. The increase in air temperature is attributed to a weaker cooling effect due to less tree coverage. However, larger spacing between trees allows more fresh air to vertically penetrate into the lower space of the street canyon, which helps to improve pollutant dispersion. When the $W_{spacing}/W_{canopy} \geq 2$, increased tree spacing causes a minor change in air temperature and pollutant concentration. Similar to the trunk height, even the largest tree spacing ($W_{spacing}/W_{canopy} = 4$) still can effectively decrease the air temperature close to the heated surface by up to 1℃. Accordingly, larger tree spacing ($W_{spacing}/W_{canopy} \geq 2$) is recommended.

Despite the obtained findings, the present study had several limitations. First, only the simplified tree canopy is considered to evaluate the influence of tree planting. An identical LAD is assumed for the entire tree crown. In effect, the tree crown should have a change in the vertical direction. Hence, the vertical distribution of LAD will be considered in the future. Second, only the aerodynamic and cooling effects induced by trees are taken into account since the present study mainly focuses on passive gaseous pollutants. The deposition effect (the deposition of pollutants onto leaf surfaces) caused by trees should be investigated, in terms of particulate matters (PMs). Third, only a high RH is assumed for the study because this study attempts to provide some suggestions of tree planting for the tropics and subtropics cities, such as Hong Kong. There is high

RH in these cities in summer. As discussed above, a different RH will result in a different vapor pressure deficit, which therefore affects the cooling efficiency of trees. Accordingly, a more universal conclusion can be drawn when a larger range of RH is considered in the future.

Chapter 6 Effects of lateral entrainment on pollutant dispersion inside a street canyon and the corresponding optimal urban design strategies

6.1 Introduction

In most of the previous studies dealing with pollutant dispersion in canyons, the length of the street canyon has been assumed to be infinite when the ambient wind was perpendicular to the street axis [29,174–176]. Consequently, the flow structure is mainly influenced by the top entrainment at the roof level of the infinite-long street canyon. From the building roof, the fresh air is entrained into the street canyon to form a clockwise recirculation with a horizontal (spanwise) axis (canyon vortex), which occupies the entire space of the street canyon [177]. In effect, the length of the street canyon is finite [178,179]; thus, the lateral entrainment exists at the street ends. The 2D simulations that consider only the top entrainment could not completely reflect the flow topology and pollutant dispersion processes in the entire street canyon [180]. At the same time, the influence of lateral entrainment on the pollutant dispersion inside the street canyon has been confirmed in early studies. In a finite-long 3D street canyon, as seen in Figure 6.1, the canyon vortex caused by the top entrainment usually appears nearby the center-plane of the street canyon [145]. However, at the ends of the street of a regular street canyon with $H/W = 1$, Hunter et al. [181] and Leitl and Meroney [182] found that there are double-eddy circulations (corner vortexes) with a vertical axis, entraining fresh air from the lateral shear layer (Figure 6.1). Accordingly, the developed flow regime consists of a canyon vortex (caused by top entrainment) in the inner area and of two corner vortices (caused by lateral entrainment) at the street ends [183,184].

In general, few previous studies are aware of the importance of lateral entrainment on the pollutant dispersion within street canyons, especially for the deep street canyon. Indeed, the distribution of pollutants inside canyons can be very sensitive to lateral entrainment. Moreover, so far, the quantitative analysis of the influence of lateral entrainment is rare. Besides, previous studies have not determined how to effectively utilize lateral entrainment to improve the air quality within the urban canopy. All these impose the need for investigating the effects of lateral entrainment on pollutant dispersion inside a street canyon and the corresponding optimal urban design strategies.

Given this background, the objectives of this chapter are (1) to elucidate the mechanisms for how lateral entrainment affects the pollutant concentrations in the canyons with different geometries (different building heights and lengths), (2) to quantify the influence of lateral entrainment on the reduction of pollutant concentrations, for the canyons with different geometries (different building heights and lengths), compared with the infinite-long canyons alternative, and (3) to explore several optimal design strategies for improving the air quality within the street canyons by enhancing the lateral entrainment.

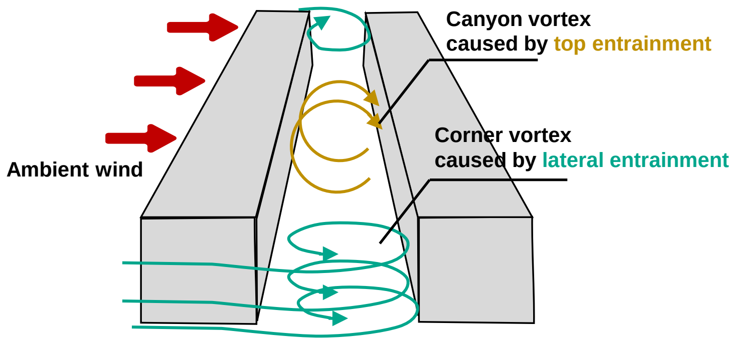

Figure 6.1 Schematic illustration of the canyon vortex caused by the top entrainment and corner vortex caused by the lateral entrainment within a 3-D regular street canyon (H/W = 1) and subjected to perpendicular approaching wind.

6.2 Description of wind tunnel experiments for CFD validation

The current computational model to reproduce the flow and concentration fields within street canyons is justified by a wind tunnel experiment conducted earlier at the Laboratory of Building and Environmental Aerodynamics, University of Karlsruhe [172,173]. The wind tunnel had a test section of 2 m long, 2 m wide, and 1 m high (Figure 6.2(a)), in which a scaled model (1:150) of a three-dimensional isolated street canyon constructed by two parallel model-buildings with the dimension of $H \times W_b \times L$= 0.12 m × 0.12 m × 1.2 m (Figure 6.2(b)) was tested. Meanwhile, the street width W

is equal to the building width W_b. This isolated street canyon was simulated in a neutral atmospheric boundary layer (ABL) by using the vortex generators and a 5m long fetch covered with roughness elements (Figure 6.2(a)). This combination produced a simulated boundary layer with a power-law exponent α of 0.30 and a friction velocity u^*_{ABL} of 0.52 m/s. The mean streamwise velocity profile of the approaching flow in the upstream can be approximated by using the following power-law form,

$$U(z) = U_{ref} \times (z / H)^{0.3} \tag{6.1}$$

where U_{ref} = 4.7 m/s is the reference velocity of the incoming flow at $z = H$ with a Reynolds number of approximately 37,600, based on the building height H and the reference velocity U_{ref}. Besides, Sulfur hexafluoride (SF6) was used as a tracer gas for simulating the release of traffic exhaust fumes and was emitted homogenously by four-line sources mounted at the bottom of the model. To account for the traffic exhaust fumes released on the street intersections, each line source exceeded the street canyon by approximately 10% on each side. For more information related to the wind tunnel experiments, the reader is referred to [172,173]. Besides, it should be mentioned that the aforementioned wind tunnel experiment mainly offers concentration data within street canyons, including the canyon with trees and the canyon without trees. Herein, the free-tree case is chosen for the validation study.

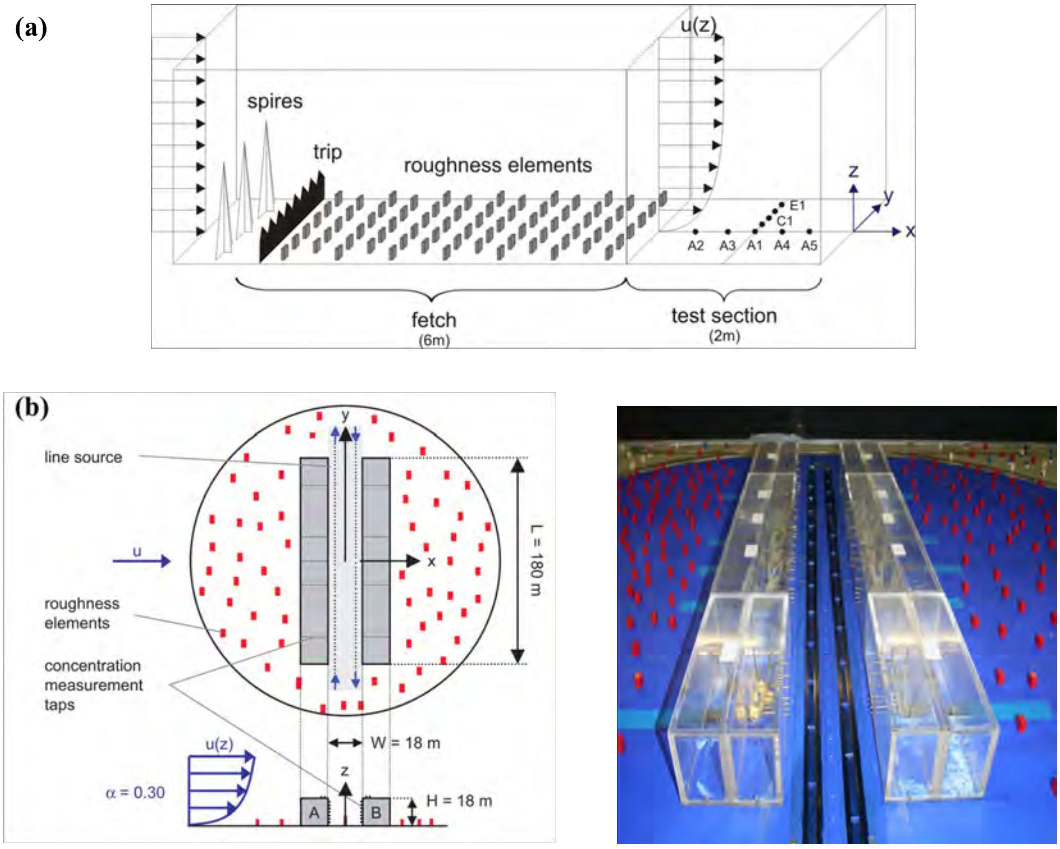

Figure 6.2 Schematics of (a) test section of the wind tunnel, and (b) wind tunnel model of the urban street canyon (scale 1:150) [172,173]

6.3 Description of CFD simulations

6.3.1 Description of case studies, computational geometry, and grid

The street canyon configurations used in this chapter are constructed based on the scaled model (1:150) of an isolated street canyon adopted in the wind tunnel experiment mentioned above. Besides the configuration studied by the wind tunnel experiment, seven more configurations with various height and length aspect ratios, which are defined as H/W (= 1 and 3) and L/W (= 1, 5, 10, and ∞), are considered to investigate the effects of the lateral entrainment (Figure 6.3(b)). These eight street canyons are first divided into two groups according to the aspect ratio of the building height to the street width (H/W), namely, the low-rise street canyons (H/W = 1) and high-rise street canyons (H/W = 3). Additionally, in each group, four aspect ratios of the building length to the street width (L/W) were considered, namely, the short street canyon (L/W = 1), the medium street canyon (L/W = 5), the long street canyon (L/W = 10), and the infinite-long street canyon ($L/W = \infty$), according to the classification of Oke et al. [185].

The size and discretization of the computational domain are referred from the practice guidelines by Tominaga et al. [97]. Thus, as shown in Figure 6.3 (a), the distances between the building and the inlet boundary, lateral boundaries, top boundary, and outflow boundary were 5 H, 5 H, 5 H, and 15 H, respectively. The computational domain was discretized into approximately 2.8 million hexahedral cells for the low-rise medium street canyon (H/W = 1 and L/W = 5). Considering the relatively large gradients of the velocity near the ground and building surfaces, the finest grids were deployed around these two types of walls. In this chapter, a grid-sensitivity analysis was performed based on two additional grids: a coarser grid and a finer grid for the low-rise medium street canyon case. For the coarse, basic, and fine grids, the minimum sizes were set to be 0.006 m, 0.003 m, and 0.0015 m, respectively. The total cell numbers for the coarse, basic, and fine grids are 0.74 million, 2.83 million, and 9.66 million, respectively. Therefore, the ratios of the two consecutive cell numbers for the grid refinement meet the criterion of 3.4 in the mesh-independent study [97]. Then, the results of grid-sensitivity analysis discussed in Section 6.3.5 indicate that the basic grid provides nearly grid-independent results, which can be further used for the remainder of this chapter.

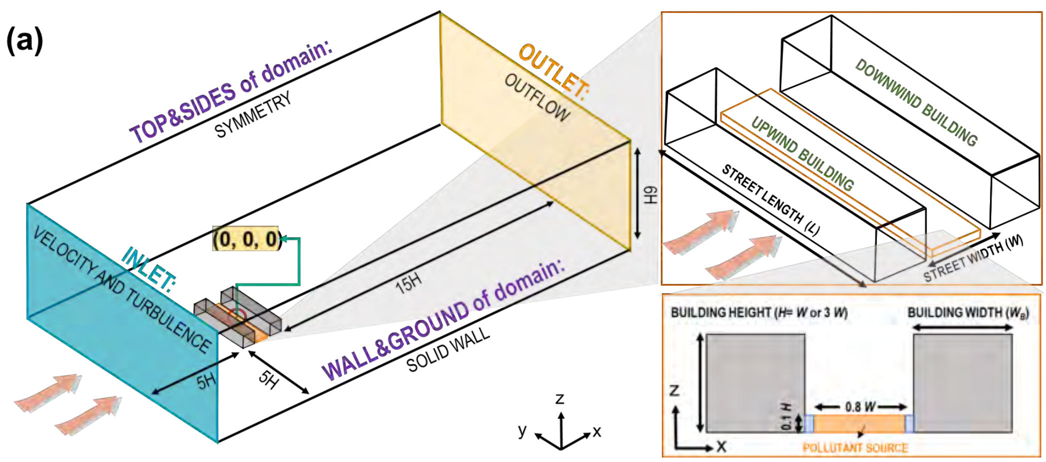

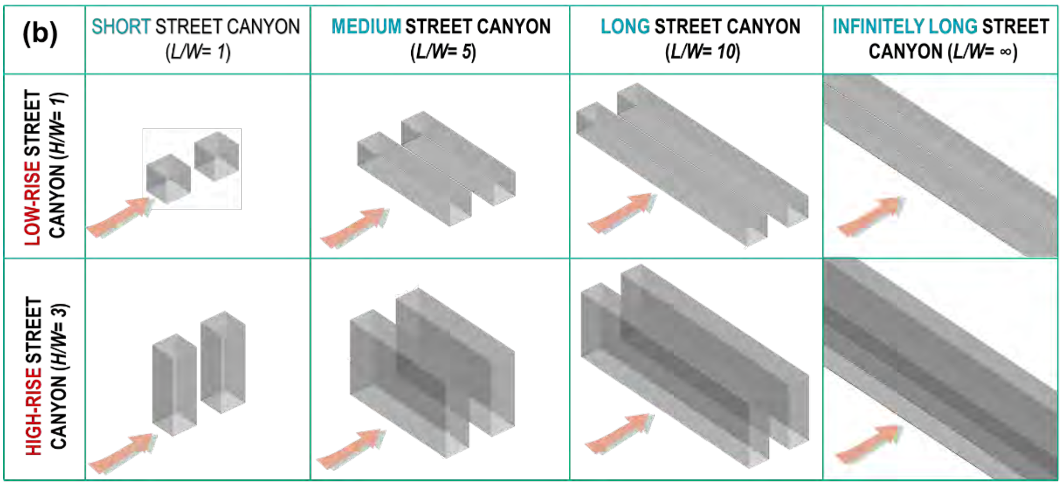

Figure 6.3 (a) Computational geometry and boundary conditions; (b) 3D street canyon configuration with for high-rise and low-rise street canyons

6.3.2 Governing equation and turbulence model

The analyses are based on the steady-state 3D RANS conservation equations of mass and momentum for the incompressible turbulent flow. The governing equations are as follows:

Continuity equation:

$$\frac{\partial u_i}{\partial x_i} = 0 \tag{6.2}$$

Momentum equation:

$$\frac{\partial u_i u_j}{\partial x_j} = -\frac{1}{\rho}\left(\frac{\partial p}{\partial x_i}\right) + \frac{\partial \tau_{ij}}{\partial x_j} \tag{6.3}$$

where the stress tensor τ_{ij} is defined as:

$$\tau_{ij} = \rho\left[\nu_t\left(\frac{\partial u_i}{\partial x_j} + \frac{\partial u_j}{\partial x_i}\right)\right] - \frac{2}{3}\rho k \delta_{ij} \tag{6.4}$$

where the term u_i denotes the i-axis component of the air velocity; p and ρ represent the pressure and density; ν_t is the turbulent kinematic viscosity; δ_{ij} is the Kronecker delta; k is the turbulence kinetic energy.

The species transport equation is solved to probe the pollutant dispersion in an urban environment, as follows:

$$\frac{\partial u_i Y}{\partial x_i} - \frac{\partial}{\partial x_i}\left[\left(D + D_t\right)\frac{\partial Y}{\partial x_i}\right] = S_p \tag{6.5}$$

where S_p is the pollutant source term (kg/(m^3·s)); D and D_t (= ν_t/Sc_t) denote the molecular and turbulent diffusion coefficients of the pollutant, respectively. Sc_t is the turbulent Schmidt number, which is set to 0.4 to account for the underestimation of the turbulent mass diffusion from the RANS models [99,152]. Y is the mass fraction of the pollutants. This dispersion of pollutants is simulated with the User Defined Scalar (UDS) option in ANSYS/Fluent®.

Moreover, the renormalization group (RNG) k-ε model [186] is chosen because of its generally good performance in predicting the flow separation by buildings and reversed flow [187], which is essential for the analysis of lateral entrainment in this chapter. Also, the RNG k-ε model complements the disadvantage of a standard k-ε model, which overestimates turbulent kinetic energy near the edges of buildings where ambient flow impinges and separates [188]. Thus, the RNG k-ε model is used to solve this steady-state isothermal flow field. The conservation equations of the RNG k-ε turbulence model for the turbulence kinetic energy (k) and dissipation rate (ε) are as follows:

$$\frac{\partial u_j k}{\partial x_j} = \frac{\partial}{\partial x_j}\left(\frac{\nu_t}{\sigma_k}\frac{\partial k}{\partial x_j}\right) + P_k - \varepsilon \tag{6.6}$$

$$\frac{\partial u_j \varepsilon}{\partial x_j} = \frac{\partial}{\partial x_j}\left(\frac{\nu_t}{\sigma_\varepsilon}\frac{\partial \varepsilon}{\partial x_j}\right) + \frac{\varepsilon}{k}(C_{\varepsilon 1}^* P_k - C_{\varepsilon 2}\varepsilon) \tag{6.7}$$

In this equation, $P_k = \nu_t S^2$, $S = \sqrt{2S_{ij}S_{ij}}$, $S_{ij} = \frac{1}{2}\left(\frac{\partial u_i}{\partial x_j} + \frac{\partial u_j}{\partial x_i}\right)$, $\nu_t = C_\mu \frac{k^2}{\varepsilon}$, $\sigma_k = 1$,

$C_{\varepsilon 1}^* = 1.42 - \frac{\eta(1-\eta/4.38)}{1+0.012\eta^3}$, $\eta = \frac{k}{\varepsilon}S$, $C_{\varepsilon 2} = 1.68$, and $\sigma_\varepsilon = 0.719$.

6.3.3 Boundary conditions

The measured inlet velocity profile from the wind tunnel experiments [172], which is given in Eq. (6.1), is used to characterize a neutral ABL. The turbulent kinetic energy

k and turbulence dissipation rate ε profiles are calculated using Eqs. (6.8) and (6.9) [189]:

$$k = \frac{(u_{ABL}^{*})^{2}}{\sqrt{C_{\mu}}} \tag{6.8}$$

$$\varepsilon = \frac{(u_{ABL}^{*})^{3}}{\kappa(z+z_{0})} \tag{6.9}$$

where u_{ABL}^{*} is the ABL friction velocity (= 0.52 [m/s]), κ is the von Karman's constant (= 0.42), z_0 is the aerodynamic roughness (= 0.0015 [m]), and C_{μ} is the model constant (= 0.085).

Besides, as seen in Figure 6.3(a), the top and lateral boundaries of the domain are set as symmetry boundaries, namely setting normal velocity and normal gradients of all variables to zero. On the outlet of the domain, a zero diffusive flux is imposed for all flow variables in the direction normal to the outflow plane since the domain downstream is long enough to ensure a fully developed outlet flow. The standard wall functions by Launder and Spalding [190] with and without roughness modification by Cebeci and Bradshaw [191] are applied at the ground surface and building surface, respectively. To reduce horizontal inhomogeneity, the sand grain roughness height k_s is calculated by the roughness constant C_s (= 9.9) and the aerodynamic roughness z_0 (= 0.0015 m) in Eq. (6.10)[192].

$$k_{s} = \frac{9.793 z_{0}}{C_{s}} \tag{6.10}$$

Besides, CO is used as the pollutant representative. As shown in Figure 6.3(a), a uniform volume source (width W_p = 0.8 W and length L_p = street length L) of CO is specified near the ground with a depth of 0.1 H to represent the traffic lanes. The constant emission rate per hour and unit street length (36.1 [g/h/m], i.e., total mass release rate of $L_p \times 1.0 \times 10^{-5}$ [kg/s]) is adopted for each CO source.

6.3.4 Solver settings

The commercial software ANSYS/Fluent® CFD software (Release 15.0) [127] is used to simulate the airflow of ambient wind over this isolated street canyon. This chapter utilizes the pressure-linked equations-consistent (SIMPLEC) numerical method for the pressure-velocity coupling. The second-order upwind scheme [103] is used to discretize both the convective terms and the diffusion terms. A double-precision solver is also selected for the CFD calculations. The convergence criterion of the normalized residual errors is set to 10^{-6} for the governing equations.

6.3.5 Grid sensitivity analysis

Three types of meshes are tested for the low-rise medium canyon under the same environmental conditions (U_{ref} = 4.7 [m/s]). Figure 6.4 and Figure 6.5(a)-(c) depict a comparison of the results for the dimensionless streamwise mean velocity (u/U_{ref}) and dimensionless pollutant concentration (K) on the three grids along three vertical lines (x= -0.25H, 0, and 0.25H) in the vertical center plane at y/H = 0. Along these lines, the fine and the basic grid provide almost identical results, while some deviations are found between the coarse and the basic grid. Then, the grid convergence index (GCI) proposed by Roache [193] (Eqs. (6.11) and (6.12)) is used to estimate the error of u/U_{ref} and K on the basic grid.

$$GCI_u = F_s \left| \frac{r^p (u_{basic} - u_{fine}) / U_{ref}}{1 - r^p} \right| \tag{6.11}$$

$$GCI_K = F_s \left| \frac{r^p (K_{basic} - K_{fine}) / K_{fine}}{1 - r^p} \right| \tag{6.12}$$

where F_s is the safety factor taken as 1.25 when three or more grids are compared, r is the linear grid refinement (= $\sqrt{2}$), p is the former order of accuracy (= 2), u and K are streamwise mean velocity and normalized concentration in one of the two grids (basic and fine), and U_{ref} is the reference wind speed of 4.7 m/s. The values of the GCI_u averaged along each vertical line are 0.04% for x/H = -0.25, 0.06% for x/H = 0, and 0.08% for x/H = 0.25 (Figure 6.4(d)-(f)). Similarly, the values of the GCI_K averaged along each vertical line are 1.80% for x/H = -0.25, 1.85% for x/H = 0, and 4.04% for x/H = 0.25 (Figure 6.5(d)-(f)). By analyzing the discrepancy in wind speed and pollutant concentration of the three grids as well as comparing GCI values of the fine and basic grids, it can be concluded that the basic grid provides nearly grid-independent results, which can be further used for the remainder of this chapter. Besides, the near-wall area was resolved by the standard wall functions directly on the condition that the $y+$ of the first near-wall mesh for building surfaces and ground was 167.7 on average, which was in the log-law layer $30 < y+ < 300$ [127,136].

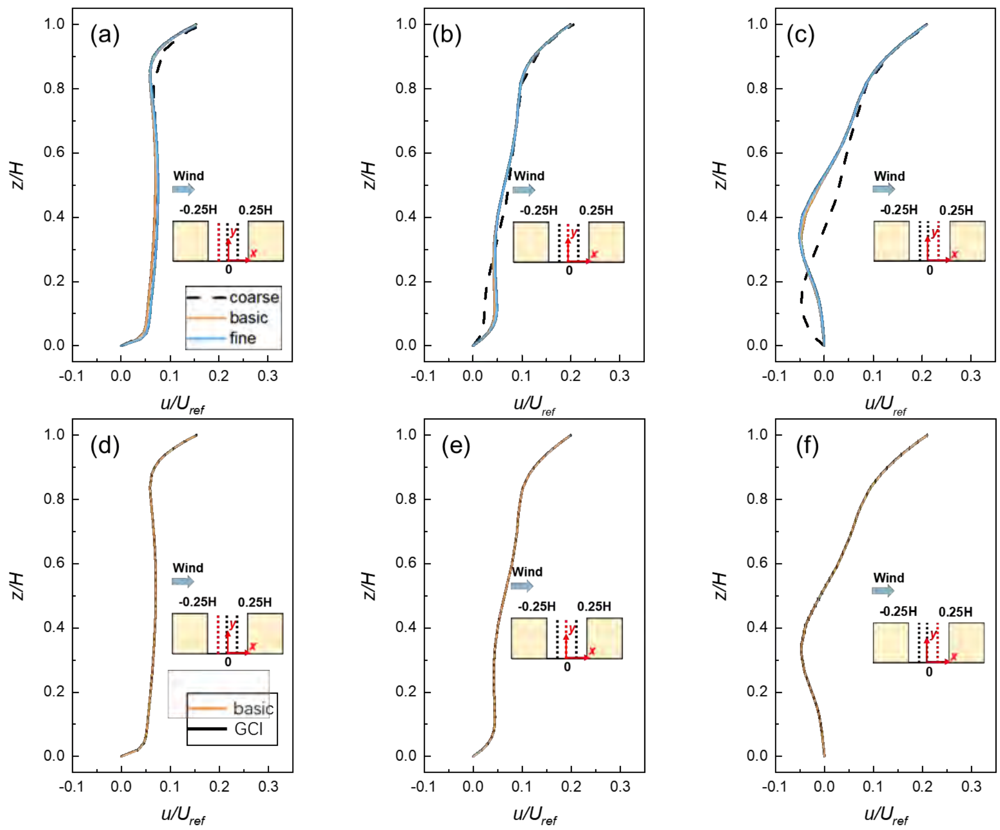

Figure 6.4 (a-c) Comparison of dimensionless streamwise mean velocity (u/U_{ref}) along three vertical lines inside the street canyon in the vertical center plane in coarse, basic, and fine grids; (d-f) grid-convergence index (GCI) along the same three vertical lines.

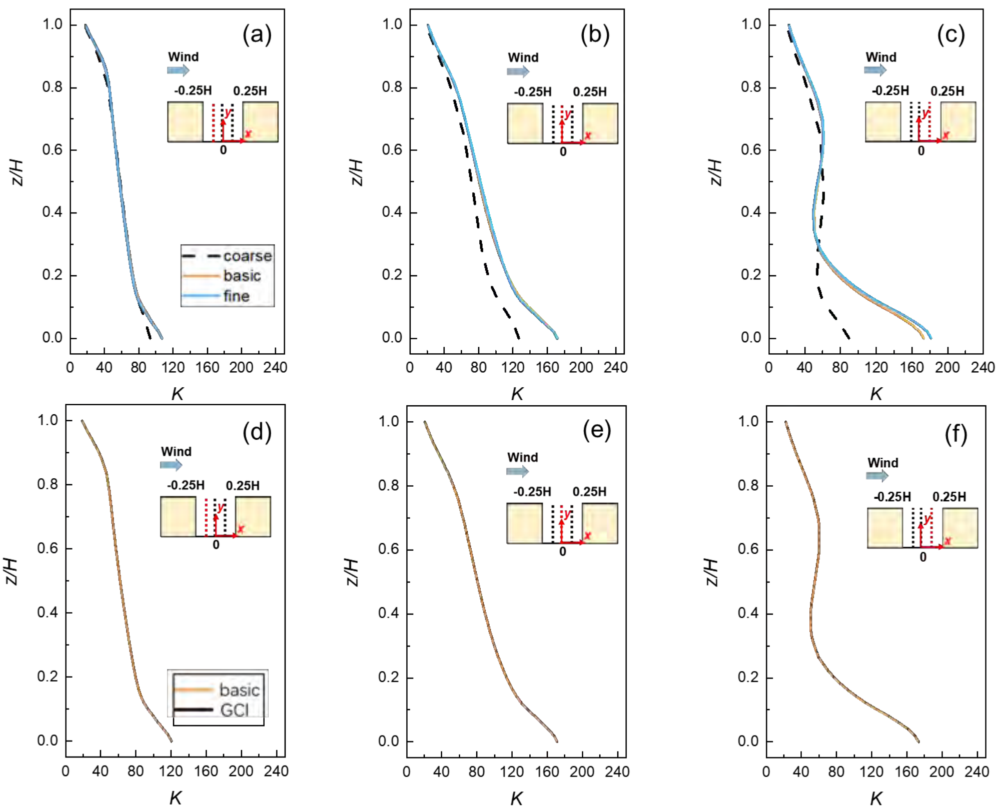

Figure 6.5 (a-c) Comparison of dimensionless pollutant concentration K along three vertical lines inside the street canyon in the vertical center plane in coarse, basic, and fine grids; (d-f) grid-convergence index (GCI) along the same three vertical lines.

6.4 Air quality indices

6.4.1 Average dimensionless pollutant concentration

The lateral entrainment can significantly affect the spanwise distribution of pollutant concentrations along the street length. Therefore, the pedestrian-level and cross-section average dimensionless pollutant concentrations are introduced to better evaluate the effects of the lateral entrainment.

The average dimensionless pollutant concentration at the pedestrian level (z = 1.5 m at full scale) along the street width is calculated by Eq. (6.13),

$$K_{ped} = \frac{\int_0^W Kdx}{W} \tag{6.13}$$

The cross-section average dimensionless pollutant concentration along the street length is calculated in Eq. (6.14),

$$K_{cross} = \frac{\int_0^W \int_0^H K dx dz}{W \times H}. \tag{6.14}$$

6.4.2 Personal intake fraction (*P_ IF*)

This chapter utilizes the personal intake fraction (*P_ IF*) as the air quality index, which stands for a fraction of the total traffic exhaust inhaled by each person on average, which is first introduced by Hang et al. [194] into CFD simulations to quantify the average personal exposure.

It is defined and calculated as follows:

$$P\_IF = \frac{\sum_i^N \sum_j^M P_i \times Br_{i,j} \times \Delta t_{i,j} \times Ce_j / m}{\sum_j^M P_i} \tag{6.15}$$

where N is the number of population groups (children, adults, elders, N = 3, i = 1 to 3), M is the number of different microenvironments (indoors at home, other indoor locations, near-vehicle locations, and other outdoor locations away from vehicles, M= 4, j= 1 to 4). Moreover, we assume the following: the near-road buildings are residential, and only a microenvironment of j= 1 (indoor at home) is considered to assess the personal intake fraction for the local residents. $Br_{i,j}$ and $\Delta t_{i,j}$ are the average volumetric breathing rate [m^3/s] [194] (Table A6.1) and time spent (s) for individuals in the ith population group in the jth microenvironment [7] (Figure A6.1(a)), respectively. P_i is the total number of people exposed in the ith population group, which can be further calculated by the demographic structure (herein, taking Shenzhen, China, as an example for this study [7], Figure A6.1(b)). Ce_j is the pollutant concentration in the jth microenvironment [kg/m^3], which could be calculated from the average concentration at each floor (3 m). In this instance, m is the total pollutant emissions (kg).

6.5 Validation study

Before validation study and case study, a simulation is conducted with an empty computational domain to check the achievement of the horizontal homogeneity of ABL, since it is a prerequisite to a reliable prediction of pollutant dispersion within street canyons [195]. First, the inlet boundary conditions of the CFD simulation based on the experimental data fit the inflow wind profile of the wind tunnel. Figure. A6.2 then shows a check of horizontal homogeneity for the present CFD simulation, which compares the dimensionless streamwise velocity and dimensionless turbulence kinetic energy of the inlet profile and incident profile (at the building position). The comparison indicates that the development of horizontal inhomogeneity is insignificant.

Besides, a solid model that included the street canyon (H/W = 1 and L/W = 10) is created by replicating the details of the geometrical shape from the wind tunnel experimental set-up of the tree-free case [172,173]. The computational domain is in line with the CFD set-up for the case study and pollutant sources are consistent with the wind tunnel setting. Moreover, the computational grid resolution results from a grid-sensitivity analysis, which yields a fully structured hexahedral grid with 4.68 million cells. Then, a cross-comparison of the dimensionless vertical velocity at the y/L = 0 and the dimensionless pollutant concentration at the walls of the street canyon between the numerical and experimental results is presented in Figure 6.6(a) and (b). The concentration value is calculated in the non-dimensional form as $C_{+} = CU_{ref}H/Q/l$, where C is the measured concentration (g/m^3), and Q/l is the tracer gas source strength per unit length (g/m/s). Generally, the experimental and numerical distributions of the dimensionless vertical wind speed are consistent (Figure 6.6 (a)). Only on the windward side, the RNG k-ε turbulence model predicts slightly higher flow velocities. Then, two Sc_ts (Sc_t = 0.4 and 0.7) are tested. As seen in Figure 6.6 (b), the predicted dimensionless concentrations are similar to those obtained in the wind tunnel for both Sc_t. Nevertheless, the numerical results agree better with the wind tunnel data when Sc_t = 0.4. The RNG k-ε model with Sc_t = 0.4 is consequently adopted for our CFD simulations.

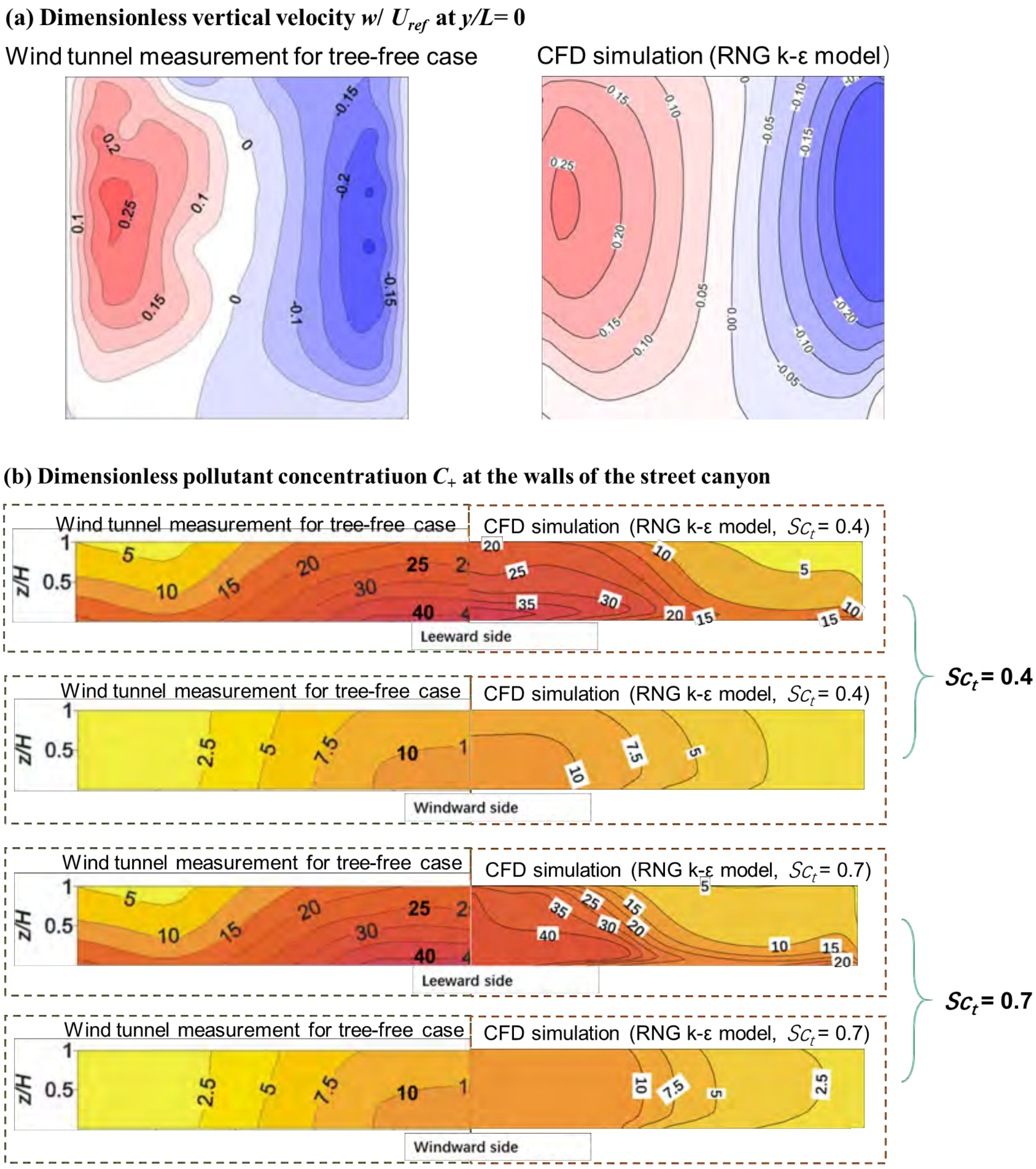

Figure 6.6 Comparison results of (a) dimensionless vertical velocity at y/L = 0, and (b) dimensionless pollutant concentration at the walls of the street canyon.

6.6 Results and discussion

6.6.1 Effects of the lateral entrainment

6.6.1.1 Low-rise street canyon (H/W= 1)

The effects of the lateral entrainment on the low-rise street canyons (H/W= 1) are explored in this section. Figure 6.7 and Figure 6.8 show the predicted dimensionless pollutant concentration K and dimensionless wind velocity (U/U_{ref}) contours for different street configurations at the pedestrian level and cross-section, respectively. To quantitatively estimate the effects, Figure 6.9 compares the average pollutant concentrations at the pedestrian level and at various cross-sections.

In a low-rise infinite-long street canyon (H/W= 1 and L/W= ∞), the flow structure within the canyon is affected only by the top entrainment at the roof level. Thus, as seen in Figure 6.8(a), the whole street canyon is occupied by the y-axis vortex. Evidently, this y-axis vortex in any cross-section of the infinite-long canyon would be identical, namely, a clockwise canyon vortex. Moreover, as evidenced in Figure 6.7(a) and Figure 6.8(a), there is relatively strong ventilation within this low-rise infinite-long street canyon since the top entrainment can readily penetrate into the ground level, thus leading to a lower dimensionless pollutant concentration at the pedestrian level (K< 66.5). In effect, in addition to the influence of the top entrainment, the airflow within the finite-long street canyon is also significantly affected by the lateral entrainment, which will be discussed later.

In a low-rise short street canyon (H/W= 1 and L/W= 1) in Figure 6.8(b), the flow structure (3D streamlines) is still mostly dominated by the y-axis vortex caused by the top entrainment, which is similar to the infinite-long street canyon in Figure 6.8(a). In contrast, the pedestrian level is occupied by the outward airflows (the along-street channeling flows toward the street ends) (Figure 6.7(b)). The possible reason is that the lateral entrainment causes a pair of corner vortices at the pedestrian level of the street ends. Following these corner vortices, the wind flows outward along the leeward side of the upwind building. As a result of this marked outward airflow, the maximum pedestrian level concentration is notably reduced by almost 65% (Figure 6.7(b)), and the average pedestrian level concentration decreases by 65-73% along the street length, as well (Fig. 10(a)), compared with the infinite-long street canyon. At the same time, as seen in Figure 6.8(b), the wind velocity is enhanced at all of the cross-sections. The upward transportation of the pollutants is also improved, which leads to a significant reduction in the concentration at all of the cross-sections. Figure 6.9(b) further confirms that the average cross-section concentration remarkably decreases by almost 73-77% along the street length due to the lateral entrainment.

In a low-rise medium street canyon (*H/W*= 1 and *L/W*= 5), there exist two evident corner vortices at the street ends (Figure 6.7(c)), although the 3D streamlines are still dominated by the *y*-axis vortex (Figure 6.8(c)). On the other hand, except for the region covered by the corner vortices, as shown in Figure 6.7(c), the whole pedestrian level is mainly occupied by the inward flows (along-street channeling flows toward the symmetry plane). In effect, these inward channeling flows can be attributed to the superposition of the canyon vortex (caused by the top entrainment) and the corner vortex (caused by the lateral entrainment). These inward channeling flows enhance the pedestrian level dimensionless wind velocity (up to nearly 0.1) and then transport the pollutants toward the symmetry plane (Figure 6.7(c)). Consequently, as seen in Figure 6.9(a), in almost 65% of the region of the street canyon, the concentrations significantly decrease, especially at the street ends (by up to 70%). However, the concentrations increase in the remaining 35% region of the street canyon near the symmetry plane (by up to 86%). This trend occurs because the accumulating pollutants in the canyon-center region caused by the inward channeling flow could not be dispersed upward effectively along with the canyon vortex, which is further confirmed in Figure 6.8(c). Clearly, the wind velocity in the most inner section of this medium street canyon is lower than that in the infinite-long case, thus leading to a significant increase in the pollutant concentration, especially near the ground. Therefore, Figure 6.9(b) reports that the cross-section average concentration declines by up to 78% from *y/L*= 0.17 to 0.5, while it increases by up to nearly 117% from *y/L*= 0 to 0.17.

In a low-rise long street canyon (*H/W*= 1 and *L/W*= 10), similar to the medium street canyon, the corner vortices and the inward channeling flow are clearly observed in Figure 6.7(d). In contrast, the inward channeling flow only penetrates approximately 2.5 times the street width from the street ends (Figure 6.7(d)). Furthermore, in the inner region of the canyon (from *y/L*= 0.3 to 0), the airflow is almost dominated by the *y*-axis vortex (canyon vortex), which is similar to the infinite-long street canyon (from the windward side of the downwind building to the leeward side of the upwind building). Accordingly, the pedestrian level dimensionless velocity is significantly enhanced by up to 0.17 from only *y/L*= 0.5 to 0.25, but it decreases by approximately 0.1 in the inner region of the canyons (Figure 6.7(d)), compared with the infinite-long street canyon. As a result, the average pedestrian level concentrations decrease by up to almost 78% in the outer region of the canyon, but it significantly increases in the inner region of the canyon, especially from *y/L*= 0.28 to 0 (even by almost 50%) (Figure 6.9(a)). On the other hand, as seen in Figure 6.8(d), a lower wind velocity is found in the inner three sections, which further deters the upward dispersion of the pollutants. Obviously, as shown in Figure 6.8(d) and Figure 6.9(b), the cross-section average concentration increases by up to 34%, from *y/L*= 0.27 to 0.

Overall, it is concluded that in the low-rise street canyon (*H*/*W*= 1), the lateral entrainment can partially improve the air quality, depending on the street length. This finding occurs because the positive effects of lateral entrainment on the pollutant concentration inside the street canyon are confined in a range of approximately 2.5 times the street width from the street ends (Figure 6.7(d)). Therefore, lateral entrainment is of great importance in reducing the pollutant concentration of the short and medium street canyon. However, the air quality of the low-rise long canyon could only be improved in the outer half of the street length by the lateral entrainment.

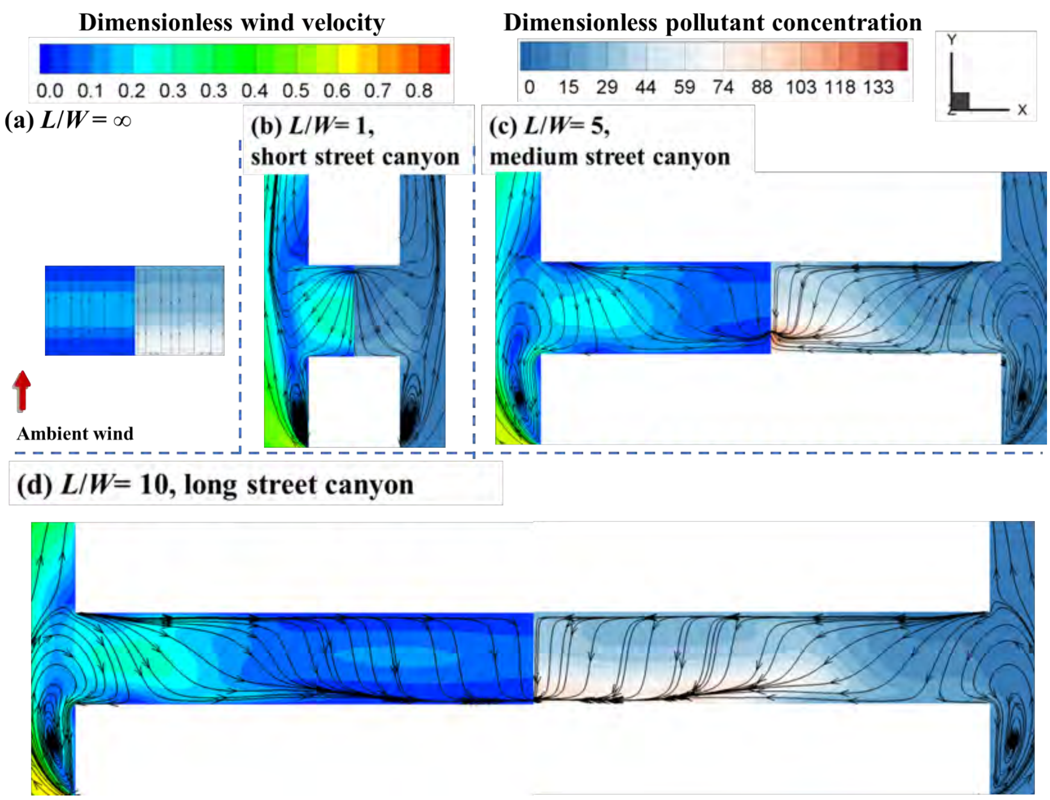

Figure 6.7 Predicted pedestrian level pollutant concentration contours, and pedestrian level wind velocity contours for the low-rise street canyons (*H/W*= 1) with various street lengths: (a) *L/W*= ∞, infinite-long street canyon, (b) *L/W*= 1, short street canyon, (c) *L/W*= 5, medium street canyon, and (d) *L/W*= 10, long street canyon.

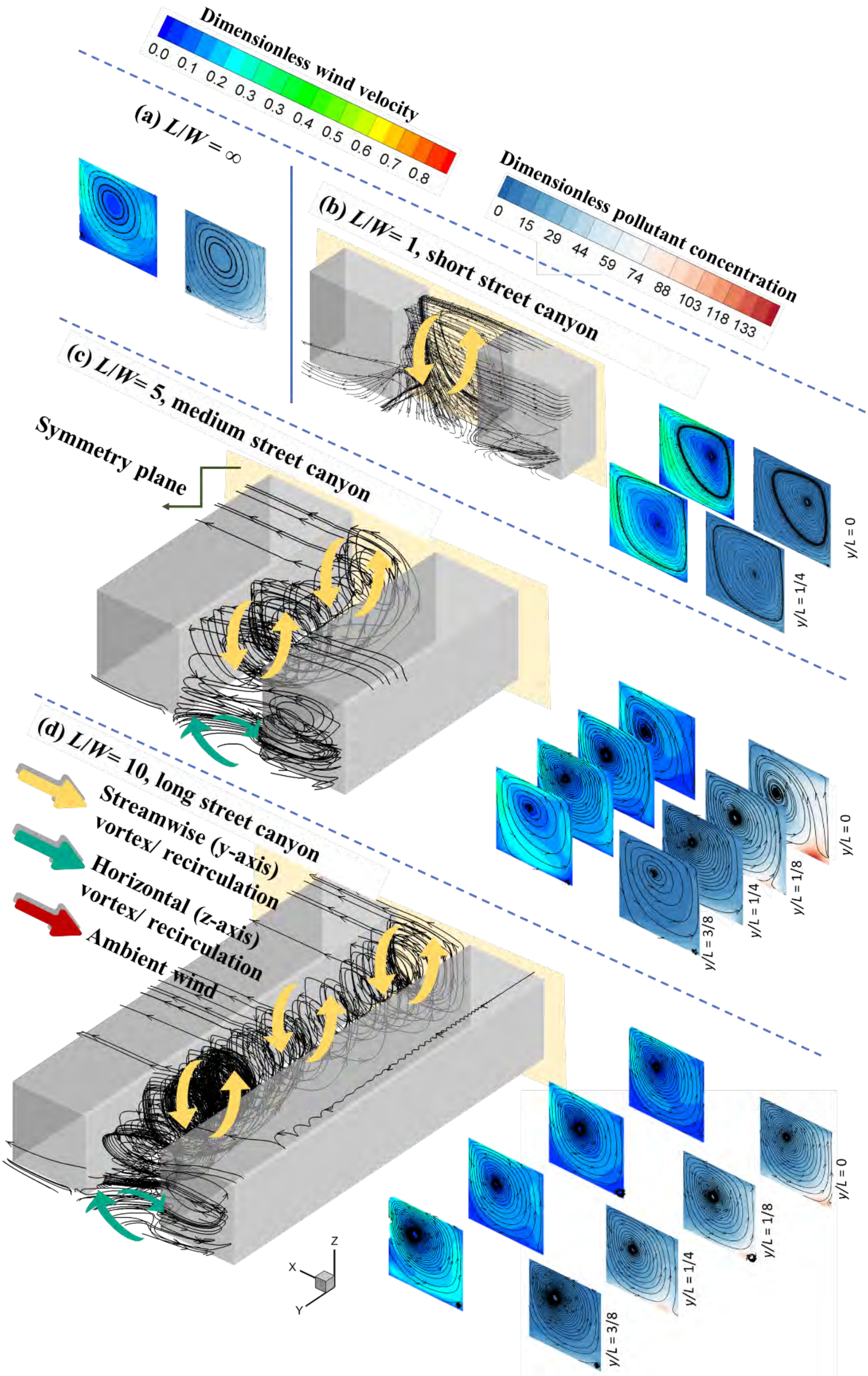

Figure 6.8 Predicted 3D streamlines, *x-z* cross-section pollutant concentration and wind velocity contours for the low-rise street canyons (*H*/*W*= 1) with various street lengths:

(a) *L/W*= ∞, infinite-long street canyon, (b) *L/W*= 1, short street canyon, (c) *L/W*= 5, medium street canyon, and (d) *L/W*= 10, long street canyon.

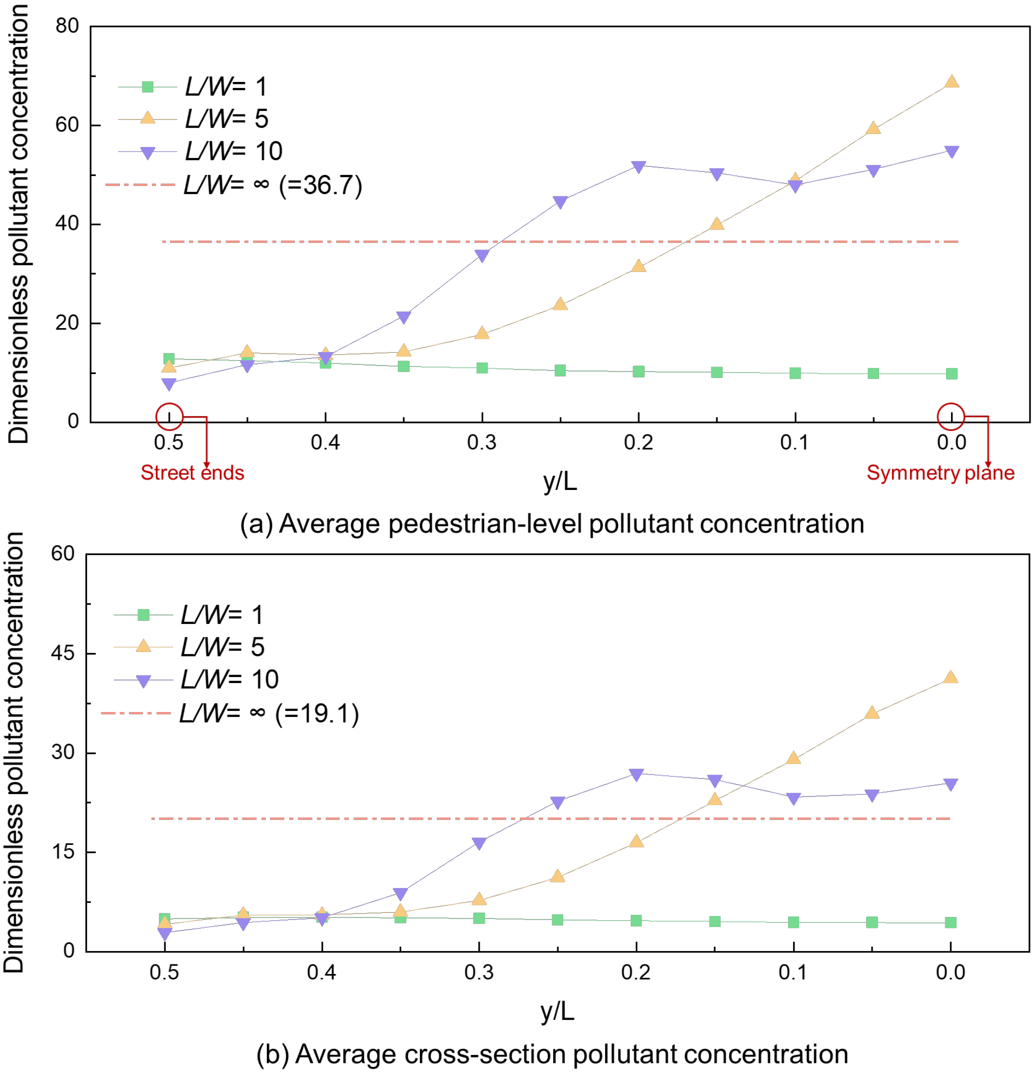

Figure 6.9 Average pollutant concentration along half of the street length for the low-rise street canyon (*H/W*= 1) with various street lengths: (a) average pedestrian level pollutant concentration and (b) average cross-section pollutant concentration

6.6.1.2 High-rise street canyon (*H*/*W*= 3)

To discuss the influence of the lateral entrainment on high-rise street canyons, the numerical results on the dimensionless wind velocity and pollutant concentration are presented at the pedestrian level in Figure 6.10 and for various *x-z* cross-sections in Figure 6.11; at the same time, the average pollutant concentrations for different street lengths are compared in Figure 6.12.

Within a high-rise infinite-long street canyon (H/W= 3 and L/W= ∞), as seen in Figure 6.11(a), the top entrainment from the roof level induces two vertically aligned vortices (y-axis vortex). Consequently, Figure 6.11(a) showed that it is pretty difficult for the top entrainment to penetrate downward into the pedestrian level where the traffic emission sources are located. The airflow within the lower two y-axis canyon vortices is too slow (dimensionless wind velocity< 0.02) to generate any upward pollutant dispersion (Figure 6.11(a)). In other words, the upward advective transport of the airflow has little contribution to the dispersion process of the pollutants (transporting the pollutant from the lower recirculation to the upper recirculation and eventually toward the roof level). Accordingly, it is evident that there exists a substantial pollutant accumulation in the lower part of the high-rise canyon (Figure 6.10(a) and Figure 6.11(a)). The highest pollutant concentration in the lower space was almost one order higher than that at the roof level. Interestingly, these results are inconsistent with the field measurements by Zhang et al. [196] in a similar deep street canyon ($H/W \approx 2.7$ and $L/W \approx 10$). As reported by Zhang et al. [196], the highest low-level concentration is only two times higher than the roof-level concentration. Thus, it could be deduced that the airflow is possibly sensitive to the lateral entrainment within a finite-long high-rise street canyon, which might extensively promote the pollutant dispersion in the lower space.

In the high-rise short street canyon (H/W= 3 and L/W= 1) in Figure 6.11(b), the top entrainment produces two separated y-axis vortices compared with the infinite-long counterpart. Interestingly, at the pedestrian level, there are noticeable divergent and outward airflows caused by lateral entrainment (Figure 6.10(b)). Although the pedestrian level wind speed is still relatively low, the pollutants could be effectively transported outward along with these divergent flows. In consequence, as seen in Figure 6.12(a), the average pedestrian level concentration is reduced by almost up to 98% along the street length, compared with the infinite-long counterpart. In other words, the lateral entrainment could affect the pollutant dispersion of the whole street canyon. Furthermore, the wind velocity and flow patterns of the various x-z cross-sections show that the canyon is almost occupied by the strong downward airflows (Figure 6.11(b)).

At the same time, the dimensionless wind velocity at the cross-section is enhanced by up to 0.5 (Figure 6.11(b)). Accordingly, the pollutants only slightly accumulate near the ground level (Figure 6.11(b)). Figure 6.12(b) reports that the average concentration of the *x*-*z* section decreases by up to 99% along the street length.

In a high-rise medium street canyon (*H/W*= 3 and *L/W*= 5), similar to the short canyon, the top entrainment still causes a *y*-axis vortex near the roof level (Figure 6.11(c)). In contrast, the lateral entrainment produces two symmetric spanwise recirculation in the lower space. As evidenced in Figure 6.10(c), the outer regions ($0.35 < y/L < 0.5$) are dominated by the outward airflows at the pedestrian level. Instead, in the inner regions ($0 < y/L < 0.35$), there exist the inward channeling airflows. Therefore, a higher pollutant concentration is found near the symmetry plane. Compared with the infinite-long case (Figure 6.10(a)), the medium street still has a markedly smaller magnitude of the concentration with the same level of wind velocity (Figure 6.10(c)). As also shown in Figure 6.12(a), the average pedestrian level concentration is reduced by 81 - 98%. A possible explanation lies in the stronger advective transport of pollutants provided by the *x*-axis recirculation, which could be substantiated in the flow patterns and wind velocity contours of various *x*-*z* cross-sections (Figure 6.11(c)). In the inner two sections, there is an upward airflow with a higher wind velocity; thus, the pollutants within the street center region could be more substantially transported out across the roof level. Compared to the results of the infinite-long case, the pollutant concentrations decrease remarkably due to the lateral entrainment for all of the *x*-*z* cross-sections (Figure 6.11(c)), and the average concentration along the street length is reduced by 75 - 98% (Figure 6.12(b)).

As shown in Figure 6.11(d), in a high-rise long street canyon (*H/W*= 3 and *L/W*= 10), the flow patterns are slightly different from those in the short and medium street canyons. Nevertheless, the *y*-axis and *x*-axis vortex dominate the pollutant transport in the upper and lower spaces, respectively. Furthermore, the *x*-axis vortex is elongated. This *x*-axis vortex causes clear inward channeling flows at the pedestrian level, transporting most of the pollutants toward the symmetry plane and leading to a more significant pollutant accumulation in the street center region, compared with the shorter canyons (short and medium street canyons). As shown in Figure 6.12(a), although the maximum pedestrian level concentration of the long street canyon is up to 10 times higher than its shorter counterparts, this maximum value is still much lower than the infinite-long street result. On the other hand, as seen in Figure 6.11(d), although the wind velocity in the lower part of most inner section begins to be stagnant, the *x*-axis vortex could still reinforce the upward advective transportation of the pollutants. Therefore, the maximum average cross-section concentration is almost three times lower than the infinite-long counterpart (Figure 6.12(b)). Besides, this high-rise long street canyon (H/W= 3 and L/W= 10) shares a similar configuration with the study of Zhang et al. [196]. The measurement position by Zhang et al. [196] is nearly 0.3L away from the street ends. The low-level concentration is two times higher than the roof-level concentration. In the present simulation (Figure 6.11(c)), the low-level concentration of the second section (y/L= 1/4) from the street ends is nearly 3-4 times higher than the roof-level concentration. The difference between this CFD simulation and field measurement is reasonable, and they are in the same order. Notably, the realistic traffic-induced turbulence [197], solar radiation [130], and building separation [71] (were not considered in this chapter) can also improve the pollutant dispersion, especially for the low-space of street canyon.

In general, in the high-rise street canyons, the lateral entrainment can reduce the pollutant concentration more significantly, compared with the low-rise street canyons. The reason is that the lateral entrainment can entirely affect the *x*-axis vortex/ recirculation in the lower part of the canyon; hence, it can increase the vertical advective transportation of the pollutants in the canyon’s center region. With an increase in the street length, the flow patterns remain unchanged, with the dominated *y*-axis vortex in the most upper space and *x*-axis vortex/recirculation in the lower space, respectively, but the influence of lateral entrainment on the pollutant concentration becomes weaker. Despite this effect, the concentrations for the short, medium, and long canyons are still far lower than that of the infinite canyon. In consequence, these phenomena demonstrate that the lateral entrainment significantly contributes to the pollutant dispersion for these high-rise street canyons. Moreover, compared with the low-rise canyon, the high-rise canyon has a significantly higher concentration, especially for the longer street length. Taking the infinite-long canyon as examples, the pedestrian level average pollutant concentration of high-rise canyon (=769.3) is about 20 times that of the low-rise canyon (=36.7), which is in line with the study of Assimakopoulos et al. [176]. Accordingly, it indicates that weaker top entrainment in a high-rise canyon greatly limits the dilution of pollutants.

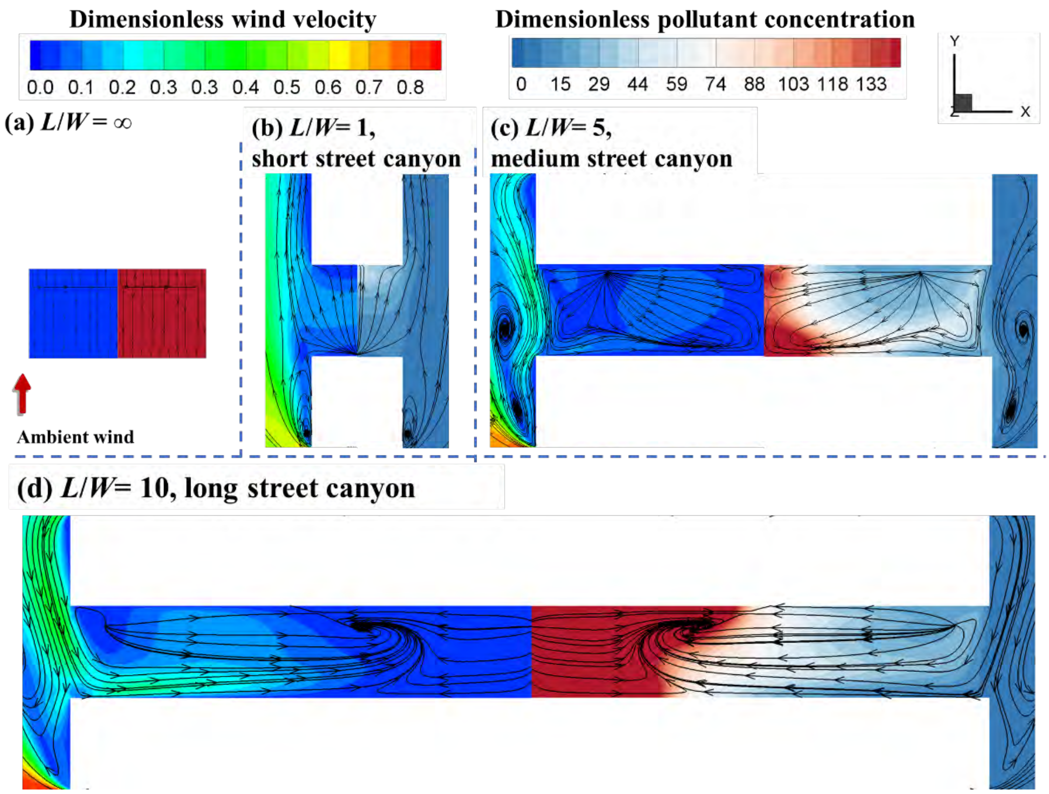

Figure 6.10 Predicted 3D streamlines, pedestrian level pollutant concentration contours, and pedestrian level wind velocity contours for the high-rise street canyons (*H/W*= 3) with various street lengths: (a) *L/W*= ∞, infinite-long street canyon, (b) *L/W*= 1, short street canyon, (c) *L/W*= 5, medium street canyon, and (d) *L/W*= 10, long street canyon.

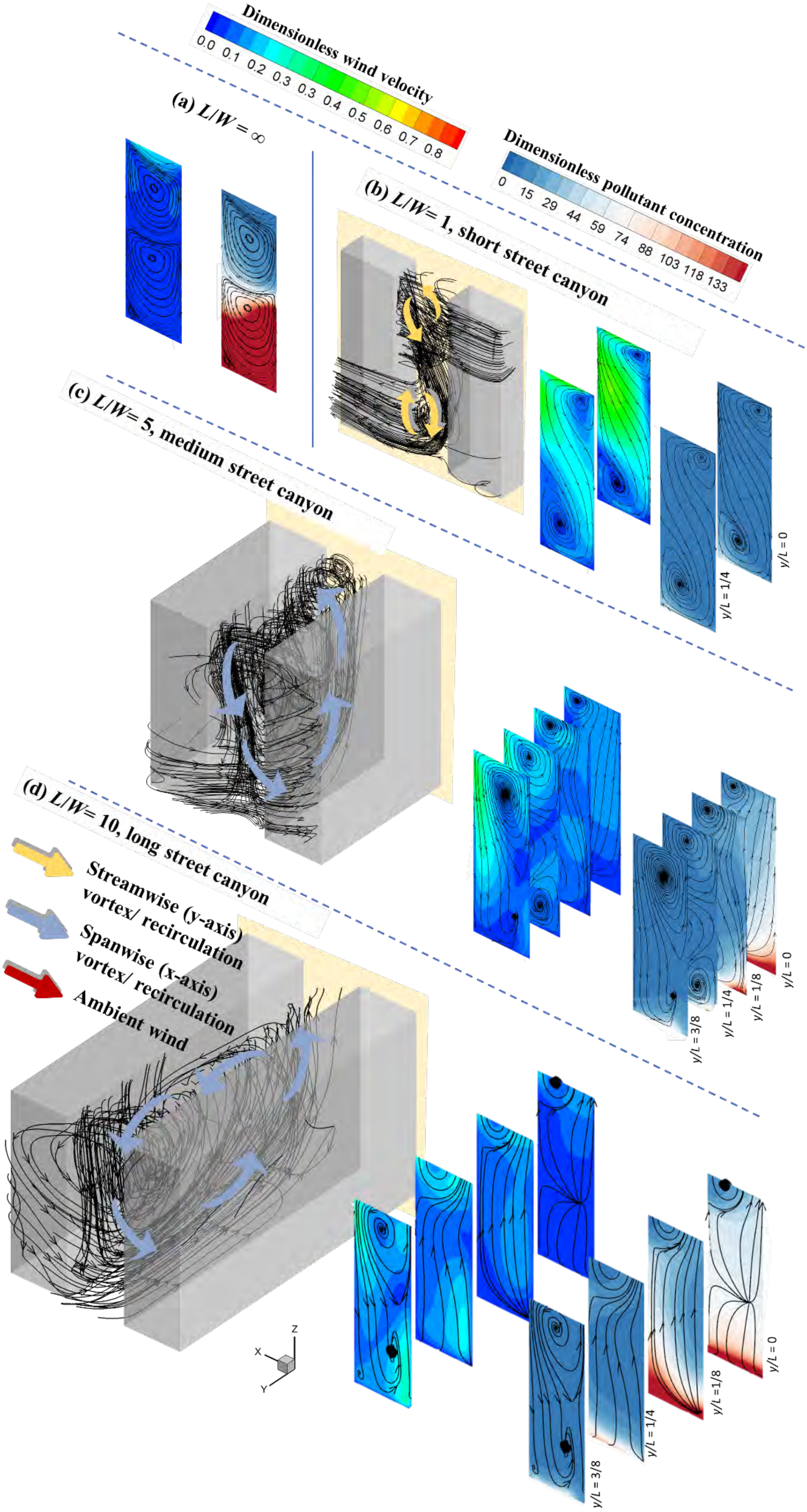
Dimensionless wind velocity
0.0 0.1 0.2 0.3 0.3 0.4 0.5 0.6 0.7 0.8
Dimensionless pollutant concentration
0 15 29 44 59 74 88 103 118 133
(a) L/W = ∞
(b) L/W= 1, short street canyon
y/L = 1/4
y/L = 0
(c) L/W= 5, medium street canyon
y/L = 3/8
y/L = 1/4
y/L = 1/8
y/L = 0
(d) L/W= 10, long street canyon
Streamwise (y-axis) vortex/ recirculation
Spanwise (x-axis) vortex/ recirculation
Ambient wind
y/L = 3/8
y/L = 1/4
y/L =1/8
y/L = 0

Figure 6.11 Predicted pollutant concentration and wind velocity contours at different *x*-*z* cross-sections for the high-rise street canyons (*H/W*= 3) with various street lengths: (a) *L/W*= ∞, infinite-long street canyon, (b) *L/W*= 1, short street canyon, (c) *L/W*= 5, medium street canyon, and (d) *L/W*= 10, long street canyon.

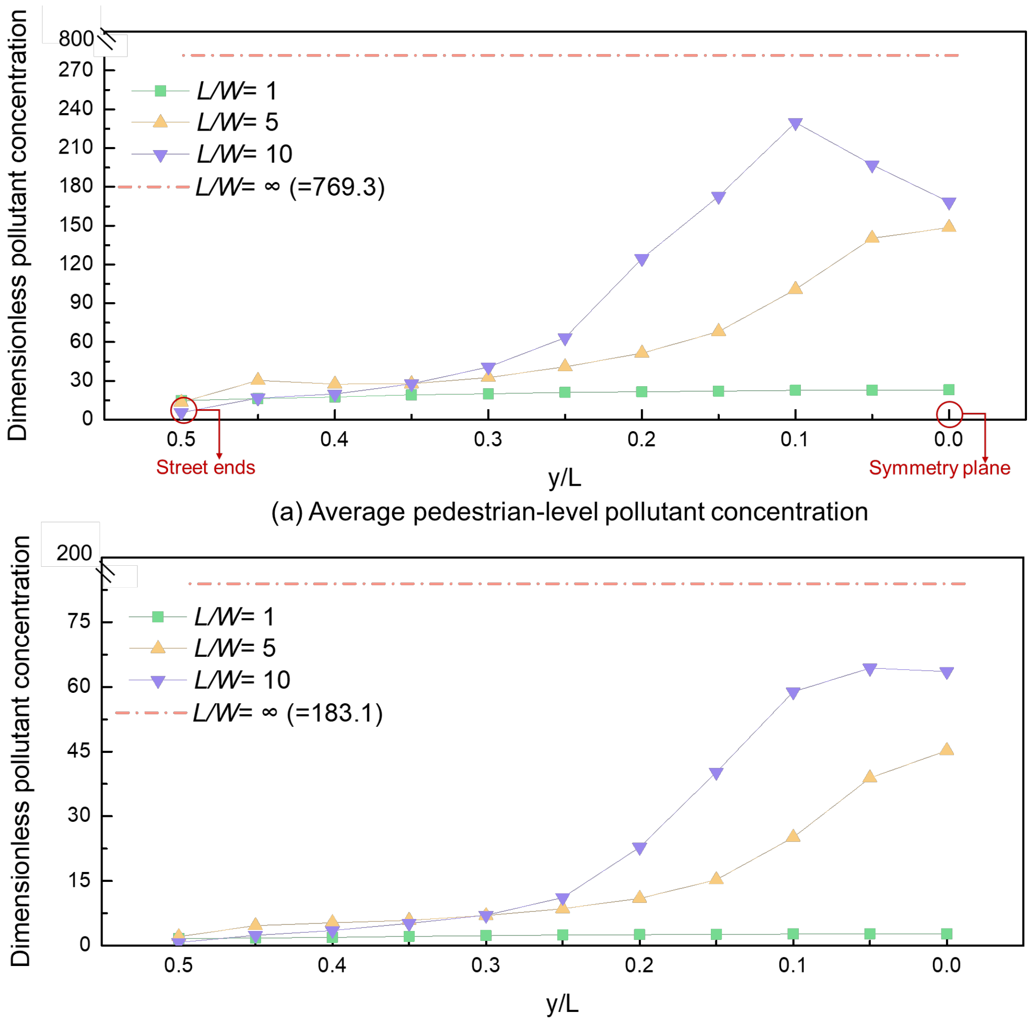

(a) Average pedestrian-level pollutant concentration

(b) Average cross-section pollutant concentration

Figure 6.12 Average pollutant concentration along half of the street length for the high-rise street canyon (*H/W*= 3) with various street lengths: (a) average pedestrian level pollutant concentration and (b) average cross-section pollutant concentration

6.6.2 Optimal urban design strategies for lateral entrainment

As discussed in the last section, lateral entrainment can effectively improve the dilution potential of the pollutants inside the street canyon, especially for the deep canyons. In the low-rise medium street canyon (*H/W*= 1 and *L/W*= 5), the lateral entrainment causes the corner vortex at the street ends, and then, it contributes to the dilution of the pollutants near the ground level. In the high-rise street canyon (H/W= 3 and L/W= 5), the lateral entrainment has a more profound impact on the flow structure compared with the low-rise canyon, thus creating the x-axis recirculation in the lower space of the canyons. As discussed above, this x-axis recirculation can effectively improve the advective transport of pollutants in the lower space. In summary, it might be useful to further improve the dilution potential of the pollutants by enhancing the intensity of the corner vortex in the low-rise street canyon or the x-axis recirculation in the high-rise street canyon. Therefore, three attempts have been made to enhance the influence of the lateral entrainments, i.e., the corner-trim of the downwind building, the short upwind building, and the lower height at the ends of the upwind building. In this section, the low-rise (H/W= 1) and high-rise (H/W= 3) canyons with the medium-long street (L/W=5) are considered to be the base cases to enhance the improvement on the pollutant concentration reduction. Also, the influence of dimensions of the corner-trim of downwind building D_{trim}, intended length of upwind building $L_{intended}$, and reduced height of upwind building $H_{reduced}$ has been examined in Fig. A6.2 to A6.4. It is suggested that even the relatively minor optimal design can effectively improve the ventilation and the potential of pollutant dilution inside street canyons. As length limits, only the cases of D_{trim} = 0.5 W, $L_{intended}$ = 0.5 W, and $H_{reduced}$ = 0.5 H are discussed in detail.

6.6.2.1 Design I: Corner-trim of the downwind building

The first attempt is to trim the corner of the downwind building, thus creating a "venturi effect" at the street ends. The dimensions of the trimmed corner are shown in Figure 6.13(a). A comparison of the results of the corner-trim and base cases in the low-rise street canyon is also presented. Notably, the maximum pedestrian level dimensionless wind velocity increases by approximately 0.2, although the flow structure changes only slightly. Hence, as illustrated in Figure 6.13(a), the concentration decreased in most of the canyons. This corner-trim design also significantly reduces the highest concentration of the base case in the canyon center region by up to almost 36%

(Figure 6.14(a)). On the other hand, in the vertical direction, this design also causes a significant reduction in the leeward side (leeward side *P_IF* reduced by almost 11%, Figure 6.14(b)) since this design significantly enhances the vertical ventilation on this side. Also, it slightly leads to a slightly lower windward *P_IF* by about 30- 100.

As seen in Figure 6.13(b), the corner-trim design has more significant implications for the reduction of the concentration in the high-rise case (*H/W*= 3). The “venturi effect” at the street ends causes a strong inward channeling flow toward the symmetry plane. Further, the intensity of the *x*-axis recirculation is also enhanced. The pedestrian level dimensionless wind velocity increases substantially by 0.5. Thus, the pedestrian level concentrations decrease in most of the canyons as a result (Figure 6.13(b)). At the same time, as shown in Figure 6.13(b), the base case has a higher concentration at both the street ends and symmetry plane. This corner-trim design can effectively reduce the pollutant concentration in these two regions (by up to almost 63%) (Figure 6.13(b) and Figure 6.14(a)). Additionally, as shown in Figure 6.14(c), the lower-story residents (level 2 to level 6) suffer high *P_IF* in the base case. The corner-trim design relieves this situation and effectively reduces leeward *P_IF* by up to 78% for the lower-story residents, although it slightly increases windward *P_IF* by 80-150.

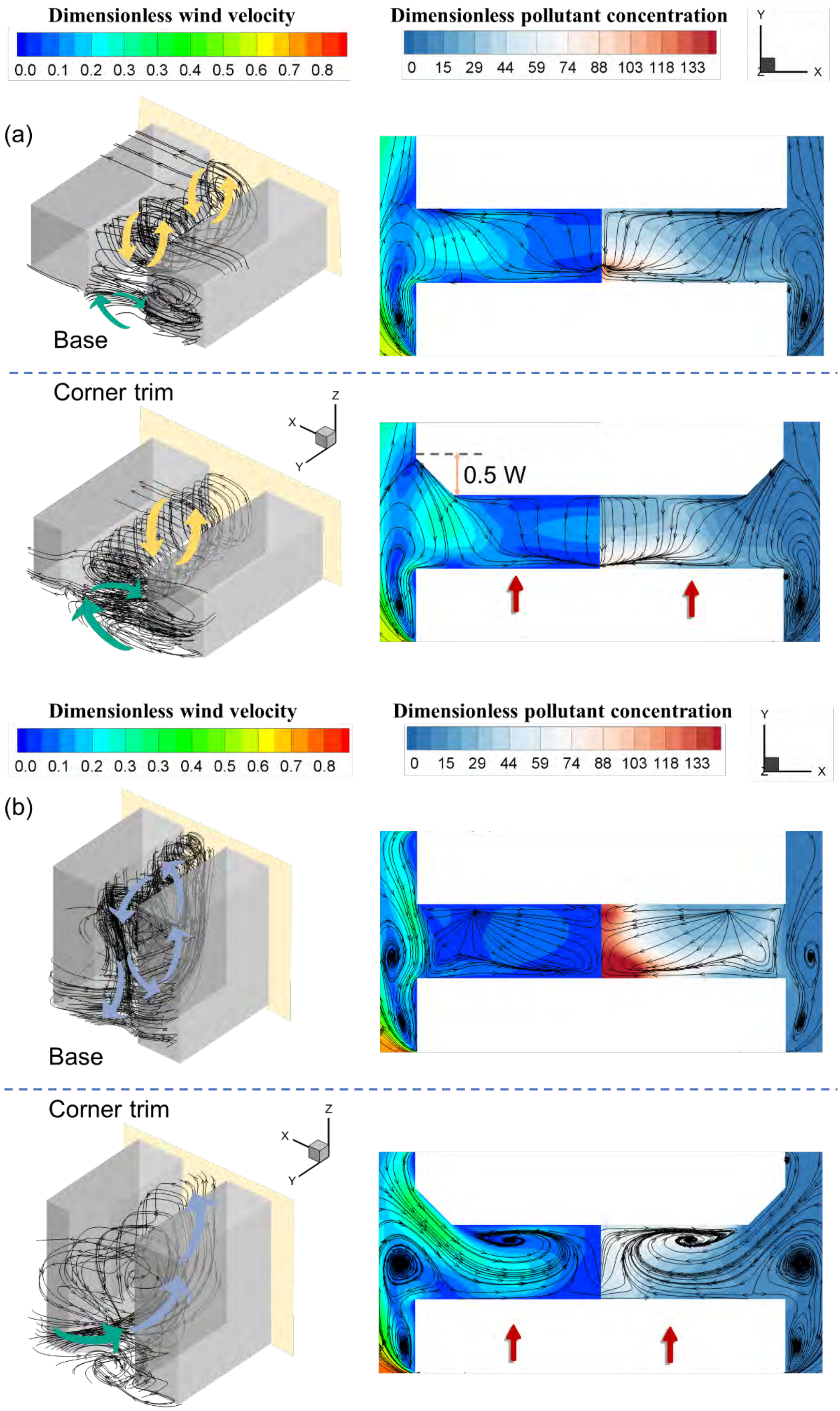

Dimensionless wind velocity
0.0 0.1 0.2 0.3 0.3 0.4 0.5 0.6 0.7 0.8
Dimensionless pollutant concentration
0 15 29 44 59 74 88 103 118 133
(a)
Base
Corner trim
0.5 W
Dimensionless wind velocity
0.0 0.1 0.2 0.3 0.3 0.4 0.5 0.6 0.7 0.8
Dimensionless pollutant concentration
0 15 29 44 59 74 88 103 118 133
(b)
Base
Corner trim

Figure 6.13 Cross-comparison of the pollutant concentration at the pedestrian level between the base case and the corner-cut design case: (a) low-rise street canyon and (b) high-rise street canyon

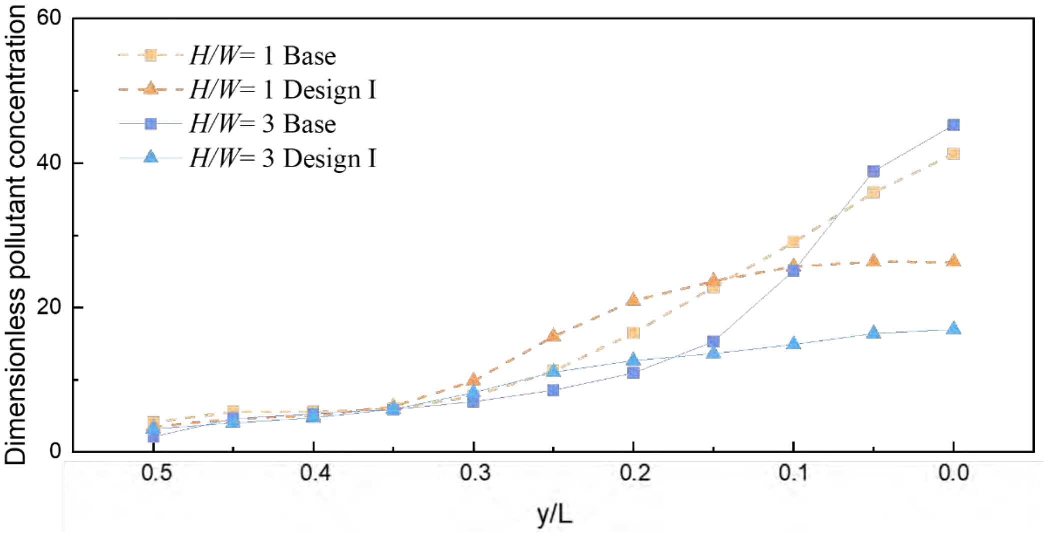

(a)Average cross-section pollutant concentration along the street length

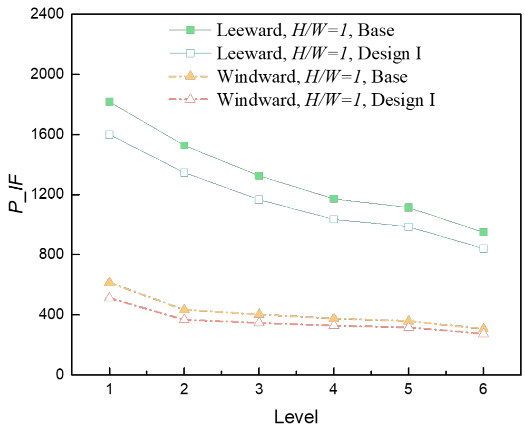

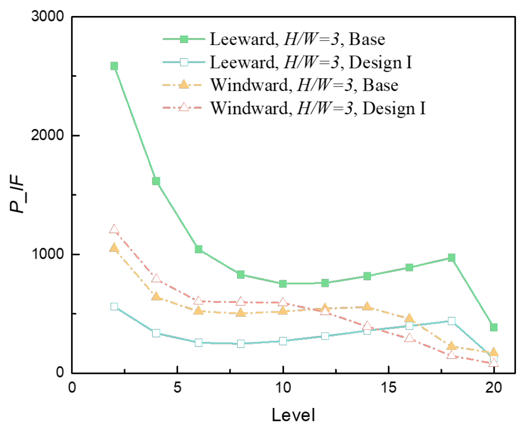

(b) *P_IF*, low-rise street canyon (c) *P_IF*, high-rise street canyon

Figure 6.14 Cross-comparison of the pollutant concentration and personal intake fraction *P_IF* along the street length between the base case and corner-trim design case: (a) Average cross-section pollutant concentration along the street length, (b) *P_IF*, low-rise street canyon, and (c) *P_IF*, high-rise street canyon

6.6.2.2 Design II: Short upwind building

To enhance the influence of the lateral entrainment, the second attempt is to shorten the length of the upwind building by 1/2 *W*. Upon shortening the upwind building of the low-rise street canyon, as seen in the 3D streamlines of Figure 6.15(a), the lateral incoming wind flows over the side of the upwind building, and it hits the windward surface of the downwind building. Then, the incoming wind flows toward the symmetry plane, hence leading to a considerable increase in the dimensionless wind velocity at the pedestrian level (up to 0.3). Correspondingly, the pedestrian level concentrations are reduced significantly, especially in the canyon center region. In addition, as evidently shown in Figure 6.16(a), there is a large decrease in the cross-section pollutant concentration from y/L= 0.35 to 0 (by up to 45%). In addition, this design substantially reduces both leeward and windward *P_IF* from level 1 to level 6 (up to 49%) (Figure 6.16 (b)).

For the high-rise street canyon (H/W=3) with the short upwind building, as Figure 6.15(b) shows, the lateral incoming wind also hits the ends of the windward surface of the downwind building, and then, it enhances the flow intensity of the x-axis recirculation. Therefore, there exists a strong upward airflow at the symmetry plane and a strong outward airflow at the pedestrian level (Figure 6.15(b)). The pedestrian level dimensionless wind velocity is remarkably improved (by up to 0.2). As a result, the accumulated pollutants in the canyon center region can easily escape from the street canyon across the street lateral boundaries. As shown in Figure 6.16(a), the concentrations reduce in almost all of the street's length, especially in the canyon center region (by up to 76%). Additionally, by enhancing the intensity of the x-axis recirculation, this design appreciably reduces the windward *P_IF* by up to 44- 69% and the leeward *P_IF* by 71- 81%, especially for the lower-story residents, who are always suffering the worst air quality.

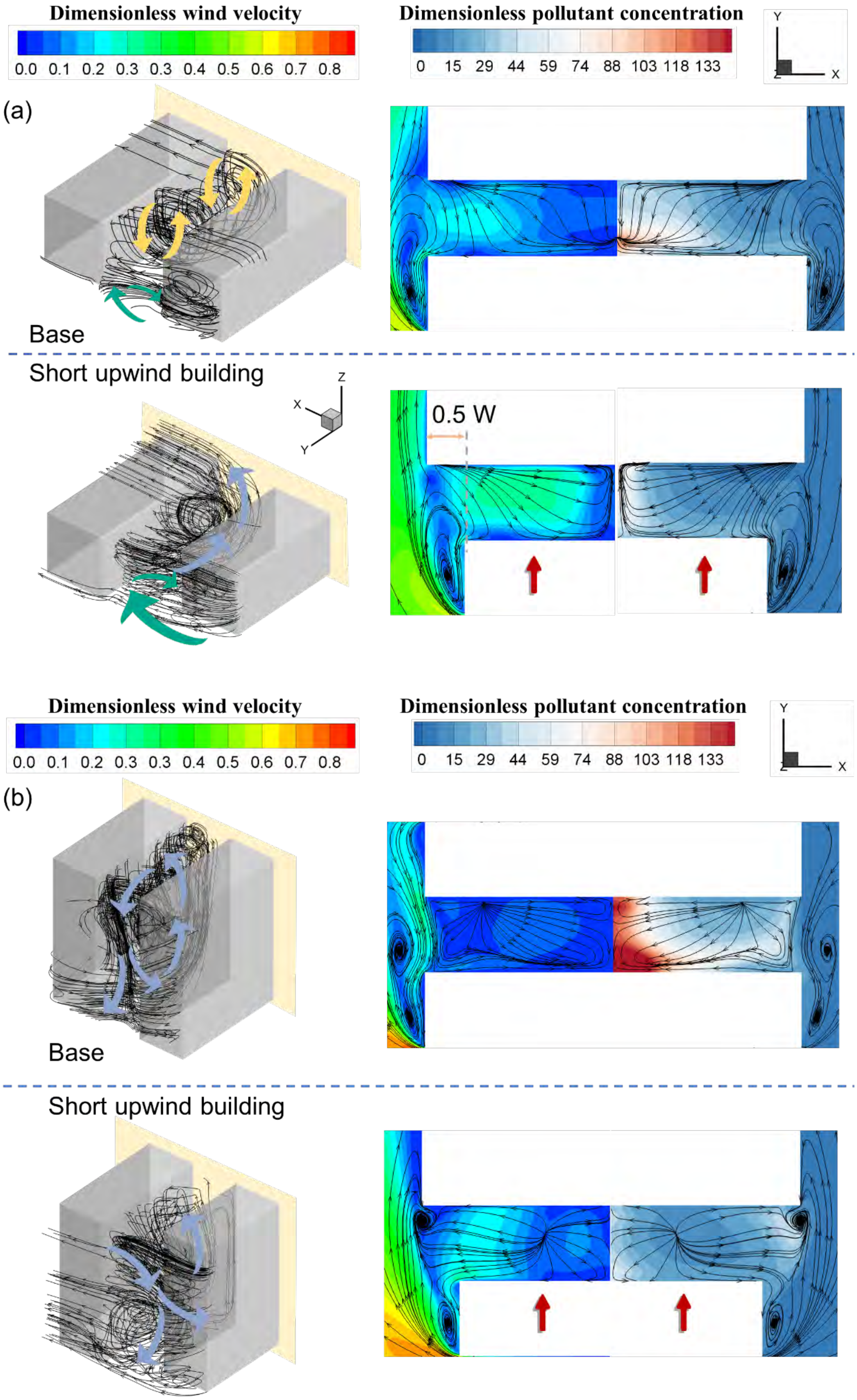
Dimensionless wind velocity
0.0 0.1 0.2 0.3 0.3 0.4 0.5 0.6 0.7 0.8
Dimensionless pollutant concentration
0 15 29 44 59 74 88 103 118 133
(a)
Base
Short upwind building
0.5 W
Dimensionless wind velocity
0.0 0.1 0.2 0.3 0.3 0.4 0.5 0.6 0.7 0.8
Dimensionless pollutant concentration
0 15 29 44 59 74 88 103 118 133
(b)
Base
Short upwind building

Figure 6.15 Cross-comparison of the pollutant concentration at the pedestrian level between the base case and design II case: (a) low-rise street canyon and (b) high-rise street canyon

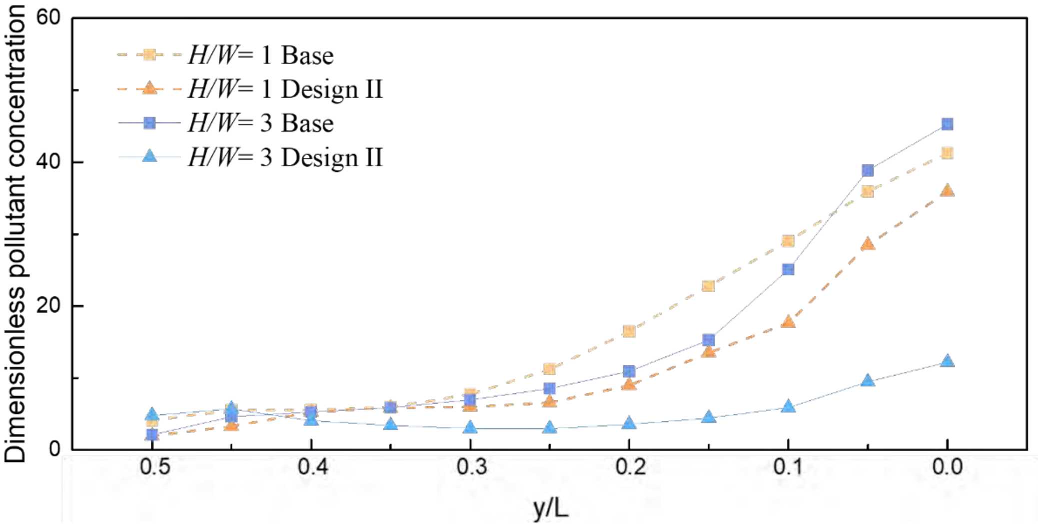

(a) Average cross-section pollutant concentration along the street length

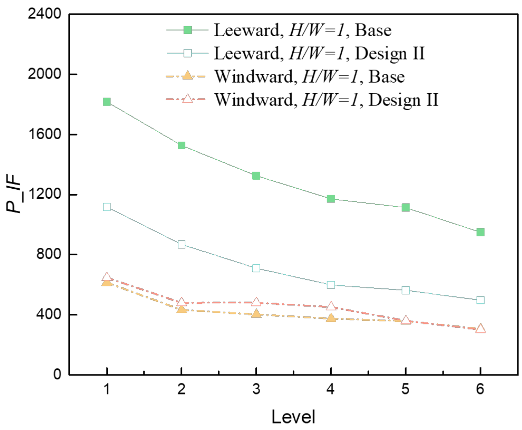

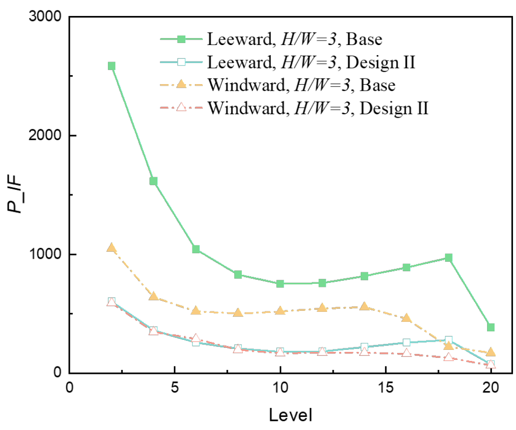

(b) *P_IF*, low-rise street canyon (c) *P_IF*, high-rise street canyon

Figure 6.16 Cross-comparison of the pollutant concentration and personal intake fraction *P_IF* along the street length between the base case and design II case: (a) Average cross-section pollutant concentration along the street length, (b) *P_IF*, low-rise street canyon, and (c) *P_IF*, high-rise street canyon.

6.6.2.3 Design III: Lower height at the ends of the upwind building

As discussed in Section 6.6.2.2, design II successfully introduces the lateral incoming flow into the street canyon from the street ends, hence increasing the flow strength of the *x*-axis recirculation and reducing the pollutant concentration. However, design II will be at the cost of a lower building coverage ratio. Thus, the third attempt is to explore whether only lowering the building height at the ends of the upwind building can also improve the ventilation in the same way (Figure 6.17(a) and (b)).

For the low-rise street canyon with design III (the indented length = 1/2 *W* and the reduced height = 0.5 *H*), as seen in the 3D streamlines of Figure 6.17(a), the pedestrian level wind velocity is markedly improved by introducing fresh air from the upper part of the lateral street boundaries, the same as in design II. Therefore, the cross-section pollutant concentrations also reduce substantially from y/L= 0.4 to 0 (by up to 34%) (Figure 6.18(a)). Clearly, for the low-rise canyons, the reduction in the pedestrian level concentrations due to design III is only slightly lower than in the design II counterpart. In terms of *P_IF* (Figure 6.16(b)), this design also reduces leeward *P_IF* from level 1 to level 6 (up to 39%), but the windward *P_IF* has little change.

For the high-rise street canyon with design III (the indented length = 1/2 *W* and the reduced height = 1/3 *H*), similar to design II, the wind velocity is also improved (Figure 6.17(b)), although the increment in the wind velocity is less than that of design II (Figure 6.15(b)). Therefore, as shown in Figure 6.18(a), there is a considerable decrease in the pedestrian level concentration along the street length, especially in the canyon center region (by up to 71%). Furthermore, the *P_IF* noticeably declines at both the leeward side (by 55-73%) and the windward side (by up to 56-73%).

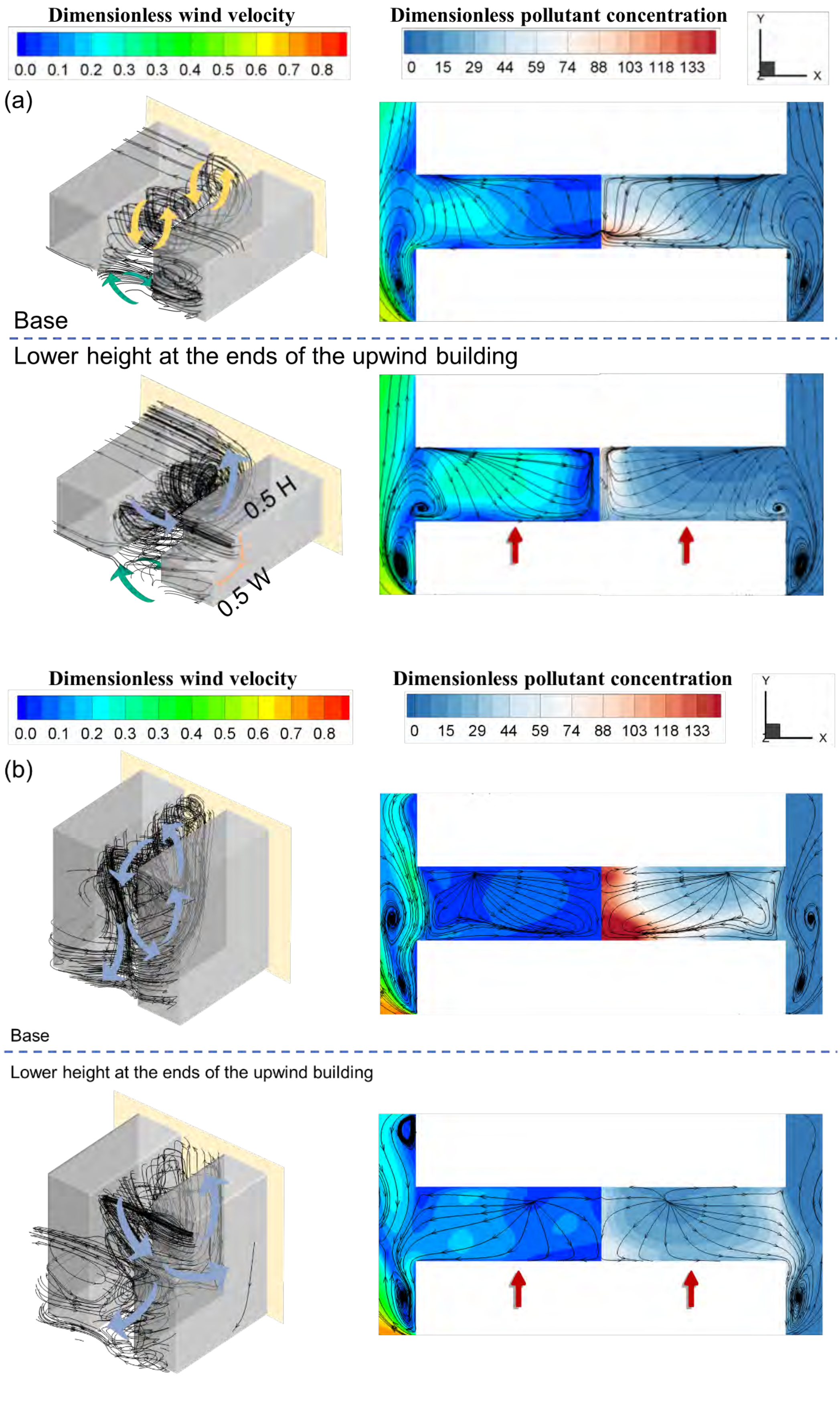

Dimensionless wind velocity
0.0 0.1 0.2 0.3 0.3 0.4 0.5 0.6 0.7 0.8
Dimensionless pollutant concentration
0 15 29 44 59 74 88 103 118 133
Y
X
(a)
Base
Lower height at the ends of the upwind building
0.5 H
0.5 W
Dimensionless wind velocity
0.0 0.1 0.2 0.3 0.3 0.4 0.5 0.6 0.7 0.8
Dimensionless pollutant concentration
0 15 29 44 59 74 88 103 118 133
Y
X
(b)
Base
Lower height at the ends of the upwind building

Figure 6.17 Cross-comparison of the pollutant concentration at the pedestrian level between the base case and design III case: (a) low-rise street canyon and (b) high-rise street canyon

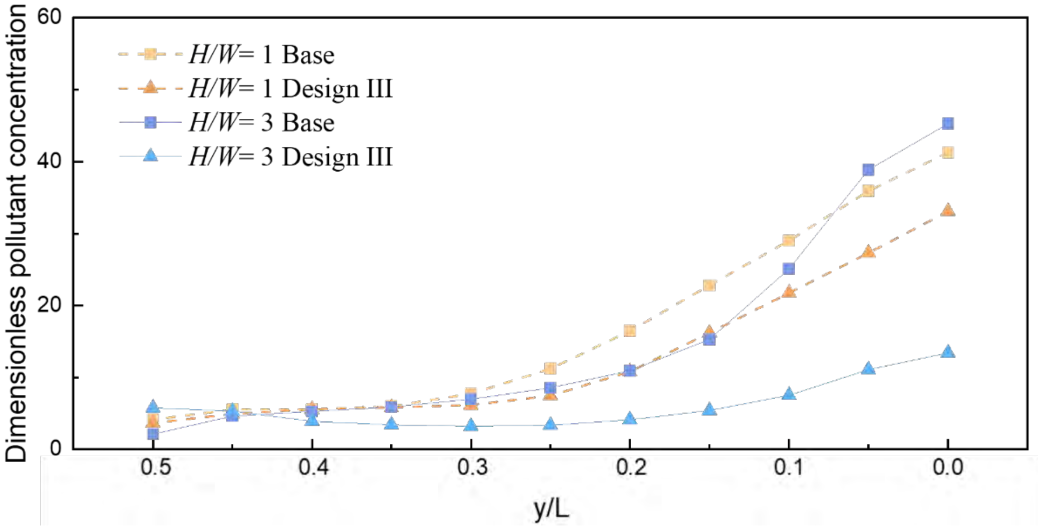

(a) Average cross-section pollutant concentration along the street length

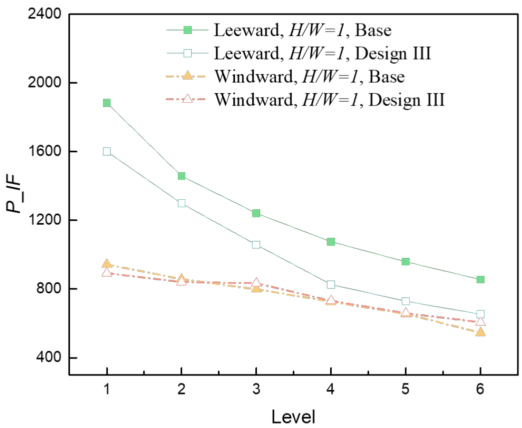

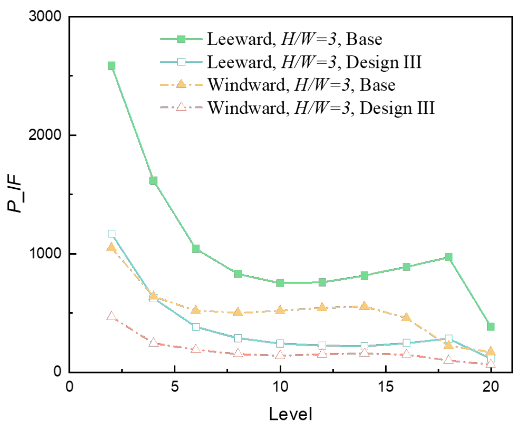

(b) *P_IF*, low-rise street canyon (c) *P_IF*, high-rise street canyon

Figure 6.18 Cross-comparison of the pollutant concentration and personal intake fraction *P_IF* along the street length between the base case and design III case: (a) Average cross-section pollutant concentration along the street length, (b) *P_IF*, low-rise street canyon, and (c) *P_IF*, high-rise street canyon

6.7 Summary

This chapter has presented numerical simulations to investigate the influence of the lateral entrainment on the pollutant concentration within the street canyons based on eight 3D street canyons with different aspect ratios of building height and length to street width (H/W and L/W) under the perpendicular wind. The simulations were based on grid-sensitivity analysis and validation of the CFD results from the literature. Based on the CFD results, the importance of the lateral entrainment was confirmed. Further, three designs were proposed to improve air quality by enhancing the influence of lateral entrainment. The major results are summarized as follows:

(1) In a low-rise street canyon, the flow structure is mainly dominated by the top entrainment. The lateral entrainment slightly alters the flow, except for the appearance of the corner vortex and the inward channeling flow near the ground level. Thus, the positive effect of the lateral entrainment on the pollutant concentration is limited (approximately 2.5 times the street width from the street end). For example, the lateral entrainment can significantly reduce both the cross-section and pedestrian level pollutant concentrations of the short and medium canyon by up to 78%. However, for the long canyon, these two concentrations decline only for the outer half of the street in the length direction due to the lateral entrainment.

(2) In a high-rise street canyon, the top entrainment causes only one canyon vortex (the axis is parallel to the street length) in the upper space. In contrast, the lateral entrainment dominates the lower space by the two symmetric vortices/recirculation with an axis perpendicular to the street length. Thus, the pollutant concentrations markedly decrease by up to almost 99% for the short, medium, and long street canyons, due to the lateral entrainment, compared with the case of only considering the top entrainment.

(3) All of the three optimal designs are considerably useful in reducing the pollutant concentration by enhancing the lateral entrainment, especially for the high-rise street canyons. First, the corner-trim of the downwind building creates a “venturi effect” at the street ends, thus significantly reducing the cross-section concentration in most regions of the street canyon (by up to almost 36% and 63% for the low-rise and high-rise canyons) and the personal intake fraction *P_IF* (by up to almost 11% and 78% for the low-rise and high-rise canyons). Second, the short upwind building notably introduces the incoming wind impinging at the ends of the downwind building; thus, the cross-section concentrations greatly decrease in both the low-rise canyons (by up to

45%) and the high-rise canyons (by up to 76%). In addition, it reduces the *P_IF* of the low-rise canyons by up to 49%, and the *P_IF* of the high-rise canyons by up to 81%. Third, the lower height at the ends of the upwind building also introduces fresh air in the same way as in the setup of the short upwind building, alleviating the cost of a lower building coverage ratio (design III is less expensive than design II). The reduction in the concentrations caused by this design is just slightly lower than the setup of a short upwind building.

By discussing those results, two suggestions can be proposed for sustainable street design to reduce pollutant concentration inside street canyons. First, the importance of lateral entrainment should not be neglected, especially for the high-rise street canyon. Therefore, less blockage should be achieved at the street ends. In other words, at the street ends, large-size advertisement boards [198] should not be installed or trees with large-size canopy and high leaf area density [89,132] should not be planted. Second, to utilize the lateral entrainment to improve the ventilation within street canyons, it might be feasible to create a corner trim of downwind buildings at the street ends. Also, the upwind buildings of the street canyon should be shorter than the downwind buildings.

Chapter 7 Conclusions and recommendations for future work

7.1 Summary of main contributions

This thesis investigates optimal urban design for outdoor thermal comfort and air quality by CFD simulation. The main contributions are summarized as follows:

(1) The results of the investigation on frontal area density λ_F reveal that with an increase in λ_F, similar trends of the wind velocity, air temperature, PET, and CO concentration are observed at 0800 LST and 1600 LST, all of which differ from those at 1200 LST. With the increase in λ_F, the PET on the four sidewalks decreases gradually, but the values are still higher than the warm level at 1200 LST. A steady reduction in the PET occurs on the east, west, and north sidewalks, but the PET on the south sidewalk increases until $\lambda_F = 0.25$ and then decreases. The PET could achieve a warm level when λ_F exceeds 0.75 at 0800 LST or 1600 LST. With the increase in λ_F, a decrease in the CO concentration occurs on the south and north sidewalks, but the CO concentrations on the east and west sidewalks increase significantly and change slightly, respectively, at 1200 LST; the maximum concentration is lower than 30000 μg/m^3 at 1200 LST. At 0800 LST or 1600 LST, the concentration first increases and then decreases on the south sidewalk; the maximum concentration is approximately 8000 μg/m3. The concentration on the east or the west sidewalk increases gradually and can exceed 30000 μg/m3 when $\lambda_F > 0.25$.

(2) The results of the study on height-asymmetric street canyon configurations indicate that for the step-up canyon, a higher upwind building is found to produce a hotter air temperature only at a low wind speed and pollutes more severely at both high and low wind speeds, compared with its lower upwind building counterpart. In contrast, for the step-down canyon, a higher downwind building is found to produce cooler air temperatures at both high and low wind speeds and accumulates more pollutants only at a low wind speed, compared with its lower downwind building counterpart. On the other hand, at the high wind speed, both air quality and thermal environment are better

in the step-up canyon than in the step-down canyon. However, at the low wind speed, the air quality is higher in the step-down canyon than the step-up canyon, while the step-up canyon still provides a better thermal environment than the step-down canyon. Moreover, a Richardson number (Ri) for the asymmetric street canyons is defined for the evaluation of the buoyancy force versus the inertial force. When $|Ri| > 20$, the flow field is mainly dominated by natural convection, and an increase of $|Ri|$ results in an increase in the air temperature and a decrease in the pollutant concentration. In contrast, when $|Ri| < 20$, the flow field is dominated by forced convection, and the variation of $|Ri|$ has an insignificant influence on air quality and air temperature.

(3) The results of the investigation on the building setback demonstrate that the horizontal building setbacks are advocated within the low-rise street canyon, which simultaneously improves the thermal comfort and air quality. By manipulating its dimensionless vertical cross-section area S_{HS} (increasing $S_{HS} = H_{HS}/W \times D_{HS}/W$) and its dimensionless aspect ratio H_{HS}/D_{HS} (lowering H_{HS}/D_{HS}), the average PET can decline by up to 2.1 ℃ and the average pollutant concentration can reduce by up to 66% at the two-side pedestrian level. The vertical building setbacks are more suitable for creating a better outdoor environment for the high-rise street canyon. The dimensionless horizontal cross-section area S_{VS} ($= L_{VS}/L \times D_{VS}/W$) should be as large as possible so that the average PET can decrease by up to 0.7 ℃ and the average pollutant concentration can reduce by up to 35% at the two-side pedestrian level.

(4) The results of the investigations on the tree plantings suggest that increasing LAD (from 0.5 to 2) results in a significant reduction of air temperature (up to 1.5 ℃), while it increases concentrations by up to 370%. The trees with LAD ≤ 0.5 are advocated since they hardly worsen the air quality but still induce a 0.5–1 ℃ reduction in air temperature. Increased H_{trunk}/H causes a lower concentration but a weaker cooling effect. Once $H_{trunk}/H > 0.375$, trees hardly increase concentrations compared to tree-free cases. The trees with $H_{trunk}/H \geq 0.375$ are suggested which still declines air temperature by up to 1.5℃. Increasing $W_{spacing}/W_{canopy}$ causes less pollutant accumulation but a poorer cooling effect. When $W_{spacing}/W_{canopy} \geq 2$, trees almost do not

worsen the air quality. The trees with $W_{spacing}/W_{canopy} \geq 2$ are recommended which still causes a 1 ℃ decrease in air temperature.

(5) The results of the investigation on lateral entrainment indicate that in a low-rise street canyon, the flow structure is mainly dominated by the top entrainment. The lateral entrainment slightly alters the flow, except for the appearance of the corner vortex and the inward channeling flow near the ground level. Thus, the positive effect of the lateral entrainment on the pollutant concentration is limited (approximately 2.5 times the street width from the street end). In a high-rise street canyon, the top entrainment causes only one canyon vortex (the axis was parallel to the street length) in the upper space. In contrast, the lateral entrainment dominates the lower space by the two symmetric vortices/recirculation with an axis perpendicular to the street length. All of the three optimal designs are considerably useful in reducing the pollutant concentration by enhancing the lateral entrainment, especially for the high-rise street canyons. First, the corner-trim of the downwind building creates a "venturi effect" at the street ends, thus significantly reducing the cross-section concentration in most regions of the street canyon and the personal intake fraction *P_IF*. Second, the short upwind building notably introduces the incoming wind impinging at the ends of the downwind building; thus, the cross-section concentration greatly decreases in both the low-rise canyons and the high-rise canyons. Third, the lower height at the ends of the upwind building also introduces fresh air in the same way as in the setup of the short upwind building, alleviating the cost of a lower building coverage ratio. The reduction in the concentrations caused by this design is just slightly lower than the setup of a short upwind building.

7.2 Suggestions for future work

The recommended future works are given based on the limitation or incomplete aspects of the study in this thesis.

1) Some details for the calculations of the thermal environment have been simplified. The calculations are conducted only for steady-state weather conditions at specified LSTs to estimate the thermal comfort and air quality of the whole day. Thus,

the temporal fluctuations in the wind velocity, direction, and diurnal temperature amplitude are not considered. Additionally, the heat storage effects of the building walls have been disregarded. The unsteady simulation can be included in future investigations to increase the prediction accuracy for practical urban environments and to achieve more comprehensive conclusions.

2) As many previous studies focused on the outdoor environment of street canyons, the present simulation models introduce the prevailing ambient wind perpendicular to the street axis. This is because perpendicular wind direction usually induces the worst street canyon microclimate. However, the effect of wind direction and the impact of street direction should be explored in future work.

3) Only the thermal effect induced by solar radiation is considered in this study. In effect, the anthropogenic heat (waste heat released into the atmosphere) also has a profound impact on the urban thermal effect and corresponds to the dilution potential of pollutants. If this surface is heated by air-conditioners, marked changes of flow characteristics might be observed. Accordingly, to provide more comprehensive building design guidelines, these anthropogenic heat sources should be considered in our future work.

4) In the future, the part of grid sensitivity analysis should be improved. In this study, only the last sub-work about the lateral entrainment adopts the GCI to ensure mesh independence for CFD simulation. Moreover, the method used in this study for GCI is a little old. A more advanced approach should be considered, such as the ASME V&V 20−2009 standard.

5) For most of the CFD simulations in this study, the RNG k-ε turbulence model is chosen. In fact, other models, such as the SST k-ω model, have been used by many researchers. Especially, the SST k-ω model shows its superior ability to predict the boundary-layer flow. Therefore, the SST k-ω model should be taken into consideration for a better prediction of air flow in urban areas.

6) The inlet profiles in this study are valid for neutrally ABL flows. Strictly, these profiles should be more suitable for simulation without considering thermal effects. In the future, vertical distribution of air temperature can be detected by unmanned aerial

vehicles (UAVs). Then, this kind of distribution of air temperature can be treated as the inlet profile of air temperature, instead of a constant inlet temperature. Also, the profiles of pollutant concentration can be considered in the future study.

REFERENCES

[1] K. Brysse, N. Oreskes, J. O'Reilly, M. Oppenheimer, Climate change prediction: Erring on the side of least drama?, Glob. Environ. Chang. 23 (2013) 327–337.

[2] P.M. Della-Marta, M.R. Haylock, J. Luterbacher, H. Wanner, Doubled length of western European summer heat waves since 1880, J. Geophys. Res. Atmos. 112 (2007).

[3] D.D. Massey, M. Habil, A. Taneja, Particles in different indoor microenvironments-its implications on occupants, Build. Environ. 106 (2016) 237–244.

[4] R. Rückerl, A. Schneider, S. Breitner, J. Cyrys, A. Peters, Health effects of particulate air pollution: a review of epidemiological evidence, Inhal. Toxicol. 23 (2011) 555–592.

[5] Y. Du, C.M. Mak, Z. Ai, Modelling of pedestrian level wind environment on a high-quality mesh: A case study for the HKPolyU campus, Environ. Model. Softw. 103 (2018) 105–119. doi:https://doi.org/10.1016/j.envsoft.2018.02.016.

[6] Y. Du, B. Blocken, S. Pirker, A novel approach to simulate pollutant dispersion in the built environment: Transport-based recurrence CFD, Build. Environ. 170 (2020) 106604. doi:https://doi.org/10.1016/j.buildenv.2019.106604.

[7] D. Cui, X. Li, Y. Du, C.M. Mak, K. Kwok, Effects of envelope features on wind flow and pollutant exposure in street canyons, Build. Environ. 176 (2020) 106862. doi:https://doi.org/10.1016/j.buildenv.2020.106862.

[8] J. Hang, X. Chen, G. Chen, T. Chen, Y. Lin, Z. Luo, X. Zhang, Q. Wang, The influence of aspect ratios and wall heating conditions on flow and passive pollutant exposure in 2D typical street canyons, Build. Environ. (2019) 106536. doi:https://doi.org/10.1016/j.buildenv.2019.106536.

[9] K. Zhang, G. Chen, Y. Zhang, S. Liu, X. Wang, B. Wang, J. Hang, Integrated impacts of turbulent mixing and NOX-O3 photochemistry on reactive pollutant dispersion and intake fraction in shallow and deep street canyons, Sci. Total Environ. 712 (2020) 135553. doi:https://doi.org/10.1016/j.scitotenv.2019.135553.

[10] A. Mochida, I.Y.F. Lun, Prediction of wind environment and thermal comfort at pedestrian level in urban area, J. Wind Eng. Ind. Aerodyn. 96 (2008) 1498–1527. doi:https://doi.org/10.1016/j.jweia.2008.02.033.

[11] Q. Xia, J. Niu, X. Liu, Dispersion of air pollutants around buildings: A review of past studies and their methodologies, Indoor Built Environ. 23 (2014) 201–224. doi:10.1177/1420326X12464585.

[12] T. van Hooff, B. Blocken, Full-scale measurements of indoor environmental conditions and natural ventilation in a large semi-enclosed stadium: Possibilities and limitations for CFD validation, J. Wind Eng. Ind. Aerodyn. 104–106 (2012) 330–341. doi:https://doi.org/10.1016/j.jweia.2012.02.009.

[13] R. Ramponi, B. Blocken, L.B. de Coo, W.D. Janssen, CFD simulation of outdoor ventilation of generic urban configurations with different urban densities and equal and unequal street widths, Build. Environ. 92 (2015) 152–166. doi:https://doi.org/10.1016/j.buildenv.2015.04.018.

[14] M. Schatzmann, S. Rafailidis, M. Pavageau, Some remarks on the validation of small-scale dispersion models with field and laboratory data, J. Wind Eng. Ind. Aerodyn. 67–68 (1997) 885–893. doi:https://doi.org/10.1016/S0167-6105(97)00126-8.

[15] X. Xie, C.H. Liu, D.Y.C. Leung, M.K.H. Leung, Characteristics of air exchange in a street canyon with ground heating, Atmos. Environ. 40 (2006) 6396–6409. doi:https://doi.org/10.1016/j.atmosenv.2006.05.050.

[16] R.A. Memon, D.Y.C. Leung, C.-H. Liu, Effects of building aspect ratio and wind speed on air temperatures in urban-like street canyons, Build. Environ. 45 (2010) 176–188. doi:https://doi.org/10.1016/j.buildenv.2009.05.015.

[17] Z. Tan, J. Dong, Y. Xiao, J. Tu, A numerical study of diurnally varying surface temperature on flow patterns and pollutant dispersion in street canyons, Atmos. Environ. 104 (2015) 217–227. doi:https://doi.org/10.1016/j.atmosenv.2015.01.027.

[18] L. Lin, J. Hang, X. Wang, X. Wang, S. Fan, Q. Fan, Y. Liu, Integrated Effects of Street Layouts and Wall Heating on Vehicular Pollutant Dispersion and their Reentry Toward Downstream Canyons, Aerosol Air Qual. Res. 16 (2016) 3142–3163. doi:10.4209/aaqr.2016.04.0148.

[19] W. Zhang, C.M. Mak, Z.T. Ai, W.M. Siu, A Study of the Ventilation and Thermal Comfort of the Environment Surrounding a New University Building under Construction, Indoor Built Environ. 21 (2012) 568–582. doi:10.1177/1420326X11419871.

[20] N. Nazarian, J. Fan, T. Sin, L. Norford, J. Kleissl, Predicting outdoor thermal comfort in urban environments: A 3D numerical model for standard effective temperature, Urban Clim. 20 (2017) 251–267. doi:https://doi.org/10.1016/j.uclim.2017.04.011.

[21] S.J. Mei, C.W. Liu, D. Liu, F.Y. Zhao, H.Q. Wang, X.-H. Li, Fluid mechanical dispersion of airborne pollutants inside urban street canyons subjecting to multi-component ventilation and unstable thermal stratifications, Sci. Total Environ. 565 (2016) 1102–1115. doi:https://doi.org/10.1016/j.scitotenv.2016.05.150.

[22] W. Wang, E. Ng, Air ventilation assessment under unstable atmospheric stratification — A comparative study for Hong Kong, Build. Environ. 130 (2018) 1–13. doi:https://doi.org/10.1016/j.buildenv.2017.12.018.

[23] J.L. Santiago, E.S. Krayenhoff, A. Martilli, Flow simulations for simplified urban configurations with microscale distributions of surface thermal forcing, Urban Clim. 9 (2014) 115–133. doi:https://doi.org/10.1016/j.uclim.2014.07.008.

[24] N. Nazarian, J. Kleissl, Realistic solar heating in urban areas: Air exchange and street-canyon ventilation, Build. Environ. 95 (2016) 75–93. doi:https://doi.org/10.1016/j.buildenv.2015.08.021.

[25] X. Xie, C.H. Liu, D.Y.C. Leung, Impact of building facades and ground heating on wind flow and pollutant transport in street canyons, Atmos. Environ. 41 (2007) 9030–9049. doi:https://doi.org/10.1016/j.atmosenv.2007.08.027.

[26] S. Sun, X. Xu, Z. Lao, W. Liu, Z. Li, E.H. García, L. He, J. Zhu, Evaluating the impact of urban green space and landscape design parameters on thermal comfort in hot summer by numerical simulation, Build. Environ. 123 (2017) 277–288. doi:https://doi.org/10.1016/j.buildenv.2017.07.010.

[27] J. Hang, Y. Li, M. Sandberg, R. Buccolieri, S. Di Sabatino, The influence of building height variability on pollutant dispersion and pedestrian ventilation in idealized high-rise urban areas, Build. Environ. 56 (2012) 346–360. doi:https://doi.org/10.1016/j.buildenv.2012.03.023.

[28] R. Buccolieri, M. Sandberg, S. Di Sabatino, City breathability and its link to pollutant concentration distribution within urban-like geometries, Atmos. Environ. 44 (2010) 1894–1903. doi:https://doi.org/10.1016/j.atmosenv.2010.02.022.

[29] S.J. Mei, J.T. Hu, D. Liu, F.Y. Zhao, Y. Li, H.Q. Wang, Airborne pollutant dilution inside the deep street canyons subjecting to thermal buoyancy driven flows: Effects of representative urban skylines, Build. Environ. 149 (2019) 592–606. doi:https://doi.org/10.1016/j.buildenv.2018.12.050.

[30] J. Liu, J. Niu, Q. Xia, Combining measured thermal parameters and simulated wind velocity to predict outdoor thermal comfort, Build. Environ. 105 (2016) 185–197. doi:https://doi.org/10.1016/j.buildenv.2016.05.038.

[31] Y.H. Juan, A.S. Yang, C.Y. Wen, Y.T. Lee, P.C. Wang, Optimization procedures for enhancement of city breathability using arcade design in a realistic high-rise urban area, Build. Environ. 121 (2017) 247–261. doi:https://doi.org/10.1016/j.buildenv.2017.05.035.

[32] P.E.J. Vos, B. Maiheu, J. Vankerkom, S. Janssen, Improving local air quality in cities: To tree or not to tree?, Environ. Pollut. 183 (2013) 113–122. doi:https://doi.org/10.1016/j.envpol.2012.10.021.

[33] X. Wang, M. Teng, C. Huang, Z. Zhou, X. Chen, Y. Xiang, Canopy density effects on particulate matter attenuation coefficients in street canyons during summer in the Wuhan metropolitan area, Atmos. Environ. 240 (2020) 117739.

[34] A. Dash, G.E. Elsinga, Air pollutant sinks on noise barriers: Where do they perform the best?, Atmos. Environ. 187 (2018) 144–154.

[35] R.-L. Hwang, T.-P. Lin, A. Matzarakis, Seasonal effects of urban street shading on long-term outdoor thermal comfort, Build. Environ. 46 (2011) 863–870.

[36] Y. Qu, M. Milliez, L. Musson-Genon, B. Carissimo, Numerical study of the thermal effects of buildings on low-speed airflow taking into account 3D atmospheric radiation in urban canopy, J. Wind Eng. Ind. Aerodyn. 104–106 (2012) 474–483. doi:https://doi.org/10.1016/j.jweia.2012.03.008.

[37] M. Taleghani, U. Berardi, The effect of pavement characteristics on pedestrians' thermal comfort in Toronto, Urban Clim. 24 (2018) 449–459. doi:https://doi.org/10.1016/j.uclim.2017.05.007.

[38] A.S. Yang, Y.H. Juan, C.Y. Wen, C.J. Chang, Numerical simulation of cooling effect of vegetation enhancement in a subtropical urban park, Appl. Energy. 192 (2017) 178–200. doi:https://doi.org/10.1016/j.apenergy.2017.01.079.

[39] Y. Xu, C. Ren, P. Ma, J. Ho, W. Wang, K.K.-L. Lau, H. Lin, E. Ng, Urban morphology detection and computation for urban climate research, Landsc. Urban Plan. 167 (2017) 212–224. doi:https://doi.org/10.1016/j.landurbplan.2017.06.018.

[40] T. Kubota, M. Miura, Y. Tominaga, A. Mochida, Wind tunnel tests on the relationship between building density and pedestrian-level wind velocity: Development of guidelines for realizing acceptable wind environment in residential neighborhoods, Build. Environ. 43 (2008) 1699–1708. doi:https://doi.org/10.1016/j.buildenv.2007.10.015.

[41] J. Yang, B. Shi, Y. Zheng, Y. Shi, G. Xia, Urban form and air pollution disperse: Key indexes and mitigation strategies, Sustain. Cities Soc. 57 (2020) 101955. doi:https://doi.org/10.1016/j.scs.2019.101955.

[42] K. Hu, S. Cheng, Y. Qian, CFD Simulation Analysis of Building Density on Residential Wind Environment., J. Eng. Sci. Technol. Rev. 11 (2018).

[43] J. Srebric, M. Heidarinejad, J. Liu, Building neighborhood emerging properties and their impacts on multi-scale modeling of building energy and airflows, Build. Environ. 91 (2015) 246–262. doi:https://doi.org/10.1016/j.buildenv.2015.02.031.

[44] T. Bentham, R. Britter, Spatially averaged flow within obstacle arrays, Atmos. Environ. 37 (2003) 2037–2043. doi:https://doi.org/10.1016/S1352-2310(03)00123-7.

[45] Y. Shi, K.K.L. Lau, E. Ng, Incorporating wind availability into land use regression modelling of air quality in mountainous high-density urban environment, Environ. Res. 157 (2017) 17–29. doi:https://doi.org/10.1016/j.envres.2017.05.007.

[46] A. Abd Razak, A. Hagishima, N. Ikegaya, J. Tanimoto, Analysis of airflow over building arrays for assessment of urban wind environment, Build. Environ. 59 (2013) 56–65. doi:https://doi.org/10.1016/j.buildenv.2012.08.007.

[47] M. Bady, S. Kato, H. Huang, Towards the application of indoor ventilation efficiency indices to evaluate the air quality of urban areas, Build. Environ. 43 (2008) 1991–2004. doi:https://doi.org/10.1016/j.buildenv.2007.11.013.

[48] M. Lin, J. Hang, Y. Li, Z. Luo, M. Sandberg, Quantitative ventilation assessments of idealized urban canopy layers with various urban layouts and the same building packing density, Build. Environ. 79 (2014) 152–167. doi:https://doi.org/10.1016/j.buildenv.2014.05.008.

[49] Y. Jiang, C. Wu, M. Teng, Impact of Residential Building Layouts on Microclimate in a High Temperature and High Humidity Region, Sustainability. 12 (2020) 1046.

[50] H. Cheng, I.P. Castro, Near Wall Flow over Urban-like Roughness, Boundary-Layer Meteorol. 104 (2002) 229–259. doi:10.1023/A:1016060103448.

[51] J. Hang, Y. Li, Ventilation strategy and air change rates in idealized high-rise compact urban areas, Build. Environ. 45 (2010) 2754–2767. doi:https://doi.org/10.1016/j.buildenv.2010.06.004.

[52] J. Hang, Y. Li, M. Sandberg, Experimental and numerical studies of flows through and within high-rise building arrays and their link to ventilation strategy, J. Wind Eng. Ind. Aerodyn. 99 (2011) 1036–1055. doi:https://doi.org/10.1016/j.jweia.2011.07.004.

[53] Z. Li, H. Zhang, C.-Y. Wen, A.-S. Yang, Y.-H. Juan, The effects of lateral entrainment on pollutant dispersion inside a street canyon and the corresponding optimal urban design strategies, Build. Environ. 195 (2021) 107740. doi:https://doi.org/10.1016/j.buildenv.2021.107740.

[54] J. Niu, J. Liu, T. Lee, Z.J. Lin, C. Mak, K.-T. Tse, B. Tang, K.C.S. Kwok, A new method to assess spatial variations of outdoor thermal comfort: Onsite monitoring results and implications for precinct planning, Build. Environ. 91 (2015) 263–270.

[55] L.W. Chew, L.K. Norford, Pedestrian-level wind speed enhancement in urban street canyons with void decks, Build. Environ. 146 (2018) 64–76. doi:https://doi.org/10.1016/j.buildenv.2018.09.039.

[56] A.U. Weerasuriya, X. Zhang, B. Lu, K.T. Tse, C.-H. Liu, Optimizing Lift-up Design to Maximize Pedestrian Wind and Thermal Comfort in ‘Hot-Calm’and ‘Cold-Windy’Climates, Sustain. Cities Soc. (2020) 102146.

[57] E. Ng, Policies and technical guidelines for urban planning of high-density cities – air ventilation assessment (AVA) of Hong Kong, Build. Environ. 44 (2009) 1478–1488. doi:https://doi.org/10.1016/j.buildenv.2008.06.013.

[58] C. Yuan, E. Ng, Building porosity for better urban ventilation in high-density cities – A computational parametric study, Build. Environ. 50 (2012) 176–189. doi:https://doi.org/10.1016/j.buildenv.2011.10.023.

[59] T. Huang, J. Niu, Y. Xie, J. Li, C.M. Mak, Assessment of “lift-up” design’s impact on thermal perceptions in the transition process from indoor to outdoor, Sustain. Cities Soc. 56 (2020) 102081. doi:https://doi.org/10.1016/j.scs.2020.102081.

[60] J. Liu, J. Niu, C.M. Mak, Q. Xia, Detached eddy simulation of pedestrian-level wind and gust around an elevated building, Build. Environ. 125 (2017) 168–179.

[61] Q. Xia, X. Liu, J. Niu, K.C.S. Kwok, Effects of building lift-up design on the wind environment for pedestrians, Indoor Built Environ. 26 (2017) 1214–1231.

[62] C. Sha, X. Wang, Y. Lin, Y. Fan, X. Chen, J. Hang, The impact of urban open space and ‘lift-up’building design on building intake fraction and daily pollutant exposure in idealized urban models, Sci. Total Environ. 633 (2018) 1314–1328.

[63] Y. Du, C.M. Mak, T. Huang, J. Niu, Towards an integrated method to assess effects of lift-up design on outdoor thermal comfort in Hong Kong, Build. Environ. 125 (2017) 261–272. doi:https://doi.org/10.1016/j.buildenv.2017.09.001.

[64] Y. Du, C.M. Mak, Improving pedestrian level low wind velocity environment in high-density cities: A general framework and case study, Sustain. Cities Soc. 42 (2018) 314–324. doi:https://doi.org/10.1016/j.scs.2018.08.001.

[65] T. Kim, K. Kim, B.S. Kim, A wind tunnel experiment and CFD analysis on airflow performance of enclosed-arcade markets in Korea, Build. Environ. 45 (2010) 1329–1338.

[66] C.Y. Wen, Y.H. Juan, A.S. Yang, Enhancement of city breathability with half open spaces in ideal urban street canyons, Build. Environ. 112 (2017) 322–336. doi:https://doi.org/10.1016/j.buildenv.2016.11.048.

[67] Y. Huang, N. Zeng, Z. Liu, S. Ye, X.U. Xuan, Wind tunnel simulation of pollutant dispersion inside street canyons with galleries and multi-level flat roofs, J. Hydrodyn. Ser. B. 28 (2016) 801–810.

[68] Y.M. Su, H.T. Chang, Influence of Summer Outdoor Pedestrian Wind Environment Comfort with Height-to-Width Ratios of Arcade in Taiwan, in: Appl. Mech. Mater., Trans Tech Publ, 2016: pp. 633–638.

[69] S. Yin, W. Lang, Y. Xiao, The synergistic effect of street canyons and neighbourhood layout design on pedestrian-level thermal comfort in hot-humid area of China, Sustain. Cities Soc. 49 (2019) 101571.

[70] X. Huang, C. Li, Z. Zhuang, Analysis of height-to-width ratio of commercial streets with arcades based on sunshine hours and street orientation, Appl. Sci. 11 (2021) 1706.

[71] W.Y. Ng, C.K. Chau, A modeling investigation of the impact of street and building configurations on personal air pollutant exposure in isolated deep urban canyons, Sci. Total Environ. 468–469 (2014) 429–448. doi:https://doi.org/10.1016/j.scitotenv.2013.08.077.

[72] X. Huang, Z. Lu, Z. Zhuang, Analysis of the Wind Environment to Improve the Thermal Comfort in the Colonnade Space of a Qilou Street Based on the Relative Warmth Index, Sustainability. 11 (2019) 4402.

[73] S. Yin, W. Lang, Y. Xiao, Z. Xu, Correlative Impact of Shading Strategies and Configurations Design on Pedestrian-Level Thermal Comfort in Traditional Shophouse Neighbourhoods, Southern China, Sustain. . 11 (2019). doi:10.3390/su11051355.

[74] R. Vervoort, B. Blocken, T. van Hooff, Reduction of particulate matter concentrations by local removal in a building courtyard: Case study for the Delhi American Embassy School, Sci. Total Environ. 686 (2019) 657–680. doi:https://doi.org/10.1016/j.scitotenv.2019.05.154.

[75] B. Blocken, R. Vervoort, T. van Hooff, Reduction of outdoor particulate matter concentrations by local removal in semi-enclosed parking garages: a preliminary case study for Eindhoven city center, J. Wind Eng. Ind. Aerodyn. 159 (2016) 80–98.

[76] V.B.L. Boppana, D.J. Wise, C.C. Ooi, E. Zhmayev, H.J. Poh, CFD assessment on particulate matter filters performance in urban areas, Sustain. Cities Soc. 46 (2019) 101376. doi:https://doi.org/10.1016/j.scs.2018.12.004.

[77] T. Lauriks, R. Longo, D. Baetens, M. Derudi, A. Parente, A. Bellemans, J. van Beeck, S. Denys, Application of Improved CFD Modeling for Prediction and Mitigation of Traffic-Related Air Pollution Hotspots in a Realistic Urban Street, Atmos. Environ. 246 (2021) 118127. doi:https://doi.org/10.1016/j.atmosenv.2020.118127.

[78] Z. Li, T. Ming, T. Shi, H. Zhang, C.-Y. Wen, X. Lu, X. Dong, Y. Wu, R. de Richter, W. Li, C. Peng, Review on pollutant dispersion in urban areas-part B: Local mitigation strategies, optimization framework, and evaluation theory, Build. Environ. 198 (2021) 107890. doi:https://doi.org/10.1016/j.buildenv.2021.107890.

[79] J.A.E. Cavanagh, P. Zawar-Reza, J.G. Wilson, Spatial attenuation of ambient particulate matter air pollution within an urbanised native forest patch, Urban For. Urban Green. 8 (2009) 21–30.

[80] S. Yin, Z. Shen, P. Zhou, X. Zou, S. Che, W. Wang, Quantifying air pollution attenuation within urban parks: An experimental approach in Shanghai, China, Environ. Pollut. 159 (2011) 2155–2163.

[81] M. Chen, F. Dai, B. Yang, S. Zhu, Effects of neighborhood green space on PM2. 5 mitigation: Evidence from five megacities in China, Build. Environ. 156 (2019) 33–45.

[82] P.J. Irga, M.D. Burchett, F.R. Torpy, Does urban forestry have a quantitative effect on ambient air quality in an urban environment?, Atmos. Environ. 120 (2015) 173–181.

[83] A. Tiwari, P. Kumar, R. Baldauf, K.M. Zhang, F. Pilla, S. Di Sabatino, E. Brattich, B. Pulvirenti, Considerations for evaluating green infrastructure impacts in microscale and macroscale air pollution dispersion models, Sci. Total Environ. 672 (2019) 410–426. doi:https://doi.org/10.1016/j.scitotenv.2019.03.350.

[84] L. Zhang, Z. Zhang, S. McNulty, P. Wang, The mitigation strategy of automobile generated fine particle pollutants by applying vegetation configuration in a street-canyon, J. Clean. Prod. 274 (2020) 122941. doi:https://doi.org/10.1016/j.jclepro.2020.122941.

[85] A. Mochida, Y. Tabata, T. Iwata, H. Yoshino, Examining tree canopy models for CFD prediction of wind environment at pedestrian level, J. Wind Eng. Ind. Aerodyn. 96 (2008) 1667–1677.

[86] F. Xue, X. Li, The impact of roadside trees on traffic released PM10 in urban street canyon: Aerodynamic and deposition effects, Sustain. Cities Soc. 30 (2017) 195–204. doi:https://doi.org/10.1016/j.scs.2017.02.001.

[87] B. Lin, X. Li, Y. Zhu, Y. Qin, Numerical simulation studies of the different vegetation patterns' effects on outdoor pedestrian thermal comfort, J. Wind Eng. Ind. Aerodyn. 96 (2008) 1707–1718.

[88] T.R. Oke, Boundary layer climates, Routledge, 2002.

[89] T. Chen, H. Yang, G. Chen, C.K.C. Lam, J. Hang, X. Wang, Y. Liu, H. Ling, Integrated impacts of tree planting and aspect ratios on thermal environment in street canyons by scaled outdoor experiments, Sci. Total Environ. (2020) 142920.

[90] T. Chen, H. Pan, M. Lu, J. Hang, C.K.C. Lam, C. Yuan, D. Pearlmutter, Effects of tree plantings and aspect ratios on pedestrian visual and thermal comfort using scaled outdoor experiments, Sci. Total Environ. 801 (2021) 149527. doi:https://doi.org/10.1016/j.scitotenv.2021.149527.

[91] B.S. Lin, Y.J. Lin, Cooling effect of shade trees with different characteristics in a subtropical urban park, HortScience. 45 (2010) 83–86.

[92] N. Nazarian, J. Kleissl, CFD simulation of an idealized urban environment: thermal effects of geometrical characteristics and surface materials, Urban Clim. 12 (2015) 141–159.

[93] S. Bottillo, A.D.L. Vollaro, G. Galli, A. Vallati, Fluid dynamic and heat transfer parameters in an urban canyon, Sol. Energy. 99 (2014) 1–10. doi:https://doi.org/10.1016/j.solener.2013.10.031.

[94] S. Bottillo, A.D.L. Vollaro, G. Galli, A. Vallati, CFD modeling of the impact of solar radiation in a tridimensional urban canyon at different wind conditions, Sol. Energy. 102 (2014) 212–222. doi:https://doi.org/10.1016/j.solener.2014.01.029.

[95] A. Aflaki, M. Mirnezhad, A. Ghaffarianhoseini, A. Ghaffarianhoseini, H. Omrany, Z.-H. Wang, H. Akbari, Urban heat island mitigation strategies: A state-of-the-art review on Kuala Lumpur, Singapore and Hong Kong, Cities. 62 (2017) 131–145.

[96] E. Ng, C. Yuan, L. Chen, C. Ren, J.C.H. Fung, Improving the wind environment in high-density cities by understanding urban morphology and surface roughness: A study in Hong Kong, Landsc. Urban Plan. 101 (2011) 59–74. doi:https://doi.org/10.1016/j.landurbplan.2011.01.004.

[97] Y. Tominaga, A. Mochida, R. Yoshie, H. Kataoka, T. Nozu, M. Yoshikawa, T. Shirasawa, AIJ guidelines for practical applications of CFD to pedestrian wind environment around buildings, J. Wind Eng. Ind. Aerodyn. 96 (2008) 1749–1761. doi:https://doi.org/10.1016/j.jweia.2008.02.058.

[98] K. Giannopoulou, M. Santamouris, I. Livada, C. Georgakis, Y. Caouris, The Impact of Canyon Geometry on Intra Urban and Urban: Suburban Night Temperature Differences Under Warm Weather Conditions, Pure Appl. Geophys. 167 (2010) 1433–1449. doi:10.1007/s00024-010-0099-8.

[99] Y. Tominaga, T. Stathopoulos, Turbulent Schmidt numbers for CFD analysis with various types of flowfield, Atmos. Environ. 41 (2007) 8091–8099. doi:https://doi.org/10.1016/j.atmosenv.2007.06.054.

[100] V. Yakhot, S.A. Orszag, Renormalization group analysis of turbulence. I. Basic theory, J. Sci. Comput. 1 (1986) 3–51. doi:10.1007/BF01061452.

[101] HKO (Hong Kong Observatory), Statistical data of weather information in Hong Kong;, (2019).

[102] S. Dugaria, M. Bortolato, D. Del Col, Modelling of a direct absorption solar receiver using carbon based nanofluids under concentrated solar radiation, Renew. Energy. 128 (2018) 495–508. doi:https://doi.org/10.1016/j.renene.2017.06.029.

[103] T. Barth, D. Jespersen, The design and application of upwind schemes on unstructured meshes, in: 27th Aerosp. Sci. Meet., 1989: p. 366.

[104] K. An, S.-M. Wong, J.C.-H. Fung, E. Ng, Revisit of prevailing practice guidelines and investigation of topographical treatment techniques in CFD-Based air ventilation assessments, Build. Environ. 169 (2020) 106580. doi:https://doi.org/10.1016/j.buildenv.2019.106580.

[105] H. Schlichting, K. Gersten, Boundary-layer theory, Springer, 2016.

[106] A. Matzarakis, F. Rutz, H. Mayer, Modelling radiation fluxes in simple and complex environments---application of the RayMan model, Int. J. Biometeorol. 51 (2007) 323–334. doi:10.1007/s00484-006-0061-8.

[107] A.H.A. Mahmoud, Analysis of the microclimatic and human comfort conditions in an urban park in hot and arid regions, Build. Environ. 46 (2011) 2641–2656. doi:https://doi.org/10.1016/j.buildenv.2011.06.025.

[108] K.-M. Wai, E.Y.Y. Ng, C.M.S. Wong, T.Z. Tan, T.-H. Lin, W.-H. Lien, P.A. Tanner, C.S.H. Wang, K.K.L. Lau, N.M.H. He, J. Kim, Aerosol pollution and its potential impacts on outdoor human thermal sensation: East Asian perspectives, Environ. Res. 158 (2017) 753–758. doi:https://doi.org/10.1016/j.envres.2017.07.036.

[109] Y.C. Chen, T.P. Lin, A. Matzarakis, Comparison of mean radiant temperature from field experiment and modelling: a case study in Freiburg, Germany, Theor. Appl. Climatol. 118 (2014) 535–551. doi:10.1007/s00704-013-1081-z.

[110] K.-M. Wai, C. Yuan, A. Lai, P.K.N. Yu, Relationship between pedestrian-level outdoor thermal comfort and building morphology in a high-density city, Sci. Total Environ. 708 (2020) 134516. doi:https://doi.org/10.1016/j.scitotenv.2019.134516.

[111] D. Liu, S. Hu, J. Liu, Contrasting the performance capabilities of urban radiation field between three microclimate simulation tools, Build. Environ. 175 (2020) 106789. doi:https://doi.org/10.1016/j.buildenv.2020.106789.

[112] M. Palme, Urban Microclimate Modelling for Comfort and Energy Studies, Springer Nature, 2021.

[113] D. Fröhlich, M. Gangwisch, A. Matzarakis, Effect of radiation and wind on thermal comfort in urban environments - Application of the RayMan and SkyHelios model, Urban Clim. 27 (2019) 1–7. doi:10.1016/j.uclim.2018.10.006.

[114] T.P. Lin, Thermal perception, adaptation and attendance in a public square in hot and humid regions, Build. Environ. 44 (2009) 2017–2026. doi:https://doi.org/10.1016/j.buildenv.2009.02.004.

[115] H. Mayer, P. Höppe, Thermal comfort of man in different urban environments, Theor. Appl. Climatol. 38 (1987) 43–49. doi:10.1007/BF00866252.

[116] P. Höppe, The physiological equivalent temperature -- a universal index for the biometeorological assessment of the thermal environment, Int. J. Biometeorol. 43 (1999) 71–75. doi:10.1007/s004840050118.

[117] E. Ng, V. Cheng, Urban human thermal comfort in hot and humid Hong Kong, Energy Build. 55 (2012) 51–65. doi:https://doi.org/10.1016/j.enbuild.2011.09.025.

[118] Y. Xie, T. Huang, J. Li, J. Liu, J. Niu, C.M. Mak, Z. Lin, Evaluation of a multi-nodal thermal regulation model for assessment of outdoor thermal comfort: Sensitivity to wind speed and solar radiation, Build. Environ. 132 (2018) 45–56. doi:https://doi.org/10.1016/j.buildenv.2018.01.025.

[119] A. Matzarakis, H. Mayer, M.G. Iziomon, Applications of a universal thermal index: physiological equivalent temperature, Int. J. Biometeorol. 43 (1999) 76–84. doi:10.1007/s004840050119.

[120] T.P. Lin, A. Matzarakis, Tourism climate and thermal comfort in Sun Moon Lake, Taiwan, Int. J. Biometeorol. 52 (2008) 281–290. doi:10.1007/s00484-007-0122-7.

[121] K. Uehara, S. Murakami, S. Oikawa, S. Wakamatsu, Wind tunnel experiments on how thermal stratification affects flow in and above urban street canyons, Atmos. Environ. 34 (2000) 1553–1562. doi:https://doi.org/10.1016/S1352-2310(99)00410-0.

[122] R.N. Meroney, M. Pavageau, S. Rafailidis, M. Schatzmann, Study of line source characteristics for 2-D physical modelling of pollutant dispersion in street canyons, J. Wind Eng. Ind. Aerodyn. 62 (1996) 37–56. doi:https://doi.org/10.1016/S0167-6105(96)00057-8.

[123] I.P. Castro, A.G. Robins, The flow around a surface-mounted cube in uniform and turbulent streams, J. Fluid Mech. 79 (1977) 307–335.

[124] L. Chen, E. Ng, X. An, C. Ren, M. Lee, U. Wang, Z. He, Sky view factor analysis of street canyons and its implications for daytime intra-urban air temperature differentials in high-rise, high-density urban areas of Hong Kong: a GIS-based simulation approach, Int. J. Climatol. 32 (2012) 121–136.

[125] Z.L. Gu, Y.W. Zhang, Y. Cheng, S.-C. Lee, Effect of uneven building layout on air flow and pollutant dispersion in non-uniform street canyons, Build. Environ. 46 (2011) 2657–2665.

[126] M. Schatzmann, B. Leitl, Issues with validation of urban flow and dispersion CFD models, J. Wind Eng. Ind. Aerodyn. 99 (2011) 169–186. doi:https://doi.org/10.1016/j.jweia.2011.01.005.

[127] A. Fluent, ANSYS fluent theory guide 15.0, Inc, Canonsburg, PA. (2013).

[128] M. Idczak, P. Mestayer, J.-M. Rosant, J.-F. Sini, M. Violleau, Micrometeorological Measurements in a Street Canyon during the Joint ATREUS-PICADA Experiment, Boundary-Layer Meteorol. 124 (2007) 25–41. doi:10.1007/s10546-006-9095-z.

[129] A.W.M. Yazid, N.A.C. Sidik, S.M. Salim, K.M. Saqr, A review on the flow structure and pollutant dispersion in urban street canyons for urban planning strategies, Simulation. 90 (2014) 892–916.

[130] X. Xie, Z. Huang, J. Wang, Z. Xie, The impact of solar radiation and street layout on pollutant dispersion in street canyon, Build. Environ. 40 (2005) 201–212.

[131] P.Y. Cui, Z. Li, W.Q. Tao, Numerical investigations on Re-independence for the turbulent flow and pollutant dispersion under the urban boundary layer with some experimental validations, Int. J. Heat Mass Transf. 106 (2017) 422–436.

[132] H. Yang, T. Chen, Y. Lin, R. Buccolieri, M. Mattsson, M. Zhang, J. Hang, Q. Wang, Integrated impacts of tree planting and street aspect ratios on CO dispersion and personal exposure in full-scale street canyons, Build. Environ. 169 (2020) 106529. doi:https://doi.org/10.1016/j.buildenv.2019.106529.

[133] C.H. Liu, C.T. Ng, C.C.C. Wong, A theory of ventilation estimate over hypothetical urban areas, J. Hazard. Mater. 296 (2015) 9–16.

[134] K. Zhang, G. Chen, X. Wang, S. Liu, C.M. Mak, Y. Fan, J. Hang, Numerical evaluations of urban design technique to reduce vehicular personal intake fraction in deep street canyons, Sci. Total Environ. 653 (2019) 968–994. doi:https://doi.org/10.1016/j.scitotenv.2018.10.333.

[135] W.H. Snyder, Similarity criteria for the application of fluid models to the study of air pollution meteorology, Boundary-Layer Meteorol. 3 (1972) 113–134. doi:10.1007/BF00769111.

[136] R. Zhang, Y. Zhang, K.P. Lam, D.H. Archer, A prototype mesh generation tool for CFD simulations in architecture domain, Build. Environ. 45 (2010) 2253–2262.

[137] F. Binarti, M.D. Koerniawan, S. Triyadi, S.S. Utami, A. Matzarakis, A review of outdoor thermal comfort indices and neutral ranges for hot-humid regions, Urban Clim. 31 (2020) 100531.

[138] A. Matzarakis, F. Rutz, H. Mayer, Modelling radiation fluxes in simple and complex environments: basics of the RayMan model, Int. J. Biometeorol. 54 (2010) 131–139.

[139] A. Matzarakis, D. Fröhlich, Influence of urban green on human thermal bioclimate-application of thermal indices and micro-scale models, in: Int. Symp. Greener Cities More Effic. Ecosyst. Serv. a Clim. Chang. World 1215, 2017: pp. 1–10.

[140] L.V. De Abreu-Harbich, L.C. Labaki, A. Matzarakis, Effect of tree planting design and tree species on human thermal comfort in the tropics, Landsc. Urban Plan. 138 (2015) 99–109.

[141] D.E. Bowler, L. Buyung-Ali, T.M. Knight, A.S. Pullin, Urban greening to cool towns and cities: A systematic review of the empirical evidence, Landsc. Urban Plan. 97 (2010) 147–155.

[142] J.A. Salmond, D.E. Williams, G. Laing, S. Kingham, K. Dirks, I. Longley, G.S. Henshaw, The influence of vegetation on the horizontal and vertical distribution of pollutants in a street canyon, Sci. Total Environ. 443 (2013) 287–298.

[143] T.E. Morakinyo, Y.F. Lam, Simulation study on the impact of tree-configuration, planting pattern and wind condition on street-canyon's micro-climate and thermal comfort, Build. Environ. 103 (2016) 262–275. doi:https://doi.org/10.1016/j.buildenv.2016.04.025.

[144] M. Moradpour, H. Afshin, B. Farhanieh, A numerical investigation of reactive air pollutant dispersion in urban street canyons with tree planting, Atmos. Pollut. Res. 8 (2017) 253–266.

[145] C. Gromke, B. Ruck, Influence of trees on the dispersion of pollutants in an urban street canyon—experimental investigation of the flow and concentration field, Atmos. Environ. 41 (2007) 3287–3302.

[146] Z. Huang, C. Wu, M. Teng, Y. Lin, Impacts of Tree Canopy Cover on Microclimate and Human Thermal Comfort in a Shallow Street Canyon in Wuhan, China, Atmosphere (Basel). 11 (2020) 588.

[147] Y. Huang, M. Li, S. Ren, M. Wang, P. Cui, Impacts of tree-planting pattern and trunk height on the airflow and pollutant dispersion inside a street canyon, Build. Environ. 165 (2019) 106385. doi:https://doi.org/10.1016/j.buildenv.2019.106385.

[148] T.E. Morakinyo, L. Kong, K.K.L. Lau, C. Yuan, E. Ng, A study on the impact of shadow-cast and tree species on in-canyon and neighborhood's thermal comfort, Build. Environ. 115 (2017) 1–17.

[149] T.E. Morakinyo, W. Ouyang, K.K.L. Lau, C. Ren, E. Ng, Right tree, right place (urban canyon): Tree species selection approach for optimum urban heat mitigation - development and evaluation, Sci. Total Environ. 719 (2020) 137461. doi:https://doi.org/10.1016/j.scitotenv.2020.137461.

[150] C. Gromke, A vegetation modeling concept for building and environmental aerodynamics wind tunnel tests and its application in pollutant dispersion studies, Environ. Pollut. 159 (2011) 2094–2099.

[151] Y. Yang, E. Gatto, Z. Gao, R. Buccolieri, T.E. Morakinyo, H. Lan, The "plant evaluation model" for the assessment of the impact of vegetation on outdoor microclimate in the urban environment, Build. Environ. 159 (2019) 106151. doi:https://doi.org/10.1016/j.buildenv.2019.05.029.

[152] J. Hang, Y. Li, R. Buccolieri, M. Sandberg, S. Di Sabatino, On the contribution of mean flow and turbulence to city breathability: the case of long streets with tall buildings, Sci. Total Environ. 416 (2012) 362–373.

[153] C. Gromke, R. Buccolieri, S. Di Sabatino, B. Ruck, Dispersion study in a street canyon with tree planting by means of wind tunnel and numerical investigations–evaluation of CFD data with experimental data, Atmos. Environ. 42 (2008) 8640–8650.

[154] R. Buccolieri, J.L. Santiago, E. Rivas, B. Sanchez, Review on urban tree modelling in CFD simulations: Aerodynamic, deposition and thermal effects, Urban For. Urban Green. 31 (2018) 212–220. doi:https://doi.org/10.1016/j.ufug.2018.03.003.

[155] M.H. Salim, K.H. Schlünzen, D. Grawe, Including trees in the numerical simulations of the wind flow in urban areas: should we care?, J. Wind Eng. Ind. Aerodyn. 144 (2015) 84–95.

[156] R. Buccolieri, S.M. Salim, L.S. Leo, S. Di Sabatino, A. Chan, P. Ielpo, G. de Gennaro, C. Gromke, Analysis of local scale tree–atmosphere interaction on pollutant concentration in idealized street canyons and application to a real urban junction, Atmos. Environ. 45 (2011) 1702–1713.

[157] J.H. Amorim, V. Rodrigues, R. Tavares, J. Valente, C. Borrego, CFD modelling of the aerodynamic effect of trees on urban air pollution dispersion, Sci. Total Environ. 461 (2013) 541–551.

[158] J.L. Santiago, F. Martín, A. Martilli, A computational fluid dynamic modelling approach to assess the representativeness of urban monitoring stations, Sci. Total Environ. 454–455 (2013) 61–72. doi:https://doi.org/10.1016/j.scitotenv.2013.02.068.

[159] B. Hong, H. Qin, B. Lin, Prediction of wind environment and indoor/outdoor relationships for PM2. 5 in different building–tree grouping patterns, Atmosphere (Basel). 9 (2018) 39.

[160] T. Grylls, M. van Reeuwijk, Tree model with drag, transpiration, shading and deposition: Identification of cooling regimes and large-eddy simulation, Agric. For. Meteorol. 298–299 (2021) 108288. doi:https://doi.org/10.1016/j.agrformet.2020.108288.

[161] L. Manickathan, T. Defraeye, J. Allegrini, D. Derome, J. Carmeliet, Parametric study of the influence of environmental factors and tree properties on the transpirative cooling effect of trees, Agric. For. Meteorol. 248 (2018) 259–274. doi:https://doi.org/10.1016/j.agrformet.2017.10.014.

[162] A. Kichah, P.E. Bournet, C. Migeon, T. Boulard, Measurement and CFD simulation of microclimate characteristics and transpiration of an Impatiens pot plant crop in a greenhouse, Biosyst. Eng. 112 (2012) 22–34. doi:https://doi.org/10.1016/j.biosystemseng.2012.01.012.

[163] J. Monteith, M. Unsworth, Principles of environmental physics: plants, animals, and the atmosphere, Academic Press, 2013.

[164] G.S. Campbell, J.M. Norman, The description and measurement of plant canopy structure, in: Plant Canopies Their Growth, Form Funct., Cambridge University Press Cambridge, 1989: pp. 1–19.

[165] Y. Tian, X. Bai, B. Qi, L. Sun, Study on heat fluxes of green roofs based on an improved heat and mass transfer model, Energy Build. 152 (2017) 175–184.

[166] B. Hong, B. Lin, Numerical studies of the outdoor wind environment and thermal comfort at pedestrian level in housing blocks with different building layout patterns and trees arrangement, Renew. Energy. 73 (2015) 18–27.

[167] D.M. Gates, Biophysical ecology, Courier Corporation, 2012.

[168] V.K. Schilling, A parameterization for modelling the meteorological effects of tall forests—a case study of a large clearing, Boundary-Layer Meteorol. 55 (1991) 283–304.

[169] M. Robitu, M. Musy, C. Inard, D. Groleau, Modeling the influence of vegetation and water pond on urban microclimate, Sol. Energy. 80 (2006) 435–447. doi:https://doi.org/10.1016/j.solener.2005.06.015.

[170] H.L. Penman, Natural evaporation from open water, bare soil and grass, Proc. R. Soc. London. Ser. A. Math. Phys. Sci. 193 (1948) 120–145.

[171] M. Bittelli, F. Ventura, G.S. Campbell, R.L. Snyder, F. Gallegati, P.R. Pisa, Coupling of heat, water vapor, and liquid water fluxes to compute evaporation in bare soils, J. Hydrol. 362 (2008) 191–205.

[172] C. Gromke, B. Ruck, On the impact of trees on dispersion processes of traffic emissions in street canyons, Boundary-Layer Meteorol. 131 (2009) 19–34.

[173] C. Gromke, CODASC: a database for the validation of street canyon dispersion models, in: 15th Int. Conf. Harmon. within Atmos. Dispers. Model. Regul. Purp., 2013.

[174] W.C. Cheng, C.-H. Liu, D.Y.C. Leung, Computational formulation for the evaluation of street canyon ventilation and pollutant removal performance, Atmos. Environ. 42 (2008) 9041–9051.

[175] D. Marucci, M. Carpentieri, Effect of local and upwind stratification on flow and dispersion inside and above a bi-dimensional street canyon, Build. Environ. 156 (2019) 74–88.

[176] V.D. Assimakopoulos, H.M. ApSimon, N. Moussiopoulos, A numerical study of atmospheric pollutant dispersion in different two-dimensional street canyon configurations, Atmos. Environ. 37 (2003) 4037–4049.

[177] F. Caton, R.E. Britter, S. Dalziel, Dispersion mechanisms in a street canyon, Atmos. Environ. 37 (2003) 693–702.

[178] Z. Li, H. Zhang, C.Y. Wen, A.S. Yang, Y.H. Juan, Effects of height-asymmetric street canyon configurations on outdoor air temperature and air quality, Build. Environ. (2020) 107195.

[179] Z. Li, H. Zhang, C.Y. Wen, A.S. Yang, Y.H. Juan, Effects of frontal area density on outdoor thermal comfort and air quality, Build. Environ. 180 (2020) 107028. doi:https://doi.org/10.1016/j.buildenv.2020.107028.

[180] W.G. Hoydysh, W.F. Dabberdt, Kinematics and dispersion characteristics of flows in asymmetric street canyons, Atmos. Environ. 22 (1988) 2677–2689.

[181] L.J. Hunter, G.T. Johnson, I.D. Watson, An investigation of three-dimensional characteristics of flow regimes within the urban canyon, Atmos. Environ. Part B. Urban Atmos. 26 (1992) 425–432. doi:https://doi.org/10.1016/0957-1272(92)90049-X.

[182] B.M. Leitl, R.N. Meroney, Car exhaust dispersion in a street canyon. Numerical critique of a wind tunnel experiment, J. Wind Eng. Ind. Aerodyn. 67 (1997) 293–304.

[183] C. Gromke, B. Ruck, Pollutant concentrations in street canyons of different aspect ratio with avenues of trees for various wind directions, Boundary-Layer Meteorol. 144 (2012) 41–64.

[184] C. Gromke, N. Jamarkattel, B. Ruck, Influence of roadside hedgerows on air quality in urban street canyons, Atmos. Environ. 139 (2016) 75–86. doi:https://doi.org/10.1016/j.atmosenv.2016.05.014.

[185] T.R. Oke, Street design and urban canopy layer climate, Energy Build. 11 (1988) 103–113.

[186] V. Yakhot, L.M. Smith, The renormalization group, the ε-expansion and derivation of turbulence models, J. Sci. Comput. 7 (1992) 35–61.

[187] J.J. Kim, J.J. Baik, A numerical study of the effects of ambient wind direction on flow and dispersion in urban street canyons using the RNG k–ε turbulence model, Atmos. Environ. 38 (2004) 3039–3048. doi:https://doi.org/10.1016/j.atmosenv.2004.02.047.

[188] J.J. Kim, D.Y. Kim, Effects of a building's density on flow in urban areas, Adv. Atmos. Sci. 26 (2009) 45–56.

[189] P.J. Richards, R.P. Hoxey, Appropriate boundary conditions for computational wind engineering models using the k-ε turbulence model, in: Comput. Wind Eng. 1, Elsevier, 1993: pp. 145–153.

[190] B.E. Launder, D.B. Spalding, The numerical computation of turbulent flows, in: Numer. Predict. Flow, Heat Transf. Turbul. Combust., Elsevier, 1983: pp. 96–116.

[191] T. Cebeci, P. Bradshaw, Momentum transfer in boundary layers, Hemi. (1977).

[192] B. Blocken, T. Stathopoulos, J. Carmeliet, CFD simulation of the atmospheric boundary layer: wall function problems, Atmos. Environ. 41 (2007) 238–252.

[193] P.J. Roache, Quantification of uncertainty in computational fluid dynamics, Annu. Rev. Fluid Mech. 29 (1997) 123–160.

[194] J. Hang, Z. Luo, X. Wang, L. He, B. Wang, W. Zhu, The influence of street layouts and viaduct settings on daily carbon monoxide exposure and intake fraction in idealized urban canyons, Environ. Pollut. 220 (2017) 72–86. doi:https://doi.org/10.1016/j.envpol.2016.09.024.

[195] H. Yu, J. Thé, Validation and optimization of SST k-ω turbulence model for pollutant dispersion within a building array, Atmos. Environ. 145 (2016) 225–238.

[196] Y.W. Zhang, Z.L. Gu, S.C. Lee, T.M. Fu, K.F. Ho, Numerical Simulation and In Situ Investigation of Fine Particle Dispersion in an Actual Deep Street Canyon in Hong Kong, Indoor Built Environ. 20 (2010) 206–216. doi:10.1177/1420326X10387694.

[197] T. Shi, T. Ming, Y. Wu, C. Peng, Y. Fang, R. de_Richter, The effect of exhaust emissions from a group of moving vehicles on pollutant dispersion in the street canyons, Build. Environ. 181 (2020) 107120. doi:https://doi.org/10.1016/j.buildenv.2020.107120.

[198] Y. Lin, G. Chen, T. Chen, Z. Luo, C. Yuan, P. Gao, J. Hang, The influence of advertisement boards, street and source layouts on CO dispersion and building intake fraction in three-dimensional urban-like models, Build. Environ. 150 (2019) 297–321.

[199] D.K. Fidaros, C.A. Baxevanou, T. Bartzanas, C. Kittas, Numerical simulation of thermal behavior of a ventilated arc greenhouse during a solar day, Renew. Energy. 35 (2010) 1380–1386. doi:https://doi.org/10.1016/j.renene.2009.11.013.

[200] C. and S. Department, Hong Kong monthly digest of statistics, (2019).

Appendices

Table A1.1 Mean hourly air temperatures in June in Hong Kong

LST	07 00	08 00	09 00	10 00	11 00	12 00	13 00	14 00	15 00	16 00	17 00
Air temperature	27	27.3	27.7	28.1	28.5	28.8	29	29.1	29.1	29.1	28.8

Table A1.2 Spectral optical and thermos-physical material properties [199]

Property	Fluid	Building	Ground
Materials	Air	Concrete	Asphalt
Density (kg/m^3)	1.225	2400	2360
Specific heat (J/kg K)	1006.43	750	920
Thermal conductivity (W/m K)	0.0242	1.7	0.75
Viscosity (kg/m S)	1.7894×10^{5}	-	-
Absorption coefficient (1/m)	0.19	0.9	0.9
Scattering coefficient (1/m)	0	0	-10
Refractive index	1	1.7	1.92
Emissivity, ε	0.9	0.7	0.95

Table A1.3 Conditions used in simulations with Rayman 1.2 [200]

Position	Hong Kong (22°18' N, 114°10' E)
Cloud coverage	0 Octa
Humidity (RH)	82%
Activity	80 W (walking)
Clothing	0.5 clo (summer clothes)
Personal data	1.72 m, 65 kg, 30 years, male

Table A1.4 Classification of thermal sensation [120]

Thermal	PET range (°C)	Thermal	PET range (°C)
Very Cold	<14	Slightly warm	30–34
Cold	14–18	Warm	34–38
Cool	18–22	Hot	38–42
Slightly cool	22–26	Very hot	<42
Neutral	26–30		

Table A6.1 Breathing rate for various age groups and microenvironments [194]

Breathing rate B_r (m^3/day)	Indoor at home (j= 1)	Other indoor location (j= 2)	Near vehicle (j= 3)	Other outdoor location (j= 4)
Children	12.5	14.0	14	18.7
Adults	13.8	15.5	15.5	20.5
Elderly	13.1	14.8	14.8	19.5

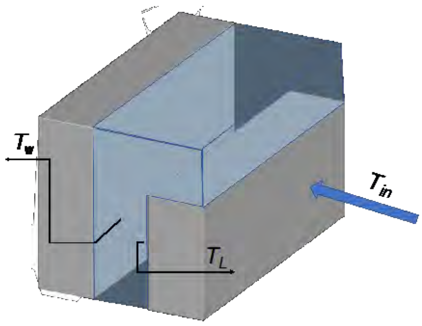

Fig. A3.1 Schematic for the calculation of Richardson number (volume-average wind speed in the asymmetric canyons is calculated within the blue region)

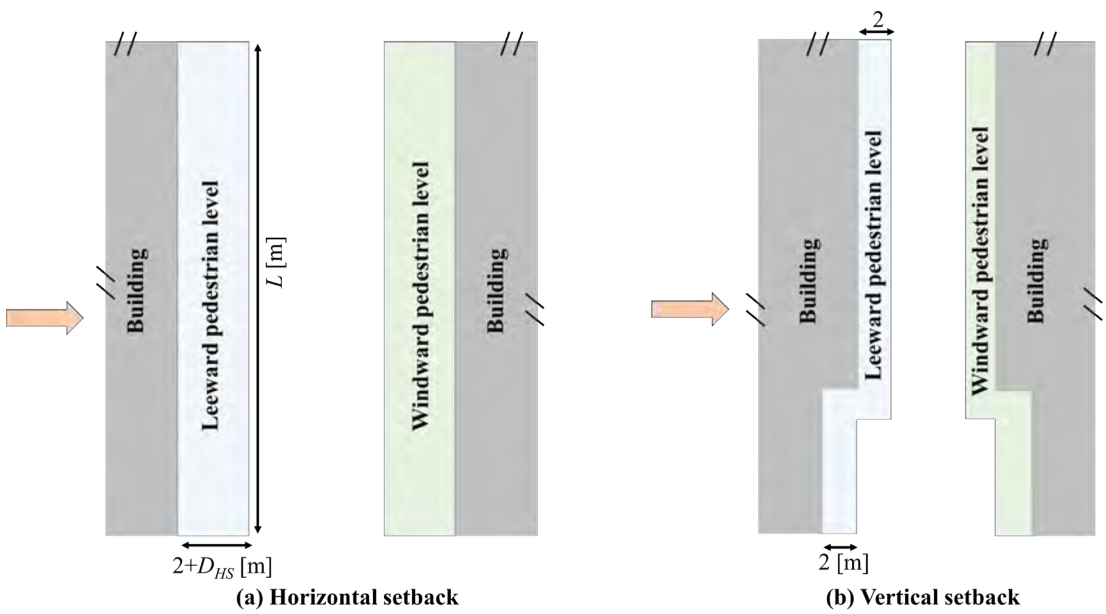

Fig. A4.1 Schematic for the leeward pedestrian level (blue region) and windward pedestrian level (green region) in the street canyon with (a) horizontal setback and (b) vertical setback

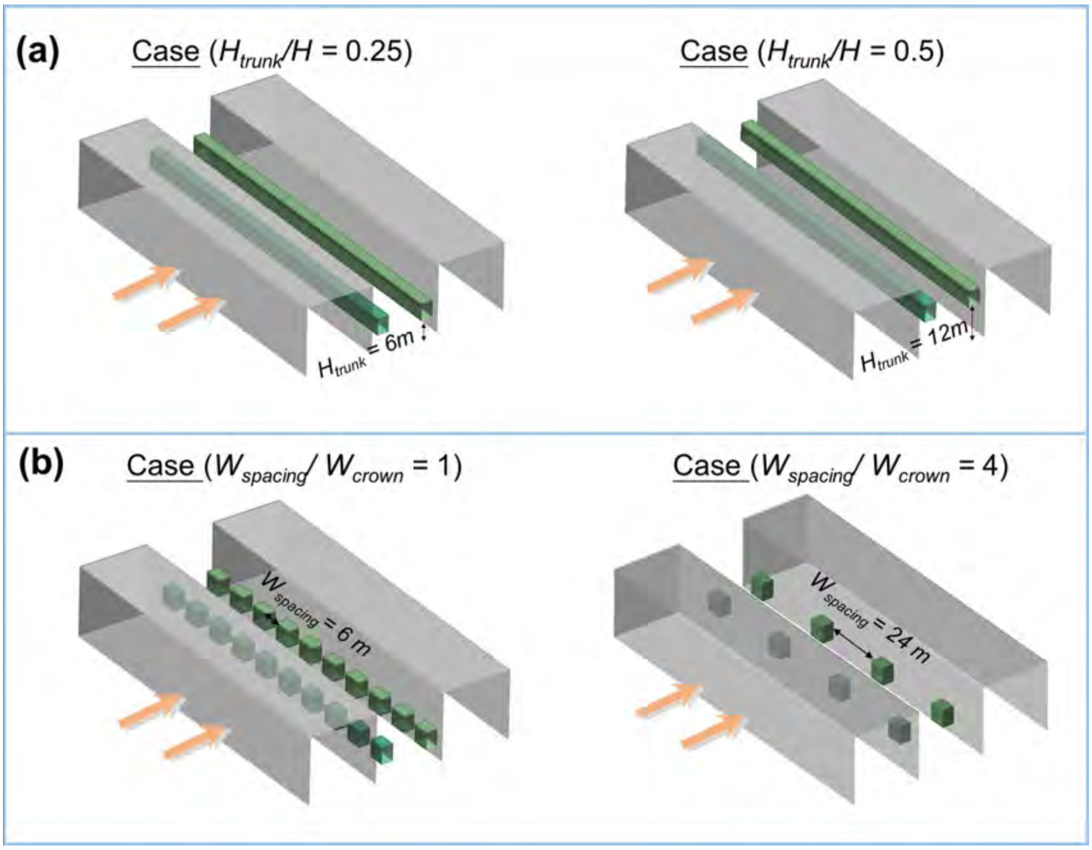

Figure A5.1 Illustrations of (a) in-canyon trees with various building heights (H_{trunk}/H) and in-canyon trees with various tree spacing ($W_{spacing}/W_{crown}$) in CFD simulations.

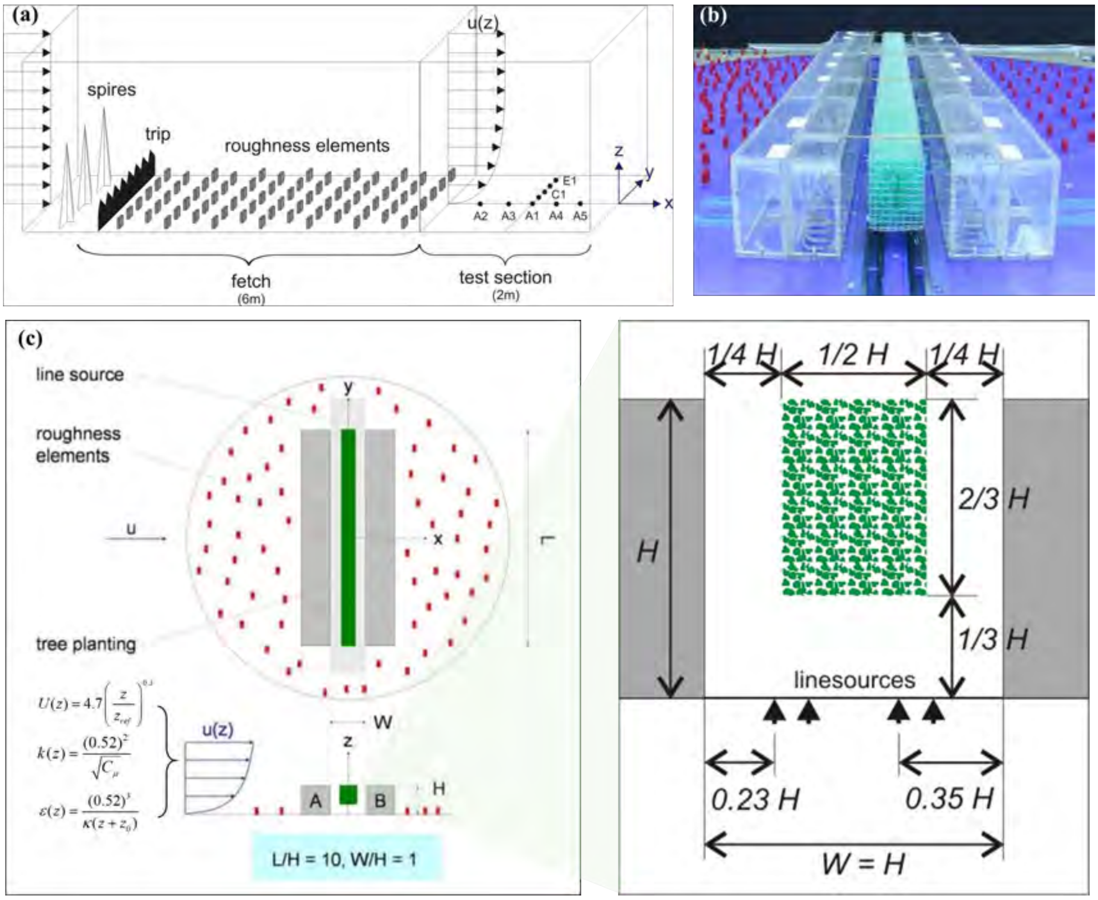

Figure A5.2 Schematics of (a) test section of the wind tunnel, (b) a photo of the urban street canyon with trees (scale 1:150) for the wind tunnel, and (c) model setups of the street canyon with trees for the wind tunnel [172,173].

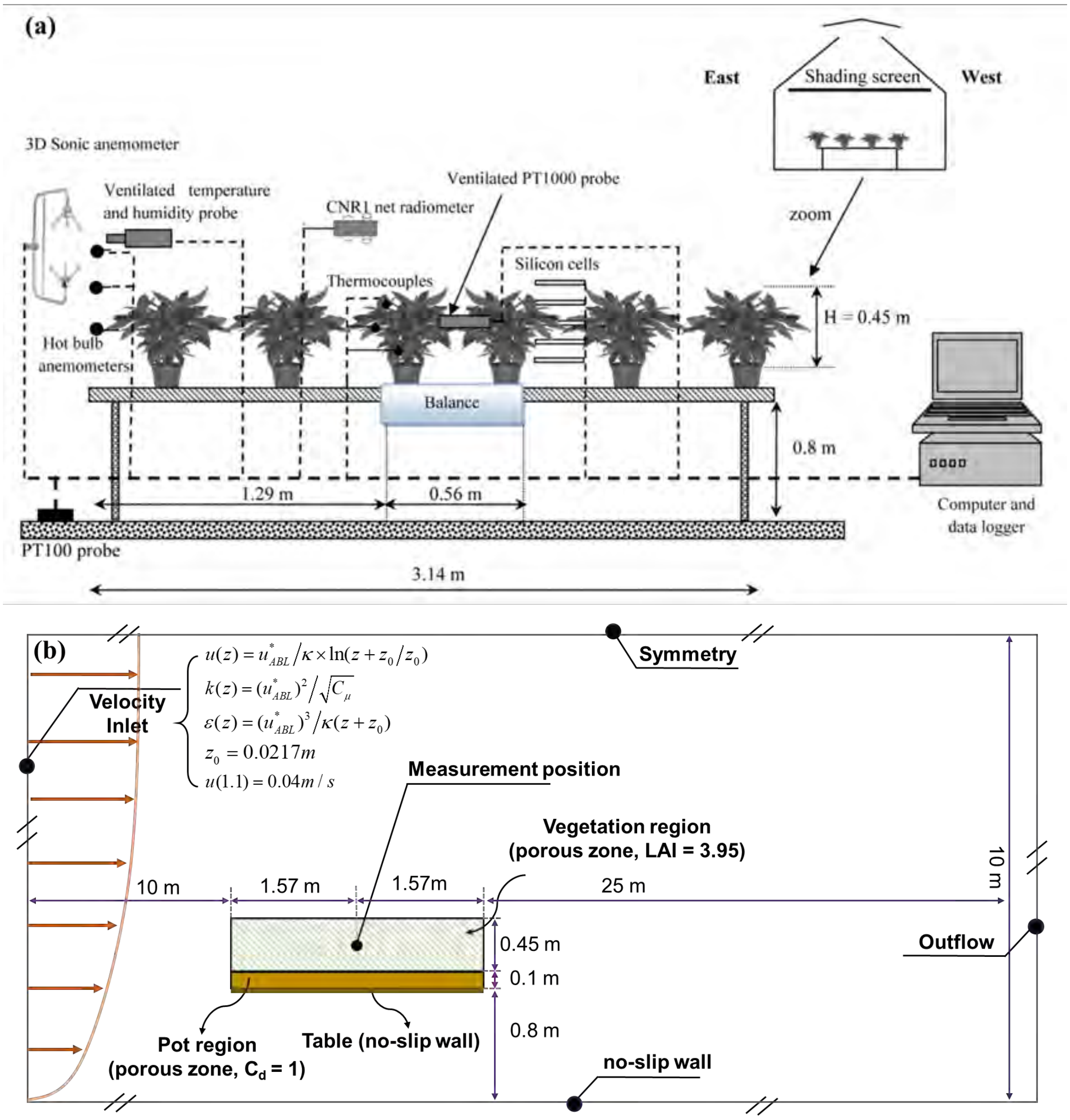

Figure A5.3 Schematics of (a) the experimental set-up [162] and CFD simulation domain, boundary conditions and measurement position for the validation case

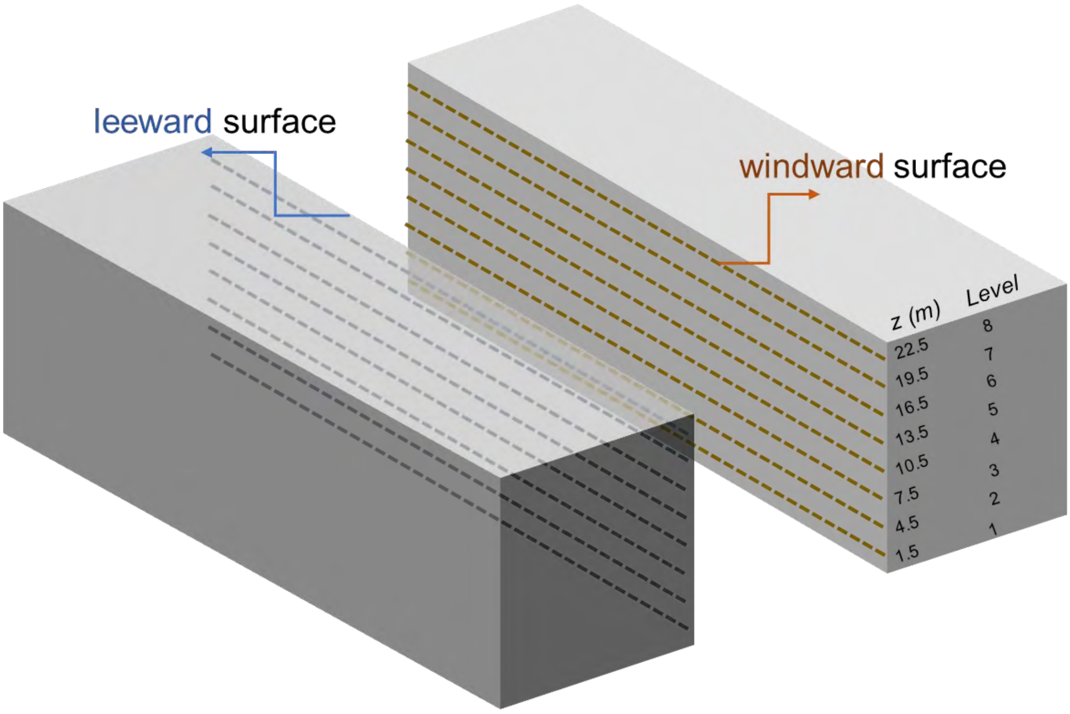

Figure A5.4 Illustration for the various horizontal lines for the calculation of average value on the leeward surface and windward surface

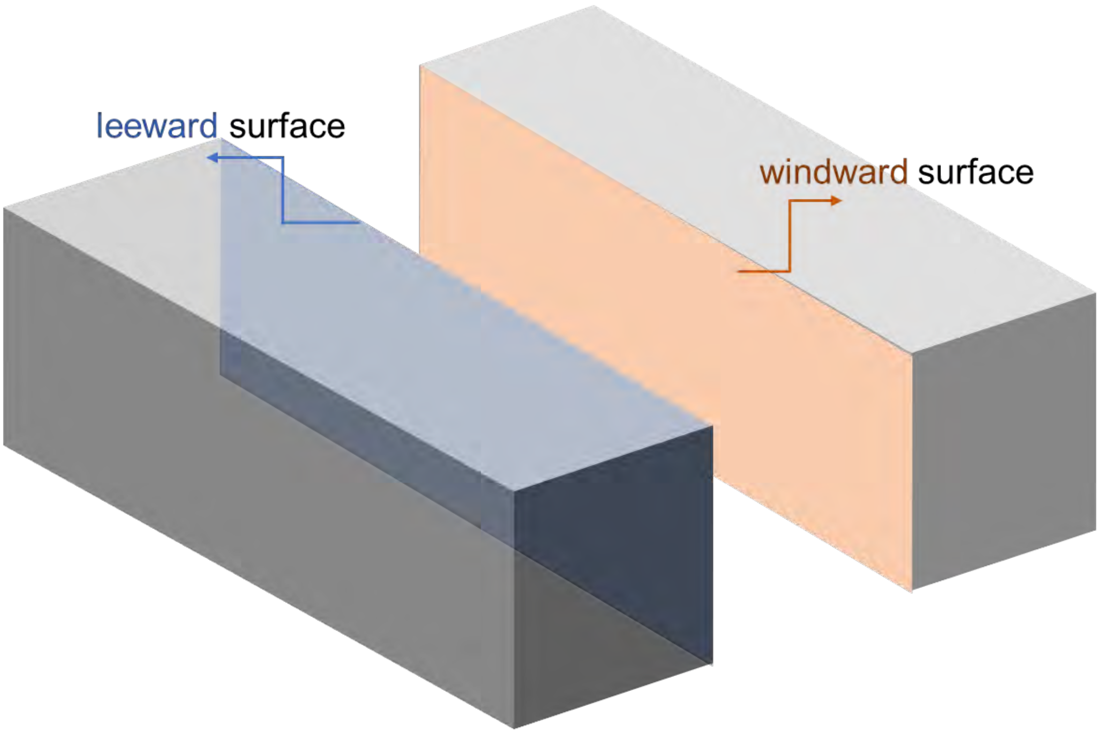

Figure A5.5 Schematics of the calculation of surface average values on the leeward and windward surface

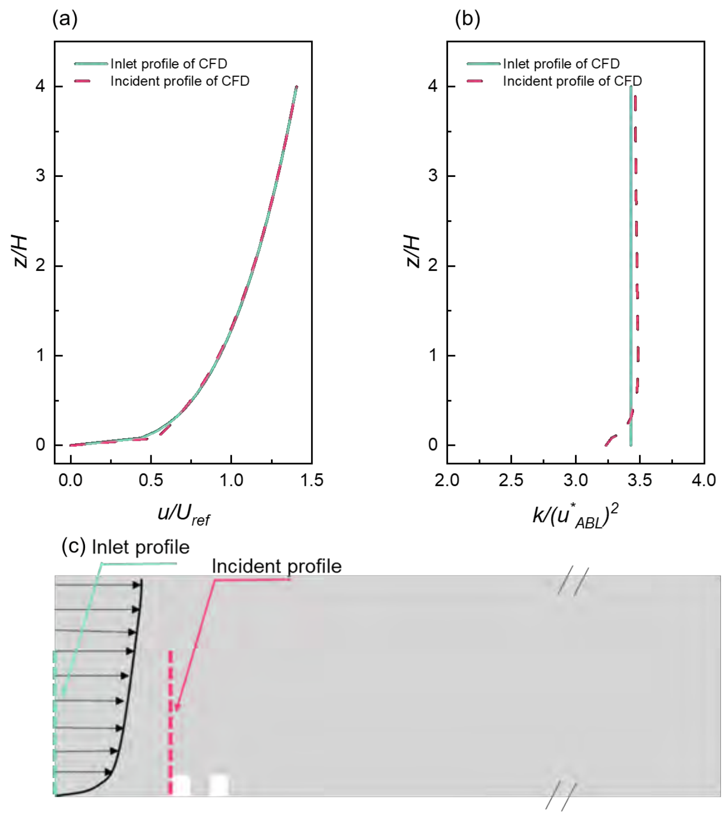

Figure. A6.1. (a) Comparison of inlet and incident dimensionless streamwise velocity (u/U_{ref}) profiles, (b) Comparison of inlet and incident dimensionless turbulence kinetic energy ($k/(u^*_{ABL})^2$) profiles, and (c) Schematic cross-section of the domain with location of inlet profile (x/H = 0) and incident profile (x/H = 5).

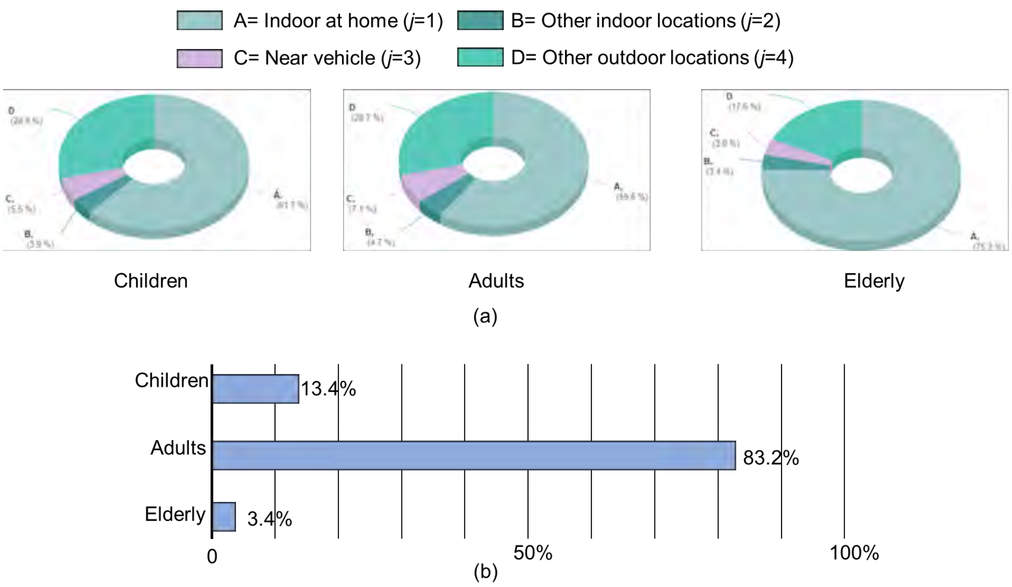

Fig. A6.2 (a) Time activity patterns for different age groups and microenvironments; and (b) demographic structure in Shenzhen, China[7].

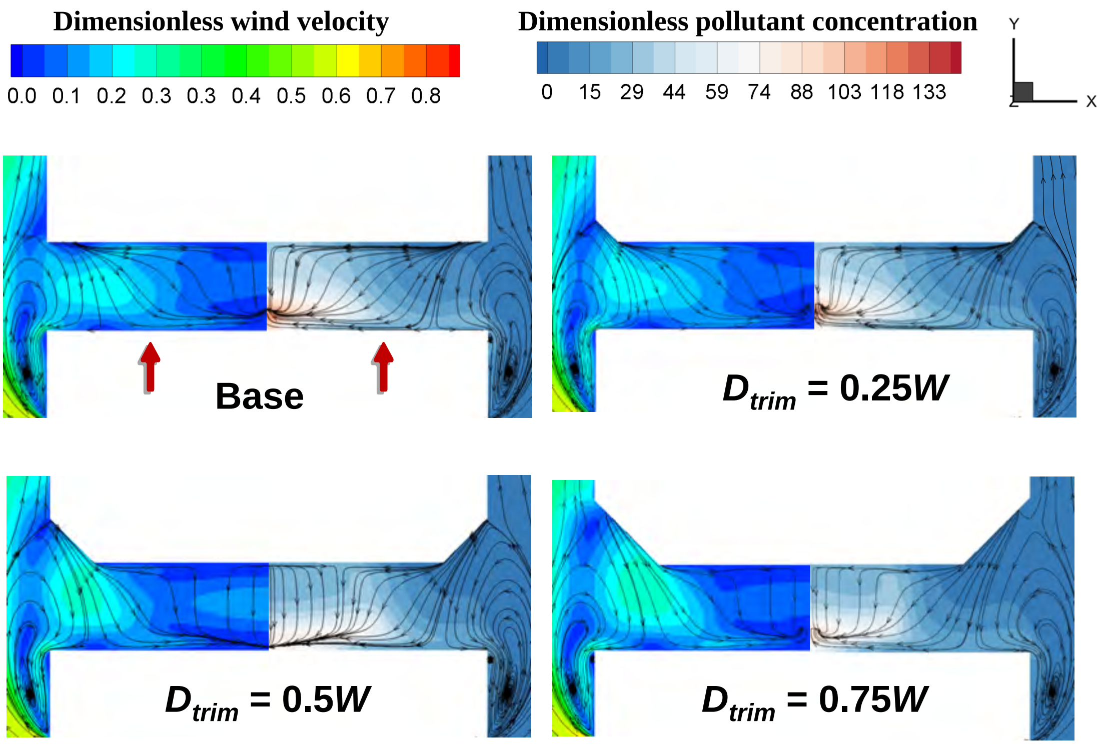

Fig. A6.2 Cross-comparison of the dimensionless wind velocity and pollutant concentration at the pedestrian level of a low-rise street canyon (H/W= 1 and L/W= 5) between the base case and design I case with different trimmed corner D_{trim}

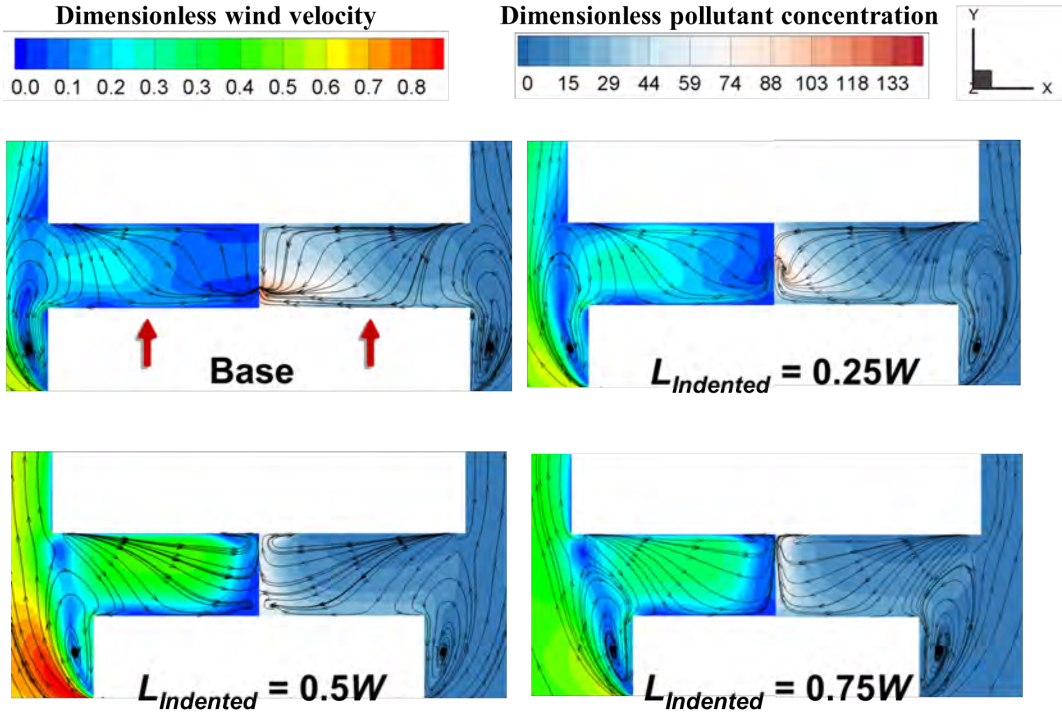

Fig. A6.3 Cross-comparison of the dimensionless wind velocity and pollutant concentration at the pedestrian level of a low-rise street canyon (H/W= 1 and L/W= 5) between the base case and design II case with different indented length $L_{indented}$

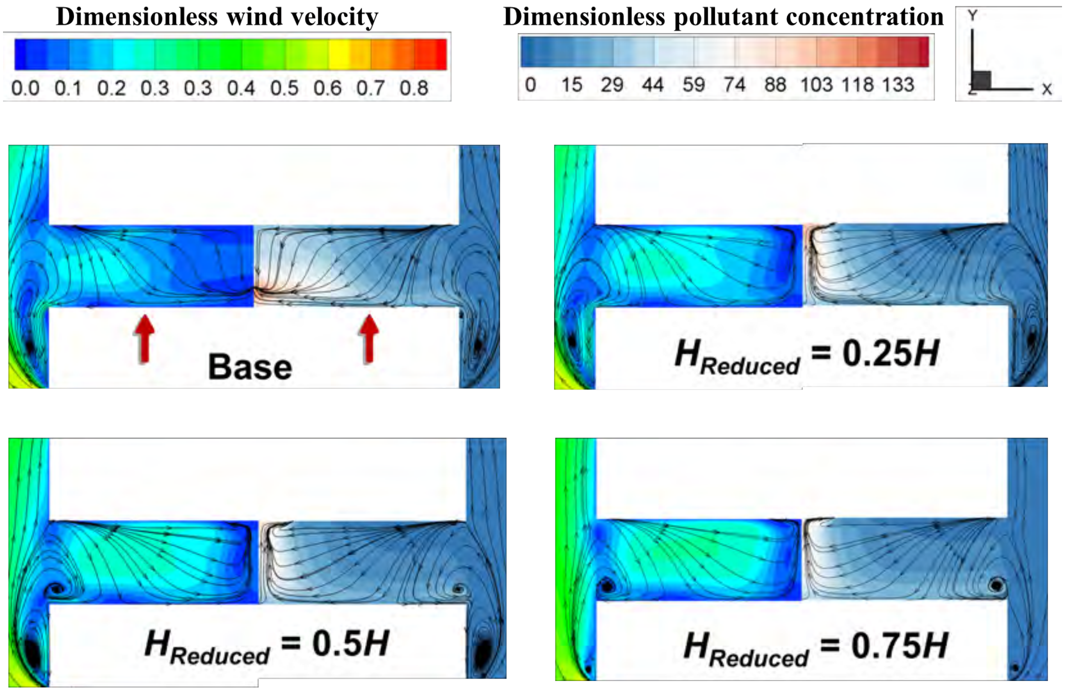

Fig. A6.4 Cross-comparison of the dimensionless wind velocity and pollutant concentration at the pedestrian level of a low-rise street canyon (H/W= 1 and L/W= 5) between the base case and design III case with different reduced height $H_{reduced}$